Climate Model Simulations of the Semi-Annual Oscillation

Aleena Moolakkunnel Jaison

Wadham College

University of Oxford

A thesis submitted for the degree of

Doctor of Philosophy

Michaelmas 2024

Acknowledgements

Well, it goes without saying, Lesley Gray and Scott Osprey, you are the best supervisors I could have asked for. I cannot thank you both enough for the incredible guidance you have given me over the past three years. Lesley, being your final student has been truly special and thank you for all the care and encouragement you have shown me. Scott, thank you for always keeping your office door wide open, and having answers to all my random silly doubts.

Big thanks to all the amazing scientists I had the privilege to meet, at Oxford and beyond, for all our discussions that shaped this thesis into a better one - Rolando Garcia, Anne Smith, Martin Andrews, Steven Hardiman, Myles Allen, Antje Weisheimer, Tim Woollings, Beena BS, Jeff knight and many others. I am deeply grateful to Peter Read and Inna Politchtchouk for examining this thesis and for the insightful discussions that greatly helped to refine my thinking. A special mention to my teachers and supervisors. Thank you, Suhas for introducing me to atmospheric physics and to Paulo for the support and patience you show as I am taking time to finish my thesis. Biggest thanks to David Richards's family and Wadham College for funding my DPhil.

Thanks to all my colleagues in the department – Olivia, Lakshmi, and Harisson- you certainly made my AOPP life extra special. Jorge, even though you left Oxford before I came, I am grateful for all those emails that made me feel like everything would be fine. Shubham, aside from all our silly fights, I hope you know you were one of the highlights of my Oxford life and how much better you made it. To all my other wonderful flatmates and friends- Ellie, Daphne, Shannon and Sam- thanks for the memories that I will cherish forever. Malavika and Arya, you are the absolute definition of girl support. I hope we will one day tick off all the libraries in our want-to-go list. And thanks to all who helped me proofread to ensure that this thesis is readable. Finally, to the postdocs at Imperial in room H713, thank you for being the best.

Now, to my favorite bunch of people in the whole world, you guys make my life so colorful just like that. I am sure I can't spell out all of you, but I am giving it a go. Akash, Jishnu, Sanjay, Vishnu, Hasna, Hashim, Sohan, Chandana, Dilsha, Nithun, Goutham, Haritha, Manji, Badeer and so on. Even if we are scattered around the world now, our countless hours of video call sessions with never-ending jokes and laughs are an irreplaceable part of my DPhil life. I love you all to the moon and back.

Finally, a very special thanks to my parents and grandparents. Appa and Amma, I cannot even write a sentence to thank you both without filling my eyes with tears. The love and support you have given me my whole life is beyond words. You made it all happen. Appa, if you had not pushed me to do that application on the last day- or, for that matter, to do most things in my life- we all know, nothing would have turned out as pretty as it has now. Amma, all those calls, even when it is late at night for you, where you just sat there and listened to my writing or presentation, even though you have nothing to do with atmospheric physics, show just how incredible you are.

Thank you all for being a part of this journey.

Abstract

The representation of the semi-annual oscillation (SAO) in models shows up a common easterly bias of several tens of ms^{-1} compared to observations, often with weaker westerly phases and stronger easterly phases in the modelled SAO. These biases in the upper stratosphere are likely a response to biases in wave forcing or the position and timing of the climatological summertime jet and Brewer-Dobson circulation (BDC). This thesis investigates the origins of SAO biases in models and explores potential methods to alleviate these biases.

The thesis begins with an analysis of the energetics of the upper stratosphere within a model and a detailed comparison with reanalysis to identify the sources of modelled SAO biases. Using the reanalysis data, the contributions of different forcing terms driving the SAO are examined through the transformed Eulerian mean momentum equation. A comparison between a climate model output from the Coupled Model Intercomparison Project (CMIP6) and reanalysis data revealed that lack of strong resolved and gravity waves, along with weakened BDC above 1hPa might be the major model deficiencies. The results suggest that increased westerly forcing from both resolved waves and gravity waves at SAO altitudes is needed to improve the SAO representation and correct the easterly bias in model.

Atmospheric waves that reach the upper stratosphere to force the SAO, first propagate vertically through the underlying region dominated by the quasi-biennial oscillation (QBO). The influence of biases in the modelled QBO on the representation of the SAO is therefore explored. A sample climate model from the QBOi project is used for detailed analysis. Analyses indicate that alleviating the QBO biases helps reduce the SAO easterly bias, with a change of up to 25% in the time-averaged equatorial SAO winds. It also improves the annual cycle representation. QBO modulation of wave filtering, primarily when the 50 hPa winds are in QBO easterly phase, was found to be responsible for a major part of the SAO enhancement, with gravity waves playing the major role.

To analyze the robustness of these results from individual climate models and to remove any model dependent biases, a multi-model analysis was conducted, examining the performance of the SAO across current state-of-the-art climate models and how these models respond to corrections in zonal-mean zonal wind QBO biases. While many models demonstrated a reasonable SAO, several had

difficulty reproducing some of the basic features of the SAO. Most models showed a reduction in easterly bias in response to the corrected QBO bias. The extent of this improvement varied significantly among models with SAO time-mean wind changes ranging from 6% to 403% with the corrected QBO. Changes in gravity wave drag (GWD) in response to the improved QBO were identified as the forcing term with the largest overall impact. A separate sensitivity experiment in which the QBO variability was completely removed was also analyzed. This did not result in an improved SAO in any of the models.

Given that GWD was identified as the dominant contributor to improving the SAO representation in current climate models, for further analysis, modifications to GW parametrization are suggested. Preliminary results from climate model runs with altered parameters in GW parametrization show promising impacts on the modelled SAO, suggesting potential future directions.

Contents

List of Figures

1 Introduction

1.1 Motivation

A reasonable representation of stratospheric variability in models is essential to improve our weather and climate predictions (Baldwin and Dunkerton, 2001). Representation of the stratospheric semi-annual oscillation (SAO), the dominant variability in the equatorial upper stratosphere's winds and temperature, is the focus of this thesis. First identified in the 1960s, our understanding of how the SAO is formed and how it influences the rest of the Earth system has significantly advanced. The influence of the SAO on the distribution and variability of atmospheric constituents like ozone which can influence our global climate have been identified early on (Gray and Pyle, 1986; Solomon et al., 1986; Jackson and Gray, 1994; Ray et al., 1994). Early studies also suggested the possible influence of the SAO on the subtropics and extratropical dynamics. Furthermore, studies in recent years strongly indicate that the SAO can influence the extra-tropics, including the time of occurrence of sudden stratospheric warmings (SSWs) (Gray et al., 2004, 2022), which have significant surface weather impacts (e.g. 'the beast from the east' in the UK (see this Met Office report - https://www.metoffice.gov.uk/weather/learn-about/weather/atmosphere/air-masses/beast-from-the-east).

The results reported in Smith et al. (2019) provide a comprehensive understanding of the representation of the zonal wind SAO in various climate models. They found that almost all climate models show an easterly bias of several tens of ms^{-1} in the SAO. Around the same time, in Gray et al. (2022), it was demonstrated that an early zonal-mean zonal wind transition from westerly to easterly phase of the SAO in the upper stratosphere can lead to an early occurrence of a SSW. This suggests that the easterly bias in the SAO noted by Smith et al. (2019), which is likely to cause an early phase transitioning to SAO easterlies, could produce a bias towards early warming predictions in models. A sample model study by Dimdore-Miles (2021) indeed showed higher occurrence of early warmings in the Met Office Unified Model (UM) (also see Menary et al. (2018)).

Therefore, an improved representation of the SAO in models is essential for simulating better atmospheric responses and improving our weather and climate predictions. However, the origins of the biases in the modelled SAO and how to tackle them remain open questions in the field. Thus, in this thesis we explore the SAO representation in climate models, identify the reasons behind the biases, and explore ways to alleviate these biases to enhance model performance.

In this thesis, as we explore the biases in model representation of SAO, the following are the primary questions we aim to address:

Q1. What are the fundamental processes that influence the SAO? Can we determine the relative contribution of various dynamical processes that drive the SAO?

Q2. Are climate models able to represent these processes accurately? What are the biases in the modelled SAO and what are the underlying reasons behind these biases? Can we identify what might be misrepresented in the models and alleviate these biases?

We aim to address these questions by analysing the SAO profile and the momentum budget of the upper stratosphere using the Transformed Eulerian Mean (TEM) momentum equation. Reanalysis data are examined to understand the momentum budget of the SAO and thus address question 1. Then, Coupled Model Intercomparison Project Phase 6 (CMIP6) data from the Whole Atmosphere

Community Climate Model (WACCM) climate model is used to compare and contrast the model's and reanalyses' budget to understand what processes are misrepresented in the model. Based on these insights, specific simulations of the Hadley Centre Global Environment Model 3 (HadGEM3) climate model, performed as part of the QBO Initiative (QBOi) project, are used to explore a potential cause for these misrepresentations in models. Previous studies have identified model biases in the underlying region that is dominated by the quasi-biennial oscillation (QBO) (Rao et al. (2020); Bushell et al. (2022); Gray et al. (2022). Correction of this bias in the QBO is a possible route to alleviate the SAO biases. The analysis is extended to a multi-model comparison to assess the robustness of our results. Lastly, recommendations for future experiments are proposed to further address the SAO biases.

1.2 Thesis structure and relation to published works

The thesis is structured as follows, where the primary findings are in chapters 4, 5 and 6:

Chapter 2 provides an overview of the middle atmosphere. It covers the large-scale circulations in the atmosphere, especially the stratosphere, and examines the roles of radiative and dynamical processes in driving these circulations. The chapter introduces the primitive equations that describe our atmosphere and explains the derivation of the TEM momentum equations. Special attention is given to atmospheric waves. Building on this background knowledge, the focus is shifted to tropical oscillations, specifically the QBO and the SAO. The chapter discusses the theory behind the formation of the SAO, the possible influence of the QBO on the SAO, the impact of the SAO on the rest of the atmosphere and our current knowledge of the biases in model representation of the SAO.

Chapter 3 describes the basic features of climate models and provides a summary of the reanalysis and model datasets utilized in this thesis. The reanalysis datasets include MERRA-2, ERA5, and ERA-Interim. Additionally, the WACCM data

that were contributed as part of the CMIP6 and the Met Office UM and its configuration Global Atmosphere (GA) 7.1 are described. The chapter also outlines the QBOi project and describes some of the methodologies employed in the subsequent chapters.

Chapter 4 explores the SAO biases in a sample climate model (WACCM). To identify the origin of the biases, the momentum budget of the upper stratosphere within the model and a more detailed comparison with reanalyses is performed. The TEM momentum equation is used to evaluate the different forcing terms that contribute to the SAO in the MERRA-2 reanalysis dataset. This is then compared with the equivalent analysis using data from a climate simulation of the WACCM. The chapter provides promising results on identifying the cause of the SAO biases. This chapter is based on a paper written by myself, co-authored by my thesis supervisors and collaborators from the WACCM modelling team, and published in the Quarterly Journal of Royal Meteorological Society (Jaison et al., 2024).

Chapter 5 builds on the results from Chapter 4, which identified that resolved and parameterized tropical waves in the upper stratosphere are both too weak. These waves propagate vertically through the QBO dominated region before reaching the SAO altitudes. The influence of biases in the modelled QBO on the representation of the SAO is therefore explored in this chapter, using the UK Met Office model. The biases in the QBO are alleviated by nudging the model lower stratospheric zonal-mean zonal winds towards ERA5 data and the response of the SAO is studied. The chapter identifies how and what forcing terms play the major role in the SAO changes and how it is correlated with QBO biases. This chapter is based on a paper written by myself, co-authored by my thesis supervisors and collaborators from the UM modelling team, and published as a discussion paper (currently in production for final publication) in Weather and Climate Dynamics (Moolakkunnel Jaison et al., 2024).

Chapter 6 is a multi-model analysis that looks at ten different present-day climate models that participated in the QBOi project, and analyses the SAO performance in them. How each of the model responds to the bias correction in the QBO is examined and quantified to understand the robustness of the results obtained in

chapter 5. The chapter explores the momentum budget to understand the drivers of SAO in each model and how they change in response to the QBO wind changes. The chapter further investigates the importance of QBO variability in models for the modelled SAO by analysing simulations where the model lower stratospheric zonal-mean zonal winds are nudged towards climatological values. Overall, the chapter provides a full assessment of which models produce a reasonable SAO, and how the SAO is dependent on the QBO in all the models. It also discusses possible routes to improve the SAO representation in our climate models.

Chapter 7 concludes by summarizing the results of the thesis presented in the previous three chapters and describes the challenges and limitations encountered during the thesis. It discusses results from a few preliminary experiments that explore possible routes for improving the modelled SAO and provides an overview of potential future directions.

2

Background

Contents

2.1 Structure of the atmosphere

Our earth's atmosphere, with its thermally and dynamically driven motions, is a fascinating physical system to study. The solar radiation, providing a constant source of energy, leads to various motions in our atmosphere. This thermal energy however does not entirely define the atmospheric circulations. The dynamical processes, by transferring energy and momentum across scales, alter the radiatively driven circulations significantly. This chapter begins with a brief introduction to the climatology of our atmosphere, with a particular focus on the stratosphere, highlighting the interaction between thermal and dynamical processes.

Our atmosphere can be categorised into different layers depending on the vertical structure of the temperature, as shown in Figure 2.1. The lowest layer, the one closest to the surface and where we experience the day-to-day weather is known as the troposphere. Depending on latitude and weather conditions, the troposphere extends from the surface up to approximately 8 to 15 kilometers in altitude. In this layer, the temperature decreases with height. This temperature profile makes the troposphere unstable and the warmer air at the surface can rise and cool down adiabatically at higher altitudes. The presence of water vapor in the troposphere adds further physical effects. The latent heat release due to condensation of water vapor plays a key role in convection and circulations in the troposphere. As the solar heating in troposphere is maximum at equator and minimum at poles, a meridional gradient of temperature is also present. This gradient, and other factors like earth's rotation and dynamical instability, give rise to large scale circulation patterns over most of the troposphere. The thermally driven Hardley cell dominates equatorial (equator to 30° in SH and NH) latitudes and the Polar cell dominates polar regions (60° to 90° in SH and NH). In between, the Ferrel cell formed due to dynamical instability dominates the mid-latitudes in both the hemispheres. The presence of temperature gradients, eddies and moisture make the troposphere a highly unstable layer, capable of producing various weather events such as storms, hurricanes and more.

Above the troposphere is the layer termed as the stratosphere. The stratosphere extends from the tropopause up to around 50 kilometers in altitude. A reasonable

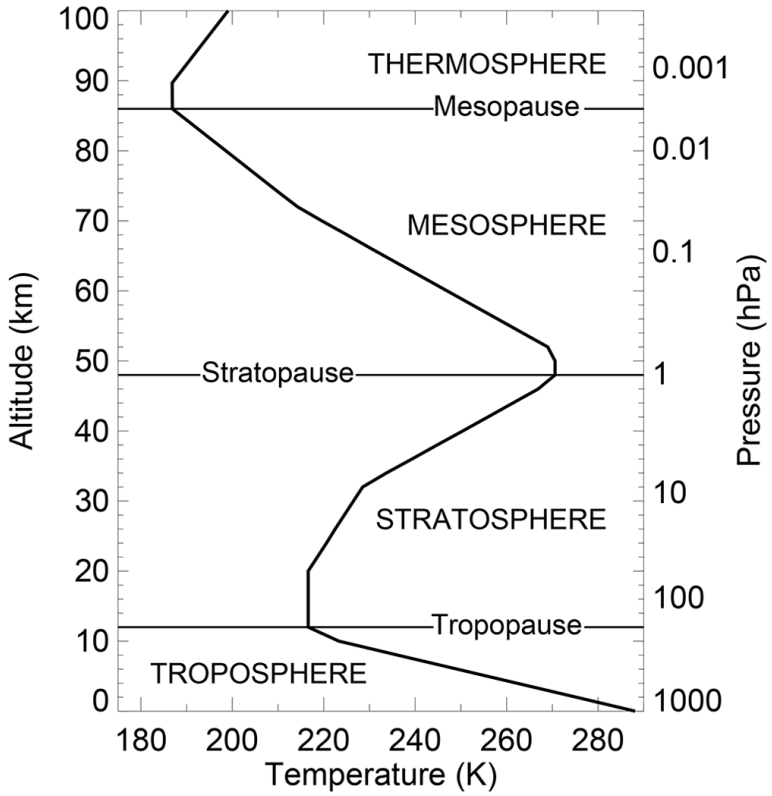

Figure 2.1: Annually averaged mid-latitude temperature profile, based on the US Standard Atmosphere (Committee on Extension of Standard Atmosphere, 1976; Minzner, 1977). From Butchart (2022).

representation of the stratosphere plays a key role in improving our weather and climate predictions (Baldwin and Dunkerton, 2001). In the stratosphere, the temperature increases with altitude due to ozone-related chemical processes that heat the atmosphere at these levels. This temperature increase with height creates a stably stratified layer, making the stratosphere different from the troposphere. In addition, the stratosphere is generally dry, thus lacking the physical effects due to latent heating present in the troposphere. The variabilities in the stratosphere are mainly driven by the forcings from troposphere, and these variabilities, in turn, influence the tropospheric weather in various ways. Large-scale circulations in the stratosphere are discussed in detail in section 2.6.

Above 50 kilometers in altitude, the temperature starts to decrease again with height, due to the diminishing levels of ozone. This layer, spanning from around 50 kilometers to 80 kilometers in altitude, is called the mesosphere. Altitudes

close to mesopause has the coldest temperatures on earth. While the stratosphere is dominated by the impacts of large-scale planetary waves, the mesosphere is dominated by smaller-scale gravity waves and tides.

Above the mesosphere, from around 80 kilometers starts the thermosphere. Interestingly, this layer is home to the well-known northern lights, and is the region where the International Space Station orbits. The thermosphere behaves significantly different from the layers described so far. In the thermosphere, the temperature increases with altitude due to increased absorption of high energy UV and X-ray by the sparse gas molecules present. As we go higher, the air becomes sufficiently thin, and molecular diffusion dominates over eddy dynamics, making the stratification of molecules based on their molecular mass. Increased ionization makes electromagnetic effects significant, and even higher, the solar wind and geomagnetic effects dominate.

2.2 Primitive equations

Mathematical equations that describe thermally and dynamically driven atmospheric motions are well-developed and consistently used in climate models to simulate the behaviour of the atmosphere. These equations can be intuitively understood as expressions of the rate of change of momentum and energy under the influence of various forces present in the atmosphere.

The major forces in our atmosphere include gravity, the pressure gradient force, dissipative forces, the centrifugal force, and the Coriolis force. Gravity is a fundamental force that acts on everything on Earth, including air parcels, pulling them towards the center of the Earth. The pressure gradient force arises when there is a difference in atmospheric pressure, causing the air parcels to move from regions of high pressure to low pressure. There are also dissipative forces in the atmosphere, such as viscous drag, which act to slow down the motion of air parcels and dissipate kinetic energy. Furthermore, because the Earth is a rotating body, air parcels experience pseudo-forces such as the centrifugal force and the Coriolis force. The Coriolis force in particular, affects the direction of

motion, causing deflection to the right in the Northern Hemisphere (NH) and to the left in the Southern Hemisphere (SH).

The first three equations in the set of primitive equations describe how these forces act to change momentum in the horizontal directions: east-west, north-south, and the hydrostatic balance in the vertical. These equations account for the contributions of gravity, pressure gradient, viscous drag, and Coriolis forces. The first three in the set of primitive equations in a log-pressure coordinate (where $z = -Hln(\frac{p}{p_s})$, p is pressure and p_s is pressure at a reference level) on the sphere can be written as follows (from Andrews et al. (1987)):

$$\frac{\mathrm{D}u}{\mathrm{D}t} - \left(f + [\frac{utan\phi}{a}]\right)v + \frac{\Phi_\lambda}{acos\phi} = X \tag{2.1}$$

$$\frac{\mathrm{D}v}{\mathrm{D}t} - \left(f + [\frac{utan\phi}{a}]\right)u + \frac{\Phi_\phi}{a} = Y \tag{2.2}$$

$$\frac{\partial\Phi}{\partial z} = \frac{RT}{H} \tag{2.3}$$

Here u and v are zonal and meridional velocities, $f = 2\Omega sin\phi$ is the Coriolis parameter, where $\Omega = 7.292 \times 10^{-5}s^{-1}$ is the rotation rate, ϕ is the latitude, λ is the longitude, a is the mean radius of Earth, Φ is the geopotential, H is the mean scale height ($\equiv \frac{RT_s}{g_0}$, and is equal to 7 km, for a reference temperature (T_s) of 240 K), R is the gas constant (for stratospheric calculations, gas constant of dry air is sufficient, which is 287 $JK^{-1}kg^{-1}$), $\kappa = \frac{R}{c_p} = \frac{2}{7}$, where c_p is the specific heat at constant pressure, (X,Y) are horizontal components of friction or other non-conservative mechanical forcing, and T is the temperature. $\frac{\mathrm{D}}{\mathrm{D}t}$ denotes the total derivative in time and ∂ notation denotes partial derivative. The subscripts are used to simplify partial derivative notation. For example, Φ_ϕ implies a partial derivative of Φ with respect to ϕ.

Another fundamental feature of the atmosphere is the conservation of mass and energy. The conservation of mass implies that no new mass is created or destroyed in the system, so the convergence or divergence of air parcels in all directions must

balance out. This is mathematically expressed through the continuity equation. The conservation of energy indicates that the rate of change of potential temperature, a measure of the thermal state of air parcels, must equal the net heating, which is the sum of radiative, conductive, and latent heat exchanges. The thermodynamic energy equation captures this balance. These two basic features are expressed in the final two equations in the primitive equations as follows:

$$\frac{\frac{\partial u}{\partial \lambda} + \frac{\partial}{\partial \phi}(v cos\phi)}{a cos\phi} + \frac{\frac{\partial}{\partial z}(\rho_0 w)}{\rho_0} = 0 \tag{2.4}$$

$$\frac{\mathrm{D}T}{\mathrm{D}t} + \frac{\kappa T w}{H} = \frac{Q}{C_p} \tag{2.5}$$

Here w is the vertical component of velocity, $\rho_0 = \frac{p}{RT_s}$ and Q is the diabatic heating term. The velocity components are defined as

$$(u, v, w) = \left((a cos\phi)\frac{\mathrm{D}\lambda}{\mathrm{D}t}, a\frac{\mathrm{D}\phi}{\mathrm{D}t}, \frac{\mathrm{D}z}{\mathrm{D}t}\right)$$

Various approximations can be applied to these equations depending on the weather system being studied, by using scale analysis (i.e. ignoring terms with negligibly small magnitude). In this thesis, we are interested in the stratosphere, and later in section 2.5, we will see how primitive equations can be rearranged in a highly useful manner to study the stratospheric variabilities.

In the following section, using the simplified primitive equations, the derivation of possible wave modes in the atmosphere is discussed. Atmospheric waves act to transfer energy and momentum across scales, thus playing a major role in stratospheric dynamics.

2.3 Atmospheric waves

Atmospheric waves are defined as quasi-periodic perturbations to the atmospheric fields like wind, temperature and pressure. Atmospheric waves, like any other waves in any physical system, are created by the displacements from the mean state and the presence of a restoring force to return the system to equilibrium.

Depending on the kind of restoring force, our atmosphere has a range of allowed wave motions, named as Kelvin, Rossby, Gravity waves (GW), etc. For example, gravity waves have the restoring force as gravity or buoyancy, while latitudinal variation of Coriolis force provide the restoring force for Rossby waves. The waves can be further classified depending on various properties such as the nature of forcing mechanisms (forced or free waves), direction of propagation (trapped waves or waves that can propagate in all directions), time dependence of amplitude (steady and transient waves), and more.

Similar to other wave motions, atmospheric waves don't transfer the actual air parcels, only the energy and momentum are transferred from one location to another. When the waves break or dissipate, the energy is transferred to the background flow. This energy transfer by waves drives various phenomena in the atmosphere, especially in the stratosphere, including the QBO, the SAO and SSWs. In this section, we will first look at the equatorial waves which are major drivers of the tropical middle atmosphere dynamics, and a brief description of extra-tropical Rossby waves is provided at the end of this section.

2.3.1 Equatorial waves

Equatorial waves are atmospheric waves confined near the equator that propagate both horizontally and vertically, typically with a period of a few days (Matsuno, 1966; Gill, 1980). Primarily generated by large-scale convective heating in the equatorial troposphere, they can travel vertically into the middle atmosphere, where they significantly influence equatorial stratospheric oscillations such as the QBO and SAO. Depending on their fundamental dynamics, equatorial waves are classified into Kelvin waves, Rossby-Gravity waves, equatorial Rossby waves and Inertio-gravity waves. Using primitive equations describing the atmosphere and by solving for wave-like solutions, the dispersion relations for these different types of waves can be found.

To derive the wave modes in atmosphere, linear wave theory can be used. The theory assumes that the wave amplitude is small compared to the wavelength and depth of the fluid. This allows the primitive equations (section 2.2) governing the

fluid motion to be linearized, simplifying the analysis. The linearization separates the flow into mean flow (e.g. $\bar{u}$) and deviations from the mean flow (e.g. u') and assumes that terms with second order deviations are small enough to be neglected. Since we are interested in the equatorial waves, a beta plane approximation ($f = \beta y$, where $\beta = 2\Omega/a$) is satisfactory as the waves are confined to equatorial latitudes. To simplify the derivation of equatorial wave theory, it is assumed that the background atmosphere is at rest ($\bar{u} = 0, \bar{\theta}_y = 0$), and nonconservative processes such as viscous dissipation are ignored. The disturbances then satisfy the following simplified form of primitive equations in beta plane cartesian coordinates.

$$u'_t - \beta y v' + \Phi'_x = 0 \tag{2.6}$$

$$v'_t - \beta y u' + \Phi'_y = 0 \tag{2.7}$$

$$u'_x + v'_y + \rho_0^{-1}(\rho_0 w) = 0 \tag{2.8}$$

$$\Phi'_{zt} + N^2 w' = 0 \tag{2.9}$$

For obtaining different wave modes, the following wave like solutions for atmospheric variables is substituted to the above equations. N is assumed to be a constant for simplicity.

$$(u', v', w', \Phi') = e^{\frac{z}{2H}} Re[u(y), v(y), w(y), \Phi(y)] e^{i(kx+mz-\omega t)} \tag{2.10}$$

The resulting equations are used to identify various wave modes possible in the equatorial atmosphere. Further details on derivations can be found in Andrews et al. (1987).

2.3.1.1 Kelvin waves

Kelvin waves are eastward propagating equatorial waves that play a key role in vertical momentum and heat transport. Kelvin waves are noted in the literature as partially responsible for the westerly phases of the QBO and SAO (Hirota, 1978; Garcia, 2000). This class of wave modes have zero meridional wind component. It should be noted that while this is based on the equatorial beta-plane assumption,

derivations on a full sphere have shown that Kelvin waves can have non-zero meridional velocities. The non-zero meridional velocities of Kelvin waves are important for slowly rotating planets like Venus, while for a rapidly rotating planet such as Earth, this component is extremely small and a beta plane approximation works well. Thus, the dispersion relation for the Kelvin waves on equatorial beta plane is obtained by keeping $v' = 0$ and substituting wave-like solutions for the remaining variable perturbations into the simplified primitive equations (Andrews et al., 1987). This gives

$$\omega = -N\frac{k}{m} \tag{2.11}$$

Where ω is the frequency, k is the zonal wavenumber and m is the vertical wavenumber. The meridional structure of Kelvin wave is proportional to $e^{-\frac{\beta k y^2}{2\omega}}$. This results in the constraint that the coefficient of y^2 must be negative for the wave to be bounded at the equator. Hence $\frac{\omega}{k}$, which is the phase velocity, must be positive. Thus, Kelvin waves can only have eastward zonal phase speed. When there is a non-zero background zonal wind, ω will be replaced by the doppler shifted frequency, which is $\omega - k\bar{u}$, thus the ω only needs to be eastward with respect to the background flow.

2.3.1.2 Non-zero meridional velocity modes

While Kelvin waves are characterized by zero meridional wind component, the rest of the equatorial wave modes are solved by allowing the v' to be nonzero. This leads to the following wavenumber-frequency relationship.

$$\frac{m^2\omega^2}{N^2} - k^2 - \frac{\beta k}{\omega} = (2n+1)\frac{\beta|m|}{N} \tag{2.12}$$

The gravest mode of this solution ($n = 0$) is called the Rossby-gravity (RG) wave. The observed RG waves have westward phase speeds relative to the background flow and are an important forcing term for the easterly phase of QBO (Maruyama, 1969; Holt et al., 2022). Equatorial modes with $n \geq 1$ give rise to the next

two classes of equatorial waves. The high frequency waves are called the inertia-gravity waves and the low frequency waves are called equatorial Rossby waves. More details on Rossby waves and gravity waves, which are not just equatorial wave modes, are provided later.

While the above linear wave theory provides a deeper understanding of the characteristics and vertical and horizontal structure of waves, a further simplified version is sometimes used to identify the equatorial waves observed in the real atmosphere. This is known as shallow water theory. Shallow water theory assumes that the depth of the fluid layer is small compared to the horizontal wavelengths. These assumptions significantly simplify the vertical structure of the waves, approximating it as the first baroclinic mode for a given equivalent depth, h. The concept of equivalent depth allows for the representation of various vertical modes of shallow water waves, by varying the value of equivalent depth. The phase velocity for gravity waves in this context is defined as $c = \sqrt{gh}$.

Figure 2.2 shows the dispersion curves of shallow water equatorial waves plotted as wavenumber versus frequency. Observations have shown that atmospheric wind and temperature perturbations roughly follow these dispersion curves, helping us to identify the various wave types present in our atmosphere at different places and times.

2.3.2 Gravity waves

Gravity waves are atmospheric waves which have buoyancy or stratification of the atmosphere as its restoring mechanism. Pure internal gravity waves are produced due to buoyancy restoring forces. At large enough scales (O(1000km)), where the effect of Earth's rotation becomes significant, the Coriolis force along with buoyancy acts as restoring force to form inertio-gravity waves. The smaller scale waves, with horizontal wavelengths of tens to hundreds of kilometers, are identified as an important source of variability in the stratosphere and mesosphere. These waves are often parametrized in weather and climate models due to the coarser resolution of the models which cannot resolve these smaller scale waves. Additionally,

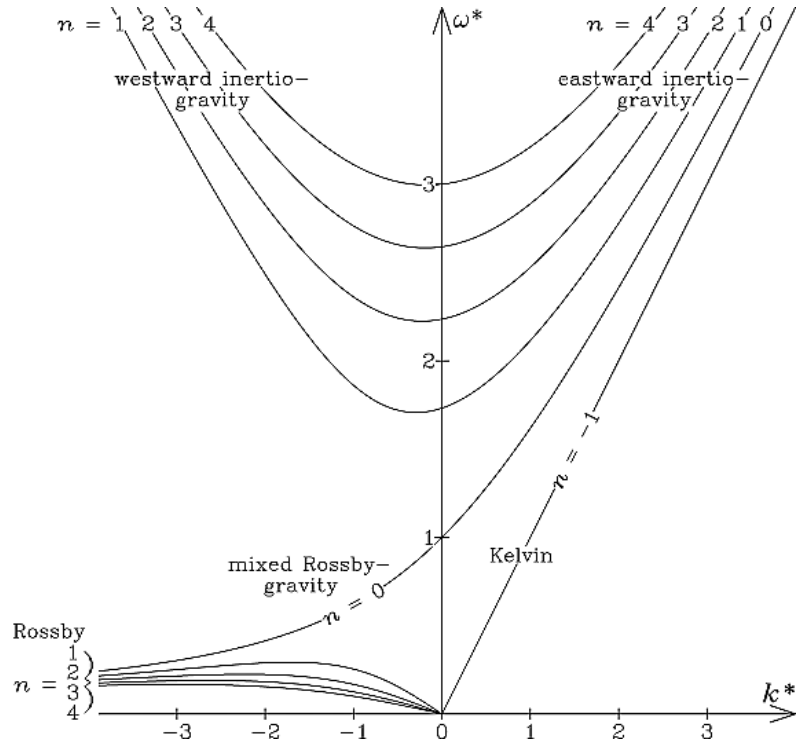

Figure 2.2: Dispersion curves for equatorial waves in a shallow water system (up to n = 4) as a function of the nondimensional frequency, ω^*, and nondimensional zonal wave number, k^*, where $\omega^* = \omega/\sqrt{\beta c}$, and $k^* = k/\sqrt{\beta/c}$. $c = \sqrt{gH}$ and H is the mean height of barotropic waves or the equivalent depth of baroclinic waves, and β is the meridional derivative of the Coriolis parameter. Westward propagating waves (relative to the zero basic state) appear on the left, and eastward propagating waves appear on the right. From Kiladis et al. (2009).

observations that detect small-scale gravity waves in middle atmosphere are still sparse. Gravity waves are often generated in the troposphere either due to orographic effects such as flow over mountains, or non-orographic processes like unstable wind shear, disturbance along the frontal boundary (boundary between two air masses with different density/temperature) and convection. Non-orographic processes are more common at equatorial latitudes. Orographic waves have horizontal phase speed distribution centered about zero, while non-orographic processes might have phase speed closer to tropospheric wind speeds. Gravity wave velocities can be in either direction relative to background flow and they can occur at any latitude. The standard dispersion relation of gravity waves can be derived from primitive equations using wave-like solutions (Gill, 1982), resulting in the following equation

$$\omega^2 = \frac{f^2 m^2}{k^2 + m^2} + \frac{N^2 k^2}{k^2 + m^2} \tag{2.13}$$

In models, the Coreolis and non-hydrostatic effects are often neglected when parametrizing the small-scale gravity waves, which result in a simpler dispersion relation $\omega = -N\frac{k}{m}$. (This is similar to Kelvin waves. Kelvin waves are indeed a special type of gravity wave which is affected by earth's rotation and confined to equatorial latitudes). As noted previously, due to the background winds, the frequency gets doppler shifted $\omega - k\bar{u}$. The dispersion relation suggests that the gravity waves have higher phase speed ($\frac{\omega}{k}$) when the vertical wavenumbers are smaller. Therefore, parameterizing waves with smaller vertical wavenumbers ensures more effective wave propagation into the upper stratospheric regions.

2.3.2.1 Non-orographic GW parametrisation

Climate models use non-orographic gravity wave (NOGW) parametrisation schemes to account for the small-scale unresolved gravity wave forcing generated by convection or frontal systems in the atmosphere. These schemes are especially important in improving the tropical wind profile in the stratosphere. Lott et al. (2024) provides a comprehensive overview of various NOGW parametrisation schemes used in models participated in QBOi, a brief summary of which is presented here. The schemes are divided into two broad categories. The first, based on Lindzen (1981), employs monochromatic gravity waves, meaning the waves have a constant phase speed and frequency. This was further modified by Alexander and Dunkerton (1999) to include a range of waves, each evolving independently. Various later studies have refined the scheme to include NOGW source parametrisation from convection and frontal systems (Beres et al., 2005; Lott and Guez, 2013; de la Cámara and Lott, 2015). The second category includes schemes developed by Hines (1991) and Warner and McIntyre (2001) to implement wave breaking better and the waves are considered as a continuous spectrum. Hines (1991) and Warner and McIntyre (2001) differs mostly in how wave dissipation is achieved. In Hines (1991), the vertical wavenumbers are doppler shifted and a wavenumber cutoff is present, with

mostly saturating lower wavelength waves. In Warner and McIntyre (2001), the saturation is achieved by an empirical criterion of shape m^{-3}, which is derived based on observations. Variations of the scheme include Scinocca (2003a). The schemes also incorporate modifications to include latitude-dependent sources.

2.3.3 Rossby waves

Rossby waves are planetary scale waves which have the latitudinal variation of Coriolis force as its restoring forcing. These waves are seen as an equatorially trapped mode and as extratropical waves with no latitudinal bounds. Extratropical Rossby waves play a key role in the extratropical winter hemisphere where they can affect the polar vortex and lead to SSWs as discussed in section 2.6.2. At high latitudes, these waves are generally forced by mountains and by land-sea thermal contrast, and can propagate to stratosphere when the background winds are westerly. The wave-like solution for Rossby waves suggests that the waves can propagate vertically only if the following condition is satisfied:

$$\bar{u} - c = \frac{\beta k}{k^2 + l^2 + \frac{f_0^2 m^2}{N^2}} < \bar{u}_c = \frac{\beta k}{k^2 + l^2 + \frac{f_0^2}{4H^2 N^2}} \tag{2.14}$$

where,

$$m^2 = \frac{N^2}{f_0^2}\left[\frac{\beta}{\bar{u} - c} - (k^2 + l^2)\right] - \frac{1}{4H^2} \tag{2.15}$$

This implies that $0 < \bar{u} - c < \bar{u}_c$, for positive vertical wavenumbers ($m^2 > 0$). This is known as the Charney-Drazin criterion for the vertical propagation of planetary waves (Charney and Drazin, 1961). Thus, waves with westward phase speeds relative to background and phase speed less than $\bar{u}_c$ can only propagate to stratosphere. Since $\bar{u}_c$ is inversely proportional to horizontal wavenumbers, waves with smaller wavenumbers are more likely to propagate to middle atmosphere. Like other waves, planetary waves can grow in amplitude with altitude and lead to planetary wave breaking, depositing momentum in the background flow. Radiative damping and critical level filtering are relevant as well.

2.3.4 Wave saturation and dissipation

Atmospheric waves transfer or exchange energy and momentum through processes like wave-wave and wave-mean flow interactions. While the wave-wave interaction allows transfer of energy between the wavenumbers, wave-mean flow interactions help to deposit momentum to the mean flow. The interactions are a bit more complex as it can involve non-linear processes and are still studied extensively. Processes like radiative damping and convective overturning of waves are important mechanisms in the tropics that attenuate waves and deposit momentum to the mean flow. This wave-mean flow interactions play a major role in driving equatorial stratospheric oscillations.

Over large enough time periods, processes like radiative damping that cause the decay of waves through radiative processes become important, while processes like convective overturning occur when waves reach saturation. The amplitude of atmospheric waves shows an e-folding growth with altitude proportional to $e^{\frac{z}{2H}}$ due to the decrease in atmospheric density. However, beyond a particular level the amplitude cannot grow further and leads to the breaking of the waves, similar to oceanic waves breaking on a beach. This 'wave breaking' leads to turbulent mixing and wave-induced motions of mean flow. Above this level, the gravity waves are saturated and cannot further grow in amplitude. The waves also transfer momentum between wavenumbers to limit further wave growth.

Wave saturation also occurs when waves approach their critical layer. When the speed of background flow is the same as the phase speed of the wave it is known as the critical layer. As the wave approaches the critical layer, the vertical wavelength and group velocity becomes small, making it susceptible to more dissipation. This critical layer filtering of waves leads to energy dissipation through turbulence or increased drag which can provide acceleration to the background flow. The vertical shear of the background wind is one of the important features that determines the characteristics of atmospheric waves and critical layer filtering. WKBJ (Wentzel–Kramers–Brillouin–Jeffreys) theory explains how the shear affects the wave-mean flow interaction. For example, theory suggests that Kelvin waves can only

exist in regions where $\bar{u} < c$. This mechanism is identified as a significant process in dissipating waves, so that their momentum is transferred to the background flow, thus accelerating the QBO and SAO winds.

2.4 Barotropic and baroclinic instability

So far, we have described the allowed wave modes in the atmosphere which are periodic and have bounded amplitudes. Solutions to linearized primitive equations also suggest the possibility of wave instabilities, in which the amplitude of a disturbance in the atmosphere grows without limit. While waves carry energy and momentum without causing any net change to the flow, instabilities can accelerate the air parcels and alter the flow significantly.

In the middle atmosphere, the two main classes of instability are barotropic and baroclinic instability. Barotropic instability is associated with the horizontal shear of a jet like flow, and generally involves the mixing of different air masses. Barotropic instability grows by converting the kinetic energy of the mean flow into perturbations and the instability tries to reduce the zonal wind shear. Baroclinic instability, on the other hand, is linked to the vertical curvature of the flow. Due to thermal wind balance, this vertical wind shear is associated with a mean horizontal temperature gradient and baroclinic instability grows by converting the potential energy of the temperature gradient.

The origin of instability can be understood as the growth of disturbance in the atmosphere when the restoring forces that usually produce an atmospheric wave act in the opposite way. For example, the restoring force for Rossby waves in a simple barotropic atmosphere is the gradient in potential vorticity (which is generally positive due to earth's absolute vorticity). The necessary condition for barotropic instability in a flow with horizontal shear and no vertical shear, is the reversal of the barotropic vorticity gradient, where the barotropic vorticity gradient is given by

$$\zeta_y = \beta - U_{yy} \tag{2.16}$$

where β is the equatorial Rossby parameter, U is the zonal-mean zonal wind and y is the distance from the equator. This is known as the Rayleigh–Kuo criterion which states that the latitudinal gradient of absolute vorticity must change sign somewhere in the flow.

More generally, Charney and Stern (1962) showed that when the gradient of quasi-geostrophic potential vorticity changes sign somewhere in a flow, this provides a necessary condition for instability growth. Previous studies have also shown that when there is a negative gradient of quasi geostrophic potential vorticity, there is the possibility for growth of two-day waves, which have similar characteristics as the Rossby gravity wave normal mode (Salby, 1981; Norton and Thuburn, 1996).

Section 2.7 discusses how the atmospheric disturbances described so far play a huge role in developing the climatology of the equatorial stratosphere.

2.5 TEM - quantifying wave-mean flow interaction

As noted earlier, the waves in our atmosphere are most relevant in transferring energy and momentum. When these waves dissipate through mechanisms like critical layer absorption and wave breaking, the waves deposit momentum to the background flow. To understand and quantify this, we make use of the Eliassen-Palm (EP) flux diagnostics. While the EP flux diagnostics described by Eliassen and Palm (1961) are more relevant in extra-tropical regions due to the inverse dependence on Coriolis parameter, the definition of the Transformed Eulerian Mean (TEM) momentum equation helps us to derive EP flux diagnostics valid in the equatorial regions as well.

To understand the behavior of the background flow and eddies, we can decompose the atmospheric fields in the primitive equations into Eulerian zonal-mean components and deviations from the zonal-mean. In the Eulerian framework, observations are made at a fixed location, where particles flow in and out. In the stratosphere and mesosphere, using the zonal mean to understand physical phenomena proves to be effective. However, a simple Eulerian mean decomposition is not sufficient for understanding the contributions of eddy flux to the zonal-mean

flow. A more effective approach involves a simple rearrangement of the equations, thus obtaining the TEM equations. A residual-mean meridional circulation $(\overline{v}^*, \overline{w}^*)$ is defined and substituted into the Eulerian-mean equations to derive the TEM. The residual-mean circulation is defined as

$$\overline{v}^* = \overline{v} - \frac{1}{\rho}\left(\frac{\rho_0 \overline{v'\theta'}}{\overline{\theta}_z}\right)_z \tag{2.17}$$

$$\overline{w}^* = \overline{w} - \frac{1}{acos\phi}\left(\frac{cos\phi \overline{v'\theta'}}{\overline{\theta}_z}\right)_\phi \tag{2.18}$$

Substituting the above equations to Eulerian mean equations and rearranging gives the TEM momentum equation as

$$\frac{\partial \overline{u}}{\partial t} = -\overline{v}^*[\frac{1}{acos\phi}\frac{\partial \overline{u} cos\phi}{\partial \phi} - f] - \overline{w}^*\frac{\partial \overline{u}}{\partial z} + \frac{1}{\rho_0 acos\phi}\nabla \cdot F + \overline{X} \tag{2.19}$$

Where,

$$\nabla \cdot F = \frac{1}{acos\phi}\frac{\partial}{\partial \phi}(F^{(\phi)} cos\phi) + \frac{\partial F^{(z)}}{\partial z} \tag{2.20}$$

And,

$$F^{(\phi)} = \rho_0 acos\phi\left(\overline{u}_z \frac{\overline{v'\theta'}}{\overline{\theta}_z} - \overline{u'v'}\right) \tag{2.21}$$

$$F^{(z)} = \rho_0 acos\phi\left(\left[f - \frac{1}{acos\phi}\frac{\partial \overline{u} cos\phi}{\partial \phi}\right]\frac{\overline{v'\theta'}}{\overline{\theta}_z} - \overline{w'v'}\right) \tag{2.22}$$

The vector F, known as the EP flux, and its divergence provide the acceleration for the background wind, as indicated by the third term on the RHS of equation 2.19. This term highlights the contribution of eddy forcings, while the first two terms on the RHS represent the advection of momentum due to the residual-mean circulation. The TEM framework can be utilized to understand the forcing mechanisms of various phenomena in the stratosphere. How the TEM forcing terms can be understood in the equatorial upper stratosphere is discussed in detail in section 2.8.

2.6 Large-scale dynamics - stratosphere

The stratosphere is the second major layer of the atmosphere, starting from around 200hPa and extending up to 1hPa. The major drivers of circulation in the stratosphere are radiative (thermal) forcing and wave (eddy) forcing.

2.6.1 Thermally driven circulation

Being higher up in the atmosphere, the global distribution of solar radiation over a year in the stratosphere is slightly different from what we have in the troposphere. During solstices, the radiative heating is maximum over the respective summer hemispheric poles while the equinoxes are marked by maximum radiation at the equator, creating a semi-annual component of forcing there. This implies that a simple thermally direct circulation in the stratosphere can be expected as follows.

During the solstices, when the summer hemisphere receives maximum radiation, it will be relatively warm and the winter hemisphere will be relatively cold. Figure 2.3a from Andrews et al. (1987) (originally from Fels (1985)) shows the radiatively determined temperature in January which indicates colder winter hemisphere and warmer summer hemisphere as expected. To reach the radiative equilibrium, the primary meridional circulation then consists of a flow originating in the summer hemisphere and extending up to the winter hemispheric pole. During austral summer, this northward flow, along with the Coriolis force will create westerly zonal winds in the northern (winter) hemisphere and easterly winds in the southern (summer) hemisphere. This can be seen from Figure 2.3b (reproduced from figure 7.1 in Andrews et al. (1987)), which shows the zonal gradient wind that is in thermal wind balance, derived from temperature distribution shown in Figure 2.3a.

The reverse is true for boreal summer. This means that the stratospheric meridional circulation completely reverses every six months. During the equinoxes, the flow originates at the equator and extend to both the poles, creating westerlies in both the hemispheres due to the Coriolis force. The zonal winds in the stratosphere are in a thermal wind balance, so that the vertical wind shear is proportional

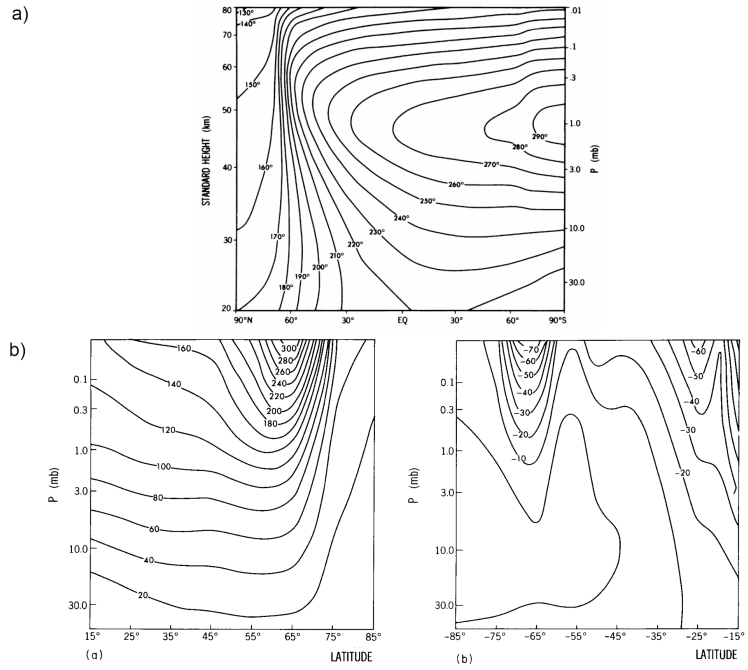

Figure 2.3: a) Zonal-Mean Vertical Profile of a Radiatively Determined Atmosphere, for January 15. Model-produced global temperature profiles. Radiative, photochemical and convective processes are used, with surface temperatures prescribed using seasonally varying observed zonal-mean values. From Andrews et al. (1987) figure 1.2 (originally from Fels (1985)). b) Zonal gradient wind that is in thermal-wind balance with the temperature field in (a) and equals the observed climatological zonal wind at 100 hPa in Northern Hemisphere (winter), and Southern Hemisphere (summer) respectively. (From Andrews et al. (1987) figure 7.1; Courtesy of Dr. S. B. Fels.)

to the meridional temperature gradient, creating westerly (easterly) wind shear in the winter (summer) hemisphere.

Although the sense of the observed meridional circulation is in the same direction as a simple radiatively-driven circulation, its strength is much greater and studies have shown that the observed temperature and wind profile in the stratosphere can only be achieved with eddy forcing (Dickinson, 1969; Fels, 1985). For example, although the Sun's radiative forcing is strongest over the equator and the summer hemisphere, the climatology of observed zonal-mean temperatures in January, indicates that the winter mesosphere has the warmest temperatures, and the summer hemisphere has colder temperatures compared to its radiative equilibrium state. While the summer stratopause temperature is relatively close to the radiatively determined temperature, the winter stratopause is observed to be almost 30K warmer.

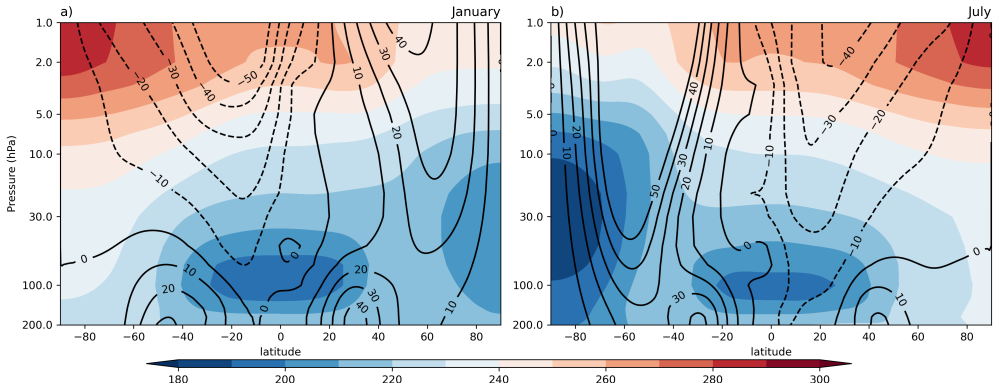

Figure 2.4: Zonal and monthly mean 1979–2020 climatology based on 6-hourly ERA5.1 reanalyses data (Hersbach et al., 2020) for temperature (K; colour shading) and zonal winds (ms^{-1}; black contours) for (a) January and (b) July. The contour interval for the winds is 10 (ms^{-1}).

It is also noted that the deviation from radiatively determined temperatures is smaller in the SH compared to the NH.

The observations also demonstrate a reversal in meridional temperature profile in the mesosphere. Figure 2.4 confirms that the observed winds deviate from the gradient wind derived from temperature profile shown in Figure 2.3. Instead of exhibiting an unrealistic increase in wind amplitude in the winter hemisphere, observations indicate that the winds moderately grow with height. The winds peak around 60 km, and then decrease to smaller values near the mesopause (not shown). The difference in wind distributions between the radiatively-driven winds and the observed winds are due to the impact of waves. The wave induced circulations in the stratosphere are described in the next section.

2.6.2 Eddy driven circulation

In the stratosphere, due to the presence of ozone, the temperature increases with altitude, providing a stably stratified environment. The stability of the atmosphere can be understood by examining the frequency of adiabatic oscillations of a fluid parcel displaced from its equilibrium position in a stably stratified atmosphere. This frequency is known as the Brunt–Väisälä frequency, N, and it can be expressed as follows:

$$N^2 = \frac{g}{\theta}\frac{d\theta}{dz}$$

When N^2 is positive, the parcel will follow an oscillatory motion and return to its initial position. If N^2 is negative, the air parcel will keep on rising, leading to an unstable atmosphere. The N^2 is positive for the stratosphere due to increasing temperatures with height, making it stably stratified. This results in an eddy growth rate (the rate at which eddies amplify) that is significantly smaller than that in troposphere and thus stratosphere is generally baroclinically stable. Thus, the waves present in the stratosphere mostly originate from the troposphere. A detailed description on different atmospheric waves are provided in section 2.3.

In the extra-tropical stratosphere, the upward propagating waves mainly include planetary scale quasi-stationary Rossby waves (forced mainly by mountains and land-sea temperature differences) and small-scale gravity waves. Since Rossby wave vertical propagation is favoured by a relative westerly flow in the background, these waves are more active in the winter hemisphere extra-tropics (Charney and Drazin, 1961). As the air density decreases with altitude, these waves grow in amplitude as these waves propagate upward. This increase in amplitude eventually leads to wave-breaking in the stratosphere (surf zone), and their westward momentum is absorbed by the background flow. The westward momentum along with the Coriolis force creates convergence and downwelling at high latitudes, giving rise to the residual mean circulation (c.f. the Brewer-Dobson circulation (BDC)) in the stratosphere during winter (Holton et al., 1995) (figure 2.5). The residual mean circulation can be understood as the part of the mean flow that remains after accounting for the wave-induced momentum fluxes impacting the Eulerian zonal-mean circulation. The downwelling component of the residual circulation near the wintertime pole causes adiabatic heating leading to the warmer winter hemispheric temperatures mentioned previously. Eddy forcing is more active in the NH than in the SH due to the presence of more landmasses, which provide greater orographic features and land-sea temperature contrasts that support the

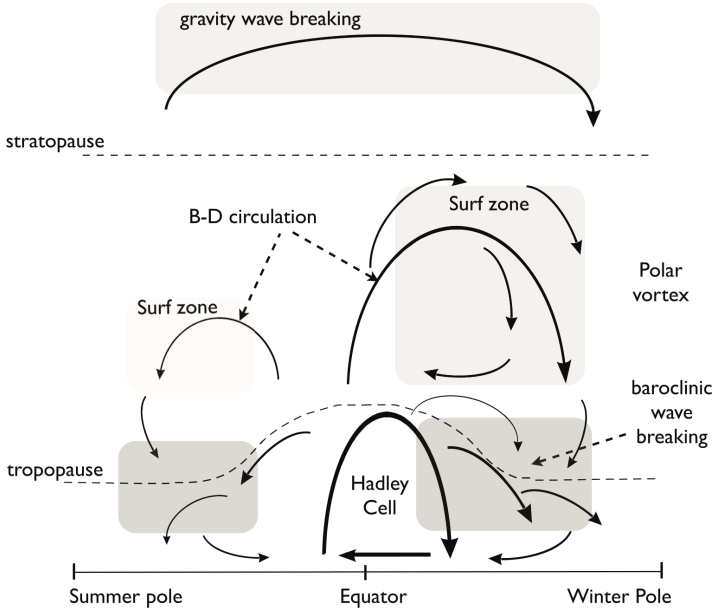

Figure 2.5: A sketch of the residual mean meridional circulation of the atmosphere. The solid arrows indicate the residual circulation (B-D for Brewer–Dobson) and the shaded areas the main regions of wave breaking (i.e., enstrophy dissipation) associated with the circulation. In the surf zone the breaking is mainly that of planetary Rossby waves, and in the troposphere and lower stratosphere the breaking is that of baroclinic eddies. The surf zone and residual flow are much weaker in the summer hemisphere. Only in the Hadley Cell does the residual circulation consist mainly of the Eulerian mean; elsewhere the eddy component dominates. From Vallis (2017).

generation of eddies. Consequently, stratospheric temperatures deviate more from the radiatively-driven temperatures in the NH.

In the mesosphere, additional dynamical heating or cooling is provided by gravity waves. These gravity waves originate in the troposphere and, if unfiltered by the background flow due to critical level filtering at lower altitudes, reach the mesosphere. In the winter (summer) hemisphere, westerlies (easterlies) dominate the stratosphere, allowing gravity waves with westward (eastward) phase speeds to propagate into the mesosphere. The gravity waves increase in amplitude as they propagate upward and eventually break in the mesosphere, imparting momentum to the mean flow according to their phase speed direction.

This process leads to the deceleration of westerlies in the winter hemisphere mesosphere, preventing the unrealistic growth of westerly winds. Similarly, it causes the deceleration of easterly winds in the summer hemisphere mesosphere. The

breaking of gravity waves also induces a mean meridional circulation from the summer to the winter hemisphere mesosphere, resulting in adiabatic heating in the winter hemisphere and adiabatic cooling in the summer hemisphere. This mechanism accounts for the deviations from the radiatively driven temperature observed earlier. Both the winds and temperatures in this region follow the thermal wind balance.

The wave breaking, depending on its strength, can alter the climatological state as well. In the winter hemisphere stratosphere, if there is sufficiently large wave forcing, by breaking large-scale waves, a complete reversal of the background westerly flow (polar vortex) can occur, resulting in a very strong induced meridional circulation. This further results in strong downwelling in the polar region and hence occasionally results in SSWs (Baldwin et al., 2021). SSWs are associated with rapidly increased temperatures in winter pole due to the strong adiabatic heating. During a strong SSW event, the reversal in wind can extend all the way down to troposphere. This has been a focus of extensive research since these events have significant impacts on surface weather (Baldwin and Dunkerton, 2001; Sigmond et al., 2013; Baldwin et al., 2021).

2.7 Stratosphere - tropical circulation

Like the extra-tropical stratosphere, equatorial variabilities are also significant in understanding our weather and climate. Oscillating zonal-mean zonal wind and temperature patterns with different periodicities are observed in this region. The equatorial stratospheric variabilities in zonal-mean zonal wind can be clearly distinguished by a frequency-amplitude spectrum, as shown in Pascoe et al. (2005) (see Figure 2.6). Above 10 hPa, there is a clear dominance of the biannual frequency, corresponding to a six-month period. This is known as the SAO. The QBO has a peak amplitude in the lower to mid stratosphere and has a periodicity of 28 to 32 months. Additionally, the presence of the annual cycle can be seen throughout the stratosphere. Studies have shown that these stratospheric oscillations cannot be forced by radiative forcing alone and wave forcing plays a major role in driving both the QBO and SAO.

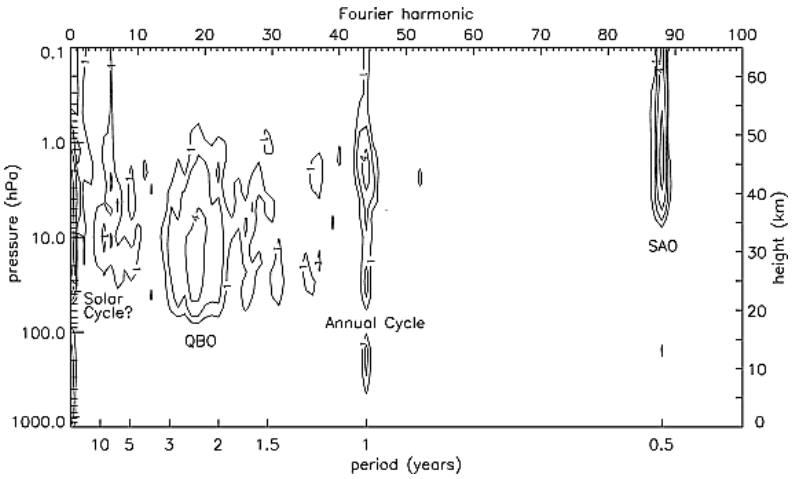

Figure 2.6: Fourier analysis of equatorial zonal-mean zonal wind. The Fourier harmonic axis indicates the number of cycles that a given periodic mode experienced during the 44 years of the ERA-40 data set. The periods of some Fourier harmonics are also indicated. Contours are drawn at Fourier amplitudes of 1, 2, 4, 8, and 16 (ms^{-1}. From Pascoe et al. (2005).

2.7.1 Quasi-biennial oscillation

The QBO was first noted as a stratospheric variability by Ebdon and Veryard (1961) and Reed et al. (1961) independently using radiosonde observations of wind at locations near the equator. Oscillating westerly and easterly winds with a periodicity of roughly 28 months were observed. Subsequent studies have shown that QBO is present in the zonal-mean wind as well. A QBO in temperature and ozone has also been identified (Angell and Korshover, 1964). This equatorial variability has a latitudinal half-width of 12 degrees.

Figure 2.7 shows the zonal-mean zonal wind QBO plotted as time versus height using MERRA-2 reanalysis data. The feature that stands out is the downward propagation of the oscillating winds from around 10 hPa to 100 hPa and the amplitude remains the same till around 40 hPa. Various dynamical mechanisms were proposed to explain the oscillation and why it propagates downwards with time, but it was Lindzen and Holton (1968) and Holton and Lindzen (1972) who considered the role of equatorial waves and successfully explained a possible mechanism. They noted that equatorial waves like Kelvin waves and Rossby-gravity waves, and small-scale gravity waves can give rise to the QBO variability.

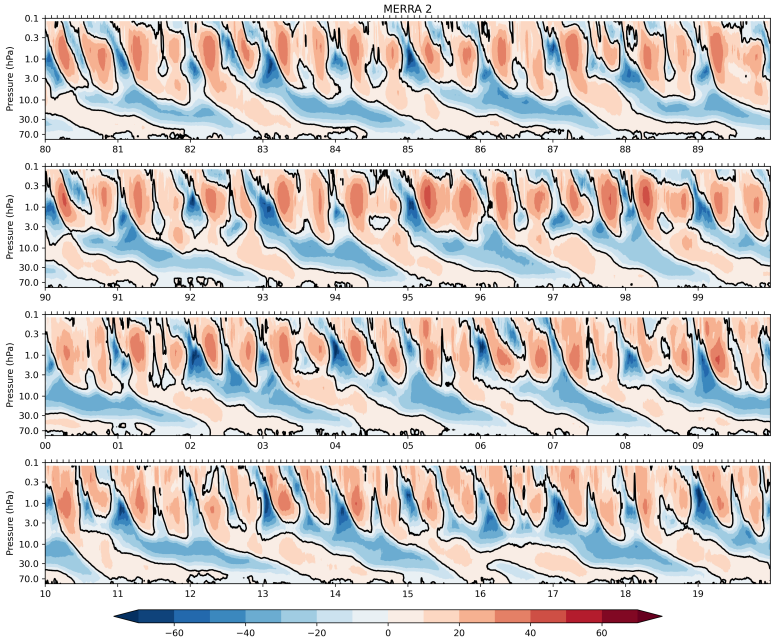

Figure 2.7: QBO in zonal-mean zonal wind. Plotted is the zonal-mean zonal wind ((ms^{-1})) averaged over 10°N to 10°S for the years 1980 to 2019 for MERRA-2.

The mechanism of QBO formation is now understood as follows. Equatorial waves, along with small scale gravity waves, propagate vertically from the troposphere to the stratosphere. These waves, when they encounter a critical layer, dissipate and deposit momentum to the background flow. Figure 2.8 from Plumb (1984) can give a clear depiction of the process. As the figure shows, from the troposphere, waves with both positive and negative phase speeds propagate up into the stratosphere. If the mean wind (u) in the lower stratosphere is westerly (Figure 2.8a), the eastward propagating waves (with positive phase speeds) with phase speed matching the u will dissipate due to critical level filtering and deposit eastward momentum to the mean flow. The westward propagating waves will pass through the westerly winds and when they meet background easterly winds with similar magnitude, they dissipate and deposit momentum. Thus, the shear zone propagates downward and once the depth of the westerly winds decreases enough, the viscous diffusion will eradicate the westerly winds. Now, the eastward propagating waves can pass freely to the upper stratosphere and the next cycle of westerly winds will eventually begin. Similarly, the easterly phase evolves as well.

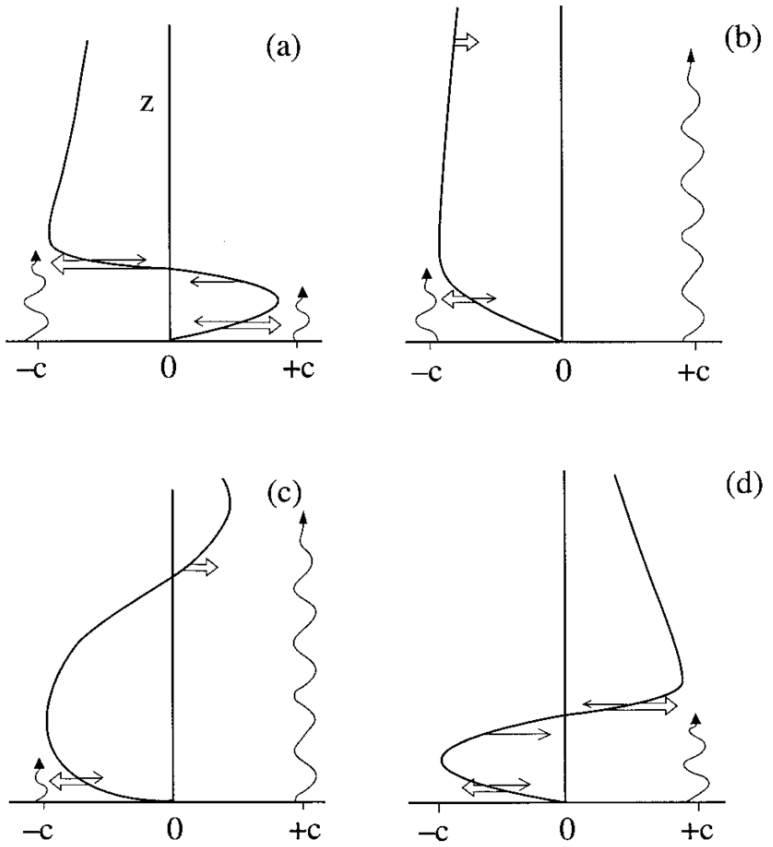

Figure 2.8: Schematic representation of the evolution of the mean flow in Plumb's [1984] analog of the QBO. Four stages of a half cycle are shown. Double arrows show wave-driven acceleration, and single arrows show viscously driven accelerations. Wavy lines indicate relative penetration of eastward and westward waves. From Baldwin et al. (2001). (After Plumb (1984)).

The upwelling due to the BDC generally opposes this downward propagation of QBO winds (see figure 2.5 for BDC). In addition, when there is westward wave forcing, there will be induced upwelling (explained in next few paragraphs), further opposing the QBO easterly descent. The reverse is true for westerly phase. Hence, the downward propagation of the easterly QBO will be slower than the QBO westerly descent. Thermal wind balance creates a QBO in temperature as well.

Thermal wind balance implies that the vertical wind gradient is proportional to the negative of the meridional temperature gradient, as expressed in the thermal wind equation below.

$$\frac{\partial u_g}{\partial z} = -\frac{R}{fH}\frac{\partial T}{\partial y} \tag{2.23}$$

Thus, when there is a westerly wind shear with height, the thermal wind balance requires that temperatures be warmer at the equator and cooler at the subtropics. This configuration necessitates downwelling at the equator, leading to adiabatic warming, and upwelling in the subtropics, thus resulting in a QBO-induced meridional circulation, as can be seen in Figure 2.9. Consequently, the temperature and wind patterns establish an induced circulation where air descends and warms near the equator and ascends and cools in the subtropics. Similarly, when there is an easterly wind shear, the reverse will be true, resulting in an upwelling at the equator and colder temperatures (Figure 2.9, from Plumb and Bell (1982)). Note that QBO-induced circulation is an additional circulation, on top of general upwelling, so this doesn't necessarily mean that there is real descent during a westerly wind shear.

This adiabatic warming and cooling associated with the induced circulation generates a QBO in temperature. The upwelling and downwelling due to the induced meridional circulation results in strong QBO signals in chemical tracers such as ozone. As the ozone mixing ratio increases with height above the tropopause, the QBO-induced circulation results in a column ozone maximum (minimum) at the equator during QBO westerlies (easterlies) and a corresponding minimum (maximum) in the subtropics. Similar to QBO, SAO also has an induced circulation associated with its wind shear.

The influence of the QBO on high-latitudes also had much attention in the past. The Holton-Tan effect proposes that, during boreal winter, if the QBO winds at 50 hPa are in the easterly (westerly) phase, the NH polar vortex is shown to be weaker (stronger) than its climatological average (Holton and Tan, 1980; Anstey and Shepherd, 2014; Anstey et al., 2022). While the observational evidence supports this Holton-Tan relationship, the exact mechanism is not well understood (Baldwin et al., 2001; Anstey and Shepherd, 2014). Proposed mechanisms indicate that the QBO influences the extra-tropics by modulating the mid-latitude Rossby wave propagation, as these waves typically weaken the westerlies and create a warmer polar vortex (see section 2.6.2). The Holton-Tan mechanism proposes that, when the QBO is in the easterly (westerly) phase, the zero-wind line (easterly to westerly

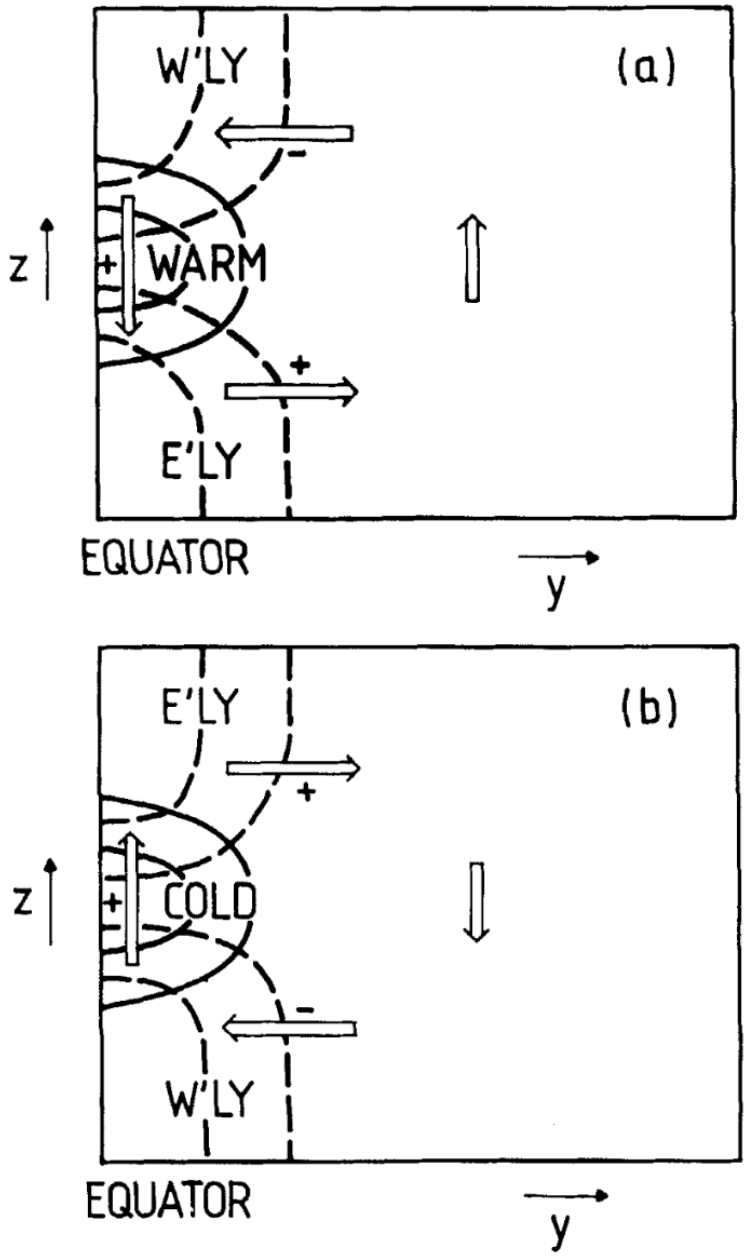

Figure 2.9: Schematic representation of latitude-height profile of the mean meridional circulation associated with the QBO equatorial temperature anomaly . Solid contours: temperature anomaly isotherms, dashed contours: zonal wind isopleths. ± signs: signs of zonal wind accelerations driven by the mean meridional circulation. (a) Westerly shear zone. (b) Easterly shear zone. From Plumb and Bell (1982).

transition) in the sub-tropics is closer to (away from) the higher latitudes, thus modulating the waveguide for upward propagating Rossby waves. A narrower waveguide during QBOE results in Rossby waves more confined to the extra-tropics and more wave breaking along polar vortex, while QBOW allows Rossby waves

to propagate more to low latitudes, resulting in a less disturbed polar vortex. A QBO induced meridional circulation is also proposed as an important factor in modulating the evolution of Rossby waves and their effect on the polar vortex. It is important to recognize that other influences are also at play, such as the 11 year solar cycle, volcanic eruptions and sea-surface temperatures. The observed Holton-Tan relationship also shows features such as interannual to decadal variations (Lu et al., 2014). In the SH, Rossby waves are less prominent. However, a significant relationship is shown between 20-30hPa QBO and SH extra-tropics during austral spring time when the planetary wave activity peaks.

2.7.2 Semi-annual oscillation

Oscillating patterns in wind and temperature fields with a periodicity of six months observed in the equatorial upper stratosphere and lower mesosphere, with a maximum amplitude at stratopause are termed as the stratopause SAO. This study focuses on the stratopause SAO and hence the properties of SAO stated here after are of the same. The first documentation of the SAO was based on rocketsonde observations in the tropics by Reed (1966) at Ascention Island and Barking Sands at altitudes of approximately 50 km. Understanding of the SAO has improved a lot since then. A comprehensive analysis of the SAO climatology in the tropical stratosphere using multiple observations can be found in Garcia et al. (1997). In recent years, reanalysis datasets (Kawatani et al. (2020); SPARC (2022), Chapter 11) and more recent satellite observations have helped us to achieve a global database to understand the climatological behavior of SAO. While the lack of direct wind observations in the whole upper stratosphere is a setback, previous studies have derived wind from available satellite geopotential height observations, and comparison to radiosonde and rocket-sonde observations have proved it realistic (Smith et al., 2017). Figure 2.10 shows the zonal-mean zonal wind climatology derived from SABER and MLS temperature observations by Smith et al. (2017).

The oscillating wind patterns of the SAO, observed between approx. 0.3hPa to 5hPa, consists of easterlies which occur closer to the solstices and westerlies

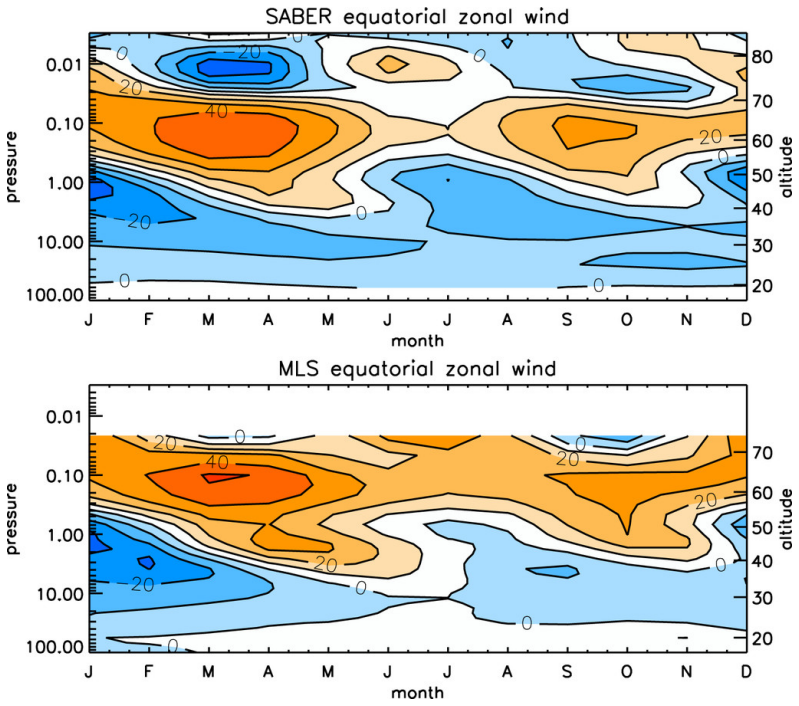

Figure 2.10: Multiyear average of monthly equatorial wind from (top) SABER and (bottom) MLS. From Smith et al. (2017). © American Meteorological Society. Used with permission.

occurring closer to the equinoxes, each on average lasting for 3 months (Reed, 1966; Hirota, 1980). The magnitude of the easterlies is higher than that of westerlies and the easterlies in the first half of the year i.e. around NH winter are observed to be stronger than in the second half, so there is also an annual component to the equatorial stratopause variability (Quiroz and Miller, 1967; Delisi and Dunkerton, 1988). The semi-annual nature of the zonal wind oscillation is visible within approximately ten degrees north and south of the equator. At higher latitudes the annual harmonics dominate (eg. Ray et al. (1998)). The SAO easterly phase (SAOE) onset occurs at a range of altitude at the same time, while the westerly phase starts at a higher altitude and propagates downward over time (Quiroz and Miller, 1967).

Roughly similar behavior of the SAO can be seen in the reanalysis as well, although large uncertainty exists among reanalyses (SPARC, 2021).

2.8 SAO forcing mechanisms

The semi-annual nature of the oscillation was first explained using radiative forcing ideas, as the sun crosses the equator twice a year (Webb, 1967). However, it was noted that radiative forcing alone cannot drive the tropical oscillations (Wallace, 1967; Wallace and Holton, 1968) and atmospheric waves were suggested as a major driver (Meyer, 1970). The role of large-scale circulations and waves in forcing the SAO is detailed in this section.

To understand the forcing mechanisms of SAO, the TEM equation we have introduced in section 2.5 is of great importance. Equation 2.19 explaining the rate of change of zonal-mean zonal wind in response to various forcing terms can be used to understand the relevant mechanisms in the upper stratosphere. The four terms on the RHS of equation 2.19 are understood as meridional advection, vertical advection, resolved waves and residual term. In the equatorial upper stratosphere, the terms in the TEM momentum equation can be physically interpreted as follows.

1. Meridional advection

The simultaneous onset of the easterly phase of the stratospheric SAO over a range of altitudes suggests that it is likely associated with the meridional circulation (Holton and Wehrbein, 1980). In the upper stratospheric region, the dominant meridional movement is the residual meridional overturning circulation in the stratosphere, generally known as the BDC, which is primarily driven by eddy forcing in the extra-tropical, winter stratosphere (Holton and Wehrbein, 1980) as discussed in section 2.6.2. The BDC involves upwelling in the summer hemisphere tropics, cross-equatorial flow with meridional movement through the winter midlatitudes and downwelling at high latitudes. Since the BDC in the mid-upper stratosphere is strongest at solstice and always flows from the summer to the winter hemisphere, the horizontal advection at those levels will be strongest at solstice (i.e., DJF and JJA).

During the solstices, the summer hemisphere features strong easterly jets (Figure 2.4). Consequently, the BDC flowing from summer to winter hemisphere will advect

this westward momentum across the equator during this time. Hence, the meridional advection forcing in the upper stratosphere consists of westward forcing during the winter months in both hemispheres. Thus, this horizontal advection is proposed as one of the main sources of westward momentum for the easterly SAO phase.

The BDC is notably stronger during the NH winter compared to the SH winter. This difference arises because the planetary wave activity in the extratropical surf zone, which drives the BDC (as explained in section 2.6.2) is more intense in the NH. This stronger wave activity leads to more substantial downwelling in the NH extra-tropics, intensifying the BDC during the NH winter. Hence the meridional advection forcing due to the BDC at SAO altitudes will be stronger in NH winter compared to SH winter. This will result in an annual variability within the SAO.

2. Vertical advection

The vertical advection contribution will depend on the strength of the Brewer–Dobson equatorial upwelling, the strength of any induced (secondary) circulation due to local wave activity (see section 2.7.1), and the vertical gradient of the zonal wind. The BDC has general upwelling close to equator throughout the year, although this is likely to be quite weak around the stratopause where the BDC is pimarily horizontal, while the locally-induced circulation will be upwelling during westward wave forcing and downwelling during eastward wave forcing to maintain approximate thermal wind balance.

Thus the strength of advection due to the BDC is modulated by the locally-induced circulation which acts to reduce/enhance it when there is westerly/easterly vertical shear. This results in an enhanced advection from below (from strengthened upwelling) during the solstices when the SAO has easterly shear zones at the equator. During equinoxes, i.e., when there are westerly shear zones at SAO altitudes, depending on the relative strength of the background BDC and the SAO-induced circulation there is likely to be either reduced advection from below (i.e.

weakened upwelling) or even advection from above (if the SAO-induced downwelling is greater than the background BDC upwelling).

3. EP flux divergence

The EP flux divergence, as mentioned in section 2.3, indicates large-scale wave forcing in the atmosphere. A negative EP flux divergence generally implies the presence of westward-propagating waves such as planetary-scale Rossby waves, which transfer westward momentum to the zonal flow and thus weakens the climatological westerlies, while a positive EP flux divergence is associated with the presence of eastward-propagating waves, such as Kelvin waves, which transfer eastward momentum. Inertia-gravity waves, which propagate both eastward and westward, are also identified at SAO altitudes.

Atmospheric waves are known to influence both phases of the SAO. Previous research has indicated that the westerly phase of the SAO is driven primarily by vertically propagating tropical waves, although this is difficult to explicitly confirm due to the lack of high-resolution observations at SAO altitudes. Planetary-scale Kelvin waves and inertia-gravity waves (Hirota, 1978; Garcia, 2000) as well as small scale eastward propagating gravity waves (Hitchman and Leovy, 1986, 1988; Ern et al., 2021) are all believed to contribute to the SAO westerly forcing. While relatively slow eastward propagating waves are absorbed at lower levels in the westerly QBO region, high speed waves can propagate through to the SAO region where they are damped and transfer their momentum to the background flow (Hirota, 1978; Dunkerton, 1979).

Waves are also proposed to play a direct role in the SAO easterly phase through the lateral momentum transfer by more localised quasi-stationary waves in the winter hemisphere subtropics (Hopkins, 1975). This has been suggested as an additional westward momentum source along with the previously discussed meridional advection. Affirming this, Ern et al. (2015) has highlighted a strong

westward forcing by planetary scale waves at the onset of SAO easterly jets using ERA-Interim reanalysis data.

4. Residual term

In TEM, the term $\bar{X}$ primarily denotes the zonal-mean component of non-conservative forces. In models, as noted earlier, gravity waves are often parametrized as their scales are smaller than the model resolution. So, in the models, the term $\bar{X}$ includes mainly the parameterized GW driving, together with other residual forcing such as that due to numerical diffusion. Both eastward and westward propagating gravity waves are suggested to reach the SAO altitudes and deposit momentum, especially forcing the SAO westerly phase (SAOW).

The four forcing terms discussed above provide insights into the mechanisms driving the easterly and westerly phases of the SAO. We note that while the eastward forcing is associated with vertically propagating wave absorption, the westward forcing is associated with meridional advection and extratropical eddy forcing which peak during the winter of each hemisphere, so it is this westward forcing that gives rise to the semi-annual nature of the oscillation. This contrasts with the QBO, in which both phases are primarily due to wave forcing (see section 2.7.1).

Inertial instability is another important phenomenon that is present in the middle atmosphere, caused by the imbalance of horizontal pressure gradient and the Coriolis force; several studies have explored the relevance of this mechanism to the SAO (e.g., Hitchman and Leovy (1986)). Due to the advection of summer easterlies into the winter hemisphere around the stratopause, it has been noted that there is an increased possibility for inertial instabilities to develop in regions close to the equator, primarily within 0 -10° latitude in the winter hemisphere although they can also be found at higher latitudes due to flow distortions by Rossby waves (Rapp et al., 2018; Strube et al., 2020). Inertial instabilities at the equator result in an eastward forcing and thus the weakening of the SAO easterly

phase (Dunkerton, 1981; Ray et al., 1998). Supporting this view, a recent case study by Lieberman et al. (2021) showed that during NH summer inertial instability sharply weakens the equatorial easterlies at the stratopause.

Present day climate models are able to reasonably reproduce the SAO, but there are some major biases that are still not fully understood. Climate model representation of the SAO has been examined by, e.g., Smith et al. (2019) and climate model simulations have also been used to study aspects of the forcings responsible for the westerly and easterly phase of the SAO (e.g., Ray et al. (1998)). An easterly bias of the SAO in climate models is a long-standing problem; all climate models unambiguously show an easterly bias, although there are variations in the extent to which the SAO amplitude and altitude range differ (Smith et al., 2017, 2019). Chapter 4 (section 4.1) discusses in detail about the easterly bias in climate models. A case study by Müller et al. (1997) using the Berlin TSM-GCM model and the model study of Smith et al. (2019) both suggest that insufficient Kelvin wave dissipation in the upper stratosphere could be a reason for the easterly bias, while Smith et al. (2019) also mention the possibility of differences in gravity wave drag (GWD). However, none of these previous studies have examined all of the individual driving mechanisms described in this section to understand the reason for the easterly bias.

2.9 SAO - influences and interactions

The SAO has been found to influence atmospheric circulations in various ways. Among them, the redistribution of tracer species in the stratosphere, influence on the SSW and interaction with the QBO are discussed in this section.

2.9.1 SAO and chemical species

The SAO influences the distribution of chemical tracers in the equatorial stratosphere. Longer lived trace gases, like N_2O and CH_4 exhibits a double peak structure in latitude, with a local minimum at the equator and maxima in the subtropics, in the upper stratosphere. This is associated with the induced meridional circulation due

to the SAO, which transports tracers to both hemispheric subtropics, producing a double peak (Gray and Pyle, 1986; Shu et al., 2013). Understanding this stratospheric chemical species distribution is important as it can give insight into ozone depletion and life cycle and distribution of pollutants and greenhouse gases.

Ozone exhibits a semi-annual signal (Ray et al., 1994). As its photo-chemical lifetime decreases with increasing altitude, at SAO altitudes ozone is a short-lived trace gas mainly controlled by photo-chemical sources and sink changes (Chipperfield and Gray, 1992), which in turn depends on the temperature. On the other hand, in the lower stratosphere below 28 km, its lifetime is of the order of months/years so ozone is considered as a long lived tracer and dynamics play an important role in its distribution (see section 2.7.1).

2.9.2 SAO and extra-tropics

The SAO may also influence the mid-latitude winter circulation, in a similar way to the QBO influence. While the peak amplitude of the SAO is observed to extend to $\pm 10°$ latitude, its influence extends poleward into the subtropics via an induced meridional circulation, required to maintain thermal wind balance as explained in section 2.7.1. Model studies have indicated that the strength of the subtropical upper stratospheric winds in early winter may impact the later evolution of the polar vortex e.g. whether it remains cold and undisturbed throughout the winter or whether it is disrupted by a SSW. Gray et al. (2004, 2022) found that wind anomalies in the early-winter subtropical upper stratosphere influence the timing of SSWs, with an easterly anomaly promoting an early to mid-winter SSW and a westerly bias promoting a late-winter or absent SSW. This suggests that an improved SAO may improve simulations of polar vortex evolution and SSW frequency. It is widely acknowledged that SSWs affect surface weather, so improved SSW characteristics is desirable for weather prediction (Scaife et al., 2005; Mukougawa et al., 2009; Butler et al., 2016; Lu et al., 2021).

2.9.3 QBO-SAO interaction

The QBO and SAO are the two major modes of variability in the equatorial stratosphere and are suggested to interact with each other (Dunkerton and Delisi, 1997; Garcia et al., 1997; Krismer et al., 2013). Depending on the QBO phase, the amplitude of the SAO is modulated. The SAO westerly phases are observed to be stronger during the easterly phase of the QBO (QBOE) and, as the QBOE descends, the successive SAOW phases also extend farther down in altitude. Once in every four to six SAO cycles the SAOW propagates sufficiently far down to merge with the onset of the westerly phase of the QBO. For example, see Figure 2.7 from 1982 to 1985, as the QBOE descends the SAOW phases extend farther and farther down until they finally merge with the next QBO westerly (QBOW) phase. The QBO westerly phase is thus suggested to be locked with SAO cycles (Rajendran et al., 2016). The influence of the QBO on the SAO is mainly because the vertically propagating waves that reach the SAO region have to pass through the QBO region. The westerly and easterly phases of the QBO can thus alter the vertical propagation of the waves, which are crucial in driving the SAO, thereby influencing the strength and depth of the SAO. Chapter 5 gives a more detailed depiction of how these two oscillations interact with each other.

3
Data and Methods

3.1 Data

To understand our atmosphere, various kinds of datasets are available – Observations, Reanalysis and Climate model data. With the advent of the satellite era, the observations of atmospheric variables have improved significantly. Unlike the radiosonde and rocket sonde like observations, which were only available at scattered locations around the globe, satellite observations are more consistent and comprehensive at regular intervals in space and time.

While satellite data is invaluable, there are still several drawbacks. These include data discontinuity due to the satellite orbit, unavailability of data at all parts of the atmosphere and the need to derive the necessary variables rather than measuring them directly. To achieve complete global data coverage with no discontinuity, we have reanalyses. Reanalysis data are from atmospheric model runs that have a physically consistent atmosphere and observations like satellite and radiosonde data are assimilated to produce the most realistic atmospheric variables at regular time intervals and spatial grid points.

This thesis focuses on the upper stratospheric region. Unfortunately, the observations at this altitude are sparse. Radiosonde observations are only possible up to around 10 hPa and satellites are often designed to enhance our understanding

of the lower levels of the atmosphere. Two relevant satellite datasets that are recently used to understand the upper stratosphere are SABER (Sounding of the Atmosphere using Broadband Emission Radiometry) and MLS (Microwave Limb Sounder). However, neither of these have wind observations. A recent study by Smith et al. (2017) has used the temperature observations to derive the zonal wind (shown in figure 2.10). Nevertheless, obtaining additional variables, such as tendency terms, from the currently available observations is unreliable. Therefore, for the purposes of this study, we have relied on reanalysis data.

Climate models on the other hand, are computer simulations of Earth's weather and climate system, often based on the same models employed for the reanalyses but they do not assimilate observations. Climate models are highly useful in understanding past climate and predicting future climate. However, climate model simulations can be understood as one possible realization of our atmosphere, but not the complete truth. To understand the uncertainty in climate projections and to capture various possible outcomes, ensembles are used. Ensembles indicate multiple model simulations that are often performed with slightly different initial conditions.

Weather and climate models solve the primitive equations (see section 2.2) to understand the global atmospheric flow of momentum, mass and thermodynamic fields and to predict the weather and climate in our earth system. To study atmospheric evolution, an atmosphere-only model can be used with appropriate boundary conditions, while a more comprehensive model could also include other components of Earth system such as coupling with ocean, ice and land processes. To start a model, initial conditions are required, which are usually either obtained from previous model runs or sometimes a model spin up is used to obtain equilibrium in a model.

As it is impossible now to perform calculations at every point in space and time, models are discretized both spatially and temporally, with the resolution limited by the availability of computer resources. The discretization is achieved through various methods in the models. Depending on how the discrete data are represented the models are classified as grid-point models and spectral models. In grid-point based models, the data are stored and the dynamics are calculated on

each grid cells. There are variations among grid-point models based on how the grid structure is defined, such as regular lat-lon grids, cubed-sphere and icosahedral geodescic grid. The grid-point model resolution is often represented as the number of grid cells in latitude and longitude direction. In spectral models the fields (like temperature, vorticity, etc) are represented as continuous global wave functions and the resolution is noted as the maximum wavenumber it can resolve. The spectral models benefit from better representation of global field and better approximation to derivatives in the calculations but there are difficulties in the representation of local processes. This is addressed by Fourier transforming the wave components to perform calculations at discrete grid points. The calculations are carried out after each time step, usually ranging from a few minutes to an hour, and the equations are solved using different vertical coordinate systems, such as height or pressure or hybrid sigma-height coordinates, depending on the specific model.

A key part of the model is its dynamical core which solves the discretized primitive equations (with appropriate approximations) to derive the evolution of the atmosphere. The discretization limits the model from resolving the small-scale features of the atmosphere at scales smaller than the resolution of the model. Sub-grid scale physics parametrization is used to account for the unresolved processes such as longwave and shortwave radiation, convection, cloud physics, surface fluxes and turbulence. Some of the climate models have additional features such as the inclusion of interactive chemical processes to more closely model the relevant middle atmosphere processes.

To account for forcings at the boundary and influences from processes that are not represented in the models, external boundary conditions and other forcings (often obtained from observations or other model simulations) are specified in the models. This enables the models to represent the observed climate as closely as possible. Imposed conditions such as solar irradiance are necessary across all the models, while many other conditions vary among models. For an atmosphere only model simulation, conditions like sea surface temperature (SST) and sea ice are specified, while these are internally generated in coupled ocean models. Other prescribed

forcings are ozone, volcanics, aerosols, solar cycle and so on. In models with interactive chemistry, the chemical processes are part of the temperature or radiation equations in primitive equations and are computed within the model, thus able to produce feedback between chemistry and climate. Models also suffer from further limitations such as uncertainties in initial conditions which are usually addressed through long spin up simulations to help achieve a stable equilibrium in the model.

Understanding the biases that still exist in our climate models and alleviating them is crucial to improve our future predictions of the atmosphere. In this thesis, as we focus on one such problem, we analyse various climate models and reanalysis datasets and some of the relevant details are outlined in this chapter.

3.2 Reanalysis data

3.2.1 MERRA-2

The Modern-Era Retrospective Analysis for Research and Applications, Version 2 (MERRA-2) (Gelaro et al., 2017) is a global reanalysis dataset provided by the National Aeronautics and Space Administration (NASA) Goddard Institute for Space Studies (GISS). The Goddard Earth Observing System-5 (GEOS-5) atmospheric general circulation model (AGCM) (Molod et al., 2015) and the Gridpoint Statistical Interpolation (GSI) analysis scheme (Wu et al., 2002; Kleist et al., 2009) is used to generate the MERRA-2 dataset. The model is grid-point based and uses a cubed sphere grid with an approximate horizontal resolution of 0.5° latitude $\times$ 0.625° longitude and a vertical resolution of 72 hybrid-model levels extending from the surface to 0.01hPa. A finite volume dynamical core is used. The analysis is calculated on a latitude-longitude grid at same spatial resolution as the model, using an algorithm based in GSI. The analysis is then gradually incorporated to the model as a correction to the background state.

The model includes physical parameterisations of long wave and short wave radiation (Chou and Suarez, 1994, 1999), moist physics with prognostic clouds (Bacmeister et al., 2006), convection (Moorthi and Suarez, 1992; Bacmeister and Stephens, 2011), boundary layer turbulent mixing (Louis et al., 1982; Lock et al.,

2000), both orographic (McFarlane, 1987) and non-orographic GW schemes (Garcia and Boville, 1994; Molod et al., 2015), a land surface model (Koster et al., 2000), a glaciated land representation and seasonally-varying sea ice albedo (Cullather et al., 2014). The non-orographic GW scheme is optimised to enhance the representation of the QBO and SAO in the tropics (Molod et al., 2015). Some of the boundary and other specified conditions include SST and sea ice, assimilation of ozone retrievals and aerosol optical depths from space-based observations, volcanic aerosols, annual global mean CO_2 concentrations following the IPCC RCP4.5 scenario which is assumed to be uniform throughout the atmosphere, and the solar cycle is included in the total solar irradiance. The radiation calculations in the forecast model uses analyzed ozone and aerosols. Artificial damping (sponge layer) is applied to horizontal winds at altitudes above 0.24 hPa by increasing the horizontal divergence damping. In addition to assimilating a large suite of ground-based and satellite observations (see SPARC (2022) for a summary), MERRA-2 has the added benefit of assimilating MLS temperature observations at altitudes above 5 hPa after August 2004. The dataset is thus constrained by additional observations in the region of interest to this thesis.

In this study, we have used the MERRA-2 3-hourly time-averaged, model level data of wind and temperature variables, available at Global Modeling and Assimilation Office (GMAO) (2015), named as MERRA-2 tavg3_3d_asm_Nv: 3d, 3-Hourly, Time-Averaged, Model-Level, Assimilation, Assimilated Meteorological Fields V5.12.4 (`10.5067/SUOQESM06LPK`). The dataset extends over a 42-year period 1980-2021. The dataset is used to calculate the relevant variables needed as described in 3.4.1. We also utilise the MERRA-2 3-hourly time-averaged, pressure level data of tendency of eastward wind due to GWD, available at GMAO and named as MERRA-2 tavg3_3d_udt_Np: 3d, 3-Hourly, Time-Averaged, Pressure-Level, Assimilation, Wind Tendencies V5.12.4 (`10.5067/CWVOG3PPPWFW`)

3.2.2 ECMWF datasets

ECMWF is the European Centre for Medium-Range Weather Forecasts and in this thesis, two reanalyses datasets, ERA-interim and ERA5, provided by ECMWF are

used. ERA-interim (Dee et al., 2011) is based on the forecast model, Integrated Forecast System (IFS) release cycle 31r2. The model uses spectral representation of basic dynamic variables. The spectral horizontal resolution of the model is T255 (approximately 79 km spacing on a reduced Gaussian grid) and the vertical resolution is 60 model levels that extends up to 0.1 hPa. The model has a hybrid sigma-pressure vertical coordinate and time stepping with 30 minute time steps. IFS consists of three fully coupled components, the atmosphere, land and ocean waves. SST and sea-ice are provided as boundary conditions. Ozone retrievals are assimilated, while climatological distribution of ozone and aerosols are used in the radiation scheme. CO_2 and trace gases are assumed to have a globally uniform distribution across the atmosphere. The solar cycle is not included in the total solar irradiance boundary condition but is present in the assimilated upper air temperatures. IFS CY31r2 incorporates several physical parametrizations, including shortwave (Fouquart and Bonnel, 1980) and longwave (Mlawer et al., 1997) radiative transfer schemes, prognostic cloud scheme (Tiedtke, 1993; Tompkins et al., 2007), deep, shallow, and mid-level cumulus convection (Tiedtke, 1989) and diffusion. The model also has an orographic GW parameterisation (Lott and Miller, 1997) but does not include a non-orographic GW parameterisation. A sponge layer is present at altitudes above 10 hPa, introduced by adding an additional height and wavelength dependent function to the horizontal diffusion. Rayleigh friction is also employed at altitudes above 10 hPa and represents the non-orographic GWD.

ERA5 (Hersbach et al., 2020) employs IFS cycle 41r2, with horizontal and vertical resolution of T639 and 137 model levels, respectively. The highest altitude is at 0.01hPa, similar to MERRA-2. Many of the physical paramterisations are similar to ERA-interim forecast model but are updated to improve and include various features. Notably, the model additionally includes a non-orographic GW parameterisation scheme following Scinocca (2003b) (see also Orr et al. (2010)), with a latitudinal dependence of non-orographic launch flux. Rayleigh friction is no longer applied. Similar to IFS CY31r2 a fourth-order hyper-diffusion (∇^4) is applied on vorticity, divergence and temperature above 10 hPa to damp vertically propagating

waves depending on model level and zonal wavenumber, and an additional first-order damping (∇) is applied on divergence above 1hPa (Polichtchouk et al., 2017). While MERRA-2 and ERA-Interim rely on single forecasts, ERA5 uses both a high-resolution forecast model and a 10-member 'ensemble of data assimilations' on a coarser grid. This ensemble approach provides more robust estimates of analysis uncertainties. In contrast to MERRA-2, temperature data from MLS are not assimilated in ERA5 (SPARC, 2022).

As noted earlier, the scarcity of observations at SAO altitudes results in a lot of uncertainty among reanalyses as well at these altitudes. In chapter 4, the above described reanalyses are used to indicate the uncertainty among reanalyses in the upper stratosphere and to choose one that resembles the observations the most. Specific issues in reanalysis data are also highlighted, such as an unrealistically strong mesospheric westerly jet in ERA5.

3.3 Models

3.3.1 CESM2-WACCM

CESM2-WACCM6 is the Community Earth System Model Version 2 (CESM2) Whole Atmosphere Community Climate Model 6, which is the 'high-top' version of the coupled climate Earth system model developed by the National Center for Atmospheric Research (NCAR). WACCM is a grid-point model using a finite volume dynamical core (Lin and Rood, 1997). The model includes a representation of both ocean and atmosphere with comprehensive component schemes for land, sea-ice, land-ice and river processes, interactive coupled atmospheric chemistry and ocean wave models that are linked via a coupler (Danabasoglu et al., 2020). The model has a horizontal resolution of approximately 1° (0.9° latitude × 1.25° longitude) and has 70 levels in the vertical from the surface to 6×10^{-6} hPa (approx.140 km). It thus extends to a higher altitude than reanalyses used in this thesis, but with slightly lower resolution. CESM2-WACCM6 (hereafter referred to as WACCM) includes orographic and non-orographic GWD parameterisation schemes (Richter et al., 2010), with orographic, frontal and convective GW sources

separately specified, hence linking GW generation to tropospheric quantities to produce model-consistent GW source fluxes (Gettelman et al., 2019). The GW scheme provides wave forcing that contributes to the internally generated QBO and SAO. Further physical paramterisations in the model include processes such as radiation, cloudy turbulent layers and cloud microphysics. A detailed description of the model and other parameterisations can be found in Gettelman et al. (2019). The specific WACCM dataset used in chapter 4 of this thesis is discussed in that chapter.

3.3.2 HadGEM3-GA7.1

The HadGEM3 is a family of climate prediction models developed by the UK Met Office. This model family includes a range of configurations with varying resolutions and coupled components. UM is the numerical model of atmosphere employed by Met Office. In this thesis, the HadGEM3 Global Atmosphere (GA) 7.1 configuration of UM is used. The UM follows a seamless modelling approach where the same dynamical core is used at a range spatial and temporal scales, such as from regional to global modelling and from weather to climate time scales. The UM dynamical core solves the non-hydrostatic equations of motion and represents the data in a regular latitude-longitude grid in the horizontal and in a terrain following hybrid height coordinate in the vertical. Model physical paramterisations include processes such as radiation, large-scale precipitation, orographic and non-orographic gravity waves, atmospheric boundary-layer turbulence, convection and land surface coupling. The model includes an optional Rayleigh damping that can be applied to the vertical velocity equation.

The UM data used in this thesis are from simulations of the HadGEM3 GA7.1 N216 model, performed as part of the UK contribution to phase 2 of the QBOi project. The model is based on the Met Office Hadley Centre AMIP model used for the CMIP6 historical runs (Eyring et al., 2016). The N216 horizontal resolution has 0.83 x 0.54 degrees latitude-longitude horizontal resolution (approx. 60 km) and 85 vertical levels extending to 85 km (0.01hPa). The recommended forcings for QBOi simulations are described in section 3.4.2 and the forcings implemented in

HadGEM3 GA7.1 are as follows. Observed SST and sea ice distributions from the CMIP6 specification were imposed at the lower boundary. The CMIP6 historical forcings were used until 2014 and CMIP6 SSP5-8.5 forcings were used from 2015-2020. CMIP6 forcings of evolving greenhouse gases, aerosols, volcanics and solar irradiance are used. The only difference from the CMIP6 set-up was the use of climatological ozone instead of the time-varying values. The GW scheme has also been updated to include convective coupling in the non-orographic parametrization (Bushell et al., 2015). A detailed description of the NOGW scheme is given in section 3.4.5.

For the detailed analyses for SAO understanding, we have used both of the above described models for various reasons. The higher top-level and hence less impacts from boundary effects at SAO altitudes motivated the use of WACCM for our understanding of physical processes that drive the SAO. HadGEM3 had additional caveats like lack of conservation of momentum at the higher altitudes. More discussion on this is provided at the end of thesis (under discussion of limitations). While analysing the QBO impact on the SAO, we have used HadGEM3 as we had more control over this model to do our own experiments. Even with above mentioned caveats, HadGEM has a decent SAO representation and forcing term profile, which validated our use of this model to study the SAO response to QBO changes.

3.4 Methods

3.4.1 MERRA-2 TEM calculation

For interpreting the dynamics of the upper stratosphere, this thesis employs the TEM formulation detailed in section 2.5. In most of the climate model runs, the terms in the TEM momentum equation are readily available as output. However, this is not the case for reanalysis datasets in the upper stratospheric region. Hence, for the MERRA-2 reanalysis dataset, TEM diagnostics are calculated following the recipe outlined in Gerber and Manzini (2016).

The direct application of TEM equations in log-pressure coordinates on model outputs has been shown to have misleading features in diagnostics, often of the same magnitude as the diagnostic itself (Hardiman et al., 2010). This issue arises due

to vertical coordinate transformation from geometric height to log-pressure before calculating the TEM diagnostics. Gerber and Manzini (2016) emphasized that the TEM calculations must be performed on fields at pressure levels as close to model levels as possible. Additionally, the sampling frequency of wind and temperature variables used for TEM diagnostics should be at least 6 hours (Gerber and Manzini, 2016) to ensure the accuracy and reliability of the calculated TEM diagnostics.

The three-hourly averaged horizontal and vertical winds and temperature fields (u, v, w, T) on model levels of MERRA-2 reanalysis are available at GMAO (2015). The details of model level to atmospheric pressure conversion and the pressure at each model level in MERRA-2 can be found in Bosilovich et al. (2015) and SPARC (2022), and are employed in this thesis to convert variables from model levels to pressure levels. Since MERRA-2 has a hybrid sigma-pressure vertical coordinate, the pressure levels near the Earth's surface vary according to the surface pressure. However, in the upper stratosphere, the model levels correspond to constant pressure levels. Following Gerber and Manzini (2016), TEM diagnostics are calculated in pressure coordinates and transformed into standard log-pressure vertical coordinates to obtain the formulation of Andrews et al. (1987) shown in section 2.19. Below are the equations in pressure coordinates used in this thesis.

First, the eddy stream function is defined as

$$\psi = \overline{v'\theta'}\frac{\partial\bar{\theta}}{\partial p} \tag{3.1}$$

EP flux vectors and EP flux divergence are:

$$F_\phi = a cos\phi\left\{\frac{\partial\bar{u}}{\partial p}\psi - \overline{u'v'}\right\} \tag{3.2}$$

$$F_p = a cos\phi\left\{\left[f - \frac{\partial\bar{u}cos\phi}{a cos\phi\partial\phi}\right]\psi - \overline{u'w'}\right\} \tag{3.3}$$

$$\nabla\cdot F = \frac{\partial F_\phi cos\phi}{a cos\phi\partial\phi} + \frac{\partial F_p}{\partial p} \tag{3.4}$$

The residual circulation $(\bar{v}^*, \bar{\omega}^*)$ and advection due to residual circulation are defined as:

$$\bar{v}^* = \bar{v} - \frac{\partial \psi}{\partial p} \tag{3.5}$$

$$\bar{\omega}^* = \bar{\omega} + \frac{\partial \psi cos\phi}{acos\phi \partial \phi} \tag{3.6}$$

$$\frac{\partial \bar{u}}{\partial t}|_{adv(\bar{v}^*)} = \bar{v}^* \left[f - \frac{\partial \bar{u} cos\phi}{acos\phi \partial \phi} \right] \tag{3.7}$$

$$\frac{\partial \bar{u}}{\partial t}|_{adv(\bar{\omega}^*)} = \bar{\omega}^* \frac{\partial \bar{u}}{\partial p} \tag{3.8}$$

The above variables calculated in pressure coordinates are then converted into log-pressure coordinate by following method:

$$F_\phi = \frac{p}{p_0} F_\phi \tag{3.9}$$

$$F_z = -\frac{H}{p_0} F_p \tag{3.10}$$

$$\frac{\partial \bar{u}}{\partial t}|_{\nabla \cdot F} = \frac{\nabla \cdot F}{acos\phi} \tag{3.11}$$

$$\bar{w}^* = -\frac{H}{p} \bar{\omega}^* \tag{3.12}$$

The above described method from Gerber and Manzini (2016) was prescribed to CMIP6 modelling teams to produce the tendency terms from their model output. As we calculate MERRA-2 tendency terms in the same manner, the comparison to models become more accurate.

3.4.2 QBOi project and nudging methodology

The QBOi project is an international collaborative project that aims to improve the understanding and representation of tropical stratospheric variabilities in climate models (see Butchart et al. (2018) for a description of the overarching aims of the project). Phase 1 of the QBOi project, for which all the core publications are out now, addressed problems like various model performances in simulating QBO, climate change influence on QBO, predictability, etc. Most models have an easterly phase QBO (QBOE) that is generally too weak and exhibits a westerly time mean wind bias throughout the depth of the QBO (see Bushell et al. (2022); Rao

Experiment	Nudging target state (tropical stratosphere)
Control	None
Nudged	Realistic
NoQBO	Climatological

Table 3.1: Summary of QBOi phase-2 nudging experiments

et al. (2020); Garfinkel et al. (2022)). Currently phase 2 of the project is going on, focusing on how QBO teleconnections will work if the biases in QBO were removed.

Twelve models are participating in phase 2 of the QBOi project, each performing simulations extending from January 1979 to December 2020 (42 years). The following boundary conditions were recommended, with flexibility provided if changes do not significantly impact the results. Observed SST and sea ice distributions from the CMIP6 specification, available via input4MIPS, were proposed as AMIP boundary conditions. For models without interactive ozone, either climatological or transient ozone which does not have a QBO signal was suggested. Historical volcanic aerosol forcing and 11-year solar cycle in total irradiance and UV irradiance were advised but not mandatory. Additionally, transient forcings of CO_2 and other radiatively active trace gases were recommended.

Three experiments are performed, the 'Control', 'Nudged-Obs' and 'Nudged-Clim' experiments. Three ensemble members are performed for each experiment. In the Control experiment the model was allowed to evolve freely and in the Nudged-Obs experiment the equatorial stratospheric zonal-mean zonal winds were nudged towards the ECMWF ERA5 zonal-mean field in the height region of the QBO. The Nudged-Clim experiment applies nudging of model zonal-mean winds towards the ERA5 climatological winds thus removing the QBO (see below for methodology of the nudging) variability completely from the model stratosphere. Table 3.1 summarizes these three experiments.

The nudging methodology followed the Stratospheric Nudging And Predictable Surface Impacts (SNAPSI) protocol (Hitchcock et al., 2022), although the nudged regions and timescale differ. The nudging was fully applied between 10-70 hPa with gradual tapering to zero by 100 hPa and 5hPa, and between 10°S-10°N, with

tapering to zero by 20° latitude. This ensured that the nudging was applied only to the QBO region and the zonal winds in the SAO region were allowed to evolve freely. The nudging time scale used was 5 days, which is thought to be enough to constrain the slowly evolving QBO winds. To mimic the effect of momentum transfer from wave damping/absorption, only the zonal winds were nudged, so the temperatures and mean meridional circulation were able to respond to the zonal wind distributions by thermal wind balance. Additionally, only the zonal-mean of the zonal winds was nudged, to allow waves to evolve freely and thus avoid any significant artifacts (Hitchcock and Haynes, 2014; Hitchcock and Simpson, 2014; Martin et al., 2021; Hitchcock et al., 2022).

The HadGEM3 GA7.1 model simulation was performed and contributed to the QBOi phase 2 project by a collaboration of Oxford University and the Met Office. While relaxing to the zonal-mean zonal wind is relatively straightforward with a spectral model, it is not so straightforward in a grid-point model. In HadGEM3 GA7.1 the nudging was performed as follows. The nudging is introduced into the model as an additional forcing term in the zonal momentum equation of the form $-\alpha(u-u_{ana})$. Here u is the model zonal-mean zonal wind, u_{ana} is the target state or analysis zonal-mean zonal wind (for example, in the Nudged run, this is the ERA5 zonal-mean zonal wind) and α is the relaxation parameter equal to the inverse of the 5-day nudging time scale, which is $2.31 \times 10^{-6}\ s^{-1}$, scaled by the latitude and altitude profiles of the nudging. The reanalysis data are interpolated to align with model's resolution before calculating the nudging forcing. Six-hourly data from ERA5 is used for the nudging, which is interpolated to match the model's 20-minute time steps. Since the model solves equations discretely, nudging is implemented by adding the specified nudging forcing term to the model's zonal-mean zonal wind at each time step, across all latitudes, longitudes, and heights (the forcing will be zero at outside the intended nudging region). As only the zonal mean is nudged, the same increment is uniformly applied at every longitude.

The altitude profile of the nudging is given by

$$\frac{\alpha}{4}\left(1 - tanh\frac{p-p_b}{\Delta p_b}\right)\left(1 + tanh\frac{p-p_t}{\Delta p_t}\right) \tag{3.13}$$

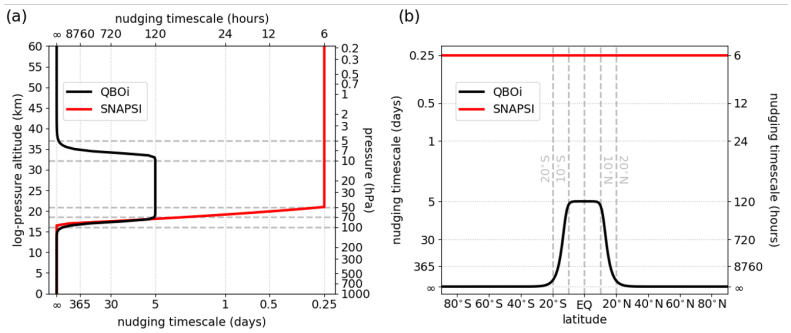

Figure 3.1: Spatial dependence of nudging timescale in the (a) vertical and (b) meridional directions. SNAPSI profiles are shown for comparison. (QBOi protocol paper)

where p is pressure, and in units of hPa:

$$p_b = 80, \Delta p_b = 5, p_t = 8, \Delta p_t = 0.5$$

The nudging rate at a given latitude remains constant across model levels and the pressure-level nudging profile shown above is converted to model levels using typical pressures on those model levels. The latitude profile of the nudging is given by

$$\frac{\alpha}{4}\left(1 + tanh\frac{\Phi - \Phi_S}{\Delta\Phi}\right)\left(1 - tanh\frac{\Phi - \Phi_N}{\Delta\Phi}\right) \tag{3.14}$$

where is latitude, and in units of degrees north:

$$\Phi_N = 12, \Phi_S = -12, \Delta\Phi = 2$$

In all other respects the Nudged experimental set-up was identical to the Control experiment. The vertical and horizontal profile of nudging as shown in Anstey et al (in preparation) is shown in Fig 3.1.

In chapter 5, the results shown are based on QBOi experiments done on HadGEM3 GA7.1. In chapter 6, the multi-model analysis chapter, QBOi nudging experiments in all models are analyzed.

3.4.3 Student's t test

To analyse the significance of results obtained in this study, a two sided Student's t test is employed in most cases. A Student's t test is a statistical test employed to understand if the mean of two groups are significantly different from one another.

Most of the analysis presented in this thesis involves comparisons of climatological means or composites of variables, between two different data sets.

We define the null-hypothesis as the assumption that the two sampled quantities, x_1 and x_2, are drawn from the same underlying distribution and have identical statistical characteristics. For x_1 and x_2, a t statistic is defined as

$$t = \frac{\bar{x}_1 + \bar{x}_2}{\sigma_{12}\sqrt{\frac{1}{n_1} + \frac{1}{n_2}}} \tag{3.15}$$

where σ_{12} is the pooled variance defined as

$$\sigma_{12} = \frac{\sigma_1^2(n_1 - 1) + \sigma_2^2(n_2 - 1)}{n_1 + n_2 - 2} \tag{3.16}$$

Here, $\bar{x}_i$, σ_i and n_i corresponds to mean, standard deviation and number of samples respectively of the quantity x_i. The obtained t value is then compared with a theoretical Student's t distribution to obtain an associated p value. Differences which yield a p value less than a set threshold (e.g., 0.05 for 95% confidence) are considered significant. In this case, the null hypothesis of identical means is rejected at this level of confidence and sampled quantities are considered to be significantly different.

3.4.4 Fourier transform and power spectra

Fourier transform is often used in meteorology to identify the patterns at timescales and spatial scales of interest. It allows the conversion of a field represented in physical space-time domain to wavenumber and frequency domain. With the discrete datasets used in meteorology, a Fast Fourier transform (FFT), which is a computationally fast method of doing a Discrete Fourier transform (DFT) is employed. If N is the number of points in time with fixed time steps, a one dimensional DFT applied to a field a_t which is a function of time from $t = 0$ to $t = N - 1$ can be written as:

$$A(k) = \sum_{t=0}^{N-1} a(t) e^{-2\pi i \frac{k}{N} t} \tag{3.17}$$

An inverse fourier transform is used to convert from fourier space to physical space, which is given by

$$a_t = \frac{1}{N} \sum_{k=0}^{N-1} A_k e^{2\pi i \frac{k}{N} t} \tag{3.18}$$

Here k is the frequency. It can also be represented as a sum of sine and cosine wave functions of a range of frequencies, each with a varying amplitude, such that the combination reproduces the original function.

Fourier transform can be used to identify the amplitude spectrum and power spectrum. This tells us what the amplitude or power present at a particular frequency is, and the power is calculated as:

$$P(k) = \frac{1}{N} |A(k)|^2 \tag{3.19}$$

And the amplitude is given by $\frac{1}{N}|A(k)|$. For instance, this analysis can help us identify the power or amplitude present at six-month and one-year frequencies in wind data, thus enabling us to identify whether there is a dominant annual or semi-annual signal in the wind patterns.

Going one step forward, a two dimensional fourier transform can be performed, where FFT is taken over both time and longitude. In longitude, the term wavenumber is used analogously to frequency in time. A wavenumber can be understood as the number of wavelengths needed to complete a circle around the globe. By applying the FFT to both longitude and time, followed by power spectral analysis, we can create a wavenumber-frequency power spectrum.

In this thesis, wavenumber-frequency power spectra are used to identify the signal of various atmospheric waves in the upper stratospheric wind in chapter 4. Zonal wind data in latitude, longitude and time at a particular altitude is analyzed. The methodology outlined in Wheeler and Kiladis (1999) is implemented. Either raw power spectra or symmetric/anti-symmetric power spectra can be calculated. The latter utilises the fact that atmospheric waves exhibit either symmetric or anti-symmetric behavior with respect to the equator. To better distinguish these wave signals, the wind data is decomposed into its symmetric and anti-symmetric components relative to the equator. For latitude ϕ, $u_{sym} = \frac{u[\phi]+u[-\phi]}{2}$ and $u_{anti} = \frac{u[\phi]-u[-\phi]}{2}$. Since the timescales of the atmospheric waves of interest

range from synoptic to intraseasonal, the data is divided into rolling 96-day windows with a 30-day overlap. Each window is detrended, low-frequency components are removed, and the window edges are tapered to zero. At each latitude, an FFT in longitude, and then in time is applied on u (or u_{sym} or u_{anti} depending on the type of power spectra) in each 96-day window. The power is calculated for each window and averaged, and then summed over the equatorial latitude band to get the wavenumber-freqency power spectra.

As detailed in the previous paragraph, this method assumes some of the properties of equatorial waves derived from linear wave theory, which might not always be accurate in the real atmosphere, where various complexities arise, such as the meridional and vertical wind shear, influence of extra-tropical waves and so on (Knippertz et al., 2022). These factors might affect the structure and characteristics of equatorial waves, causing deviations from the linear theory. In our analysis, to better filter out the wave signals, we leverage the fact that equatorial waves tend to be symmetric or anti-symmetric about the equator. While it is possible that this assumptions could result in missing some of the signals, various previous studies have shown that this approach remains a valid method for identifying wave signals in the stratosphere. For example, Ern et al. (2008) applied this decomposition, whereas Ern and Preusse (2009) excluded it, in order to assess the validity of the assumption. Their 2009 study, which analyzed temperature data, found that Kelvin wave acceleration signals in the stratosphere were roughly symmetrically distributed relative to the equator. We note that there are limitations to this approach, but for the cases we are analysing, these assumptions are shown to be good enough to separate the different wave signals in Earth's atmosphere.

3.4.5 NOGW parametrisation in UM

The UM uses Ultra-Simple Spectral Parametrization (USSP) scheme that represents the effects of the propagation and dissipation of NOGW spectra through the atmosphere based on the Warner and McIntyre scheme (Warner and McIntyre, 1999, 2001; Scaife et al., 2002).

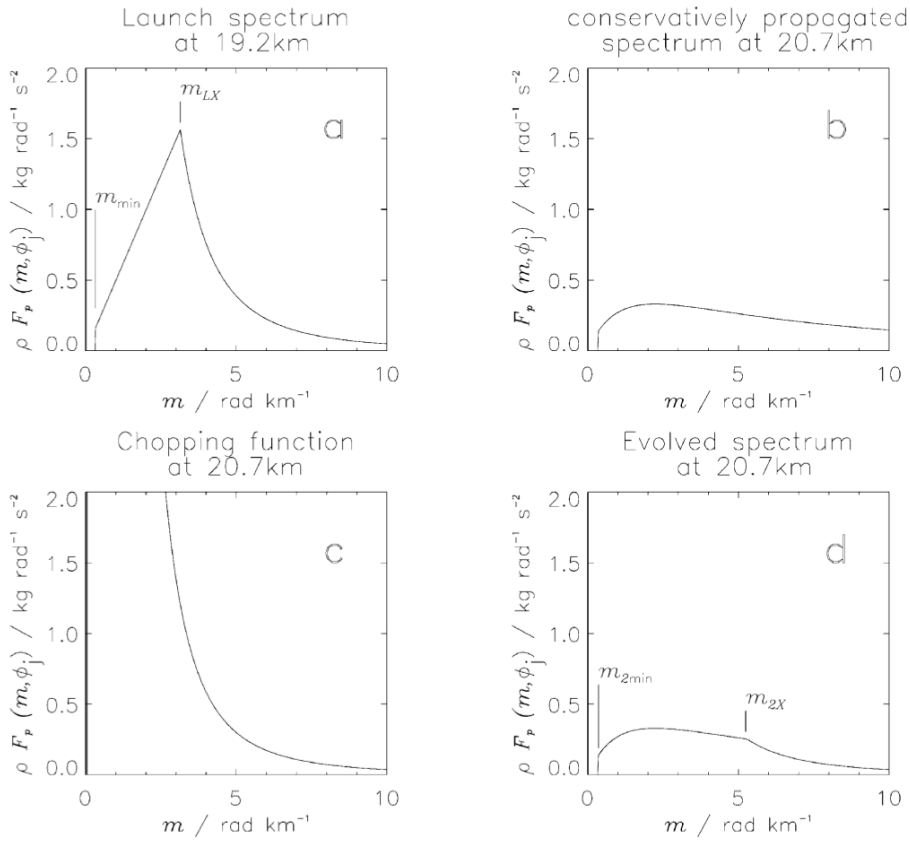

Figure 3.2: Computational procedure for the ultra-simple spectral parameterisation for a positive background wind shear with increment $U_2 - U_1 = 5ms^{-1}$. Launch spectra of the vertical flux of horizontal pseudo-momentum (a), conservatively propagated spectrum (b), chopping function (c) and evolved spectrum (d).(From Warner and McIntyre (2001)). In this thesis, m_{LX} is denoted as m^*, following the notation currently used in the Unified Model documentation.

.

The Warner and McIntyre (1996) scheme employs a NOGW launch energy spectrum based on the empirical form used by Fritts and Vanzandt (1993). By that time, numerous observational and theoretical studies had investigated the frequency and vertical wavenumber spectra of horizontal velocity in terms of gravity waves (e.g., VanZandt (1982); Allen and Vincent (1995); Burrage et al. (1996). See Warner and McIntyre (1996) for more details). As the full three dimensional power spectral model of gravity waves is computationally expensive, following Fritts and Lu (1993), Warner and McIntyre (1999) defined a simplified two-part launch spectrum while neglecting Coriolis and non-hydrostatic effects in the dispersion relation. The two-part launch spectrum is shown in figure 3.2a from Warner and McIntyre (1999). This

idealisation is in the spirit of Fritts and Lu (1993), where the two distinct parts of the spectrum differentiate between small and large wavenumbers, each exhibiting a different power law dependence. Warner and McIntyre (1999) notes that waves with wavelengths greater than 20km are rarely observed in stratosphere and introduces a sharp cut-off, setting the momentum flux to zero for wavelengths larger than 20km. Following suggestions from Fritts and Vanzandt (1993), the next part of the spectrum is directly proportional to wavenumber, m (see between m_{min} and m_{LX}) in figure 3.2a). At larger wavenumbers, m, gravity wave spectra follow the m^{-3} relationship, which is roughly independent of time, place and altitude, though not always (see for wavenumbers higher than m_{LX} in figure 3.2a). This m^{-3} relationship is supported by observations and theory (Fritts et al., 1989; Dewan and Good, 1986; Smith et al., 1987), and is suggested to be associated with saturation by wave breaking.

In the UM, an isotropic initial launch spectrum of the vertical flux of horizontal component of NOGW pseudomomentum is defined at a height level close to the surface, currently at the model level nearest to η=0.045 ($\sim$4000m) at each grid column. This spectrum incorporates all the characteristics described above as shown in the figure 3.2a. The net NOGW flux is zero below the launch level and gets eroded above the launch level, so the maximum total flux is at the launch level. As the launch spectrum propagates to higher altitudes, in the presence of vertical wind shear, the NOGW flux is modified due to Doppler shifting of frequency and the vertical wavenumber is modified (see figure 3.2b for an example of modified spectrum in a positive background wind shear). As the spectra changes in wavenumber, growth at large wavenumbers is expected to be limited by wave dissipation due to saturation. The wave breaking is introduced based on empirical knowledge, and regardless of the mechanism, limits the large m part of gravity wave spectrum to a ceiling $\propto m^{-3}$. To implement this in the UM, a saturation spectrum, termed as chopping function is introduced at each vertical level (see figure 3.2c for an example of chopping function). The launch spectrum is transformed as it propagates upward, and at each level, the spectrum shape is eroded to match the chopping function slope, thus ensuring the large m part of gravity wave spectrum do

not exceed the chopping function (notionally the local saturation spectrum), and the lost flux is converted to equivalent force in horizontal winds (see figure 3.2d for an example of evolved spectrum). The computational implementation further involves an artificial backward propagation to the surface so as to calculate changes in gravity wave momentum flux, details of which can be found in Warner and McIntyre (1999).

The general parameters of the launch spectra in the UM can be seen in figure 3.2a (parameters such as launch altitude and scaling factors shown in the figure differ from the version implemented in UM). Following the notation currently used in the UM documentation, the launch spectrum has two main characteristic features m_{min} and m* (shown as m_{min} and m_{LX} respectively in figure 3.2a). m_{min} is the cut off wavenumber that decides the maximum wavelength of waves in the spectrum. This is of particular interest because the SAO is driven by high-phase-speed waves. Our limited understanding of wavenumbers at this part of the spectrum leads to the sharp cut off at m_{min}. m* on the other hand is the wavenumber at which the launch flux is maximum, with the flux dropping off proportionally to m^{-3} at lower wavenumbers. A larger (smaller) m* increases (decreases) the flux of larger wavemuber waves, and a smaller m_{min} allows more high-speed waves. The amplitude of the gravity wave source is proportional to the square root of total precipitation to capture the spatial and temporal variability of their generation (Bushell et al., 2015). A parameter to tune the amplitude of NOGW generated by precipitation is also available. At the end of thesis, we investigate a few scenarios by adjusting the NOGW parametrization in UM, by modifying the above-mentioned parameters, to understand the response of SAO.

4

A Momentum Budget Study of the Semi-annual Oscillation

4.1 Introduction

Since the discovery of the SAO in the upper stratosphere, so many studies have advanced our understanding of the SAO characteristics and the mechanisms behind its formation (see section 2.7.2). However, as noted earlier, the representation of the SAO in current climate models still suffers from significant biases. The main aim of this chapter is to understand the source of the easterly bias in the modelled SAO in our climate models.

The attempt to model the general circulation of middle atmosphere started in the early 1960s (Murgatroyd and Singleton, 1961), and eventually the representation of SAO in climate models as well. Some of the earlier studies like Meyer (1970) and Holton and Wehrbein (1980) explored the modelling of SAO using simplified models. These studies were crucial in expanding our understanding of the driving forces of SAO, like the importance of advection and planetary waves in driving the easterly phase of SAO. Simulating the westerly phase of the SAO was a challenging problem from the early years, as many models generated the SAO variability with only the easterlies present in the upper stratosphere. An observational analysis by Hirota (1978) indicated the role of high-speed Kelvin waves in driving the SAO westerlies,

and incorporating the Kelvin wave driving in the models led to improvements in the simulation of the SAO westerlies (e.g. Dunkerton (1979)). However, many models still struggled. Hitchman and Leovy (1988), while quantifying the contribution of Kelvin waves to the zonal-mean momentum budget, suggested that gravity waves may contribute to the driving of the westerly phase of SAO. Modelling studies like Hamilton and Mahlman (1988) and Jackson and Gray (1994) confirmed that including gravity wave parametrization could improve the representation of SAO westerly phase in models. Even though the necessity of small-scale gravity waves were already known and many models started incorporating parametrization of gravity waves, a multi-model analysis in 2001 showed that models were not simulating a good SAO westerly phase (Amodei et al., 2001). And, as we have briefly discussed in Chapter 2, Smith et al. (2019), has highlighted that most of the current day climate models still have an easterly bias at the SAO altitudes.

The influence of the SAO on the rest of the atmosphere was discussed in section 2.9. Of particular interest is the possible role of SAO on extra-tropical winter circulation, which has been a topic of discussion for several years as well (Gray, 2003; Gray et al., 2004, 2022). The suggested role of the SAO in influencing SSWs was outlined in section 2.9.2. This highlighted the necessity to reduce the easterly bias in SAO. This influence of the SAO on other processes in the atmosphere suggests that reducing the SAO bias could help in modelling our atmosphere better, not just the equatorial upper stratosphere.

Figure 4.1 shows the height profile of multi-year mean of zonal-mean zonal wind in 11 present-day climate models along with winds derived from observed geopotential height, presented by Smith et al. (2019) (see their Figure 4). It is immediately apparent from the figure that nearly all the climate models exhibit an easterly bias in zonal-mean zonal wind SAO (see at 1 hPa in figure 4.1). While the SAO representation in models has improved over the years, with models successfully generating the alternating westerlies and easterlies, it is important that we understand the reasons behind the easterly biases that still exists and try to alleviate them. Could the easterly bias be the result of an overly strong

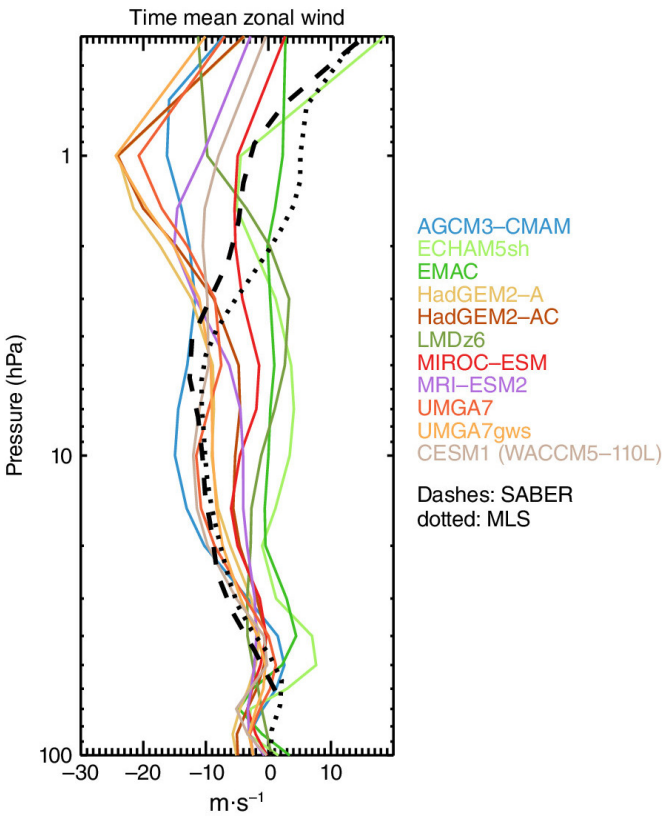

Figure 4.1: Coloured lines show the multi-year time average of the equatorial zonal-mean zonal wind (ms^{-1}) for 11 models. The dashed (SABER) and dotted (MLS) black lines are values derived from satellite geopotential height observations (From Smith et al. (2019))

westward forcing or a weaker eastward forcing and what is the dynamical origin of this bias? As none of these earlier studies have examined all of the individual driving mechanisms in order to draw a solid conclusion on the reason for the easterly bias, this chapter aims to address that gap.

Although there exists a sound theoretical basis for the mechanism of SAO formation, lack of enough observational data in the SAO altitudes has made it difficult to fully understand what happens in our atmosphere. Due to this scarcity of observations, in this chapter, reanaysis data is chosen to analyse and understand the mechanism of SAO formation. We note that there exists large uncertainty among the reanalysis as well in the representation of SAO. Kawatani et al. (2020) provides a comprehensive comparison of the up-to-date reanalysis available in representing the SAO. It can be seen that all the reanalyses show variations from satellite derived winds in one way or another. Lack of in-situ measurements at SAO altitudes is a

huge problem in representing a correct SAO in reanalysis. This chapter provides a brief comparison of some of the reanalysis datasets, selecting the one with an SAO profile that resembles the available observations the most, and then explores the contribution of different forcing terms to the formation of the SAO.

By carefully examining individual contributions to the momentum budget of the SAO region in a specific climate model and comparing it with reanalyses, we aim to determine which momentum forcing terms are most influential and which terms contribute to the easterly bias. The chapter is laid out as follows: section 4.2 describes the data and analyses used in this chapter. Results are presented in section 4.3 and section 4.4 summarises our findings.

4.2 Data and methods

This chapter utilizes the TEM equation (see section 2.5) to quantify the contribution of different momentum forcing terms in both reanalyses and the model. Comparisons between the model and reanalysis terms are conducted to identify possible model biases. Three reanalysis datasets are initially evaluated: MERRA-2, ERA-Interim and ERA5, which are described in section 3.2 and based on the evaluation presented in section 4.3.1, the MERRA-2 dataset is employed as the primary reanalysis dataset used in this chapter.

CESM2-WACCM, described in section 3.3, has been selected as the sample climate model for a more comprehensive investigation. It is a coupled chemistry model that extends much higher in altitude than most other models, which helps to avoid potential complications arising from having the model top close to SAO altitudes. It also demonstrates a reliable representation of the QBO, reducing the impact of QBO biases on the SAO (see section 2.7.1 for a review on QBO). Initially HadGEM was examined to conduct this study. However, the momentum budget calculation showed that there are some problems with the accuracy of the result in the uppermost levels of the model, which could be due to issues regarding interpolation from model levels to pressure coordinates, or some unknown/numerical

diffusion processes. To ensure the comparison is as accurate as possible, we decided to proceed with WACCM.

The WACCM model dataset used is the CMIP6 pre-industrial control (pi-Control) simulation (Eyring et al., 2016). This coupled atmosphere-ocean simulation was run with prescribed pre-industrial (1850) levels of greenhouse gas and aerosols. It therefore has no time-varying external forcing apart from daily and seasonal radiative variations, so any variability on other time scales is internally-generated. We choose to use the WACCM pi-Control simulation, even though its imposed external forcings are not directly comparable with the MERRA-2 reanalysis dataset, because the climatology of its forcing can be assessed with many more available years and its SAO climatology was found to be very similar to the corresponding WACCM present-day CMIP6 simulation. The CMIP6 data is published by the Earth System Grid Federation; more details on the WACCM pi-Control simulation can be found at Danabasoglu et al. (2020). All analyses were performed using data from the first 500 years of the simulation. For the power spectral analysis described in section 4.3, only the first 42 years of data are used so that the data length matches that of MERRA-2. Tests were performed to check that similar results were found with different 42-year intervals.

A detailed description of the methodology employed in the chapter, including the momentum budget analysis, power spectra and estimation of statistical significance of the results, is described in section 3.4. The zonal-mean momentum budget of the SAO is analysed using the TEM momentum equation (Andrews et al., 1987) in spherical geometry and log-pressure coordinates (section 2.5). Using the three-hourly averaged horizontal and vertical winds and temperature fields (u, v, w, T) from the MERRA-2 datasets, TEM diagnostics contributing to the SAO forcing are calculated in pressure coordinates and transformed into a standard log-pressure vertical coordinate to obtain the formulation of Andrews et al. (1987), as outlined in section 3.4.1. For WACCM, the CMIP6 data archive repository includes the pre-calculated TEM variables. Daily mean values of the TEM variables are presented in this chapter.

To assess statistical significance in model-reanalysis comparisons, a two-sided Student's t-test, described in section 3.4.3, is used. The null-hypothesis states that the reanalysis and model data are drawn from the same underlying distribution and have identical statistical characteristics. A p-value less than 1% is considered indicative of a significant difference between the model and reanalysis means.

4.3 Results

4.3.1 SAO in reanalyses

Figure 4.2a-c shows the time-height section of equatorial daily-mean zonal-mean zonal winds (5°N-5°S) from the MERRA-2, ERA-I and ERA5 reanalysis datasets for a sample of 10 years. Alternating westerlies and easterlies, consistent with the stratospheric SAO, are evident over an altitude range of 10 hPa to 0.1 hPa.

While the three reanalysis datasets agree well in terms of the broad structure of the alternating winds that form the SAO there are major differences, particularly in the strength and duration of the westerly phase. MERRA-2 and ERA5 have stronger and longer-lasting westerly wind regimes, while ERA-I shows westerly and easterly phases that are similar in both strength and duration. The relatively weak SAO westerly phase in ERA-I is likely associated with the lack of a non-orographic gravity wave parameterisation. However, the ERA5 reanalysis has unrealistically strong SAO westerlies (>70 (ms^{-1})) near the stratopause, as noted by previous studies (Shepherd et al., 2018; Ern et al., 2021). The MERRA-2 dataset is considered to be the more realistic when compared with SABER and MLS observational data (Kawatani et al., 2020). MERRA-2 assimilates MLS temperature data above 5 hPa starting in August 2004, so a close resemblance to the observations is perhaps not surprising (Ern et al. (2021); SPARC (2021) Chapter 11). Nevertheless, the sharp weakening of the MERRA-2 SAO amplitude above 0.03 hPa is unrealistic compared to observations (Kawatani et al., 2020). Since among the three reanalyses MERRA-2 most closely resembles the winds derived from satellite observations, we use MERRA-2 for comparison with the WACCM model in the remainder of the chapter (MERRA-2 is the reanalysis used for comparisons to models in the

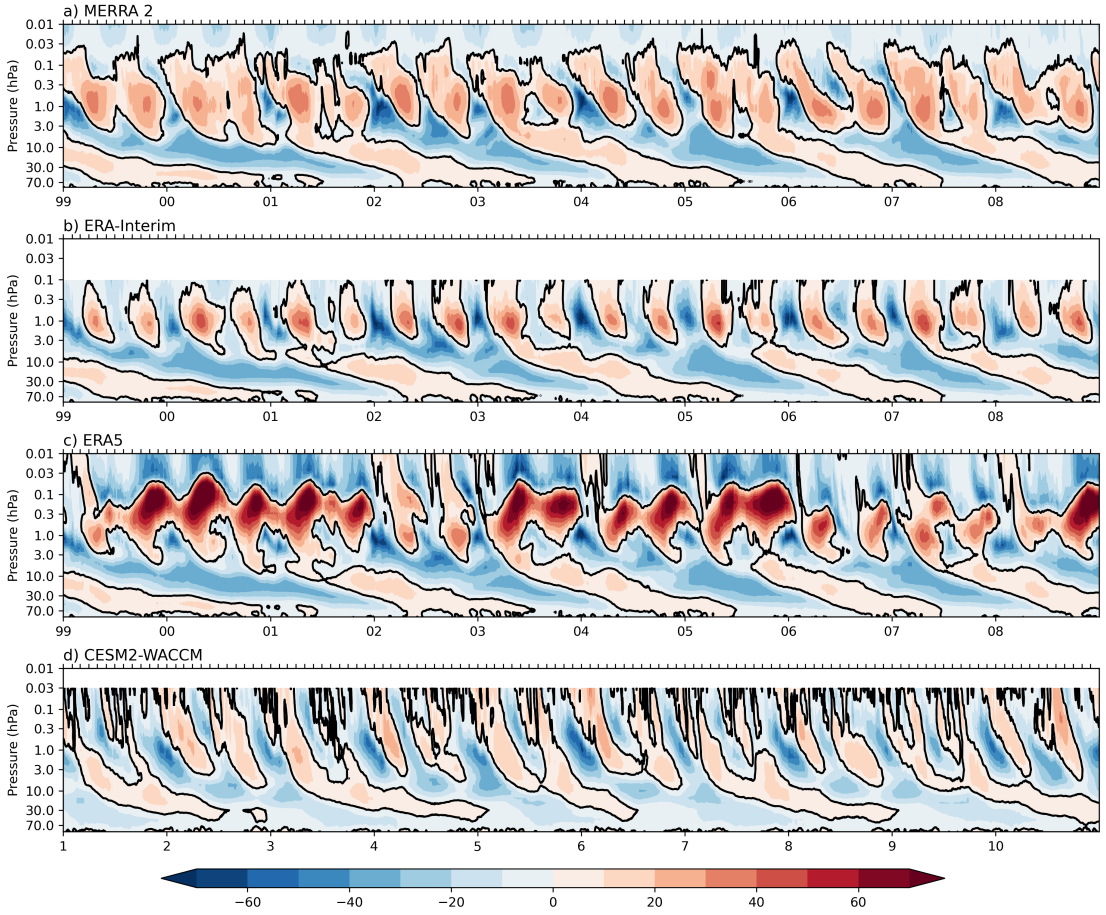

Figure 4.2: zonal-mean zonal wind ((ms^{-1})) averaged over 5°N to 5°S for the years 1999 to 2008 for (a) MERRA 2, (b) ERA-interim, (c) ERA5 and (d) a sample 10 years from the WACCM model simulation.

rest of the thesis as well). We compare diagnostics for altitudes below 0.03 hPa because the WACCM CMIP6 TEM dataset was only archived up to this level, focusing primarily on the region below 0.24 hPa (the level where artificial damping is introduced in the MERRA-2 dataset) to learn more about the forcing contributing to the peak in SAO amplitude centred around 1 hPa.

Figure 4.3a-b shows the climatological equatorial zonal-mean zonal winds from the MERRA-2 reanalysis dataset. The time-series are shown in six-month subsections (November-April and May-October), centred around the MERRA-2 peaks in stratopause easterlies that occur in February and August. In this way, we can highlight the differences between the first and second SAO cycles that contribute to the presence of an annual cycle. As expected, Figure 4.3a-b shows alternating

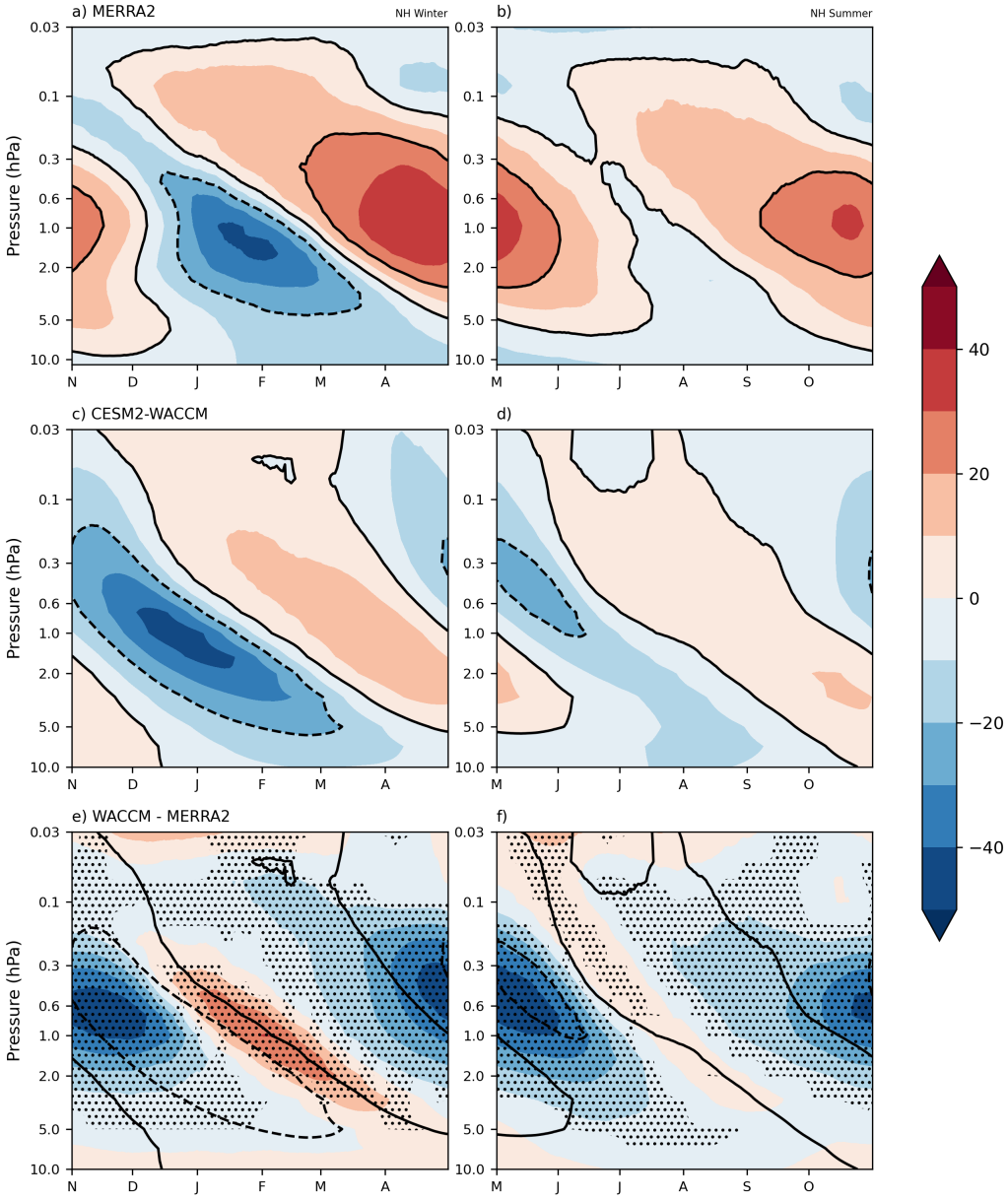

Figure 4.3: Daily mean climatology of zonal-mean zonal wind (ms^{-1}) averaged over 5°N to 5°S for (a,b) MERRA 2 based on 42 years (1980-2021). (c,d) WACCM, based on the first 500 years of the CMIP6 pi-Control simulation (see section 4.2 for details). Contours of -20, 0, 20 (ms^{-1}) are overlaid, with dashed contours denoting negative values. For clarity, the time-axis has been separated and centred around the onset of the easterly phase. (e,f) WACCM minus MERRA-2 differences, with overlaid wind contours from the WACCM distribution. Stippling denotes 99% confidence interval.

westerlies and easterlies forming the SAO spanning from 5 hPa to 0.1 hPa with an approximate period of 6 months. The SAO in MERRA-2 at 1 hPa aligns closely with the satellite-derived wind magnitudes from the SABER and MLS satellite data shown in Smith et al. (2017) (see figure 2.10), particularly during the easterly phase, although there are some small differences in the westerly phase amplitudes, with SABER and MLS indicating westerly SAO magnitudes around 20-25 (ms^{-1}), whereas MERRA-2 shows magnitudes reaching up to 30 (ms^{-1}).

4.3.2 The modelled SAO

The time-height section of daily-mean zonal-mean equatorial zonal winds (5°N-5°S) from WACCM for a sample of 10 years is shown in Figure 4.2d. The alternating westerlies and easterlies of the SAO over the altitude range of 10 hPa to 0.1 hPa are similar to the reanalyses, including the gradual descent of the westerly phase so that it merges with the onset of the QBO westerly phase. However, the amplitudes of the easterly and westerly SAO phases are roughly equal in magnitude, similar to ERA-I, such that there is a noticeable easterly bias at ∼1 hPa when compared with MERRA-2.

The easterly bias is confirmed in Figure 4.4 which shows latitude-height sections of climatological zonal-mean zonal winds, averaged over each three-month seasonal window from MERRA-2 (Figures 4.4a-d) and WACCM (Figures 4.4e-h), together with the WACCM minus MERRA-2 difference (Figures 4.4i-l). A negative difference therefore denotes an easterly bias in WACCM, while a positive difference denotes a westerly bias. The most obvious differences between WACCM and MERRA-2 in the SAO region are the weaker westerly regimes near 0.5 hPa at the equinoxes in WACCM. The model shows a maximum deviation from the reanalysis in the spring and autumn seasons, i.e., during the westerly phases of SAO. For example, during MAM and SON, MERRA-2 has westerly winds extending from one hemisphere to the other with a secondary peak at equator. While the model captures this broad pattern, the equatorial westerlies are much weaker, by greater than 30 (ms^{-1}) at the equinoxes (Figure 4.4j,l). The easterly phases in DJF and JJA are more comparable,

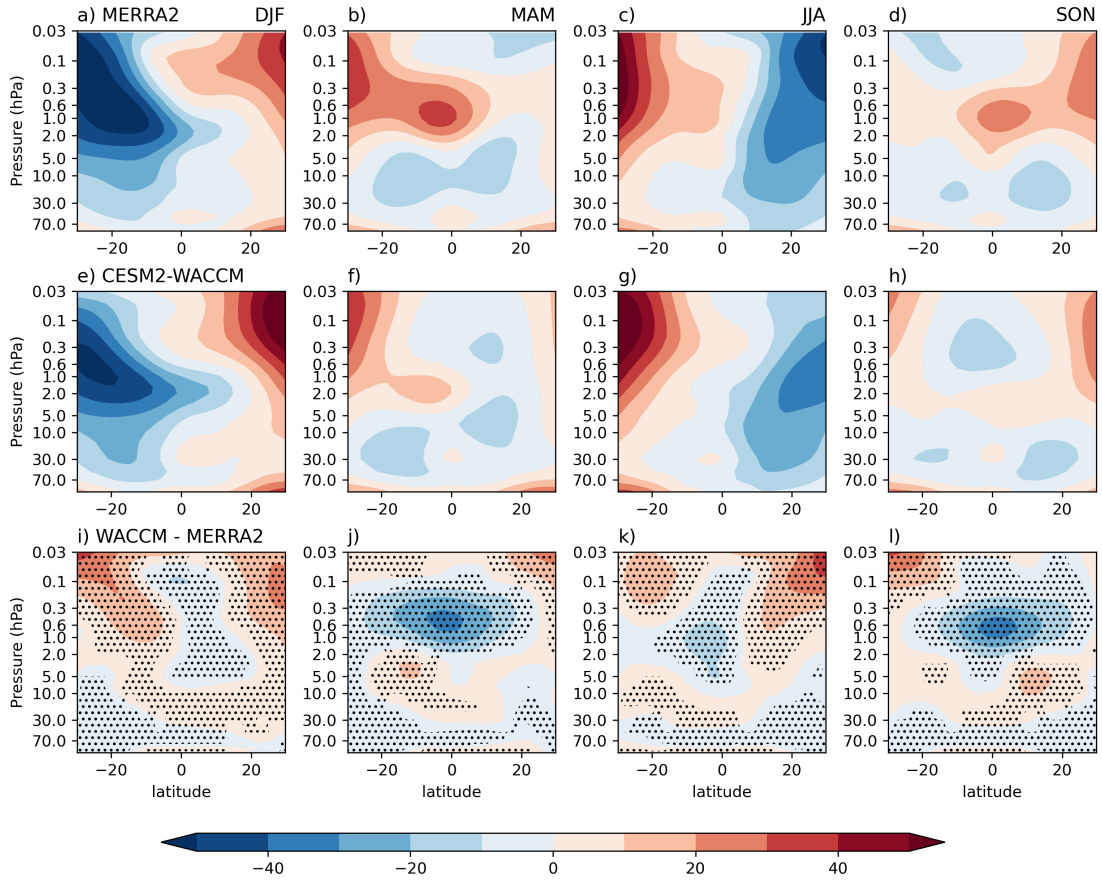

Figure 4.4: Latitude-height sections of 3-month averaged zonal-mean zonal wind (ms^{-1}) between ± 30 degrees latitude from (a-d) the MERRA-2 42-year (1980-2021) climatology, (e-h) the 500-year WACCM climatology, and (i-l) the WACCM minus MERRA-2 differences. Stippling denotes 99% confidence interval.

although the 'nose' of easterlies that extends from the SH subtropics into equatorial latitudes at ∼2 hPa in DJF is slightly over-estimated in WACCM. The annual cycle is readily apparent at the equator in both MERRA-2 and WACCM; e.g., the DJF 1 hPa equatorial winds in MERRA-2 and WACCM are ∼ -30 (ms^{-1}) while in JJA, WACCM has easterlies of -10 (ms^{-1}) and MERRA-2 still has westerlies.

To confirm the presence of the annual cycle, Figure 4.5 shows the frequency amplitude spectra of zonal-mean equatorial (5°S-5°N) zonal winds over a range of altitudes in the stratosphere, derived from the initial 42 years of WACCM data. It confirms that variability in both MERRA-2 and WACCM is dominated by QBO periodicities of around 2 years at altitudes below 5 hPa, while between 5 hPa and 0.1 hPa it is dominated by 6-month SAO periodicities and a less

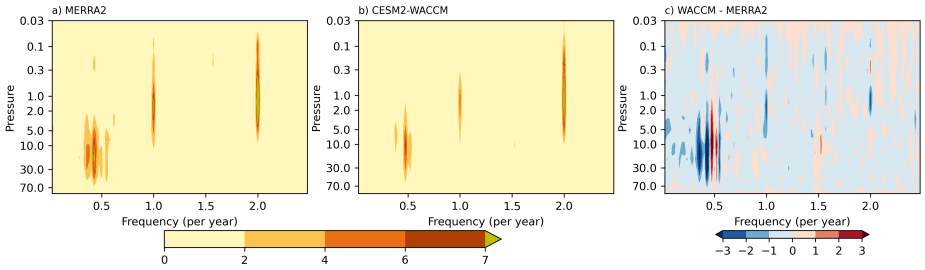

Figure 4.5: Frequency amplitude spectrum of climatological zonal-mean zonal wind from 5°S-5°N as a function of altitude from (a) MERRA-2, (b) WACCM and (c) the WACCM minus MERRA-2 differences. The colour contours are Fourier amplitudes (square root of power). Units are (ms^{-1}).

pronounced annual variability, as noted above. However, the WACCM power is consistently lower across all frequencies, suggesting that the amplitudes of the QBO, SAO and annual variability are all under-estimated in this 70-level version of WACCM. Note also that the WACCM QBO has a shorter period which shows up as a dipole in the differences plot.

4.3.3 Momentum budget

In this section the primary focus is to examine the climatology of the different forcing terms that contribute to the wind distributions in the SAO region. Returning to a closer examination of the zonal wind evolution shown in Figure 4.3, the peak winds of the westerly phase of the WACCM SAO (Figure 4.3c-d) are less than 20 (ms^{-1}) for the majority of the period, while MERRA-2 (Figure 4.3a-b) shows winds of up to 40 (ms^{-1}). The onset of the WACCM easterly phase is too early; for example, at 1 hPa the WACCM westerlies reverse to easterlies in mid-April and October, almost two months before MERRA-2. The onset of the WACCM westerly phase also occurs slightly early, compared to MERRA-2, but the amplitude of the westerly phase fails to develop sufficiently strongly and does not last long enough compared to MERRA-2. In summary, Figure 4.3 confirms the results of earlier studies (Smith et al. 2019) that WACCM, along with most other models, has a substantial easterly bias near the stratopause. It also highlights a mismatch in the timing of the phase onsets.

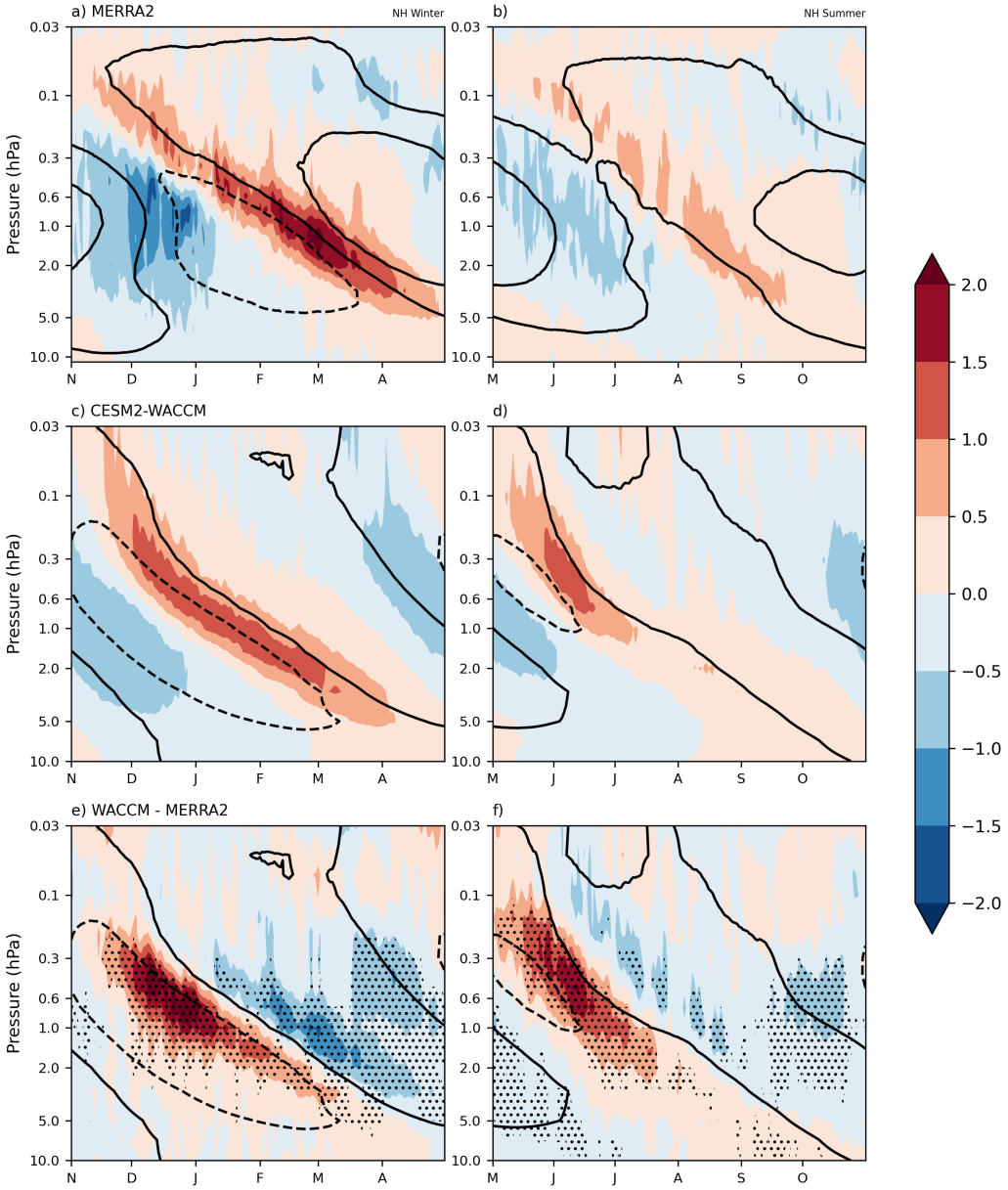

Figure 4.6: Climatology of zonal-mean zonal wind tendency ($ms^{-1}day^{-1}$) averaged over 5°N to 5°S for (a,b) MERRA 2, (c-d) WACCM, (e-f) WACCM minus MERRA-2 differences. The respective climatological zonal-mean zonal wind contours of -20, 0, 20 ms^{-1} are overlaid. Stippling denotes 99% confidence interval.

To further investigate those factors influencing the SAO evolution, we examine the individual components of the TEM momentum equation, Equation 2.19, as described in section 2.5. Figure 4.6 shows the time evolution of the climatological total rate of change of equatorial zonal-mean zonal winds from MERRA-2 and WACCM averaged over ±5° latitude. The data are plotted only in the stratosphere above 10 hPa, such that the region dominated by the SAO is highlighted. Also plotted (in contours) are the respective climatological equatorial zonal winds from Figure 4.3.

In MERRA-2 the strongest eastward acceleration is evident at the onset of both westerly SAO phases, as expected, and follows the zero-wind contour as it descends with time. Similarly, the maximum westward acceleration is evident around the onset of each easterly phase. However, at the onset of the first easterly phase in November-January the maximum acceleration occurs simultaneously over a range of altitudes between 5 and 0.3 hPa, while it descends more gradually with time at the onset of the second easterly phase, starting at 0.3 hPa in May and descending to around 5 hPa by July.

For WACCM, the corresponding time-series shows similar behaviour, but with differences in timing that reflect the differences in timing of the SAO phases noted above. Moreover, the westward acceleration phase centred around December gradually descends with time, in contrast to MERRA-2 where it appears simultaneously over an extended height region. In the difference plots (Figure 4.6 e-f), at altitudes below 0.1 hPa the values are mostly negative during the westerly SAO phase periods, which suggests a weaker eastward forcing during this phase. The exception is the period of strong positive difference immediately before the westerly phase onset. Normally, this would suggest a greater eastward forcing in the model, but in this case, the discrepancy in timing is primarily responsible. For example, the WACCM eastward acceleration at 1 hPa starts almost a month before MERRA-2 and this partly contributes to the strong positive value in the difference plot, since the reanalysis still has westward acceleration at this time. Furthermore, during the rest of the westerly phase, the model fails to show sufficiently strong eastward

acceleration, especially at altitudes between 1 hPa and 5 hPa, resulting in the low magnitude of the westerly winds that was previously noted.

As described in subsection SAO forcing terms under section 2.7.2 (see this section for a review of how each forcing term affects the SAO), the forcing of the SAO can be analysed as a combination of four terms in the TEM equation: meridional advection, vertical advection, EP flux divergence and a residual term that includes gravity wave forcing. We now examine each of these in detail to identify how they evolve over time and how the model differs from the reanalyses.

4.3.3.1 Advection

Figure 4.7 a-b shows the contribution of meridional advection in MERRA-2 to the forcing of the SAO winds (first term on the RHS of Eq. 2.19). The part of this term associated with the BDC advects easterlies from the summer hemisphere. The forcing increases with height above the stratopause and is strongest above ~ 0.1 hPa, reflecting the GW-driven mean meridional circulation at those altitudes, with a secondary peak at $\sim$1 hPa centred around the solstice period. It is important to note that although there is GW driven mean meridional circulation above 0.1hPa, due to upper boundary conditions in MERRA-2, the meridional advection above this altitude might not be realistic. The overlaid zonal-mean zonal wind contours in Figure 4.7 confirm that the westward forcing due to meridional advection matches very well the arrival of easterly winds of the SAO, as suggested by previous studies (Holton and Wehrbein, 1980). Even though there is a predominant westward forcing pattern for the majority of the months appearing at all levels almost simultaneously (Figure 4.7a,b May and November), there is also evidence of descent in the peak forcing, for example between November and February in the height range 0.2 – 5 hPa.

The meridional advection pattern in WACCM (Figure 4.7c-d) is similar to MERRA-2, but the magnitude is noticeably smaller. Despite the reduced magnitude of westward forcing due to meridional advection, WACCM nevertheless achieves realistic easterly SAO amplitudes since the intervening westerlies are also weaker. When compared to MERRA-2 (Figure 4.7e-f) the westward forcing due to meridional

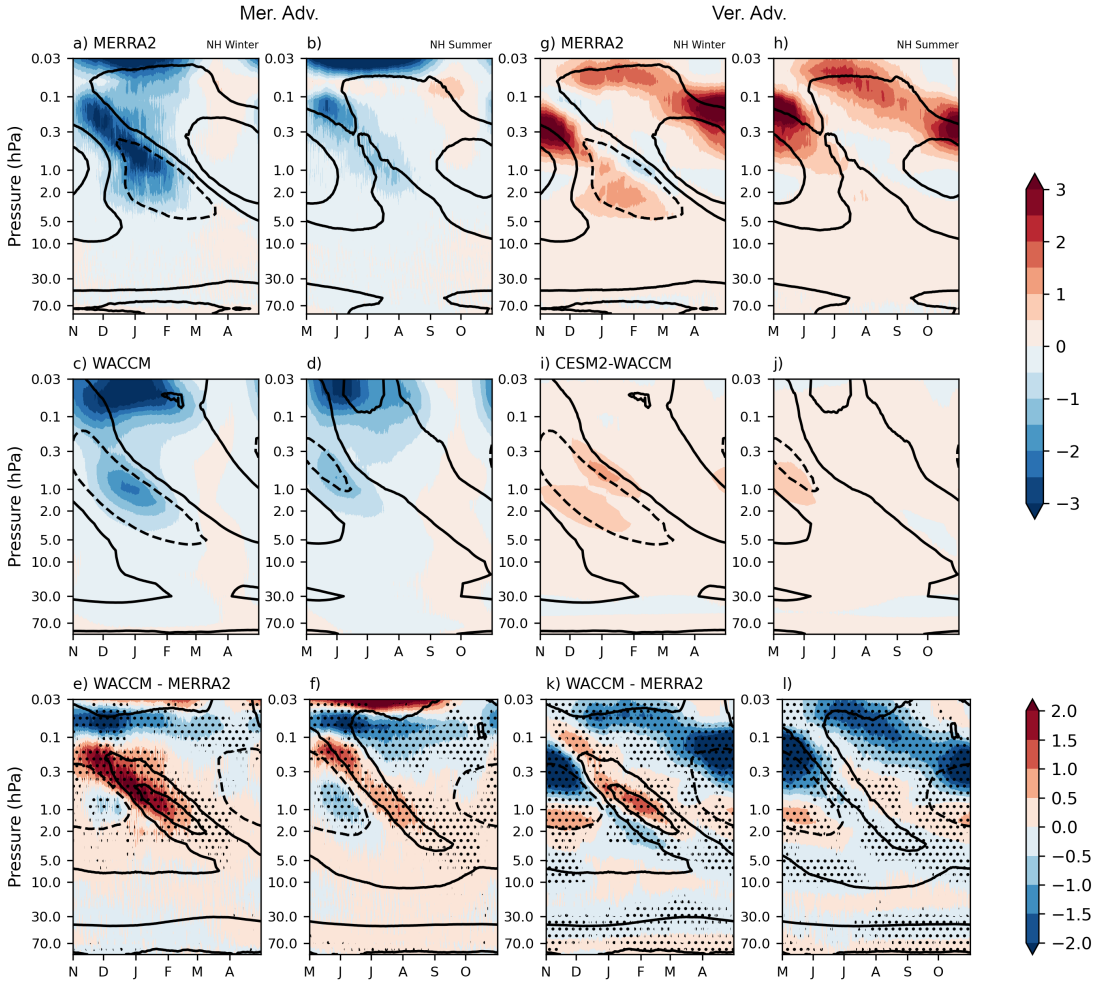

Figure 4.7: Climatology of zonal-mean zonal wind tendency due to meridional advection ($ms^{-1}day^{-1}$) averaged over 5°N to 5°S for (a,b) MERRA 2, (c,d) WACCM, (e,f) WACCM minus MERRA-2 differences. Climatology of zonal-mean zonal wind tendency due to vertical advection ($ms^{-1}day^{-1}$) for (g,h) MERRA-2, (i,j) WACCM, (k,l) WACCM minus MERRA-2 differences. Corresponding zonal-mean zonal wind contours of -20, 0, 20 ms^{-1} are overlaid(a-d,g-j). Differences in zonal-mean zonal wind contours of -20, 0, 20 ms^{-1} are overlaid in e-f, k-l. Stippling denotes 99% confidence interval.

advection in WACCM is stronger early on at lower altitudes (Figure 4.7c, d at 1 hPa), which contributes to the early termination of the westerly phase in WACCM.

As noted in section 2.6.2, Northern Hemispheric winter has more planetary wave breaking in the mid latitudes than the SH winter and hence a stronger BDC, leading to stronger meridional advection in DJF. Weaker meridional advection in JJA compared with DJF is apparent in both MERRA-2 and WACCM below 0.1 hPa. However, even though the earlier analysis shown in Figure 4.4 suggests that

WACCM succeeds in capturing a reasonable annual cycle, the overall magnitude of advection is much weaker in WACCM, especially in DJF (as the difference plots in Figure 4.7e,f clearly show). Further analysis of the contributions to the horizontal advection term in Equation 2.19 was performed (Figure 4.8) by separately examining the meridional residual circulation ($\bar{v}^*$) and meridional gradient of zonal-mean zonal wind ($\frac{d\bar{u}}{dy}$). Differences in $\frac{d\bar{u}}{dy}$ are a major contributor to the generally weaker magnitudes of meridional advection in WACCM compared to MERRA-2. The figure also shows that while WACCM $\bar{v}^*$ during NH winter resembles that of MERRA-2, it appears overly strong during SH winter. Consequently, WACCM does not capture the strong difference in magnitude of $\bar{v}^*$ between the NH and SH winter, which is evident in MERRA-2. This shows that the anomalously weak annual cycle amplitude in WACCM horizontal advection is primarily due to the $\bar{v}^*$ term, suggesting that the well-known difference in mid-latitude planetary wave breaking (or the role of gravity wave driving) between the two hemispheres that produces a stronger BDC around January than July is not well simulated by WACCM.

Figure 4.7 g-h shows the corresponding MERRA-2 plots for the contribution of vertical advection (second term on the RHS of Eq. 2.19). In contrast to the meridional advection term, vertical advection is dominated by eastward forcing. The strength of the vertical advection consists of two contributions - the vertical advection associated with the large-scale BDC, and a more locally induced vertical circulation associated with in-situ equatorial wave forcing. The balance of the two contributions will vary both with height and with time of the year. The BDC is known to consist of upwelling at equatorial latitudes throughout the year, while locally induced circulations will produce upwelling during periods of westward wave forcing (negative vertical wind shear) and downwelling during periods of eastward wave forcing (positive vertical wind shear), thus maintaining approximate thermal wind balance. Thus, depending on the strength of the localised wave forcing (and the resulting induced circulation), there is likely to be weakened upwelling (or possibly even downwelling) at the onset of the SAO westerly phase and upwelling for the rest of the year.

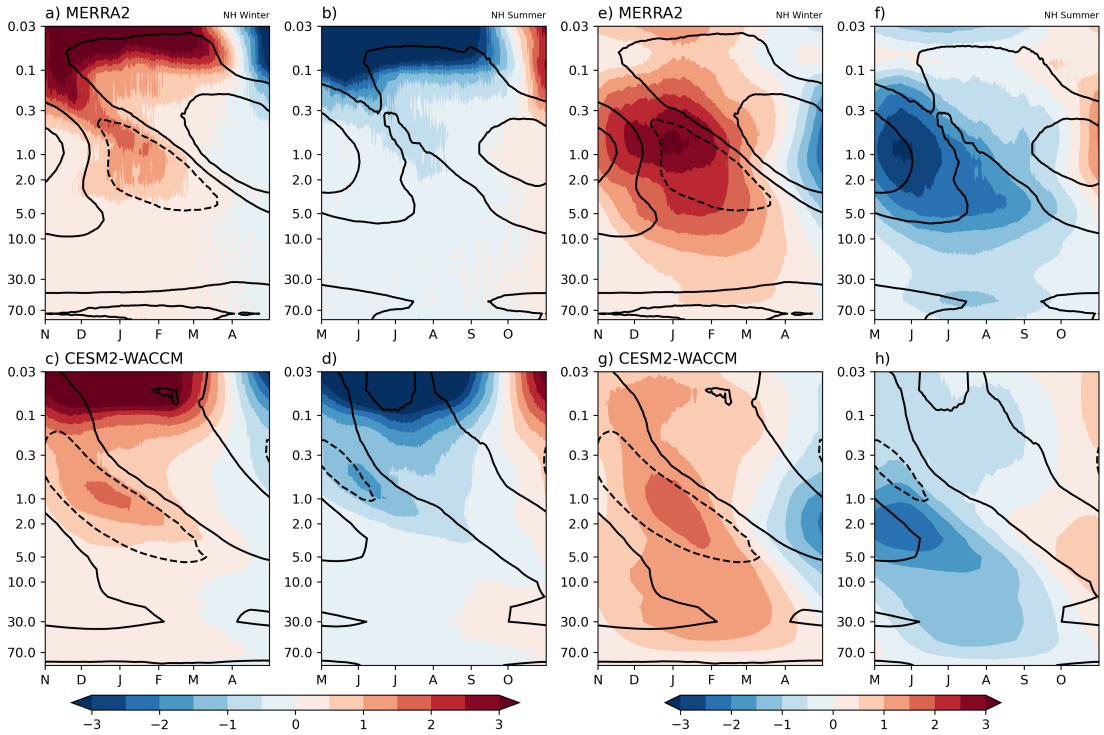

Figure 4.8: Climatology of meridional residual velocity ($\bar{v}^*$) ((ms^{-1})) averaged over 5°N to 5°S for (a,b) MERRA 2 and (c,d) WACCM. Climatology of meridional gradient of zonal-mean zonal wind(s^{-1}) for (e,f) MERRA-2 and (g,h) WACCM. Corresponding zonal-mean zonal wind contours of -20, 0, 20 ms^{-1} are overlaid.

The analysis of MERRA-2 indicates that the primary effect of vertical advection is to produce an eastward acceleration, with peak forcing around 0.3 hPa just above the maximum westerlies at 1 hPa in April/May and in November (Figure 4.7 g,h). This aligns with the start of the transition from the maximum westerly phase towards the easterly phase. Conversely, at the transition towards the westerly phase there is an opposing westward forcing, but it is much shorter-lived and weaker. These patterns are consistent with vertical advection driven by upwelling throughout the year. The presence of upwelling throughout the year was verified by examining the residual-mean vertical velocities $\bar{w}^*$ (Figure 4.9) which are positive, i.e., consistent with upwelling throughout the year, but with decreased magnitude at both equinoxes. Upwelling at this height advects westerly winds from the peak westerlies at 1 hPa during the equinox periods (April/May and November) into the region around 0.3 hPa, where the greatest eastward forcing is seen in Figure

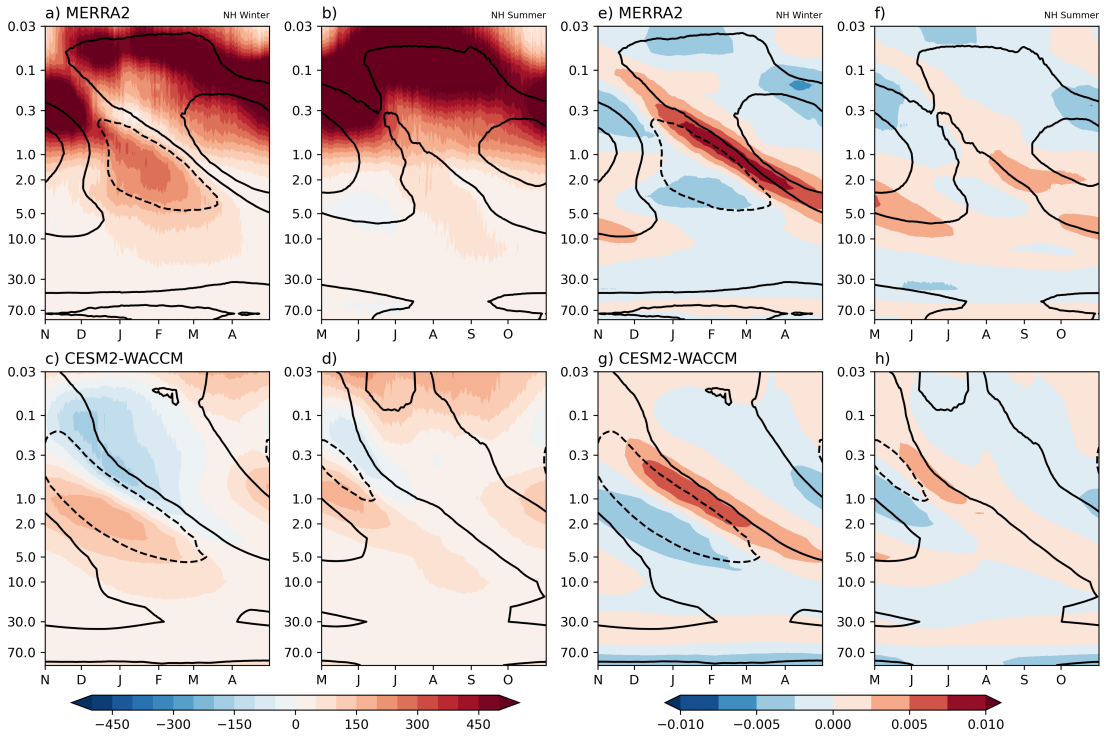

Figure 4.9: Climatology of vertical residual velocity $(\bar{w}^*)(mday^{-1})$ averaged over 5°N to 5°S for (a,b) MERRA 2 and (c,d)WACCM. Climatology of vertical gradient of zonal-mean zonal wind(s^{-1}) for (e,f) MERRA-2 and (g,h) WACCM. Corresponding zonal-mean zonal wind contours of -20, 0, 20 ms^{-1} are overlaid.

4.7 g,h. This acts against the increasing westward forcing, thus weakening and slowing the onset of the easterly phase. Similarly, upwelling during the solstice periods (Jan/Feb and July/August) advects easterlies from below, but the easterly SAO phase at 1 hPa in MERRA-2 is relatively weak, so the forcing that would counteract the incoming westerly phase is correspondingly weak. These diagnostics demonstrate that vertical advection counteracts the SAO winds above 1 hPa and is particularly effective at slowing the onset of the easterly phase through advection of westerly winds from below. It is thus an important contribution to lengthening the westerly phase in the MERRA-2 dataset, especially above 1 hPa.

The effect of vertical advection in WACCM (Figure 4.7i, j) is quite different from MERRA-2. Despite the overall vertical advection forcing being eastward in WACCM, the timing and amplitude of the forcing are very different. Especially during the westerly phase of the SAO (at equinox), vertical advection forcing is

virtually absent, thus failing to provide a forcing to help maintain the westerly phase of the modelled SAO at the upper levels (and this is confirmed by the difference plot). This absence can be partly explained by the fact that the westerlies below the level of the peak SAO westerlies are much weaker in the model (Figure 4.7) and thus the vertical advection contribution is correspondingly weaker. This deficiency in vertical advection suggests one possible source for the easterly bias, especially above 1 hPa. However, the key to understanding this lack of vertical advection forcing lies in understanding the reason for the weaker westerlies at the lower levels. The presence of eastward forcing caused by vertical advection during the transition from easterly to westerly winds in DJF around 1 hPa and above is also rather unexpected when compared to the reanalysis. This observation suggests the occurrence of net downwelling during this period, advecting the westerly winds from 0.3 hPa or higher and this is confirmed by examination of the WACCM $\bar{w}^*$ fields (Figure 4.9). WACCM exhibits downwelling during May-June and November-February above 1 hPa in contrast to MERRA-2 which has upwelling all year round. The WACCM global-scale BDC upwelling thus appears to be weaker during equinox than the locally induced circulation due to the onset of the westerly SAO winds. This suggests that either the tropical upwelling component of the BDC above 1 hPa associated with mid-latitude wave forcing is weaker in WACCM than in MERRA-2, or the induced downwelling at the onset of the SAO westerly phase is larger in WACCM than in MERRA-2. In the following section we explore this further and show that the net downwelling in WACCM at equinox is associated with GWD and its induced circulation.

In summary, horizontal advection is important in producing the easterly SAO phase at solstice and is also an important contribution to the observed annual cycle because of the hemispheric asymmetry in planetary wave driving and BDC strength. The modelled WACCM horizontal advection forcing is weak compared with MERRA-2 at SAO altitudes. Vertical advection mostly acts as counteracting force at levels above the peak of the SAO winds, since upwelling from below throughout the year advects winds whose sign opposes that of the incoming SAO

phase. In MERRA-2, vertical advection in this way plays an important role in perpetuating the equinoctial westerlies in the region above 1 hPa, since the winds below this level are predominantly westerly. In WACCM this vertical advection forcing is missing, which suggests that the model lacks an important contribution to the westerlies above 1 hPa.

4.3.3.2 Resolved wave forcing

The resolved wave forcing is examined using the EP flux divergence term in Equation 2.19, shown in Figure 4.10 a-f. The major feature of the resolved wave forcing in WACCM (Figure 4.10c-d) is the dominance of westward wave forcing, which is presumably due to Rossby waves propagating into the region from mid-latitudes and/or tropical inertia-gravity waves. MERRA-2, on the other hand, shows eastward forcing as well as westward forcing. The eastward forcing is present particularly in NH winter along the westerly shear zones as the winds transition from easterlies to westerlies, which is consistent with (but does not demonstrate) wave-breaking at critical layers (Pahlavan et al., 2021). It indicates that resolved waves contribute to the westerly SAO phase in MERRA-2 but the WACCM model fails to capture this contribution.

To explore this further, a wavenumber frequency spectral analysis of the daily zonal winds from 5°N to 5°S was conducted using the method outlined in section 3.4.4, following Wheeler and Kiladis (1999). Section 3.4.4 provides a detailed description on how the calculations are done and the limitations. Since we are interested in wave forcing of the westerly phase of SAO, we focus on the symmetric power spectra quantifying the Kelvin waves. The symmetric power spectrum is calculated using zonal wind anomalies symmetric with respect to equator, separated into 96-day windows with two-month overlap (for a detailed description of wavenumber frequency power spectra calculations, see Wheeler and Kiladis (1999)).

Figure 4.11 shows the symmetric wavenumber frequency power spectra of the zonal wind summed over 5°N to 5°S at 10 hPa, 5 hPa and 1 hPa level normalised by the background power. In the difference plots figure 4.11c,f,I, the difference

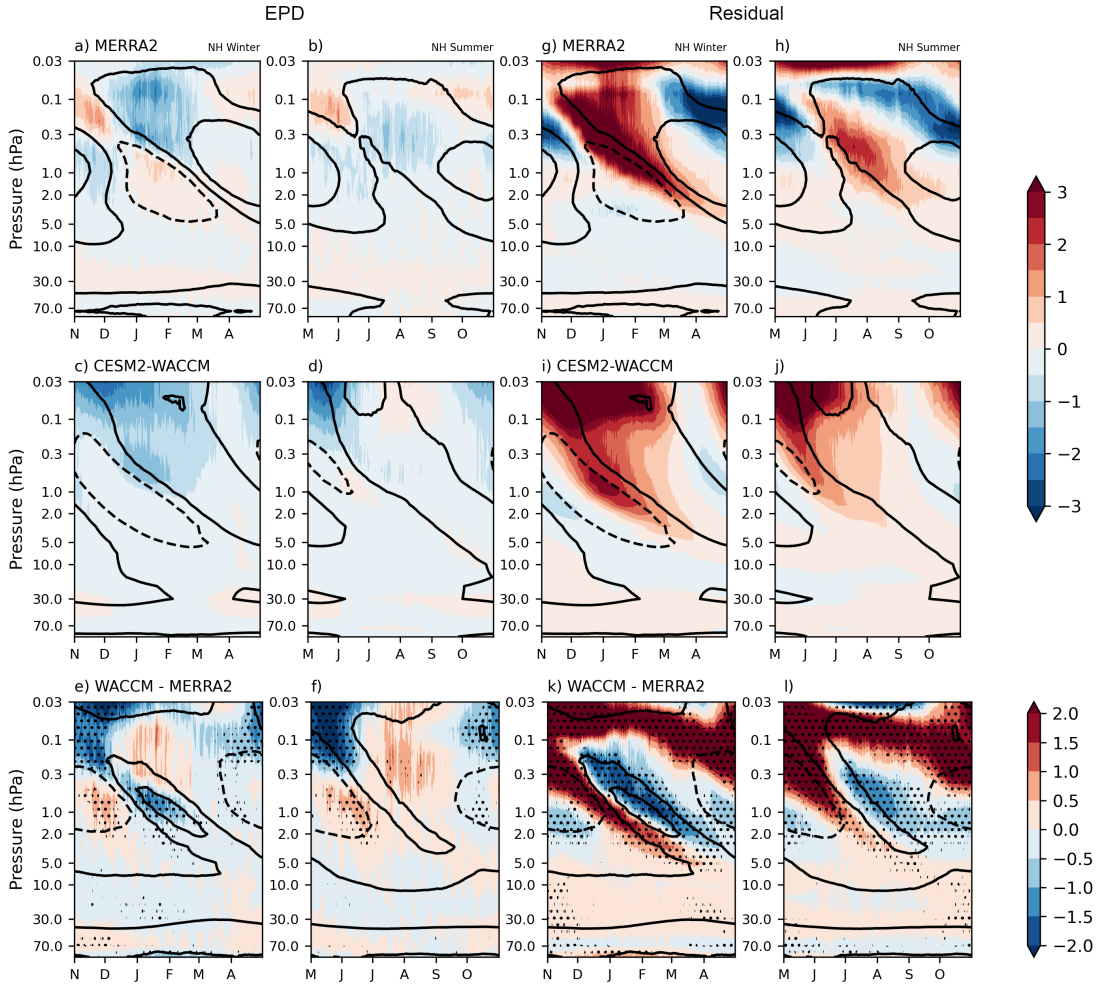

Figure 4.10: Climatology of zonal-mean zonal wind tendency due to EP flux divergence ($ms^{-1}day^{-1}$) averaged over 5°N to 5°S for (a,b) MERRA 2, (c,d) WACCM, (e,f) WACCM minus MERRA-2 differences. Climatology of zonal-mean zonal wind tendency due to the residual term in equation 1 ($ms^{-1}day^{-1}$) for (g,h) MERRA-2, (i,j) WACCM, (k,l) WACCM minus MERRA-2 differences. Corresponding zonal-mean zonal wind contours of -20, 0, 20 ms^{-1} are overlaid(a-d,g-j). Difference in zonal-mean zonal wind contours of -20, 0, 20 ms^{-1} are overlaid in e-f, k-l. Stippling denotes 99% confidence interval.

between WACCM and MERRA-2 raw power spectra, without normalizing with respect to the background, is shown. This obviates problems that might arise from differences in the background power between WACCM vs. MERRA-2.

Negative wavenumbers correspond to westward propagating waves and positive wavenumbers correspond to eastward propagating waves. Hirota (1978) noted that Kelvin waves of 10-day period play a crucial role in reversing the SAO winds from easterly to westerly. Superimposed in Figure 4.11 are the theoretical

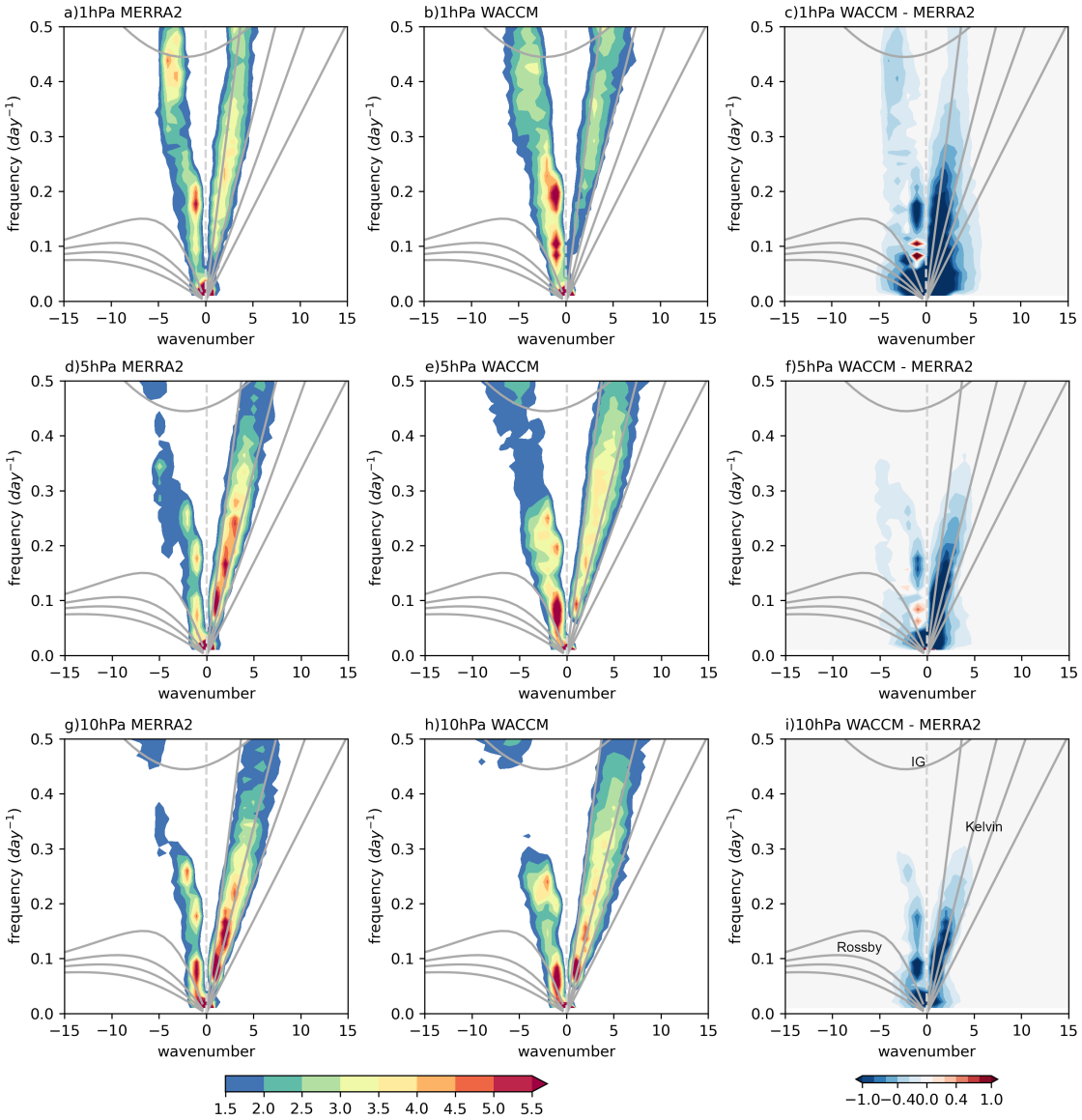

Figure 4.11: Wavenumber-frequency power spectra of zonal-mean zonal wind normalised by the background power at 1 hPa, 5 hPa and 10 hPa for (a,d,g) MERRA-2 and (b,e,h) WACCM . The overlaid dispersion curves correspond to shallow water Kelvin waves and Rossby waves of equivalent depth 25, 50, 100 and 400 m, as identified in panel (i). WACCM minus MERRA-2 differences between symmetric raw power spectra (m^2/s^{-2}) are shown in panels c, f and i.

dispersion curves for Kelvin waves (positive wavenumbers) and Rossby waves (negative wavenumbers). The plot immediately confirms that the Kelvin waves reaching the stratopause in the MERRA-2 analysis are of relatively high phase speed ($\sim$45 (ms^{-1}), i.e., between dispersion curves of equivalent depth 100 and 400), as expected. The increasing slope of the Kelvin wave power spectra in MERRA-2 as we move up from 10 hPa to 1 hPa confirms the filtering of slower waves at lower altitudes. The WACCM power spectra show similar changes with pressure but the Kelvin wave power in WACCM at fast phase speeds is considerably weaker than in MERRA-2 at 1 hPa. In fact, at all altitudes shown, WACCM Kelvin wave power is significantly weaker compared to MERRA-2 (figure 4.11c,f,i), which is consistent with the reduced eastward forcing at these altitudes.

The spectra also indicate power in the westward-propagating wave region. MERRA-2 and WACCM have spectral peaks at lower wavenumbers (less than 3) of periodicities 10 to 20 days and 5 to 6 days at all presented altitudes (Figure 4.11 a-i). These are wave modes often observed at midlatitudes, indicating westward forcing by extratropical travelling Rossby waves (Salby, 1984). At 1 hPa (as shown in Figure 4.11a, b), a notable contribution is evident at wavenumbers 3 and 4, exhibiting a frequency range of 0.4 to 0.5 cycles per day (cpd). Earlier studies suggest that these wavenumber and frequency range align with the 2-day waves frequently observed in the mesosphere during solstices originating from jet instabilities (Plumb, 1983; Ern et al., 2013). However, wavenumber 3, 2-day waves are documented to be a Rossby-gravity wave mode, which is not expected to show up in the symmetric zonal wind spectrum near the equator.

To better understand the origins of these waves, figure 4.12 explore the spatio-temporal structure of resolved waves in the upper stratosphere and mesosphere using EP flux vectors and EP flux divergence. Meridional EP flux vectors overlaid in Fig 4.12a,b show two main pathways of westward momentum transport towards the equator. During November-April and May-October, westward waves propagate from NH and SH extra-tropics respectively to the equator through the background westerly winds and deposit the westward momentum along the latitudinal critical

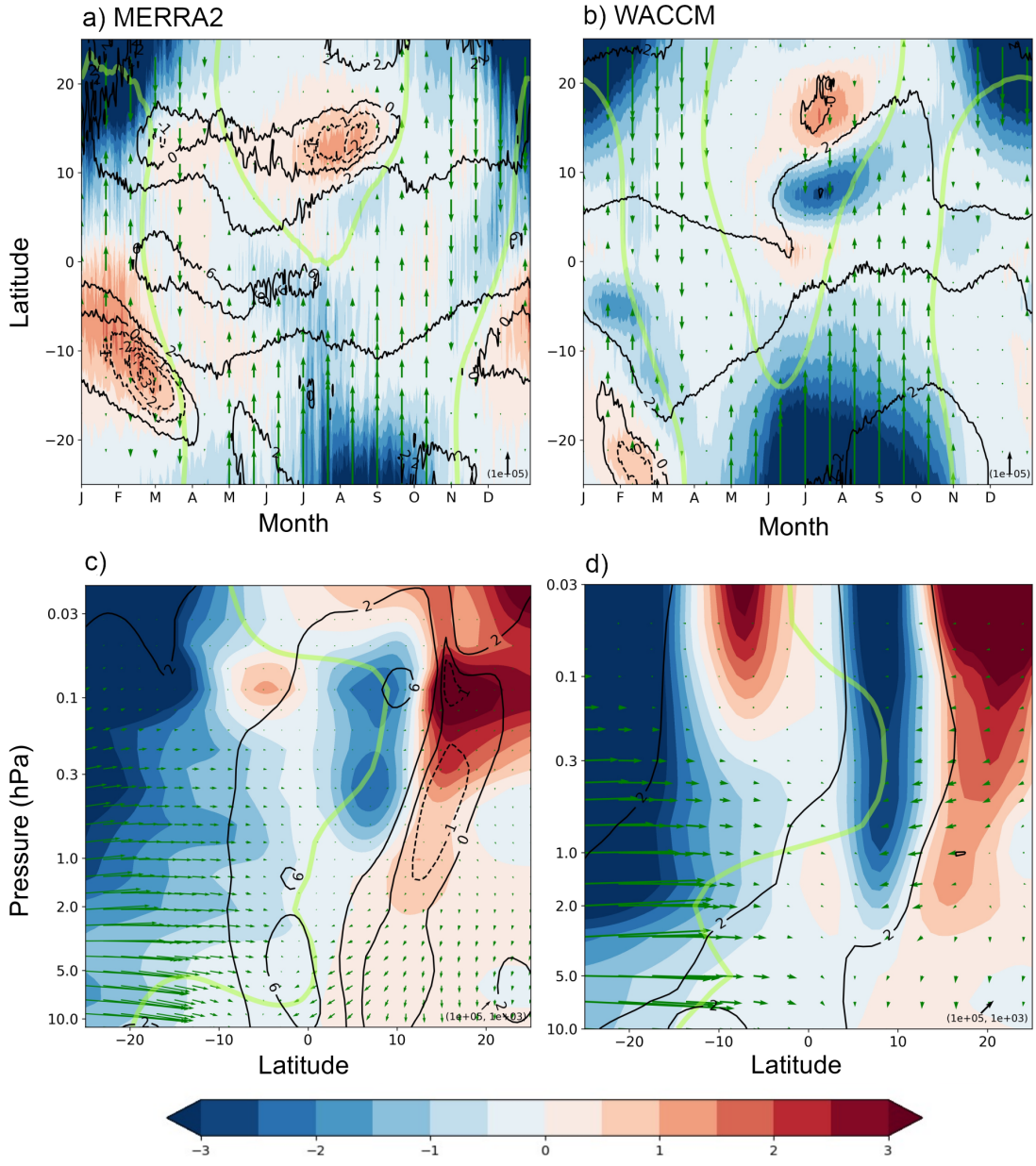

Figure 4.12: Climatology of EP flux divergence ($ms^{-1}day^{-1}$) at 1hPa between ± 20 degrees latitude of (a) WACCM and (b) MERRA-2. Latitude-height section of EP flux divergence in July from (c) the 500-year WACCM climatology and (d) the MERRA-2 42-year (1980-2021) climatology. Corresponding EP flux vectors m^3s^{-2} are overlaid as green arrows. Black contours overlaid is barotropic vorticity gradient ($10^{-11}m^{-1}s^{-1}$). The thick lime green line shows the zero zonal-mean zonal wind contour.

line. The second source of westward momentum is during solstices from the summer hemisphere. The black contour lines in Figure 4.12 represent the barotropic vorticity gradient (see section 2.4). The negative barotropic vorticity gradient indicates a barotropic instability which occurs during solstices from 10° to 20° latitudes in summer hemisphere and coincides with the positive EPD. The meridional EP flux vectors suggest that the instability region act as a source of waves and the momentum is transferred equatorward and break between 0° to 10° of latitude in summer hemisphere. 2-day waves are associated with barotropic instability regions of wave generation in the summer hemisphere during solstices, which aligns with the properties seen here. Figure 4.12c,d shows the latitude height structure of EPD during July. The plots indicate that below 2 hPa, the major contribution to westward waves is from extra-tropics, while at 1 hPa features associated with a 2-day waves are also evident. This is consistent with the wavenumber frequency power spectra in Fig 4.11.

The barotropic instability present at 1 hPa during solstices (Figure 4.12) suggests that the instability likely excites a broad spectrum of waves such that the zonal wind velocity pattern of RG waves near the equator is altered, and thus showing signals in symmetric power spectra in figure 4.11. The strength and position of regions of barotropic instability slightly differs between WACCM and MERRA-2, which can be attributed to the difference in jet characteristics. The stronger EP flux convergence and divergence near regions of weaker negative barotropic vorticity gradient that are seen in the figure are consistent with waves acting to reduce the instability (e.g., Figure 4.12a JJA). Figure 4.12 confirms that EPD close to equator has components of Rossby waves propagating from mid-latitudes, and in-situ waves generated at instability. Further exploration of these waves is outside the scope of this chapter, especially since Figure 4.10 indicates that the resolved wave contribution to SAO is much weaker than the residual term in both datasets.

4.3.3.3 Gravity wave forcing

To obtain a complete picture of the wave driving we also need to examine the parametrized gravity wave drag (GWD). The MERRA-2 GWD data are only available up to 0.1 hPa. For this reason, we employ the methodology similar to Ern et al. (2021) and calculate the residual term by subtracting all three previous forcing terms from the total rate of change of zonal-mean zonal wind (Figure 4.10g-j). For MERRA-2, this residual term will include parameterized gravity wave forcing and analysis increments, while for WACCM this term will include GW forcing and other effects such as numerical diffusion, associated with the dynamical core. In Figure 4.13e-h, we show the difference between residual terms and parametrised GWD at equatorial latitudes in both MERRA-2 and WACCM. The differences in both datasets demonstrate that the residual term primarily consists of GWD. The differences are almost negligible apart from certain regions, e.g., in January between 1-2 hPa in WACCM (Figure 4.13g). Thus, we will consider the residual term as GWD in this chapter, diverging from the approach in Ern et al. 2021, where EPD with wavenumbers exceeding 20 is incorporated to residual term to define GWD.

The residual (GWD) term derived in this way, shown in Figure 4.10 g-l, indicates that in MERRA-2, GWD plays a major role in the initiation of both the westerly and easterly SAO phases. The westward GW forcing is, however, slightly weaker than the eastward forcing (i.e., the blue shading is lighter than the red shading) and is confined to heights above 0.6hPa. Recent studies using satellite data have highlighted that, at the source level and in the lower stratosphere near the equator, the eastward convective gravity wave momentum flux is larger than its westward component (Liu et al., 2022; Lee et al., 2022). This observation implies a diminished availability of momentum for westward forcing. In addition, the easterly phase of the QBO has larger amplitude and hence there will be more filtering of westward GWs at lower altitudes. These two factors contribute to the weaker westward GW forcing seen in Figure 4.10g-l. The GW forcing (of either sign) generally appears where the vertical wind shears are strongest and strengthens the respective phase further by providing momentum forcing in the same direction. Figure 4.10g-h

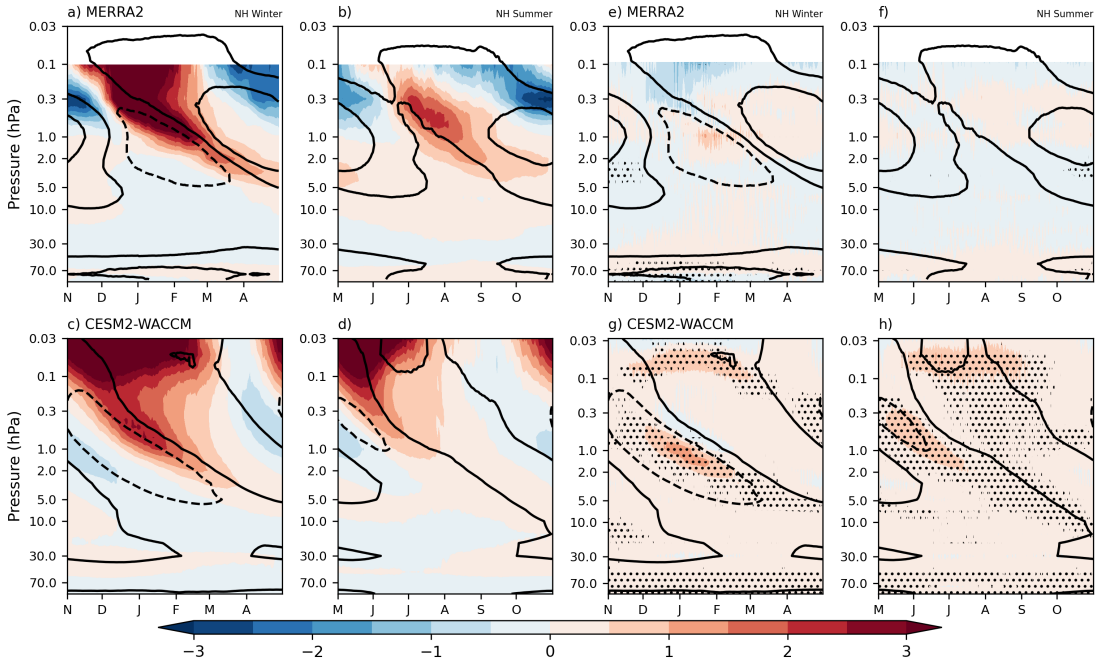

Figure 4.13: Climatology of zonal-mean zonal wind tendency due to gravity wave drag ($ms^{-1}day^{-1}$) averaged over 5°N to 5°S for (a,b) MERRA-2 and (c,d) WACCM. Difference between residual term($ms^{-1}day^{-1}$) and zonal-mean zonal wind tendency due to GWD for (e,f) MERRA 2 and (g,h) WACCM. Corresponding zonal-mean zonal wind contours of -20, 0, 20 ms^{-1} are overlaid. Stippling denotes 99% confidence interval.

confirms that the transition between SAO phases coincides with the peak of GW forcing, making it an important component in forcing the SAO in MERRA-2.

In the case of WACCM, figures 4.10 and 4.13 suggest that GW plays a major role in the initiation of the westerly phase only, although as indicated by the difference plot (Figure 4.10 k,l), the model does not reproduce correctly the strength and timing of this forcing. As noted previously, the modelled easterly phase starts to weaken slightly too soon, consistent with the early weakening of the meridional advection forcing, so the eastward GW forcing starts sooner. Since the GWD parametrization also depends on the vertical gradient of the wind, some of this inconsistency in timing and strength could also be associated with the slightly lower vertical resolution of this version of WACCM compared with MERRA-2 so that it cannot represent sharp vertical gradients so well. However, while Garcia and Richter (2019) have shown that a version of WACCM with improved vertical resolution (110 levels) can produce a much better QBO than the version analyzed

here, the impact of improved resolution was primarily on the resolved waves rather than on the parametrized GWD.

An interesting side note here is that the timing of occurrence of GW forcing in WACCM exactly matches the downwelling described earlier in the vertical advection analysis. This suggests that the stronger downwelling at equinox in WACCM compared to the reanalysis is indeed caused by the eastward forcing due to GW. If this is the case, this could also explain the reduced vertical advection of westerlies during the westerly phases of SAO in WACCM. Since there is a lack of strong westward GWD at this time, there is no induced upwelling, thus failing to provide the strong westerly wind advection from lower levels (Figure 4.9i,j). In contrast, we note that in MERRA-2, the westward forcing due to GWD and the eastward forcing associated with vertical advection occur around the same time. Because of this, they almost cancel each other in MERRA-2 so there is roughly no net eastward forcing due to vertical advection after the westerly wind maxima of each SAO westerly phase, similar to WACCM (Figure 4.9i,j). This implies that the weakened resolved Kelvin waves and weakened eastward parameterized gravity waves likely play a more important role in the weakening of the SAO westerly phase in WACCM than the vertical advection deficiencies.

In summary, both GWD and resolved wave forcing contribute to the westerly SAO phase transitioning in MERRA-2 and mostly act to reinforce each other, although the GWD is clearly the dominant contribution. In WACCM, however, the eastward wave forcing is driven almost entirely by the GWs since the resolved eastward wave forcing is substantially underestimated. The MERRA-2 analysis also suggests a contribution to the easterly SAO phase from the GWs, but this contribution is much weaker in WACCM.

4.4 Summary

A comparison of how the SAO is forced in MERRA-2 and WACCM has been performed by examining the different forcing terms in the TEM, to identify possible reasons for the common easterly bias in climate models. The results are summarised

by a schematic, (Figure 4.14) which highlights the dominant forcing terms and their relative roles in forcing the SAO.

In MERRA-2, the westerly phase of the SAO is initiated by the combined forcing from both resolved waves (EPD term) and gravity waves (residual term). The resolved waves primarily contribute to weakening of the existing easterly phase, while the gravity waves act to accelerate the new westerly phase in its first 1-2 months. Once the westerly SAO phase begins, the resolved waves then act to weakly oppose the flow. Since the net residual circulation in MERRA-2 near the Equator is upward throughout the year, once the SAO is well established the vertical advection term additionally advects westerlies from below which helps to maintain and strengthen the westerly phase of the SAO at the upper levels (although we note that the maximum amplitude of this term in MERRA-2 is at 0.2 hPa where the reanalysis is considered less reliable). Nevertheless, the eastward gravity wave forcing eventually weakens at the upper levels due to wave absorption below, and the upper-level flow slowly starts to decelerate, beginning to create an easterly shear zone at the higher altitudes. Thus, in the second half of the westerly SAO phase, strong westward forcing from gravity waves occurs, which acts to further weaken the westerly winds at the higher altitudes. Eventually the westward GW and meridional advection weaken the flow sufficiently, thus facilitating the shift to the easterly SAO phase. In summary, while GWD provides the largest SAO eastward forcing in MERRA-2, the resolved waves and vertical advection also contribute to its strength and evolution.

In contrast, while GWD initiates the westerly phase of the SAO in WACCM, it is weaker and dies out sooner than in MERRA-2. Contributions from the resolved waves are weak and do not play any appreciable role in the initiation stage. Once the westerly SAO phase starts, the resolved waves counteract the eastward GWD forcing and thus reduce the westerly wind magnitude. The vertical advection contribution to maintaining the westerly phase at the upper levels is also absent, because there is net downwelling at the equator during equinox.

In the case of the easterly SAO phase, the meridional advection and GW forcing both play major roles in MERRA-2. The resolved wave forcing helps to weaken

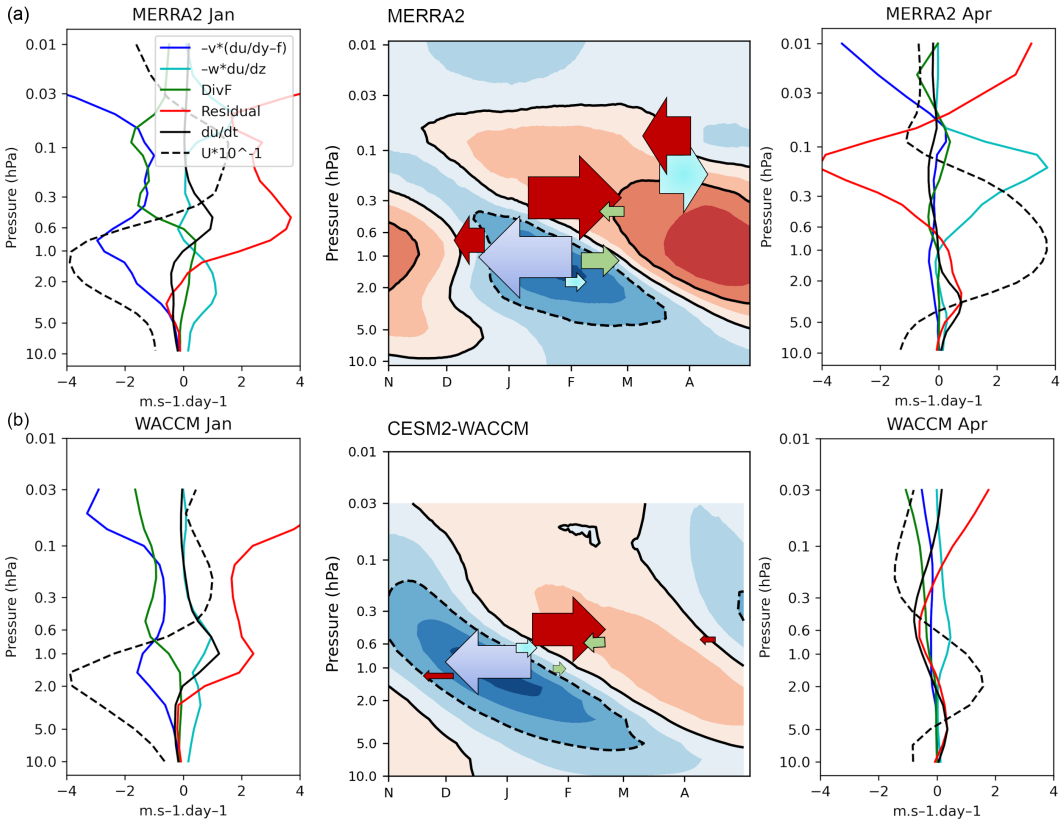

Figure 4.14: Schematic summarising the different forcing terms acting on the SAO westerly and easterly phases of (a) MERRA-2 and (b) WACCM. The arrows in the middle column plots represent different forcing terms with colours that correspond to those in the line plots. Arrows pointing to the right indicate eastward forcing and arrows pointing to the left indicate westward forcing. The length and width of the arrows roughly indicates the relative duration and strength of the forcing. The line plots represent the amplitude of each of the forcing terms in (left) January and (right) April.

the westerly phase but does not contribute much once the easterly phase starts. Vertical advection, however, weakly opposes this phase. The greater GW westward forcing and meridional advection in DJF compared to JJA contributes to the annual cycle in the SAO easterly phase. In WACCM, even though most of the relevant forcings are slightly weaker than in MERRA-2, the model is more successful in reproducing the easterly phase of SAO and its forcings compared to the westerly phase. The weaker vertical advection noted earlier (see figure 4.9) also points to a weaker BDC upwelling above 1 hPa than in MERRA-2.

In conclusion, this chapter suggests that increased eastward forcing from both resolved waves and gravity waves at SAO altitudes would help to improve the SAO

representation in WACCM and correct the easterly bias. There are several possible routes by which this could be achieved. The generation of Kelvin waves within the troposphere could possibly be deficient due to inaccuracies in the temporal or spatial variability of tropical convective activity. Increased horizontal and vertical resolution would make it possible to better resolve and improve the vertical propagation of resolved waves and improved resolution of vertical gradients could also help to increase the GW forcing. It might also help to refine the GW parameterization scheme to increase the magnitude of higher phase speed waves that can reach up to the upper stratosphere. Another important aspect is the influence of the biases at QBO altitudes in the model, the region through which the waves propagate before reaching the SAO altitudes. From figure 4.2, it can be seen that the QBO, especially in the lower stratosphere, is weaker in WACCM compared to MERRA-2 and other reanalysis. Improving the QBO representation might also play a role in improving the SAO. Thus, studying the biases in both the wave sources and wave filtering could help to improve the representation of the SAO in the model. Nevertheless, we note that these results are based on a comparison with MERRA-2 reanalysis and there are still many uncertainties in observations and reanalyses in the upper stratosphere, especially at equatorial latitudes (Ch 11, SPARC (2021)).

5

Role of the Quasi-Biennial Oscillation in Alleviating Biases in the Semi-Annual Oscillation

5.1 Introduction

Chapter 4 has shown that the resolved and parameterized tropical waves in the WACCM model upper stratosphere are both too weak. While that chapter focused on WACCM climate model, nearly all the models have the same easterly bias (see section 4.1) and the results in chapter 4 are likely to be relevant to most models. The lack of eastward wave forcing from both resolved and parameterized waves in the model suggests either a lack of wave generation or excess dissipation at lower levels (below 1hPa). These waves propagate vertically through the underlying region dominated by the stratospheric QBO before reaching the SAO altitudes. This motivates the exploration of the role of low-to-middle stratospheric wind biases in modulating the wave propagation to the upper stratosphere. Therefore, in this chapter, the influence of biases in the modelled QBO on the representation of the SAO is explored.

Models, reanalyses and observational data sets have been used to understand the QBO and the SAO and to examine their relationship (e.g. Burrage et al. (1996); Dunkerton and Delisi (1997); Garcia et al. (1997); Ray et al. (1998); Garcia and

Sassi (1999); Richter and Garcia (2006); Peña-Ortiz et al. (2010); Smith et al. (2017, 2023)). The modulation of the westerly phase of the SAO by the QBO is widely acknowledged. Garcia et al. (1997) and Dunkerton and Delisi (1997) have shown using rocket-sonde observations that the altitude of maximum descent of the westerly SAO can be modulated by the QBO. Later studies have confirmed this result using global models (Peña-Ortiz et al., 2010) and satellite data (Ern et al., 2015; Smith et al., 2023). Smith et al. (2023) further examined satellite observation data and found that the QBO modulates not only the depth but also the magnitude of the SAO westerly phase, with an almost 10 ms^{-1} increase during the QBOE phase. The generally acknowledged mechanism of this QBO influence on the SAO is wave filtering. Smith et al. (2023) showed that the differences in the SAO winds in the upper stratosphere due to the phase of the QBO are confined to the low latitudes which led them to suggest that the QBO influence is mainly through vertical wave coupling, in agreement with prior studies that have shown that both resolved waves and parameterized GWs reaching SAO altitudes depend on the wind profiles at QBO altitudes (Garcia et al., 1997; Peña-Ortiz et al., 2010).

Early studies using rocket-sonde observations did not find a convincing relationship between the QBO and the easterly phase of the stratospheric SAO (Dunkerton and Delisi, 1997; Garcia et al., 1997). Since the SAO easterly phase is widely accepted to be driven by meridional advection associated with the BDC, an absence of direct vertical coupling from the QBO in this phase is not surprising. However, Peña-Ortiz et al. (2010) found a modulation of both the strength and altitude of maximum descent of the SAO easterly by the QBO in their model analysis using MAECHAM. While this is consistent with some reanalysis studies that identified the presence of a QBO signal in the upper stratosphere during NH winter, suggesting a QBO modulation of the SAO easterly phase (Pascoe et al., 2005; Calvo et al., 2007; Peña-Ortiz et al., 2008), the paucity of validatory observations means that overestimation of the influence of resolved and small-scale waves by the models (employed by both Peña-Ortiz et al. (2010) and in the generation of the reanalysis products) cannot be excluded. Later, Ern et al. (2015) noted

that in one of their case studies using reanalysis and satellite data during times when the QBO filtering of westward waves was minimal, westward waves were found to travel through to the upper stratosphere and the SAO easterly phase exhibited a downward propagation, suggesting a modulation of the phase descent by the vertically-propagating waves. However, Ern et al. (2015) also questioned the reliability of this result. In their study of SABER satellite data Smith et al. (2023) concluded that the QBO primarily affects the SAO westerly phase rather than the easterly phase. Additionally, no evidence for a QBO modulation of the SAO easterly phase component of the annual cycle has been reported.

Another mechanism through which the QBO could influence the SAO easterlies is via the extra-tropics. The QBO is generally believed to influence mid latitude Rossby wave propagation through the Holton-Tan mechanism (Holton and Tan, 1980; Anstey and Shepherd, 2014; Anstey et al., 2022). The BDC is strengthened during extreme events known as SSWs when the polar vortex is substantially weakened or destroyed as a result of the transfer of westward momentum from large-scale Rossby waves to the zonal flow at mid- and high-latitudes (Baldwin et al., 2019). This momentum transfer in turn strengthens the BDC and hence the cross-equatorial flow that generates the SAO easterlies through meridional advection. The frequency and timing of SSWs is known to be sensitive to the QBO (Gray et al., 2004; Pascoe et al., 2006; Anstey et al., 2022) and thus will likely influence the strength and timing of the incoming easterly SAO. There is also evidence that the QBO influences the height of the maximum cross-equatorial flow (Lu et al. (2020), see their Figure 11) which may therefore influence the depth to which the SAO easterlies penetrate. However, none of the previous studies have examined the impact of this mechanism in detail since, as mentioned above, the QBO modulation of the easterly SAO phase appears to be much smaller than its modulation of the westerly SAO phase.

In this chapter we extend previous studies by exploring the impact of the QBO on the SAO using simulations performed as part of the QBOi phase 2 project (see section 3.4.2). The modelled QBO wind biases are corrected by nudging the zonal-mean zonal wind in the equatorial low-mid stratosphere towards reanalysis

data in the QBOi simulations. The representation of the SAO is then examined to determine whether biases in the SAO have been alleviated. We examine the HADGEM3 model simulations here, rather than the WACCM simulations because we were involved in performing these simulations and thus have more control over their output and it allows the possibility of further experiments to test any resulting hypotheses (More on this in section 7.2). The chapter is structured as follows: Section 5.2 outlines the data and techniques employed in the study, results are presented in Section 5.3, and Section 5.4 summarizes the findings.

5.2 Data and methods

The model data used in this study are from simulations of the HadGEM3 GA7.1 N216 atmosphere-only model (section 3.3), performed as part of the UK contribution to phase 2 of the QBOi project. The details on QBOi project and model experiments used in this chapter are discussed in section 3.4.2.

In this chapter, two reanalysis datasets were utilized. Firstly, the ECMWF ERA5 reanalyses (section 3.2.2) were used in the nudging scheme to ensure a good representation of the QBO, in accordance with the QBOi protocol. Although ERA5 has a good representation of the QBO compared to observations (Ern et al., 2023) the SAO winds in ERA5 are unrealistic, with westerly phase magnitudes reaching as high as $150ms^{-1}$ (see section 4.3.1) which are much larger than estimates of 40 ms^{-1} from satellite derived winds (Smith et al., 2017). For this reason, the MERRA-2 dataset was employed for comparison with the model results in the SAO region. Chapter 4 has identified MERRA-2 as the reanalysis dataset most similar to observations in the SAO region (also see Ern et al. (2021)). As noted earlier, this may be due to the assimilation of MLS temperature data at altitudes of 5hPa and above, along with a non-orographic gravity wave parameterization tuned to better represent equatorial stratospheric variability (Molod et al., 2015).

Similar to chapter 4, the TEM equation (section 2.5) was used to analyze the processes driving the SAO. For MERRA-2, following chapter 4, the residual term ($\bar{X}$) is calculated by subtracting the first three forcing terms on the right-hand side

of equation 2.19 from the total rate of change of zonal-mean zonal wind. In chapter 4, $\bar{X}$ is shown as a valid indicator of GWD in MERRA-2 reanalysis. Given that the MERRA-2 GWD values are only available on a limited number of vertical levels, $\bar{X}$ is used to represent GWD for MERRA-2 in section 5.3.4. The tendency terms were available as direct outputs from our model runs. All diagnostics presented in this chapter were compiled using individual ensemble-members before an average of the three ensemble members was taken. Unless otherwise stated, the average was found to be similar to results from the individual members. Wherever a comparison is made between the Control and Nudged experiment results, the differences are assessed for statistical significance using a two- sided Student's t-test (see section 3.4.3). The null hypothesis states that the Control and Nudged data are drawn from the same statistical distribution and have identical (population) averages. A p-value less than 5% is considered statistically significant, i.e., there is a statistically significant difference between the Control and Nudged means.

5.3 Results

5.3.1 SAO bias alleviation

The climatology of zonal-mean zonal wind from MERRA-2 is displayed as a time-height cross section in Figure 5.1a, with alternating easterlies and westerlies of SAO evident. The MERRRA-2 profile is the same as the one presented in Chapter 4, with a detailed description available in section 4.3.1. For comparison with HadGEM3 simulations, the figure has been re-plotted here.

The corresponding time-series of the HadGEM3 control simulation is displayed in Figure 5.1b. The model exhibits a pattern that is consistent with the observed SAO. However, a clear distinction in the amplitude and duration of each phase between Figure 5.1a and b is evident, with an overall easterly bias evident in the model, similar to WACCM shown in chapter 4 and consistent with that found by Smith et al. (2019). The easterly SAO phase, particularly during JJA near 1hPa, is much stronger in the HadGEM3 Control with a strength difference of $30ms^{-1}$ compared to the reanalysis. The MERRA-2 easterly phase is clearly weaker in JJA

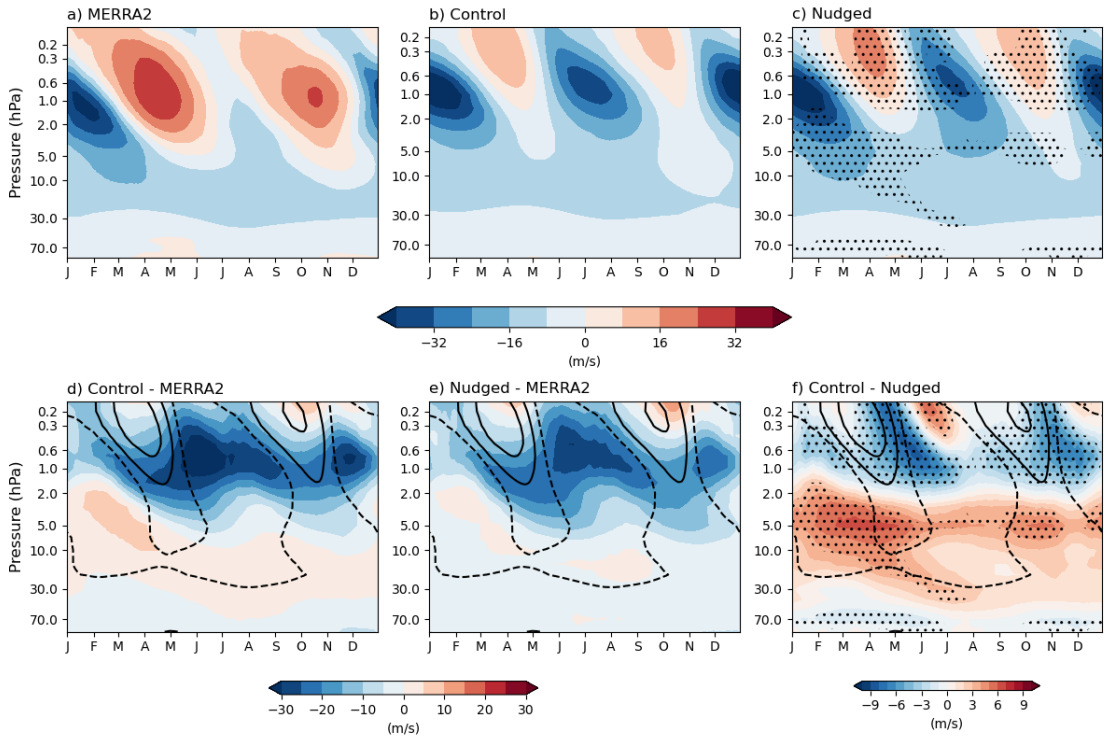

Figure 5.1: Daily mean climatology of zonal-mean zonal wind (ms^{-1}) averaged over 15°N to 15°S for (a) MERRA-2, (b) Control ensemble-mean and (c) Nudged ensemble-mean, (d) Control minus MERRA-2 differences, (e) Nudged minus MERRA-2 differences and (f) Control minus Nudged differences. Overlaid are the wind contours from the Control ensemble-mean at -10, 0 and 10 ms^{-1}. Stippling denotes 95% confidence interval. Stippling in (c) is the same as in (f) to easily identify where the nudged experiment is statistically different from control.

(SH winter) than in DJF (NH winter) but this imbalance is much weaker in the Control experiment, leading to a weaker annual cycle. Both phases of the Control westerly SAO phase also show an easterly bias of at least 25 ms^{-1} at 1hPa.

To assess changes in the SAO characteristics between the Control and Nudged experiments, the corresponding climatology from the Nudged experiment is shown in Figure 5.1c. It shows a promising reduction of the easterly bias of the modelled SAO. The magnitude of the SAO westerly phase has increased in both equinoxes. Most notably, the easterly phase in JJA (SH winter) appears slightly reduced in magnitude around 1hPa and the westerly phase in MAM is strengthened, which will improve the annual cycle as well.

To confirm this improvement the Control-minus-MERRA-2 and the Nudged-

minus-MERRA-2 differences are shown in Figure 5.1d-e, noting that negative (positive) values indicate stronger easterlies (westerlies) than MERRA-2. Comparison of the figures confirms that the westerly bias in the QBO region from around 70 hPa to 5 hPa in the Control experiment has been eliminated by the nudging, as expected. (It also confirms that nudging towards ERA5 data in this region while using MERRA-2 as validation data is acceptable, since the two datasets are almost identical in this height region). Above that region, although there is still clearly an easterly bias in the SAO in the Nudged experiment, the amplitude of the bias has been reduced.

The nature of the bias reduction can be seen more clearly in Figure 5.1f which shows the Control-minus-Nudged differences. The reduction in easterly bias occurs almost throughout the year between 1 hPa and 0.3 hPa, reaching its maximum difference of about 8 ms^{-1} during the SAO phase transition from westerly to easterly (Apr-Jun, Oct-Dec). The timing of this maximum bias reduction can be attributed to a slightly prolonged SAO westerly phase duration and a delayed onset of the easterly phase in the Nudged experiment. However above 0.3hPa, the easterly phase magnitudes increase faster in the Nudged compared to the Control experiment and this is seen as positive values at these altitudes in June and December in the difference plot (Figure 5.1f).

In summary, Figure 5.1 demonstrates that decreasing the wind biases in the lower stratosphere improves the SAO representation, although the biases are not completely alleviated. A time mean of zonal-mean zonal wind from 15°S to 15°N for all 42 years (see figure 5.2) indicates that the maximum SAO wind correction between 2 hPa to 0.6 hPa reaches up to 25%. At each altitude, the ratio of difference in Control and Nudged winds to the Control winds is used to calculate the percentage of wind change at that altitude. While the winds from the Nudged experiment align more closely with the reanalysis there remains considerable room for improvement (figure 5.1d and e). In particular, the easterly phase during JJA is still too strong, while the westerly phase is too weak and does not extend far enough downward. Nevertheless, alleviation of the QBO bias has clearly improved the simulation of

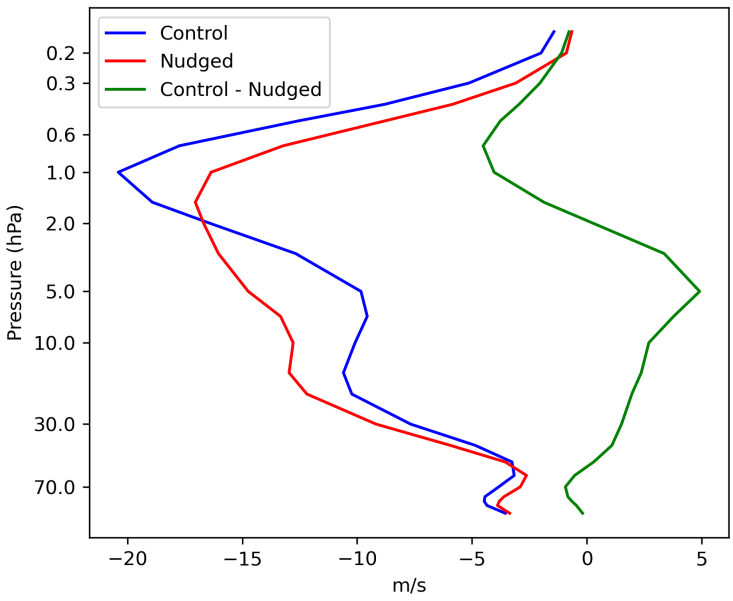

Figure 5.2: multi-year time average of the equatorial zonal-mean zonal wind (ms^{-1}) averaged over 15°N to 15°S for Control ensemble-mean, Nudged ensemble-mean and Control minus Nudged differences.

the SAO. In the remaining sections of the chapter, we therefore examine in more detail how the QBO corrections have led to a reduction in SAO bias.

5.3.2 QBO modulation of SAO and biases

Examining a QBO composite can help to gain a better understanding of how the SAO is impacted by correcting the QBO winds and how the QBO influence extends to the upper stratosphere. The QBO composite is calculated using the following method. Firstly, the QBOE-to-QBOW transition months are found using the raw monthly-mean zonal-mean zonal wind data averaged over 15S to 15N. The months in which the QBO transitions from easterlies to westerlies at 5hPa are identified. Moreover, the zonal wind average for the next 4 months is required to be westerly to avoid counting occasional SAO westerly phases descending to 5hPa, without concomitant QBO westerlies. Figure 5.3a and b show the QBO transition months which satisfy these conditions for the Control and Nudged simulations respectively (using different colours for the three ensemble-members). Depending on whether the month is closer to the NH spring equinox (i.e. between Jan-Jun) or

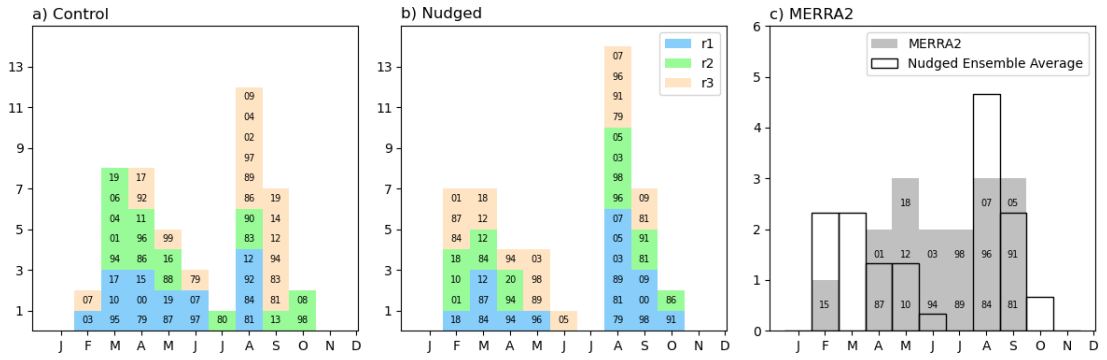

Figure 5.3: Histogram of QBOE to QBOW phase transition months at 5hPa for the (a) Control and (b) Nudged ensemble members and (c) at 10 hPa for MERRA-2. Corresponding years for the (a) Control and (b) Nudged and (c) MERRA-2 are listed. In figures a-b the colours denote the different ensemble-members. Averages of the three Nudged run ensemble members are overlaid in (c).

autumn equinox (between Jul-Dec), data for 1000 days starting from either March 1st or September 1st is extracted and used to form the composite. A 1000-day time-series has been chosen so that the full QBO cycle can be captured, since the QBO period can typically range up to 34 months (Baldwin et al., 2001). It is important to note that the Figure 5.4 shows an average over many QBO cycles. Especially in the QBO region, the cycle-to-cycle variability in duration and depth of each QBO phase, along with the generally higher magnitude of the QBOE phase compared to the QBOW phase affects the compositing. Nevertheless, using this composite allows the visualization of, for example, the evolution of the SAO as the westerly phase of the QBO descends.

In Figure 5.1, it was noted that the overall westerly bias in the QBO region is eliminated through nudging. Figure 5.4 illustrates the impact of nudging on each QBO phase. In the QBOW phase the QBO westerlies of the Control experiment (Figure 5.4a) are stronger and last longer at altitudes around 5 hPa and as the westerlies propagate downward they become weaker than in the Nudged experiment (compare above and below 30 hPa). In the Nudged experiment (Figure 5.4b), the QBOW phase strength and duration is roughly the same throughout the QBO altitude range. This suggests possibly excessive eastward wave momentum deposition at higher altitudes in the Control experiment. The QBOE phase on the

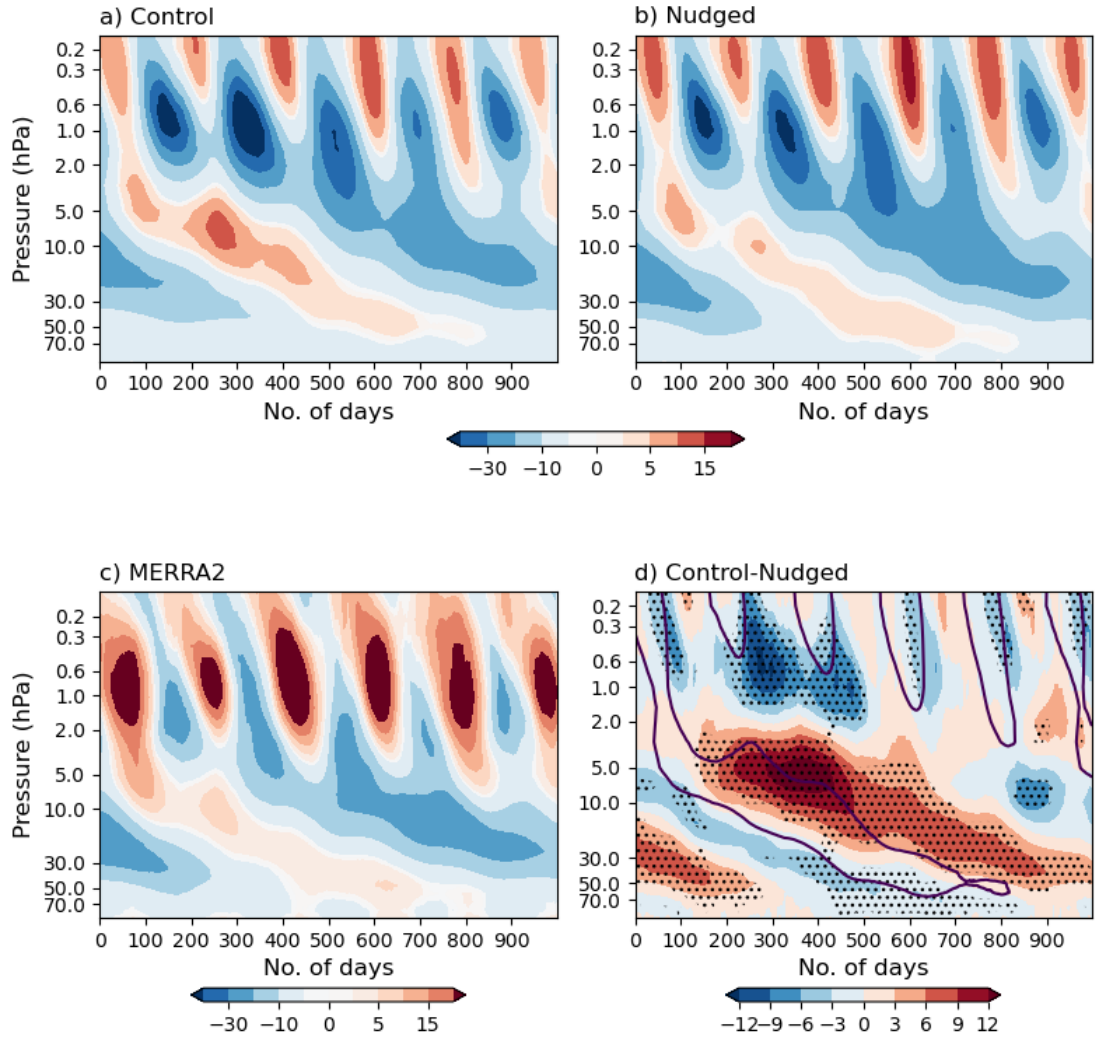

Figure 5.4: QBO composite of zonal-mean zonal wind (ms^{-1}) for the (a) Control experiment, (b) Nudged experiment and (c) MERRA-2. The composite members start from 1st of March or 1st of September whichever is closest to the start of the QBOW phase. The 5hPa reference level is used to identify the start of the QBO westerly phase in model and 10 hPa is used in MERRA-2 (see text for more details). (d) Difference between the Control and Nudged experiments, with the QBO composite winds from the Control experiment overlaid as black contours. Stippling denotes 95% confidence interval.

other hand appears to be weaker throughout the altitude range 70-10hPa in the Control experiment compared to the Nudged experiment, confirming the westerly bias of the QBO in the free-running model.

Focusing on altitudes above the 2 hPa level where the maximum in SAO amplitude is found (see Figure 5.1), both the Control and Nudged experiments

clearly indicate that the strength of the SAO is modulated by the QBO (Figure 5.4a, b). As the QBOW phase progresses downward, the depth to which the SAO westerly phase extends also increases, finally merging with the next QBOW phase. In contrast to the observations (Garcia et al., 1997; Smith et al., 2023), the SAO easterly phase also appears to be modulated by the QBO in the simulations. The SAO easterly phase is stronger and lasts longer when QBO westerlies are present around 10 hPa (i.e. when the QBO at 50 hPa is in its easterly phase). Previous studies suggest that this might be due to an overestimation of the influence of westward gravity waves in modulating the SAO easterly phase in models (see section 5.1).

Figure 5.4c shows the corresponding MERRA-2 QBO composite of zonal-mean zonal winds except that the QBO transition month has been selected based on the sign of the winds at 10 hPa instead of 5 hPa since the SAO westerlies in MERRA-2 frequently extend to levels below 5 hPa. Figure 5.3c shows the QBOW to QBOE transition months chosen for the composite in MERRA-2. We note that there is only one MERRA-2 ensemble member, so the MERRA-2 QBO composite has been calculated using only 16 1000-day samples whereas the model experiments have 3 ensemble-members and each of the experiment composites contains 45 1000-day samples. Although the reanalysis has stronger westerlies and weaker easterlies compared to control in the SAO region, as already seen in Figure 5.1, the characteristics of the SAO modulation by the QBO are nevertheless quite similar to those displayed by the model.

Figure 5.4d shows the Control-minus-Nudged differences between the QBO composites and illustrates in more detail how correcting the QBO biases has affected the SAO. Consistent with previous findings (Figure 5.1d), the differences maximise during the transition from QBO westerlies to QBO easterlies and in the months when the SAO transitions from westerlies to easterlies. The figure highlights how complementary the improvements in the QBO and the SAO are to each other. Irrespective of the SAO phase, whenever a correction is made to the westerly bias at QBO altitudes, a corresponding easterly bias correction occurs at the SAO altitudes. For instance, between days 200 and 400, the most statistically significant changes in

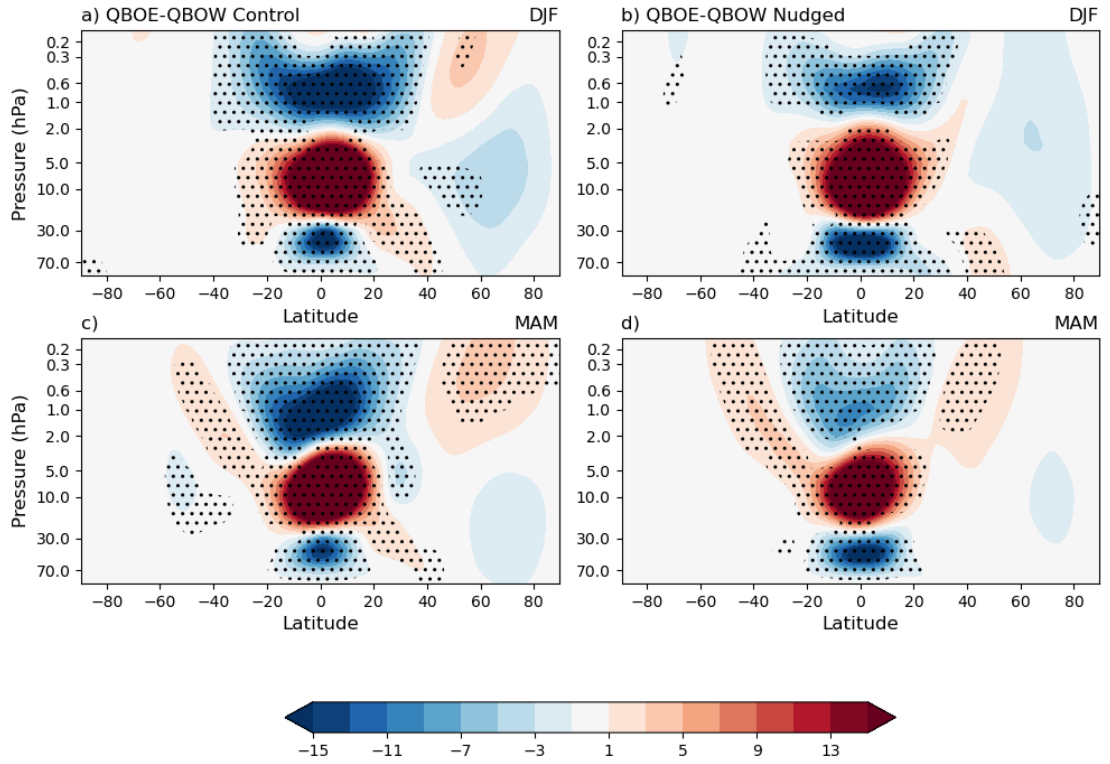

Figure 5.5: Latitude-height seasonal composites of QBOE minus QBOW zonal-mean zonal winds (ms^{-1}) from a) Control experiment DJF, b) Nudged experiment DJF, c) Control experiment MAM and d) Nudged experiment MAM. The phase of the QBO has been defined at 50 hPa. Stippling denotes at 95% confidence interval.

the QBO occur at 5hPa, coinciding with the most pronounced easterly bias reduction at the altitudes of the SAO. During this period, the QBO westerlies diminish while the easterlies intensify. It is noteworthy that the SAO easterlies and QBO easterlies converge at 5hPa. Meanwhile, the SAO westerly (easterly) phase around days 200 to 400 at 2hPa and higher are stronger (weaker) in the Nudged experiment (Figure 5.4b) compared to the Control experiment (Figure 5.4a) and extends further down in altitude. It is noted that the most significant SAO corrections occur when the lower stratospheric QBO winds at 50 hPa are easterly and the mid stratospheric QBO winds at 10hPa are westerly (both roughly coincide).

Figure 5.5 shows the latitude-height cross section of QBOE-minus-QBOW composite differences in zonal-mean zonal winds for both the Control and Nudged

experiments during DJF and MAM (results are similar for JJA and SON as well). In constructing these composite differences, the QBO phase is determined by whether the 50 hPa QBO winds are westerly (>2 ms^{-1}) or easterly (<-2 ms^{-1}). The additional benefit of choosing 50 hPa QBO winds as a reference is that the observed Holton-Tan (HT) relationship is associated with the winds at this level, and any changes associated with the HT effect might also be evident (See section 2.7.1 for details on the HT relationship). Figure 5.5 reaffirms that during the QBOE phase at 50 hPa the SAO easterlies in DJF are stronger than during the QBOW phase (negative values in Figure 5.5a,b from 2 hPa to 0.2 hPa at the equator) and the SAO westerlies in MAM are weaker (negative values in Figure 5.5c,d from 2 hPa to 0.2 hPa at the equator). When the 50 hPa QBO winds are easterly, most of the stratosphere i.e., from 30 hPa to 5 hPa is occupied by westerly winds, thus filtering out more eastward travelling waves and allowing more westward travelling waves to pass through. Another notable result is that the SAO wind strength difference between QBOE and QBOW is clearly reduced in the Nudged experiment compared to the Control experiment. This reduction can be attributed to the SAO bias corrections (reducing the SAO easterly bias) primarily occurring during QBOE, hence reducing the difference in SAO during QBOE and QBOW.

Both the Control and Nudged experiments show a weak HT relationship, with weaker DJF westerlies at mid-to-high latitudes during the QBOE phase (see Elsbury et al. (2021)). The sign of the differences near the equatorial stratopause SAO region is consistent with this, since weaker mid-latitude winds suggest stronger planetary wave forcing of the BDC. However, determining whether the changes to the SAO have arisen as a result of the filtering of vertically propagating waves at the equator or as a result of changes to the BDC is not possible from these zonal wind diagnostics, and requires a more detailed examination of the various contributions to the momentum equation (see next section).

5.3.3 Forcing terms

The climatological height-time evolutions of the four forcing terms in equation (2.19) are shown in Figure 5.6. The average behavior of all four terms is similar in both the experiments. Above 1 hPa both the experiments indicate that (i) meridional advection is the major westward forcing term (Figure 5.6a,b), (ii) GWD and vertical advection provide, on average, eastward forcing (Figure 5.6d,e and 5.6j,k), and (iii) eastward forcing by EPD is strongest at the equinoxes from 5hPa to 0.6hPa (Figure 5.6g,h). This is consistent with earlier research which found that the westerly SAO phase is primarily driven by wave forcing and the easterly phase is largely driven by meridional advection (Meyer, 1970; Holton and Wehrbein, 1980).

The Control-minus-Nudged differences in the final column in Figure 5.6 outline the changes in the four forcing terms as a result of the bias corrections in the lower stratosphere zonal-mean zonal winds. We note that negative (positive) values indicate more eastward (westward) forcing in the Nudged experiment, and that increased eastward forcing is desired to reduce the easterly bias of SAO.

The strength of the meridional advection forcing in the Nudged simulations shows a shift in altitude compared to the Control simulations, which is evidenced by the dipole structure in DJF and JJA above 2hPa in Figure 5.6c. However, the difference is statistically significant only in JJA above 0.6 hPa where the increase in westward meridional advection occurs. This increased westward forcing may explain the easterly phase magnitudes increasing faster in the Nudged compared to the Control experiment, above 0.6 hPa, as noted in the discussion of Figure 5.1.

Vertical advection does little to reduce the SAO easterly bias. The vertical advection forcing is mostly present when there is a strong vertical gradient in zonal wind (compare Figure 5.6 d,e to Figure 5.1). Between 1.0-0.6 hPa the SAO winds reach their maxima so they have the least vertical gradient and thus vertical advection forcing at these levels is minimal. The difference plot in Figure 5.6f, between 1.0-0.6 hPa confirms that changes associated with vertical advection changes have minimal impact at these altitudes. This coincides with the levels where the reduction in the SAO easterly bias is maximum (Figure 5.1). Thus,

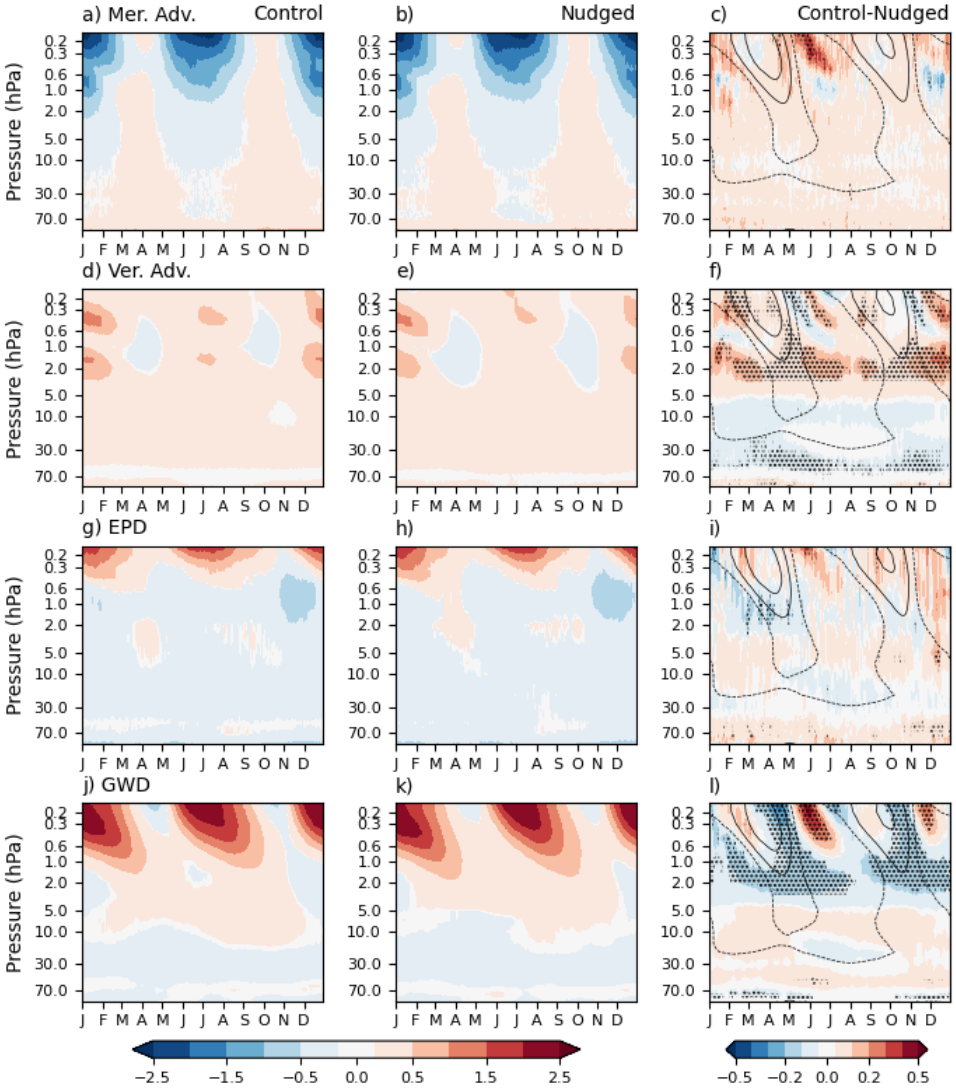

Figure 5.6: Climatology of TEM forcing terms averaged over 15°S-15°N. (a) and (b) show the forcing due to meridional advection in the Control and Nudged ensembles respectively. (c) shows the corresponding Control-minus-Nudged differences. Similarly (d-f) shows the corresponding forcing due to vertical advection, (g-i) EPD and (j-l) GWD. Units are $ms^{-1}day^{-1}$. Zonal-mean zonal wind contours of -10, 0, 10 ms^{-1} are overlaid on (c), (f), (i) and (l). Solid contours denote westerlies and dashed counters denote easterlies. Stippling denotes 95% confidence interval.

the opposing force from vertical advection has minimal impact between 1.0-0.6 hPa. The maximum change in vertical advection is seen at altitudes between 1 hPa and 2 hPa. This is consistent with the changes in wave-driven induced circulation as the GWD shows an increased eastward forcing at these altitudes. However, these vertical advection changes are outside the altitude range of the maximum SAO bias correction.

There is some evidence for a statistically significant increase in eastward wave forcing associated with resolved waves during the SAO transition from its easterly to westerly phase (Figure 5.6g-i), which compares better with corresponding diagnostics from the MERRA-2 reanalysis (see chapter 4, Figure 4.10). Starting at 0.3hPa and descending to 2hPa from January to May, the improvement in EPD appears as negative values close to the zero-wind contour in Figure 5.6i, aiding a faster transition to the SAO westerly phase. Similar, but weaker, improvements can be seen in Aug-Nov as well. In the QBO region the waves are damped along the strongest shear zones (Pahlavan et al., 2021), thus aiding the phase transition. The improvement in resolved wave forcing here implies more wave damping along the strongest westerly shear zones, thus aiding the faster phase transition to SAO westerlies. Additionally, during the SAO westerly phase months, especially during MAM below 0.6 hPa (Figure 5.6i), there is an increase in eastward wave forcing, which will act to strengthen the SAO westerly phase.

The variations in GWD are shown in Figure 5.6j–l. One notable feature is that according to Figure 5.6l, the most significant changes in GWD occur during the transition from the westerly to easterly SAO phase (Apr-May, Oct-Nov), precisely during the months when the zonal-mean zonal wind improvement is at its highest (Figure 5.1f). A westward GWD forcing is visible at SAO altitudes in the Control experiment during this time, as shown in Figure 5.6j, and the forcing is noticeably reduced in the Nudged experiment where eastward forcing prevails (Figure 5.6k), helping to increase the SAO westerly phase duration in the Nudged experiment. At altitudes below 1 hPa, the improvements associated with the GWD forcing are

compensated by the increased eastward forcing in vertical advection, while above 1hPa vertical advection has little to no effect on the GWD improvements.

In summary, the analysis indicates that in the Nudged experiment both meridional advection and GWD contribute to diminishing the magnitude of the easterly phase of the SAO at around 1 hPa, whilst the wave forcing terms EPD and GWD act to improve (increase) the amplitude and duration of the westerly phase.

5.3.4 QBO modulation of TEM variables

Figure 5.7 explores the influence of the individual QBO phases on modulating the time-mean SAO forcing terms and how the forcings are affected by the nudging of the QBO. The forcing terms are calculated for the QBOE and QBOW phase chosen depending on whether the zonal-mean zonal wind at 50 hPa is less than –2 ms^{-1} or greater than 2 ms^{-1} respectively (the QBO index is determined for each month independently and then the diagnostics are composited into a time-mean; it is therefore not an annual-mean). The evolution of the composite zonal winds during both the QBO phases are shown in Figure 5.7a,b. When the winds are easterly at 50 hPa they reverse to westerly at around 10 hPa. When the winds are westerly at 50 hPa, they reverse to easterlies at around 30 - 10 hPa. Above the 10 hPa level, where the SAO dominates, the averaged winds are easterly in both QBO phases which is a manifestation of the easterly bias in the model SAO.

For comparison, MERRA-2 QBOE and QBOW composites of zonal-mean zonal wind and TEM diagnostics are shown in Figure 5.7e, f. As expected, in MERRA-2, the SAO winds are westerly on average during both QBO phases, while the SAO winds are easterly in the model control ensemble. SAO forcing terms at altitudes above the 1 hPa level show various discrepancies between MERRA-2 and the model (similar discrepancies seen between MERRA-2 and WACCM is discussed in chapter 4). However, it is readily noticeable that at 1hPa, the model lacks eastward GWD strength during both QBO phases.

The influence of the QBO phase on the SAO forcing terms is seen in Figure 5.7a and b. Comparing Figure 5.7 a and b, among the four forcing terms, the model

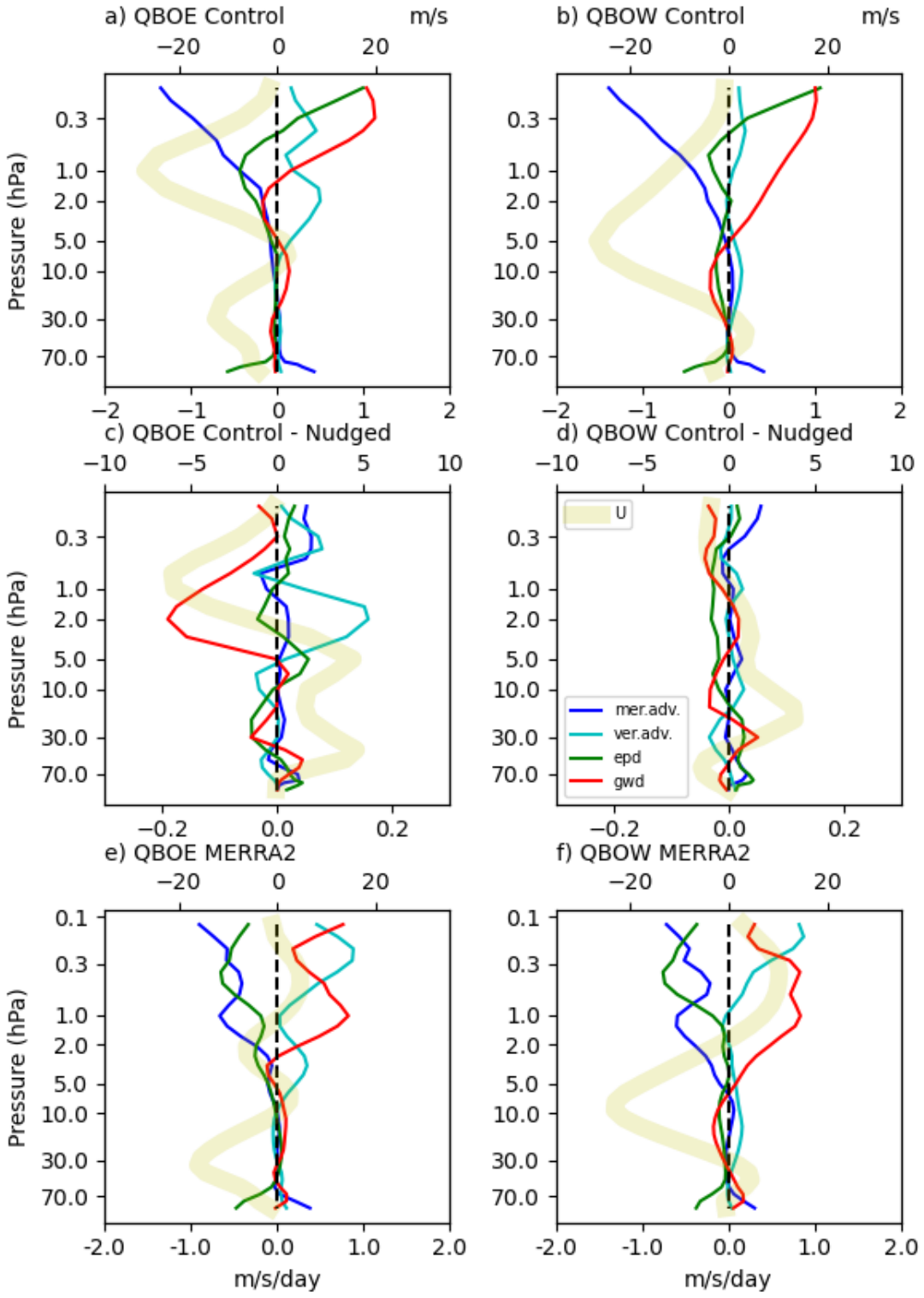

Figure 5.7: Composite of time-mean TEM forcing terms (see eq 2.19, and legend in panel (d)) and zonal-mean zonal winds ('U' thicker light-yellow line) averaged over 15°S-15°N for (a) Control experiment in QBOE months, (b) Control experiment in QBOW months, (c) Control minus Nudged differences during QBOE months, (d) Control minus Nudged differences during QBOW months, (e) MERRA-2 in QBOE months and (f) MERRA-2 in QBOW months. Units of TEM forcing terms are $ms^{-1}day^{-1}$ (lower axis) and zonal-mean zonal wind is ms^{-1} (upper axis).

meridional advection term appears to be least impacted by the QBO phase. Vertical advection, on the other hand, is substantially modulated by the QBO. In addition to the BDC, local induced circulations contribute to the vertical advection term. The BDC is known to consist of generalized upwelling at equatorial latitudes throughout the year, while locally induced circulations will produce upwelling during periods of westward wave forcing (negative vertical wind shear) and downwelling during periods of eastward wave forcing (positive vertical wind shear), thus maintaining approximate thermal wind balance. During the QBOE phase, winds at around 2hPa have a negative wind shear on average, thus creating an overall stronger upwelling in addition to the BDC upwelling. This then advects westerly winds from below, resulting in the positive vertical advection forcing seen in Figure 5.7a above 10hPa.

For resolved waves and GWD, a direct response to the QBO is visible. When QBO westerlies are present in most of the low-mid stratosphere, more eastward waves are filtered out and thus at altitudes above 5hPa westward drag dominates. However, above 0.6 hPa, wave forcings are eastward on average in both QBO phases. This is consistent with the larger filtering of westward waves in the QBO region suggested by previous studies.

The major message from Figure 5.7c,d is that changes in forcing as a result of the nudging are dominated by the GWD and vertical advection terms and these occur primarily in the QBOE phase (since these are approximately four times larger than during QBOW). Above 10 hPa during the QBOE phase, GWD and vertical advection show changes as large as 0.2 $ms^{-1}day^{-1}$ on average. This is consistent with the results in Figure 5.4a,b, where it was noted that the major bias in the QBO is during QBOE and thus the zonal winds are most altered during QBOE when nudging is applied.

Changes in zonal winds are directly reflected in the GWD profile. Nudging in the QBO height region led to increased QBO easterly winds, thus increasing the filtering of westward waves, resulting in the negative GWD difference values seen in Figure 5.7c. Vertical advection changes are also a direct consequence of the zonal wind profile changes. As the westerlies at 10hPa weaken in the Nudged experiment during

QBOE the vertical wind shear dampens, thus weakening the induced upwelling and creating the positive values of vertical advection changes in Figure 5.7c.

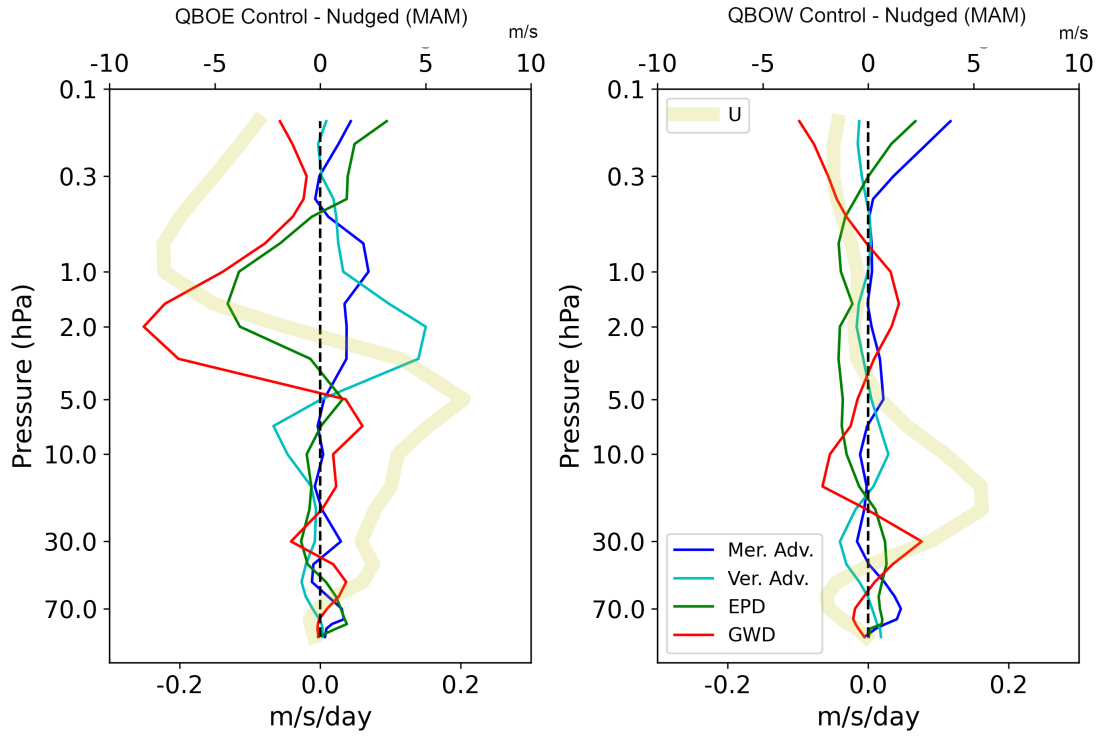

Figure 5.8: Composite of time-mean TEM forcing terms (see eq 2.19, and legend in panel (b)) and zonal-mean zonal winds ('U' thicker light-yellow line) averaged over 15°S-15°N for (a) Control minus Nudged differences during QBOE MAM seasons, (b) Control minus Nudged differences during QBOW MAM seasons. Units of TEM forcing terms are $ms^{-1}day^{-1}$ (lower axis) and zonal-mean zonal wind is ms^{-1} (upper axis).

Averaging of all months to form the QBO composite is slightly misleading for interpreting the EPD diagnostics, as a QBO phase typically lasts around a year or more, so the seasonal variations are averaged out in the composites. Figures 5.7c,d show that the differences in EPD forcing between the Control and Nudged experiments are small and independent of the QBO phase. However, Figure 5.6g-i showed that improvements associated with the EPD term are maximum during MAM. Seasonal QBO composites (see MAM composite in figure 5.8) have revealed that the main improvements associated with the EPD term occur in MAM primarily during the QBOE phase. The meridional advection term also suffers from the same averaging of seasonal variations, but Figure 5.6 shows that the meridional advection contribution is small and insignificant. In summary, Figure 5.7 highlights

the individual QBO phase modulation of the SAO forcing terms and demonstrates that the nudging to reduce the QBO bias has most impact on the SAO forcing terms during the QBOE phase.

5.4 Summary

Modelling the upper stratosphere presents various challenges due to the limited availability of observations and the dependence on parameterization of small-scale processes. An easterly bias of the SAO has been reported in various climate models, and chapter 4 indicated that increased eastward wave forcing is required in the models. However, it is not clear if this underestimation of eastward wave forcing in the height region of the SAO is due to an underestimation of wave generation in the troposphere (e.g., associated with convection or frontogenesis) or whether there is excessive wave damping/filtering as the waves propagate vertically through the lower stratosphere, in the region dominated by the QBO (e.g., due to lower-level circulation biases). This chapter has investigated the latter and, specifically, whether reducing biases in the QBO winds can lead to an improved representation of the SAO. This has been achieved using simulations of the HadGEM3 GA7.1 N216 that were performed as part of phase 2 of the QBOi model intercomparison project. SAO diagnostics have been compared from a 3-member ensemble of the free-running model (the Control experiment) and a corresponding 3-member ensemble in which the lower stratospheric winds in the height region of the QBO were nudged towards reanalysis to correct the well-known westerly zonal wind bias in the modelled QBO (the Nudged experiment).

The easterly bias of the SAO was found to be reduced in the Nudged experiment. The 42-year time-mean of equatorial zonal-mean zonal winds in the Nudged simulations changed as much as 25% compared to the Control simulations between 2 hPa and 0.6 hPa. A decrease in wind bias between 1 - 0.6hPa throughout the year indicates an improvement in both the SAO phases, i.e., a decrease of wind strength in the SAO easterlies and an increase in the SAO westerlies. The most significant

reduction in the easterly SAO bias was during the transition from SAO westerlies to easterlies, with the westerlies persisting for longer in the Nudged experiment.

It was found that the QBO and SAO improvements are strongly coupled in the vertical. QBO composites (defined at 50hPa) showed that nudging towards the reanalysis produced the greatest QBO corrections when the 50 hPa QBO winds are in their easterly phase. This roughly coincides with the months when the 10 hPa QBO winds are in a westerly phase. An overall strengthening of the 50 hPa QBOE winds as well as the correction of the significant westerly bias in the 10 hPa westerly winds are the most likely factors leading to this maximum correction of QBO winds during the QBOE phase. The diagnostics confirmed that this is the precise period during which the SAO bias was also improved.

The study further explored how the QBO correction impacted the processes that drive the SAO. QBO modulation of wave filtering, primarily during the QBOE phase, was found to be responsible for the major part of the SAO enhancement. Both resolved waves and parameterized gravity waves contributions were enhanced during the equinoxes leading to enhanced SAO westerly phases. However, gravity wave forcing was found to play the major overall role, with the reduced westward forcing and improved eastward forcing in the nudged ensemble during periods of SAO westerly-to-easterly phase transitions, leading to longer and deeper SAO westerly phases and shorter easterly phases.

Changes in the advection forcing terms were also found. Except in the height range between 1 hPa to 0.6 hPa, vertical advection was found to counteract the SAO improvement by providing more westward forcing in the Nudged experiment. Meridional advection above the 0.6hPa level was found to strengthen as well, thus also counteracting the SAO improvements, especially in JJA. At all other levels changes in meridional advection forcing were small and insignificant. Since the BDC is the main contribution to the meridional advection, the QBO modification of advection is likely to originate from an extratropical pathway, where changes in wave forcing cause corresponding changes in BDC. Exploring the details of these

extratropical routes is outside the scope of this study and the impacts are small compared to the tropical wave forcing changes.

The analysis presented in this study suggests that correcting biases in the lower altitude circulation alone is insufficient to completely mitigate all biases in the SAO. While correcting the underlying QBO wind bias has led to an improvement in wave filtering and thus the resulting representation of the SAO, there nevertheless remains a substantial easterly bias in the SAO. This suggests that enhanced momentum flux from high-frequency waves that are not absorbed in the QBO region are likely to be required to achieve a more accurate representation of the SAO. Such improvements might come through a better representation of tropospheric wave sources such as those associated with precipitation, convection and frontogenesis. The results in this chapter are based on simulations performed in a single climate model. In the next chapter, a multi-model comparison is done to understand if all the models respond similarly to the correction of QBO biases and to account for any potential biases in the current results that may arise from inherent model limitations.

6

QBO Modulation of the SAO in QBOi Models

6.1 Introduction

In this thesis, so far, we have explored the potential causes of SAO biases and the role of lower altitude biases on alleviating these SAO biases. In the earlier chapters, selected models were used to enable a detailed analysis, focusing on understanding the above-mentioned problems in depth. However, in this chapter, a different approach is taken. As mentioned earlier, previous studies have highlighted that biases in SAO representation are a common issue across most of the current climate models. Therefore, in this chapter, the aim is to conduct a multi-model analysis and assess the robustness of the results obtained in the previous two chapters. SAO biases in ten contemporary climate models are examined to determine whether these biases persist even after addressing the biases in the lower stratospheric zonal-mean zonal winds.

Smith et al. (2019) compared the modelled SAO in 11 climate model versions and noted that nearly all the climate models exhibit an easterly bias in zonal-mean zonal wind SAO. Despite this bias, the study highlighted that the climate models were able to simulate many important properties of SAO. Most of the models were noted to have particularly good agreement with the available observations

in SAO amplitudes and phase. The annual cycle of the SAO (section 2.7.2) and tilt of its peak magnitude towards the SH were also captured in several of the models. The study further noted that because waves play a critical role in forcing the SAO, the accuracy of SAO simulations in these models is heavily reliant on the parameterization of non-orographic gravity waves. However, the lack of observations makes it difficult to examine the correctness of the GW parametrisations.

The role of the QBO in modulating the SAO is thoroughly discussed in sections 2.9.3 and 5.1. Smith et al. (2019) briefly explored the impact of QBO phases on SAO across all the models by examining QBO phase composites calculated based on the direction of zonal winds at 10 hPa, and comparing how the SAO zonal-mean zonal wind behaves during the QBO westerly and easterly phases. The models consistently aligned with previous studies, showing that when zonal winds at 10 hPa are more easterly, the zonal winds at 1 hPa tend to be more westerly. They noted that the variations in GWD are consistent with the wind profile in models, with stronger eastward GWD forcing at SAO altitudes when the zonal winds are easterly at 10 hPa, indicating less filtering of eastward waves during the QBO easterly phase. Resolved waves roughly showed similar patterns but with smaller magnitude. This demonstration of SAO-dependence on the QBO phase suggests that if the models have a wind bias at QBO levels then it is likely to result in a corresponding wind bias at the SAO levels.

In this chapter, we will first briefly explore how the current climate model versions perform compared to what was presented in Smith et al. (2019). Following this, we will shift our focus to this chapter's main objective, which is to understand how the SAO in various models respond to reductions in the QBO biases. The same approach as in the previous chapter is followed. The zonal-mean zonal wind climatology and TEM diagnostics in the Control and Nudged runs of each model is analyzed to understand how the SAO winds and forcing terms have changed in response to nudging. We then explore if the model SAO biases are linked to biases in specific QBO phases using QBO phase composites of zonal-mean zonal wind and different forcing terms. Section 6.2 outlines the data and methods

used in this chapter. Section 6.3 describes the results of this chapter, and the summary is provided in section 6.4.

6.2 Data and methods

For the multi-model analysis presented in this chapter, the QBOi phase 2 datasets described in section 3.4.2 are utilized. The dataset is particularly suitable for analyzing SAO representation, as most models in the project have their top model lid in the mesosphere or thermosphere. As can be seen from QBOi phase 2 protocol (Anstey et al. 2024, in preparation), 12 models are participating in phase 2 of the QBOi project. In this chapter we will be analyzing 10 of them as listed in table 6.1, along with the horizontal and vertical resolution of the models noted. One model was avoided due to a lower model lid which falls within the SAO altitude, and one model due to unavailability of data at this stage.

Models	**Institute**	**Horizontal Resolution**	**No. of vertical levels**	**Model lid (hPa)**
HadGEM3GA7.1	MOHC, Oxford	N216	85	0.01
MIROC6.1(p1)	JAMSTEC	T85	90	0.004
MIROC6.1(p2)	JAMSTEC	T85	90	0.004
LMDz	LMD	2.5°(lon)x1.25°(lat)	79	0.01
CAS-ESM	CAS/IAP	1.4°(lon)x1.4°(lat)	69	0.01
E3SM2	DOE	ne30(110km) atmosphere	72	0.1
ESM4	GFDL	C96 (100km)	49	0.01
MRI	MRI	TI159	80	0.01
EC-Earth3	CNR	T255 (80km)	91	0.01
CESM2(CAM6)	NCAR	∼1°(1.25°lonx0.9°lat)	83	0.008

Table 6.1: Details of the resolution and model lid altitude of models from QBOi phase 2 that are used in this study. (In chapter 4, the CMIP6 contribution of CESM2 model WACCM is used. In this chapter, another version of the CESM2 model CAM6 is analysed. CAM6 has a low top and limited chemistry compared to WACCM6).

The QBOi phase 2 data is made available on specified pressure levels and frequencies. The zonal-mean diagnostics are available at daily and monthly

frequency, with a top available altitude of 0.4 hPa for all models, except HadGEM3 and EC-Earth3, which provide data at higher altitudes. Daily and monthly data of zonal wind and TEM diagnostics are used in this study. CESM2 (CAM6) TEM diagnostics data were not available at the time of this study and only the monthly 3D zonal wind values were provided up to the SAO altitudes. Hence, the CESM2 data is used merely for understanding the zonal wind changes. In QBOi Phase 2, the models have been updated from the versions that participated in Phase 1 of the project, and the run now cover a 42-year period compared to the 30-year period used in the previous phase. Most models have three ensemble members available for each experiment (see table 6.2) and the average of all available ensemble members are presented in the results unless otherwise stated (similar to chapter 5).

The details of the nudging methodology used in the QBOi phase 2 are outlined in Chapter 3. While nudging only the zonal-mean zonal wind was requested in the protocol, in some models this was not feasible and full-field nudging was implemented. Details of the nudging implemented in each model are shown in table 6.2.

As the current climate models are unable to produce tropical stratospheric oscillations with only resolved waves, physical parametrization of GW is unavoidable. The GW parametrization usually involves representation of wave generation, propagation and dissipation by filtering at critical levels and wave saturation. All the models analysed in this chapter have a parametrized non-orographic GW. Some models, instead of using a fixed wave source, parametrize the source of non-orographic GWs by linking to convection or frontal systems, as these are the primary sources of non-orographic GW in our atmosphere. The references for non-orographic GW used in each model along with the type of source parametrization is listed in table 6.2.

CMIP6 forcings are generally used by most models. For the ocean boundary, AMIP boundary conditions for observed SST and sea-ice from input4mip (`https://aims2.llnl.gov/search/input4MIPs/`) were prescribed. The models also include CMIP6 forcings from volcanic aerosols (except in LMDz), 11-year solar cycle (except in LMDz) and trace gas concentrations. Some participating models have interactive ozone, while the observed climatological or transient ozone is specified in other

Models	Nudging	GWD Source	non-orographic GWD	ozone (hPa)	Nunmber of Ensemble (Control,Nudged, NoQBO)
HadGEM3GA7.1	Zonal mean	Convective (Bushell et al., 2015)	Warner and McIntyre (1999)	Not interactive (1979-2014 climatological ozone)	3,3,3
MIROC6.1(p1)	Zonal mean	fixed	Hines (1997)	Not interactive	3,3,3
MIROC6.1(p2)	Zonal mean	fixed	Hines (1997)	Not interactive	3,3,3
LMDz	Zonal mean	Convective (Lott and Guez, 2013), and Fronts (de la Cámara and Lott, 2015)	Lott et al. (2012)	Not interactive	1,3,2
CAS-ESM	Zonal mean	convective GWs (Beres et al., 2004) and GWs from frontal systems (Charron and Manzini, 2002)	Lindzen (1981)	Not interactive	3,3,3
E3SM2	full-field	convective GWs (Beres et al., 2004), GWs generated by frontal systems (Charron and Manzini, 2002)	Lindzen (Lindzen, 1981)	Interactive, linearized	3,3,3
ESM4	full-field	fixed	Alexander and Dunkerton (1999)	Interactive, full chemistry	3,3,3
MRI	Zonal mean	fixed	Hines (1997)	Interactive, full chemistry	3,3,3
EC-Earth3	full-field	fixed	Orr et al. (2010)	Not interactive (CMIP6)	1,1,1
CESM2(CAM6)	Zonal mean	convective GWs (Beres et al., 2004), Frontal GWs (Charron and Manzini, 2002)	Lindzen (1981)	Not interactive	3,3,3

Table 6.2: Details of the nudging and GWD in models from QBOi phase 2 that are used in this study

models. In the QBOi 2 protocol it was proposed to use the observed monthly climatological ozone field in models with non-interactive chemistry, rather than a fully transient ozone field since the latter will contain a QBO signal that is inconsistent with the spontaneous QBO generation in the Control runs (Butchart et al., 2023). However, this means that in the Nudged simulations of models with non-interactive chemistry and climatological ozone with no QBO signal, the diabatic effects of the ozone QBO (which is known to have significant effects on temperature QBO) and the zonal wind QBO might not be in agreement. This might have an impact on the QBO, and induced circulation associated with the QBO, and further influence on teleconnections.

Similar to previous chapters, MERRA-2 reanalysis data is used when a comparison is made between models and reanalysis. When a comparison between two data sets is presented, a Student's t test is used to calculate if the distributions are significantly different (see section 3.4.3).

In this chapter, to compare the SAO among models, the semi-annual amplitude and phase are calculated, hence filtering out the other variabilities. This analysis was carried out using Fourier transform (section 3.4.4). In the time series data (of length T), Fourier analysis was performed to obtain the Fourier coefficients of the nth harmonic, $a(n)$ and $b(n)$, corresponding to the six-month variability (hence $\frac{T}{n} = 6$ months). The amplitude is then calculated as

$$SAO_{amplitude} = \sqrt{a(n)^2 + b(n)^2}$$

The phase was calculated as the inverse tangent of $\frac{b(n)}{a(n)}$, with the resulting value in radians. To present the phase more intuitively, the value in radians was converted into a corresponding number of days (by scaling with $(\frac{1}{2\pi}) \times (\frac{T}{n})$).

6.3 Results

6.3.1 SAO wind characteristics in QBOi models

To gain a broad understanding of how models perform in generating the SAO, the climatology of zonal-mean zonal wind from 100hPa to 0.4hPa (or the top model level where data is available) averaged over 15°S to 15°N, is examined in Figures 6.1 and 6.2. The objective is to assess the models' ability to capture the time profile of wind in the upper stratosphere and to observe how the model performance changes when biases in the zonal-mean zonal wind in the lower to middle stratosphere are removed. Chapter 5 provided a detailed examination of the SAO in HadGEM3 and the response to bias alleviation in QBO. Building on that, for ease of comparison, the models presented here are divided into two groups. The first group includes models showing patterns like HadGEM3 and the climatology of zonal-mean zonal wind pattern of these models are displayed in Figure 6.1. A second group of models displaying distinctly different characteristics compared to HadGEM3 are shown in Figure 6.2. The first group of models will be addressed as the 'Similar group' of models and second group as the 'Distinct group' from here on.

The Similar group, shown in Figure 6.1, is comprised of HadGEM3, two versions of MIROC6.1, LMDz and CESM2 (CAM6). Figures 6.1a,d,g,j and m, showing the Control runs, indicate that across all these models, from 2hPa to highest plotted altitude, a reasonable representation of the SAO is evident. The easterly phase roughly occurs during solstices and appears over a range of altitudes at the same time (except in LMDz) and the westerly phase occurs during equinoxes and propagates down with time. An annual cycle is also observable in the easterly phase for all models, where the SAOE around NH winter is stronger than the one during SH winter. The NH winter SAOE peak occurs mostly around 1 hPa, while the altitude of the peak of the SH winter SAOE varies among models. A notable characteristic across the Similar group models is that either the second easterly phase of the SAO or the westerly phase reaches its peak magnitude at 0.4 hPa or possibly at a higher altitude, although higher altitudes cannot be verified due to data availability

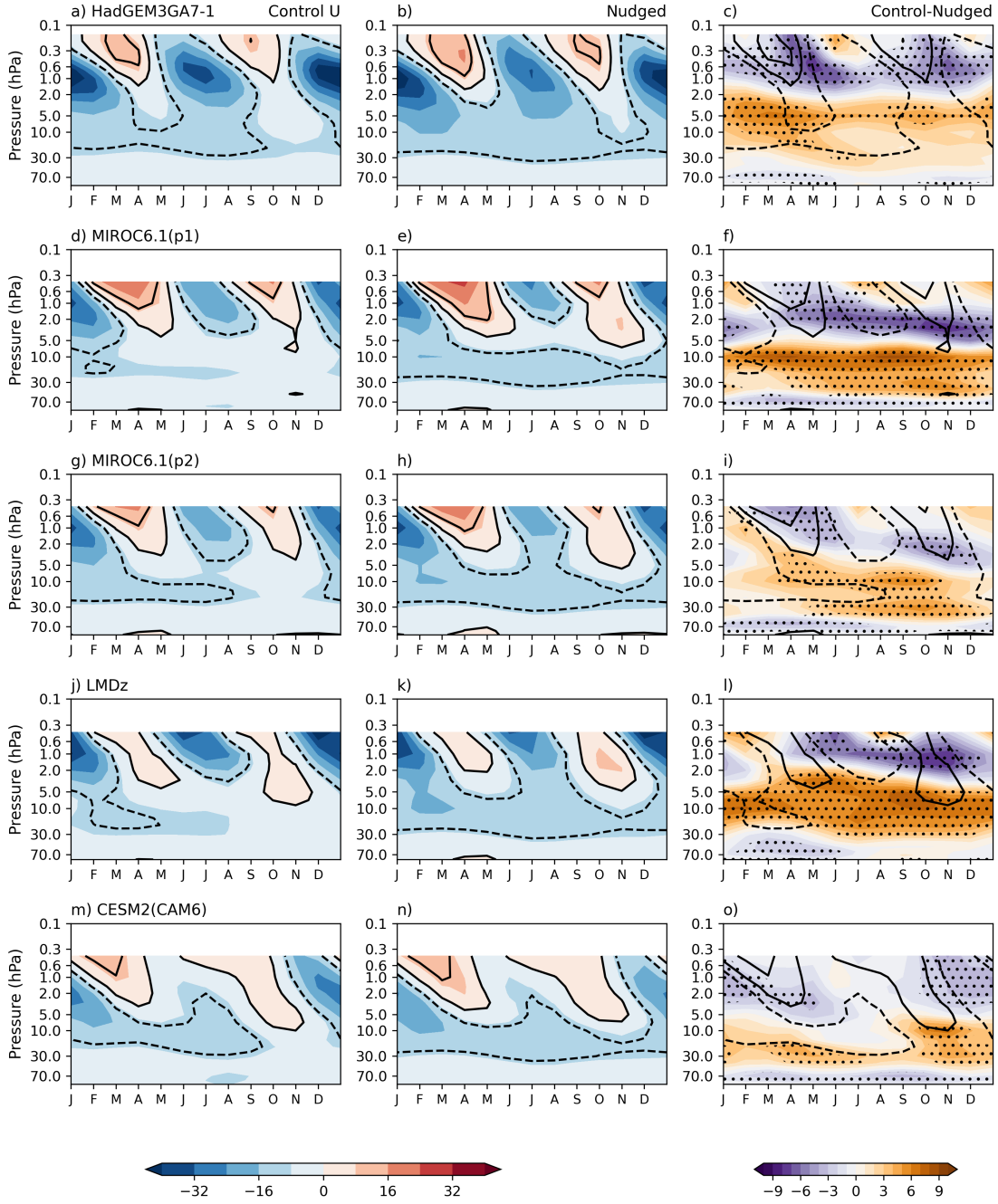

Figure 6.1: Daily mean climatology of zonal-mean zonal wind (ms^{-1}) averaged over 15°N to 15°S for Control ensemble-mean, Nudged ensemble-mean and Control minus Nudged differences respectively in (a-c) HadGEM3, (d-f) MIROC6.1(p1), (g-i) MIROC6.1(p2), (j-l) LMDz and (m-o) CESM2(CAM6). Contours of -10, 0, 10 ms^{-1} are overlaid, with dashed contours denoting negative values. Overlaid in c, f, i, l and o are the wind contours from the Control ensemble-mean at -10, 0 and 10 ms^{-1}. Stippling denotes 95% confidence interval.

limitations. Although the SAOW phase magnitude is weaker and the easterly phase stronger than that of MERRA-2 SAO (see chapter 4, figure 4.3), the models in the Similar group still capture the major characteristics of the SAO.

The Similar group models exhibit similar changes in the SAO in response to the QBO bias correction. From Figure 6.1b,e,h,k and n, the models' SAOW has generally increased in magnitude and/or propagated farther down in altitude, in response to the QBO bias reduction. The SAOE, especially the one during the SH winter, has reduced in magnitude around 1 hPa (although in CESM2 (CAM6), the NH winter changes are dominant). These features indicate a reduction in the easterly bias of SAO in these models.

Panels c,f,i,l,o which display the differences between Control and Nudged runs for the models in the Similar group, reveal that the magnitude of QBO wind changes due to nudging in the QBO altitudes (from 10 hPa to 100 hPa) are roughly similar across all the models shown. This similarity is also observed at the SAO altitudes, where a similar magnitude change in winds is evident. The time of the year at which the SAO differences peak matches with that of the QBO corrections in most models. As noted in previous studies, the models initially displayed a westerly bias at the QBO altitudes. This bias is corrected in the Nudged runs, as evidenced by the positive values in the difference plots. The negative values dominating the upper stratosphere in the difference plot imply that winds became more westerly in the Nudged runs, which is a change in the right direction to improve SAO representation in models.

The comparable biases in QBO winds and the similar vertical profiles of SAO winds across the models may explain why members of the Similar group have similar SAO responses to the QBO nudging.

Figure 6.2 illustrates the SAO in the zonal-mean zonal wind from the Control and Nudged runs of the Distinct group models. While E3SM2 and MRI display alternating easterly and westerly phases of the SAO clearly, the other three models, CAS-ESM, ESM4 and EC-Earth3 struggle to replicate SAO variability around 1 hPa. In the latter models, although the easterly phase of the SAO is reasonably

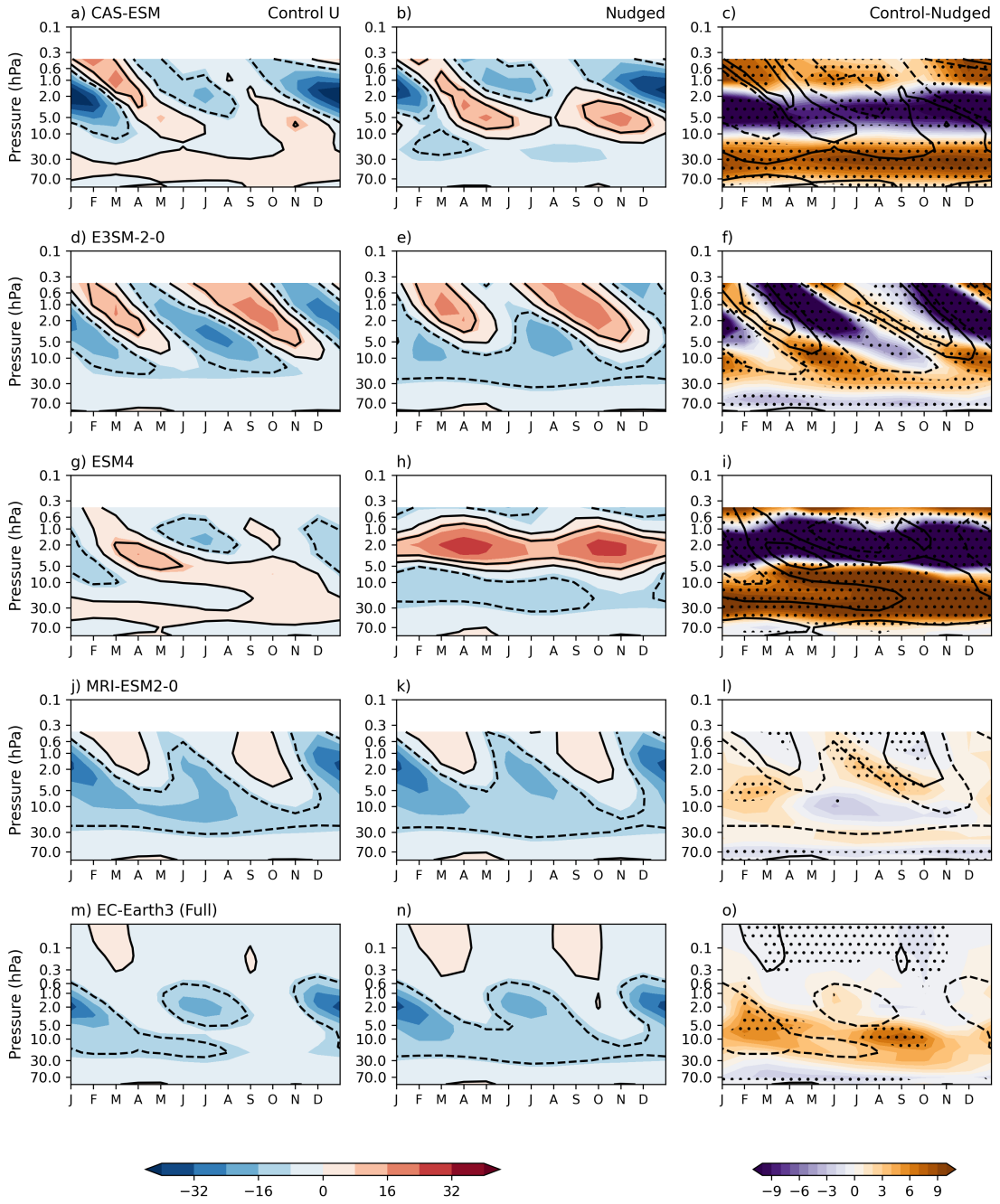

Figure 6.2: Daily mean climatology of zonal-mean zonal wind (ms^{-1}) averaged over 15°N to 15°S for Control ensemble-mean, Nudged ensemble-mean and Control minus Nudged differences respectively in (a-c) CAS-ESM, (d-f) E3SM2, (g-i) EMS4 , (j-l) MRI and (m-o) EC-Earth3. Contours of -10, 0, 10 ms^{-1} are overlaid, with dashed contours denoting negative values. Overlaid in c, f, i, l and o are the wind contours from the Control ensemble-mean at -10, 0 and 10 ms^{-1}. Stippling denotes 95% confidence interval.

represented, the westerly phase, particularly the second cycle of SAO westerlies (occurring during September to November), is nearly absent in these models at 1hPa. Even within E3SM2 and MRI, notable differences are evident compared to reanalysis: E3SM2 lacks annual cycle variability (in which the easterly winds in the second half of the year are stronger than in the first half), and MRI exhibits very weak westerlies (less than 8 ms^{-1}). The altitude of peak SAO easterlies or westerlies in Distinct group models is below 1hPa, which is different from the Similar group models. Except MRI, all models in the Distinct group are struggling to produce the major SAO characteristics.

Based on the response to the nudging, the Distinct group models can be further classified into subgroups. CAS-ESM, E3SM2 and ESM4 can be categorized together. All three models exhibit very strong changes in the SAO winds due to nudging, shifting towards westerly in most regions, with differences exceeding 10 ms^{-1} for most of the year (as shown in Figure 6.2 c, f, i difference plot). The E3SM2 Nudged runs show stronger SAOW and weaker SAOE, consistent with an improved SAO characteristic, however, the model still fails to have a proper annual cycle. Since E3SM2 lacks strong internally generated QBO variability (see Figure A1), introducing nudging significantly alters the winds at QBO altitudes, although the overall climatology changes are less. Figure A1 also suggests that nudging in CAS-ESM is unsatisfactory as the QBO winds continue to exhibit a westerly bias. From the difference plot, the changes in the CAS-ESM and ESM4 winds at QBO altitudes are evidently drastic, persisting all year round. Similar amplitude changes are also observed at SAO altitudes of these models, lasting throughout the entire year, although the SAO characteristics have not necessarily improved. ESM4 is particularly intriguing, as it appears to have no phase separation at SAO altitudes, showing only westerly winds. Among the models analyzed in this study, CAS-ESM, E3SM2, and ESM4 have the lowest vertical resolution, with 69, 72, and 49 levels, respectively. Although E3SM2 has 72 levels, its model lid is at 0.1 hPa, placing it within SAO altitudes. The drastic changes in SAO observed in these models in

the Nudged runs could be attributed to factors such as lower vertical resolution, significant alterations in QBO winds, and the SAO peak occurring below 1 hPa.

The final two models in the Distinct group, MRI and EC-Earth3, show the smallest response at SAO altitudes to the nudging of the QBO. From figure 6.2l, MRI is evident to have the least significant changes in the QBO altitudes. This lack of change at the lower altitudes could therefore explain the little to no variation observed in the SAO.

On the other hand, figure 6.2o suggests that nudging in EC-Earth3 leads to considerable changes in the model QBO winds, which is comparable in magnitude to the QBO changes in the Similar group models. However, the winds at SAO altitudes in EC-Earth3 fail to respond to the substantial QBO wind changes. The Control run already shows poor SAO representation in this model. In Döscher et al. (2022) describing the EC-Earth 3 model in CMIP6 (which is the same version as used in QBOi) also noted that the model fails to have a realistic SAO representation, with easterlies completely dominating the upper stratosphere. The model was noted to use both non-orographic parametrisation and Rayleigh friction (from 10 hPa to higher altitudes). Serva et al. (2024) explored the momentum budget of the SAO and suggested that the Rayleigh friction at upper model levels in EC-Earth3 could explain the lack of SAO westerlies around 1 hPa. Thus, even though the QBO in the model is corrected, it appears that due to the Rayleigh drag in the upper stratosphere, the SAO is unable to change significantly. Because of these strong non-physical effects in the upper stratosphere of EC-Earth 3 and marginal changes in SAO, the model is excluded from further analysis. Note that, except for MRI and EC-Earth3, all other models show a maximum of at least 3 ms^{-1} or greater changes at SAO altitudes. With an understanding of the general SAO characteristics in the presented models, the next section will focus on analyzing the multi-model mean behaviors.

Figure 6.3a, b, and c display the time-mean, semi-annual amplitude, and phase propagation of the equatorial zonal-mean zonal wind, respectively, across all models in the Control runs. In the time-mean profile, while most models exhibit mean

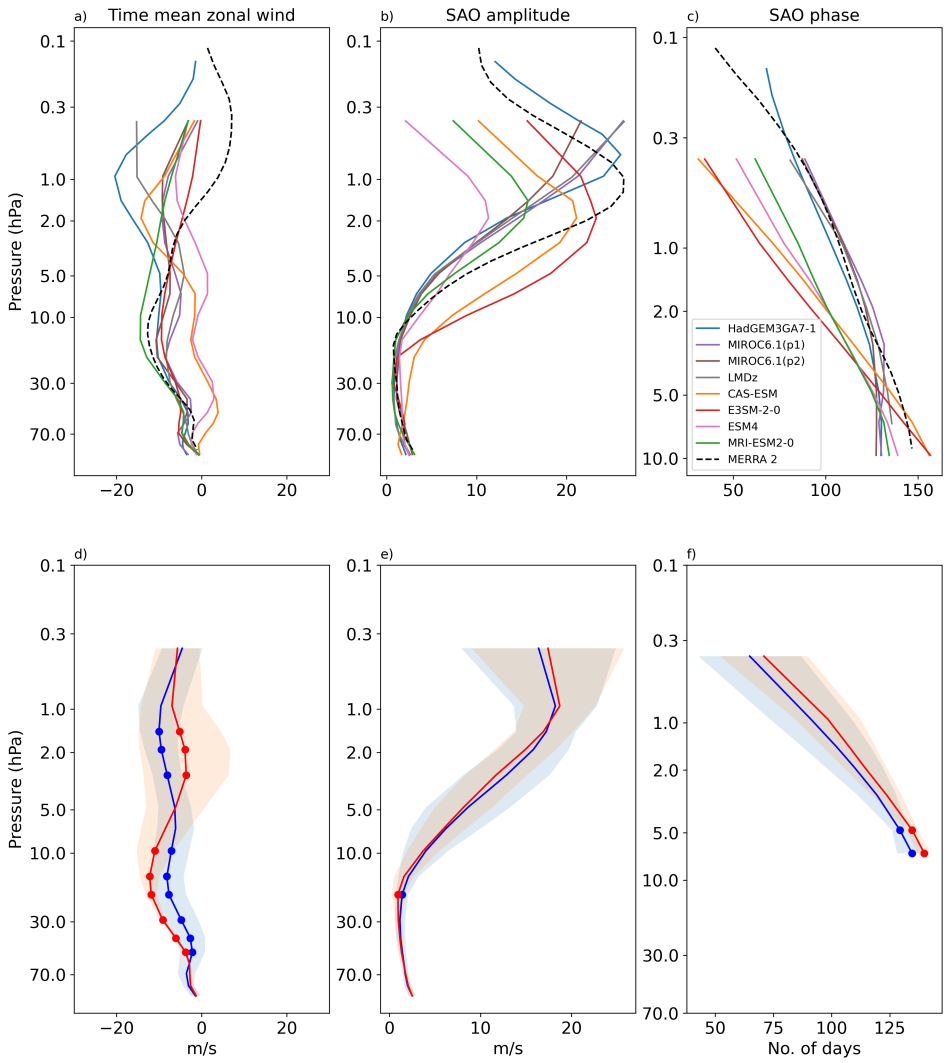

Figure 6.3: Height profiles of (a) the multi-year climatology of equatorial zonal-mean zonal wind, (b) amplitude of the semi-annual component and (c) phase of the semi-annual component derived from the Control simulations of 8 different models. Units are ms^{-1}. The multi-model mean (red line) and standard deviation (red shading) are shown in (d-f) along with the corresponding profile from the Nudged simulations (blue line and blue shading). Significantly different data points at 95% confidence interval are marked as blue and red dots in (d-f).

easterly winds in the QBO region, CAS-ESM and ESM4 show westerly winds, with a difference of nearly 10 ms^{-1} compared to the other models. At SAO altitudes, aside from an overall easterly average, where HadGEM3 shows the largest easterly magnitude, no particularly outstanding patterns are observed. At 1 hPa, all models show an easterly bias when compared to the MERRA-2 mean wind.

The semi-annual amplitude provides insight into the location of the peak six-month variability in the models (6.3 b). Below 10 hPa, this amplitude is minimal as this region is primarily influenced by the QBO. Above 10hPa, the semi-annual variability increases, peaking somewhere above 5 hPa in all the models, before generally decreasing at higher altitudes. The Similar group models (HadGEM3, MIROC 6.1(p1), MIROC 6.1(p2) and LMDz) show peak SAO variability between 1hPa and 0.3 hPa (except for HadGEM3, 0.4hPa is the highest altitude for which model data is available from these models). This magnitude compares well with the SAO amplitude of MERRA-2 (which peaks at 1 hPa). E3SM2 shows a similar magnitude peak, but at a much lower altitude, between 5hPa and 2hPa. The model lid of E3SM2 is at 0.1 hPa, which might explain the lower altitude peak. Among the Distinct group models, all except E3SM2 exhibit peaks between 2 hPa and 1 hPa, with significantly smaller SAO amplitudes, reduced by nearly 10 ms^{-1} in MRI, and ESM4. This is consistent with Figure 6.1, where these models show much lower wind amplitude compared to the remaining models.

The phase, defined as the timing of first maximum of the semi-annual variability (see section 6.2 for details of calculation), varies from early-March to mid-April (roughly from days 60 to 110) depending on model. The Similar group models with higher altitude SAO peak have faster downward phase propagation, which is similar to MERRA-2. Based on both SAO amplitude peak and phase, the Similar group models are closer to MERRA-2 in replicating SAO characteristics, although they have an easterly wind bias in terms of magnitude.

Figure 6.3 d, e and f illustrate the multi-model ensemble average (MME) of time-mean, semi-annual amplitude, and phase propagation of the zonal-mean zonal wind of the eight models discussed. The blue line represents the average of the

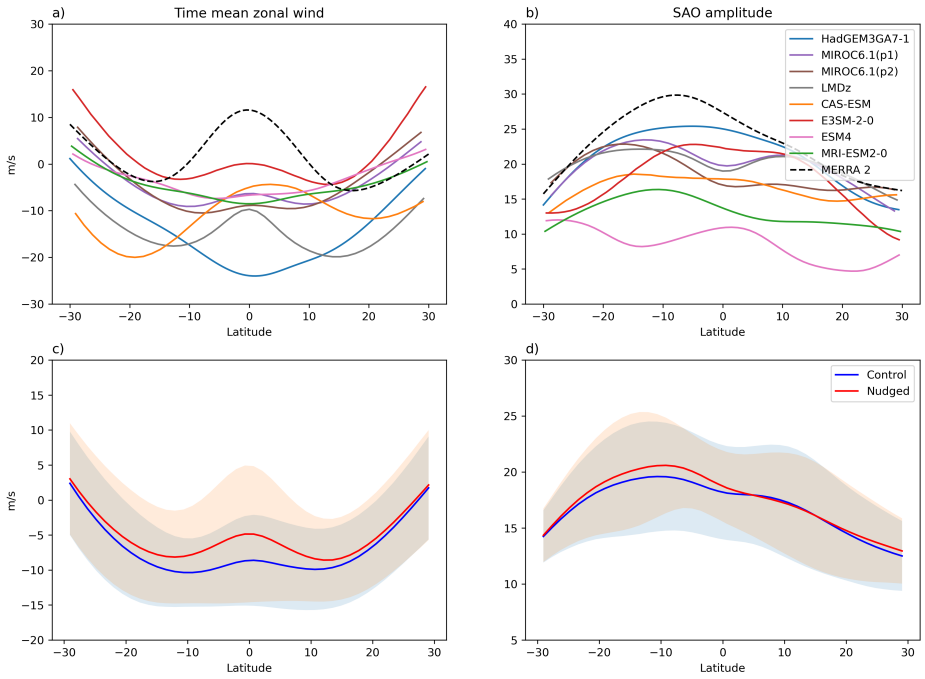

Figure 6.4: Climatology and amplitude of semi-annual component of zonal-averaged zonal winds as in figure 6.3 but showing the latitudinal variation at 1 hPa.

Control runs, as seen in Figure 6.3a-c, while the red line indicates the properties of the Nudged runs. The shading shows the standard deviation of the variable across the models. The time-mean profile (6.3d) clearly suggests that nudging has caused the QBO winds (from 70 hPa to 5 hPa) to become more easterly, while the SAO winds have shifted to more westerly. This adjustment reduced the westerly bias in the QBO within the models which, in turn, helped to decrease the easterly bias of the SAO. The amplitude and phase (6.3e,f) show little to no change, with the phase slightly shifting to later days but this is statistically insignificant around 1hPa.

The latitudinal profile of SAO in the models is explored in Figure 6.4. The figure presents the latitudinal profile of time-mean and semi-annual amplitude of zonal-mean zonal wind at 1 hPa, where all models showed reasonable SAO variability in Figure 6.3b. The Control run behavior is consistent with the QBOi phase 1 models (Smith et al., 2019). In terms of the mean wind, MERRA-2 exhibits a peak at the equator which falls off away from the equator and then slightly

increases around 30 degrees in both the hemispheres. However, the models show inconsistent behavior. About half of them display a peak at the equator, while the others show a minimum, and none have the time-mean wind at the equator as westerly as observed in MERRA-2.

The latitudinal profile of the amplitude of the semi-annual harmonic is more consistent across models. All the models, except ESM4, show a maximum amplitude south of the equator within 20 degrees. MERRA-2 displays a similar feature as well but with a slightly higher amplitude.

The figure 6.4c,d indicates that the Nudged run (red) becomes noticeably more westerly at the equator compared to the Control run (blue), shifting towards the reanalysis data. However, the difference between the Control and Nudged runs is statistically insignificant and diminishes at higher latitudes, around 20 to 30 degrees. Since nudging is applied between 15°S and 15°N in all models, this latitudinal profile suggests that the QBO's influence on the SAO might be primarily vertical. In the NH, time-mean wind values align with MERRA-2 after 20 degrees. The SAO amplitudes in the Nudged MME are slightly higher in the SH compared to the Control, though the overall changes appear minimal and statistically insignificant.

Figure 6.5 shows the equatorial zonal-mean zonal wind distribution of each model at a particular altitude, presented as the kernel density distribution of the frequency of occurrence (number of days) of wind strengths, to quantify the difference between the SAO winds in the Control and Nudged runs. From figure 6.3, it is evident that the altitude at which the multi-year wind climatology and the semi-annual amplitude peaks varies among models. Thus, instead of selecting a standard pressure level to analyze all the models, we have selected a separate altitude for each model, depending on their wind distribution. The difference of the multi-year zonal-mean equatorial zonal wind climatology (averaged over 15°S to 15°N) between the Control runs (see figure 6.3a for Control climatology) and Nudged runs has been calculated, and the altitude above 5 hPa where this difference is maximum has been identified (see table 6.3). The change in wind characteristics at the chosen altitude for each model is then displayed in figure 6.5.

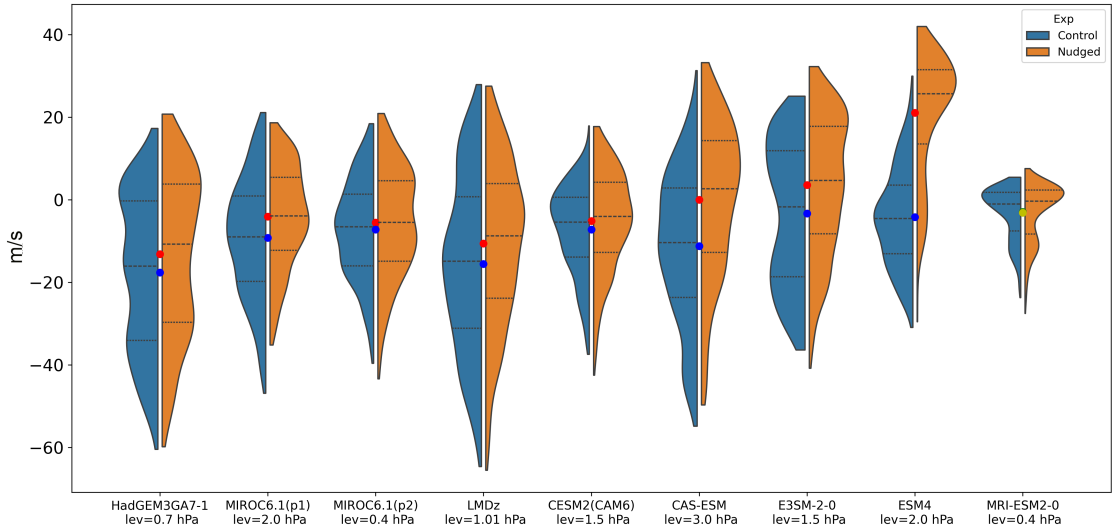

Figure 6.5: Violin plot of zonal-mean equatorial zonal wind, averaged over 15°S to 15°N, at a selected pressure level for each QBOi model with daily data from all the available years. The width of a distribution roughly indicates the number of days equatorial winds are at a certain strength, smoothed with kernel density estimate. For visualization purposes, maximum width is kept the same for all the distributions. The model name and selected pressure level is shown in the x axis label. The pressure level was selected for each model depending on the maximum wind differences between the Control and Nudged runs (see text). The blue (orange) shading shows the distribution of the Control (Nudged) simulations, with the blue (red) dots showing the mean of the distributions. The dashed lines show the quartiles of the distribution. The difference between the mean of the Control and Nudged distributions is significant for all models except for MRI-ESM2.0 (where the means are shown as green and yellow dots).

In all the models the mean value of the Nudged run is consistently more westerly than the Control run (although the changes in MRI were found to be insignificant). Table 6.3 shows that in six out of nine models, the mean wind has shifted by a minimum of 4 ms^{-1}. The percentage change in winds (Nudged – Control) with respect to the Control run winds in each model, calculated using the mean values from figure 6.5, is also indicated in table 6.3. We note that the mean value of the Control run wind differs across models, however, using percentage change offers an effective method for comparing the models. The Similar group models show that the winds became 23% to 57% more westerly in the Nudged run with respect to the Control runs. While the changes in the Distinct group models, as expected, are either much higher (two to four times increase) or much lower (6% in MRI).

Not only the mean but also the median has shifted to less negative/more positive

Models	Pressure at which maximum wind change occur (hPa)	Difference in mean (Nudged-Control) (ms^{-1})	Percentage change with respect to Control (%)	Control run wind (ms^{-1})	Skew value Control run	Skew value Nudged run
HadGEM3GA7.1	0.7	4.4	24.9	-17.6	-0.18	-0.26
MIROC6.1(p1)	2.0	5.2	56.3	-9.2	-0.18	-0.329
MIROC6.1(p2)	0.4	1.7	23.6	-7.2	-0.146	-0.269
LMDz	1.01	4.95	31.9	-15.5	-0.024	-0.342
CESM2(CAM6)	1.5	2.1	29.1	-7.2	-0.549	-0.465
CAS-ESM	3.0	11.3	100.5	-11.3	-0.283	-0.534
E3SM2	1.5	6.9	208	-3.3	-0.111	-0.358
ESM4	2.0	16.9	403.6	-4.2	0.255	-0.984
MRI	0.4	0.2	6	-3.1	-0.953	-0.984

Table 6.3: Characteristics of equatorial zonal-mean zonal wind at the SAO altitude where maximum difference between Nudged and Control simulation winds occurs in each model.

values in all the models. Additionally, the skew values have become more negative (except in CAM6), indicating a reduction in the distribution of easterly winds and a concentration of values toward the westerly side. These 'violin' plots in figure 6.5 are consistent with these shifts in skewness, showing that the width of the density distribution has decreased on the easterly end and increased on the westerly end in the Nudged runs for most models. The analysis suggests that in the Nudged runs, the number of days in which the winds are westerly (easterly) has increased (decreased) and, in some models, the maximum value of westerly winds at the selected altitude has increased as well.

6.3.2 Processes driving the SAO

So far, we have seen that while all the models exhibit an easterly bias in the SAO, nudging has helped reduce this bias by shifting the SAO winds more eastward in most models, particularly in the Similar group models where a noticeable improvement in the SAO characteristics and evolution is evident. In this section, the various

forcing terms of the SAO are examined to identify which factors play a major role in modifying the SAO in these models. In Chapter 5, GWD was identified as the most changed forcing term at SAO altitudes in HadGEM3. Here, the differences in TEM terms between the Control and Nudged runs across all models are analyzed to identify the dominant term and investigate the robustness of the result obtained in Chapter 5.

Figure 6.6 illustrates the vertical profile of the difference in TEM terms between the Control and Nudged runs. The TEM diagnostics for each model separately are provided in the appendix (see Figure A2). As noted in previous chapters and earlier studies, meridional advection typically contributes to westward forcing, while GWD and vertical advection primarily generate eastward forcing. Additionally, the resolved wave components average out as a source of westward forcing (Figure A2). The remaining forcing (difference between rate of change of zonal-mean zonal wind and the sum of advection and wave forcings) is included in Figure A2, which suggests that in some models, the TEM momentum budget is not closed. We note that in all the models, this remaining term is weaker than most TEM forcing terms at SAO altitudes.

In Figure 6.6, the broad yellow line represents the difference between the zonal-mean zonal wind in the Control and Nudged runs. The wind profiles for all models, except for MRI, align with the MME average characteristics outlined in Figure 6.3d. Specifically, positive differences in the QBO region indicate that nudging effectively alleviates the westerly QBO bias in these models, resulting in a corresponding eastward shift (negative values) at SAO altitudes.

In all the models, among the TEM forcing terms, GWD (red line in Figure 6.6) is the predominant factor showing the strongest difference between Control and Nudged runs at SAO altitudes. Changes in GWD are closely aligned with changes in the wind profile, although the peak GWD change occurs at slightly lower altitudes. In some models, vertical advection also shows changes of a similar magnitude but in the opposite direction, which could be due to an induced circulation (see section 2.7.1 in introduction) from increased eastward GWD forcing. At higher altitudes, the opposing changes in vertical advection diminish first, while GWD changes

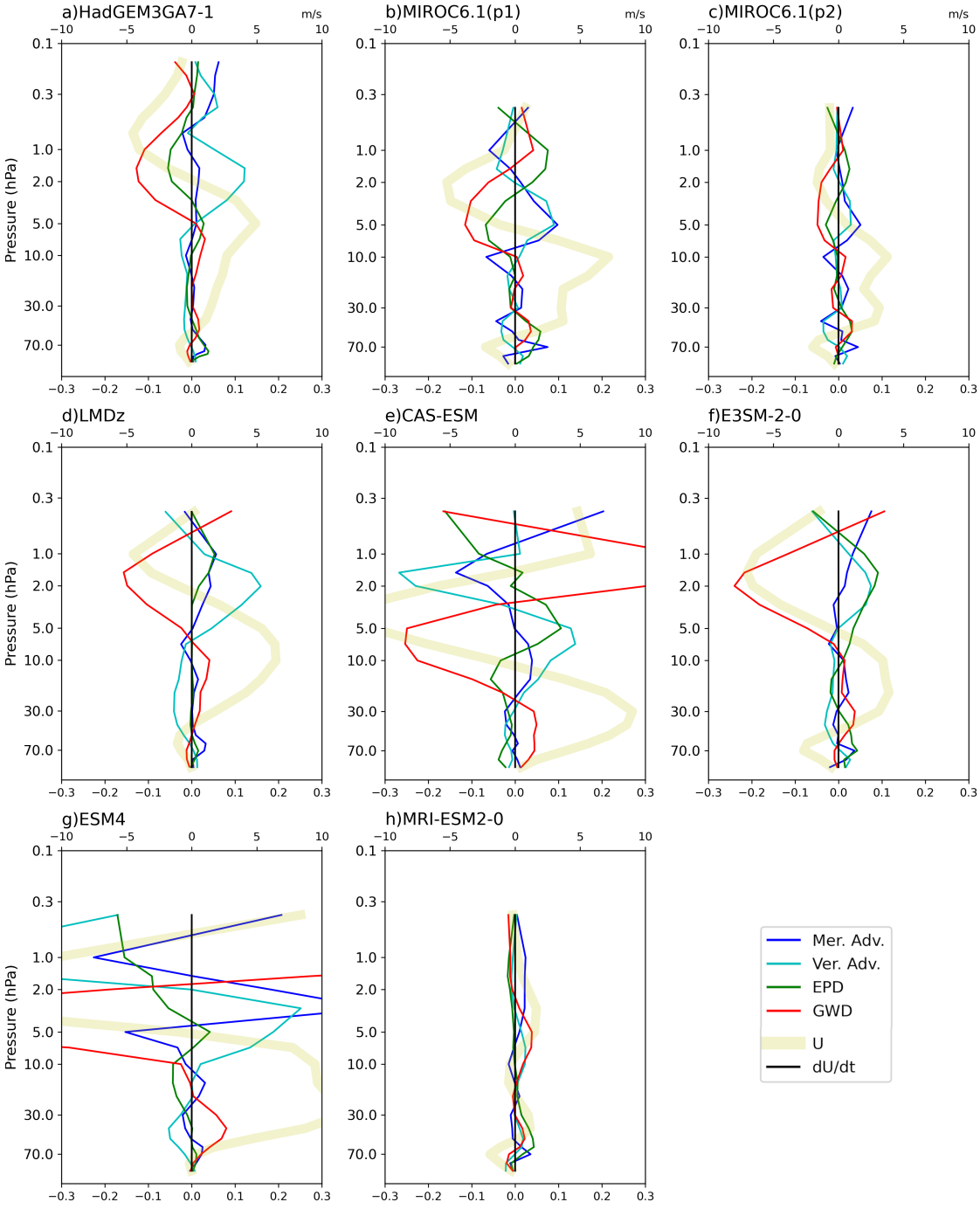

Figure 6.6: Multi-year annual mean of TEM forcing terms (see legend) and zonal-mean zonal winds ('U' thicker light-yellow line) averaged over 15°S-15°N for Control minus Nudged differences for 8 models, indicated by labels. Units of TEM forcing terms are $ms^{-1}day^{-1}$ (lower axis) and zonal-mean zonal wind is ms^{-1} (upper axis).

persist, thus the peak wind changes occur slightly above the peak GWD changes. In the Similar group models, resolved waves also exhibit increased eastward forcing, similar to GWD, but at lower SAO altitudes. In MIROC, meridional advection seems to contribute to increasing westward forcing, working alongside vertical advection to counteract the effects of GWD.

The models with the most significant changes in SAO winds, CAS-ESM, ESM4, and E3SM2, are also associated with the largest changes in forcing terms. While GWD remains the dominant term, other terms exhibit substantial changes as well. In these models, the GWD changes in the QBO region, particularly between 100 and 30 hPa, are notably large as well. This excess GWD, which propagates to SAO altitudes, can lead to considerable wind changes due to the lower air density at those heights. MRI, as expected, shows the least changes in forcing terms.

The comparison of TEM diagnostics in all the models suggests that the result from HadGEM3, indicating that GWD is the TEM forcing term affected the most by the nudging, is robust across all the models where a strong change in SAO winds is observed. Hence, the GWD profile in each model is explored further.

Figures 6.7 and 6.8 display the climatology of GWD, plotted as time of year versus height. These figures are organized similarly to the zonal-mean zonal wind climatology figures (see figures 6.1, 6.2), with the Similar group models shown in Figure 6.7 and the Distinct group models in Figure 6.8.

In the Similar group models, all exhibit strong eastward GWD forcing at altitudes above 2 hPa, and the maximum forcing is at the uppermost levels. The eastward GWD forcing in the Control and Nudged runs is strongest prior to the onset of the SAOW (refer to Figure 6.1). Figure 6.7c, f, i and l showing the difference between Control and Nudged runs reveal that at altitudes where the SAO westerly winds increased (as shown in Figure 6.1), there is a corresponding increase in eastward GWD or a decrease in westward GWD.

In the Distinct group models (figure 6.8), CAS-ESM, E3SM2 and ESM4 exhibit a distinct GWD pattern compared to all other models. While the GWD eastward forcing is comparable to that in other models, the westward GWD forcing in

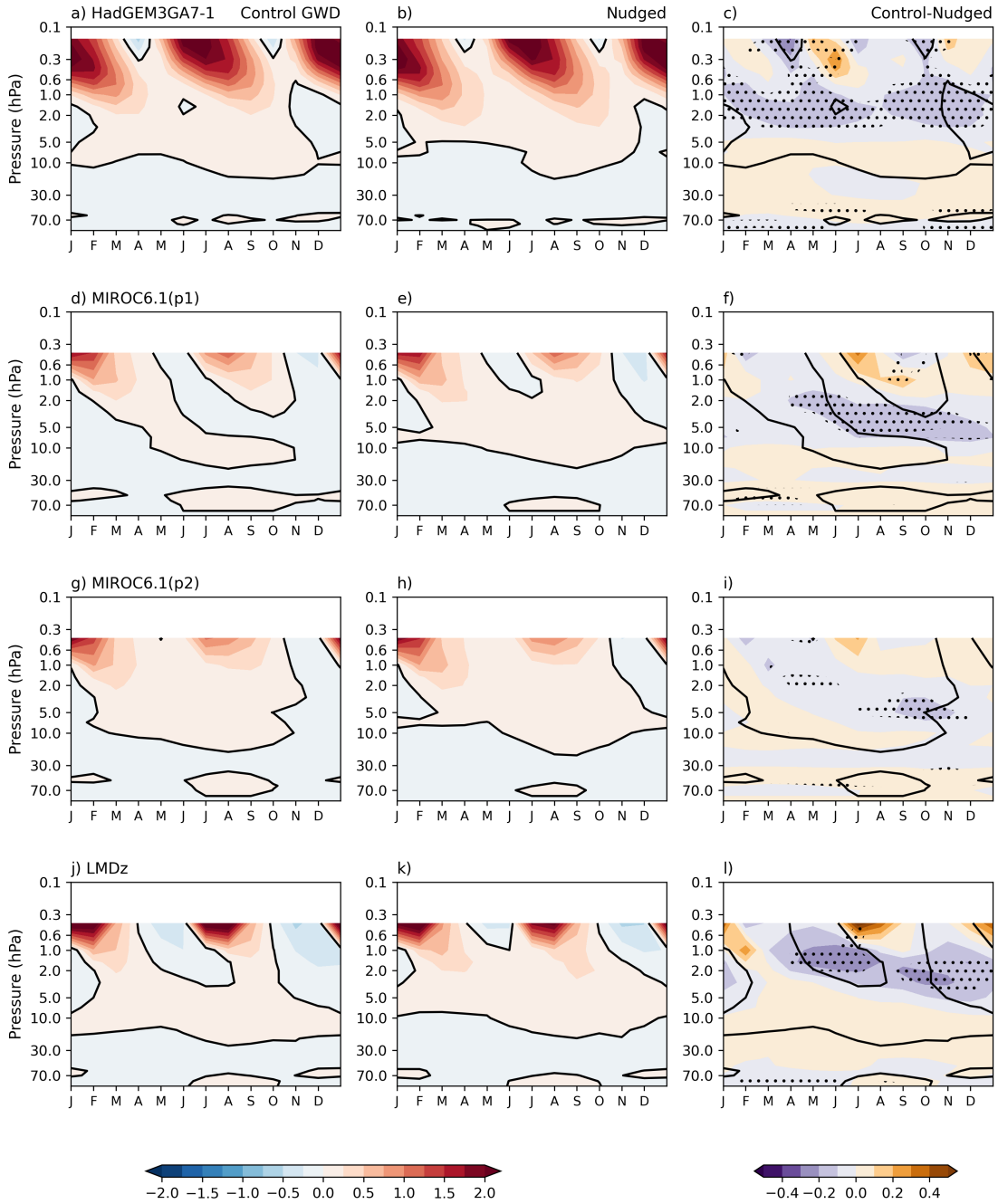

Figure 6.7: Daily mean climatology of zonal-mean non-orographic gravity wave drag ($ms^{-1}day^{-1}$) averaged over 15°N to 15°S for Control ensemble-mean, Nudged ensemble-mean and Control minus Nudged differences respectively in (a-c) HadGEM3, (d-f) MIROC6.1(p1), (g-i) MIROC6.1(p2) and (j-l) LMDz. Contour of 0 $ms^{-1}day^{-1}$ is overlaid. Overlaid in c, f, i and l is the GWD contour from the Control ensemble-mean 0 $ms^{-1}day^{-1}$. Stippling denotes 95% confidence interval.

these models is also quite strong. Examining the meridional advection profile (see figure A3), which typically contributes significantly to the SAOE, reveals that it peaks above 1 hPa. However, the SAO easterly phase itself peaks closer to 2 hPa in these models (see figure 6.2). The prominent peak of westward GWD at these altitudes (around 2hPa) indicates that, in these models, GWD is a major driver of the easterly phase.

The strong westward GWD at SAO altitudes in CAS-ESM, E3SM2 and ESM4 is likely linked to the highly biased QBO in these models. E3SM2, which lacks QBO variability in the Control run, allows westward waves to propagate higher due to the absence of critical level filtering at QBO altitudes. In the Nudged run, it is clear that the westward GWD at SAO altitudes in this model is reduced (Figure 6.8e), leading to weaker easterly SAO winds in the model (Figure 6.2e). Conversely, CAS-ESM and ESM4 have strong westerly winds in the QBO region, potentially facilitating more westward waves reaching the SAO altitudes. However, nudging does not reduce this westward GWD magnitude, instead the altitude of wave forcing has shifted. The eastward wave forcing has shifted to lower SAO altitudes in these models, while the forcing above 2hPa became more westward. Notably, ESM4 demonstrates continuous eastward forcing between 10hPa and 2hPa throughout the year in the Nudged run (figure 6.8h), corresponding with the model's persistent westerly winds. Overall, the pattern of GWD changes aligns closely with wind changes in these models. MRI has a similar GWD profile as the Similar group models in the Control and Nudged runs. The pattern of GWD changes in all the models discussed here matches very well with the changes in zonal-mean zonal wind shown in figures 6.1 and 6.2.

The time height profile of climatology of the remaining TEM diagnostics (meridional advection, vertical advection and EPD) are shown in the appendix as Figures A3, A4 and A5. A notable characteristic is in figure A3, showing the meridional advection profile, where the meridional advection in E3SM2 has stronger advection during SH winter compared to NH winter. This is likely the cause of incorrect representation of the annual cycle in SAO winds in that model, mentioned

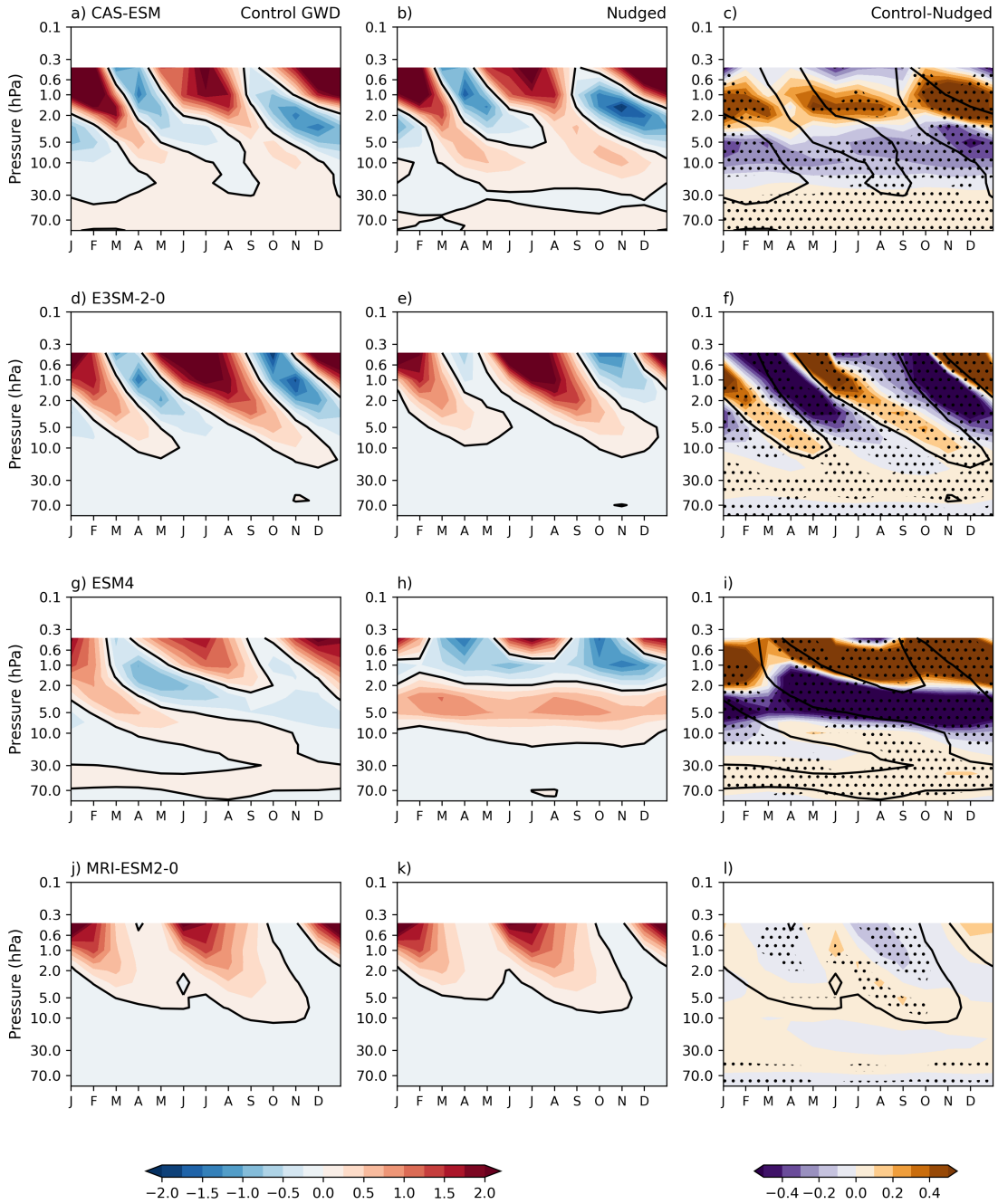

Figure 6.8: Daily mean climatology of zonal-mean non-orographic gravity wave drag ($ms^{-1}day^{-1}$) averaged over 15°N to 15°S for Control ensemble-mean, Nudged ensemble-mean and Control minus Nudged differences respectively in (a-c) CAS-ESM, (d-f) E3SM2, (g-i) EMS4 and (j-l) MRI. Contour of 0 $ms^{-1}day^{-1}$ is overlaid. Overlaid in c, f, i and l is the GWD contour from the Control ensemble-mean 0 $ms^{-1}day^{-1}$. Stippling denotes 95% confidence interval.

earlier. Planetary wave breaking is stronger in the NH winter extra-tropics, so we expect the BDC and hence the meridional advection to be stronger in NH winter. The absence of this feature in E3SM2 might be due to some incorrect representation of extra-tropical variability. Further analysis of this is outside the scope of this chapter.

6.3.3 QBO modulation of SAO

To examine the impact of the QBO on the SAO in each model, a QBO composite plot has been created, similar to the HadGEM3 QBO composite of zonal-mean zonal wind presented in Chapter 5 (see figure 5.4). In this analysis, 10 hPa is used as a reference level to define the phase of the QBO, which differs from Chapter 5 where the 5 hPa level was used in HadGEM3. The change to using the 10 hPa level was necessary because, in some models, the SAO extends further down than 5 hPa. Thus the 10 hPa winds are used as a reference to identify months when QBO winds transition from westerly to easterly. Depending on whether the transition aligns with NH or SH autumn, a 1000-day window is selected, starting either from March 1st or September 1st, and the composite is calculated.

The Control run of the Similar group models again display similar characteristics (figure 6.9 first four subfigures in leftmost column). As the QBO descends over time, the SAOW also propagates to lower altitudes. The SAOE is also modulated by the QBO, with the easterly phase magnitude peaking when the QBO westerlies are present between around 5hPa to 10hPa. From the Nudged runs of these models, (figure 6.9 first four subfigures in center column), it is evident that nudging reduces the magnitude of the QBO westerly winds, occurring around 100 to 300 days and increases the QBO easterly magnitude. In response, the SAO westerlies propagate further down, and the SAO easterlies have reduced in magnitude. This is also evident in the difference plot (figure 6.9 first four subfigures in rightmost column) as strong positive values, which further propagate downward over the time window shown. Simultaneously, a similar pattern in SAO winds emerges as negative values, indicating increased SAO westerly winds, decreased easterly winds, or SAO westerlies extending further down in altitude in the Nudged runs.

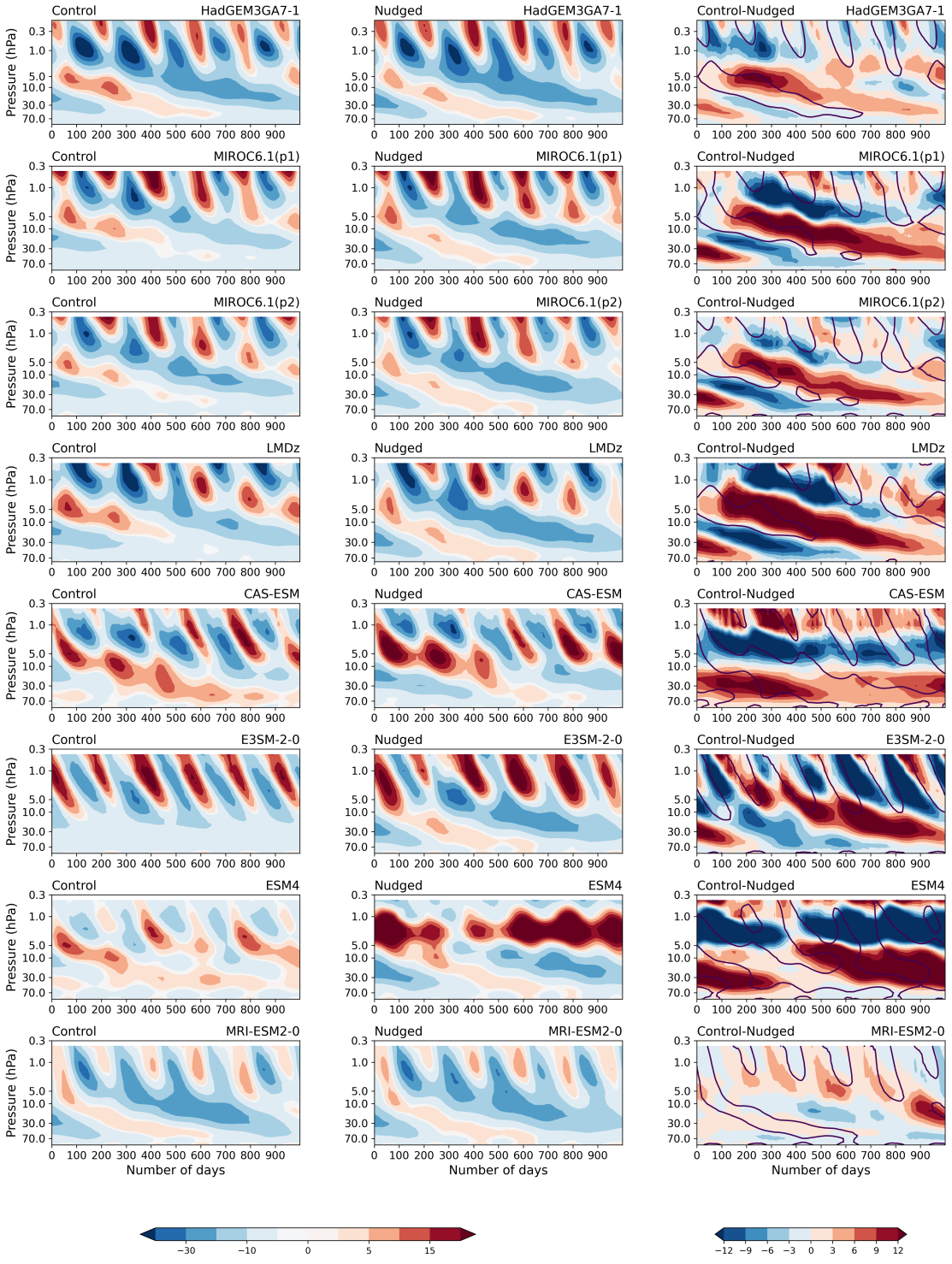

Figure 6.9: QBO composite of zonal-mean zonal wind (ms^{-1}) for the Control (left column) experiment and Nudged (middle column) experiment for 8 models, as labelled. The composite members start from 1st of March or 1st of September whichever is closest to the start of the QBOW phase. The 10hPa reference level is used to identify the start of the QBO westerly phase in the models (see text for more details). Difference (right column) between the Control and Nudged experiments, with the QBO composite winds from the Control experiment overlaid as black contours in rightmost column.

In the next three models from the Distinct group, the QBO is not very well simulated (see Control run of CAS-ESM, E3SM2 and ESM4 in figure 6.9). E3SM2 lacks QBO variability, while CAS-ESM and ESM4 have westerlies covering the QBO altitudes for most of the period shown. It is known that the QBOE phase is typically stronger than the QBOW phase, with QBO easterlies usually being nearly twice as strong as westerlies. However, the persistent presence of westerlies in the QBO region indicates that these latter two models exhibit unrealistically strong QBO westerly winds in the Control run (figure A1 confirms this westerly bias).

Due to the strong QBO biases in CAS-ESM, E3SM2 and ESM4, the nudging results in significant changes. The CAS-ESM Nudged composite indicates that model nudging is not entirely effective, as its QBO is not comparable to that of other models' Nudged simulations. In all three models, the Nudged runs (figure 6.9 second column) have stronger easterlies in the QBO altitudes compared to Control, which could lead to more eastward waves propagating to higher altitudes unfiltered. This is justified by strong eastward GWD forcing seen in figure 6.8 above the nudged region in these models. Consequently, the SAO westerlies became too strong. In the difference plot (figure 6.9 rightmost column), for CAS-ESM and ESM4, this change in winds is seen throughout the period as positive and negative values in QBO and SAO altitudes, respectively.

The final model, MRI, behaves as expected since there is little change in the QBO of MRI and hence little to no change in the SAO. The SAO in MRI is modulated by the QBO in both Control and Nudged runs but there is no improvement in the magnitude of the SAO winds.

In figure 6.10 the SAO wind dependency on each phase of QBO is explored using QBOE and QBOW monthly composites created based on 10hPa winds. The months in which the zonal-mean equatorial zonal wind (15°S to 15°N) at 10hPa are classified into QBOE and QBOW depending on whether the magnitude is negative and positive respectively. As noted in the previous section, CAS-ESM, E3SM, and ESM4 show unreliable QBO characteristics in their Control runs, either exhibiting excessive westerly winds or lacking QBO variability altogether. Therefore, these

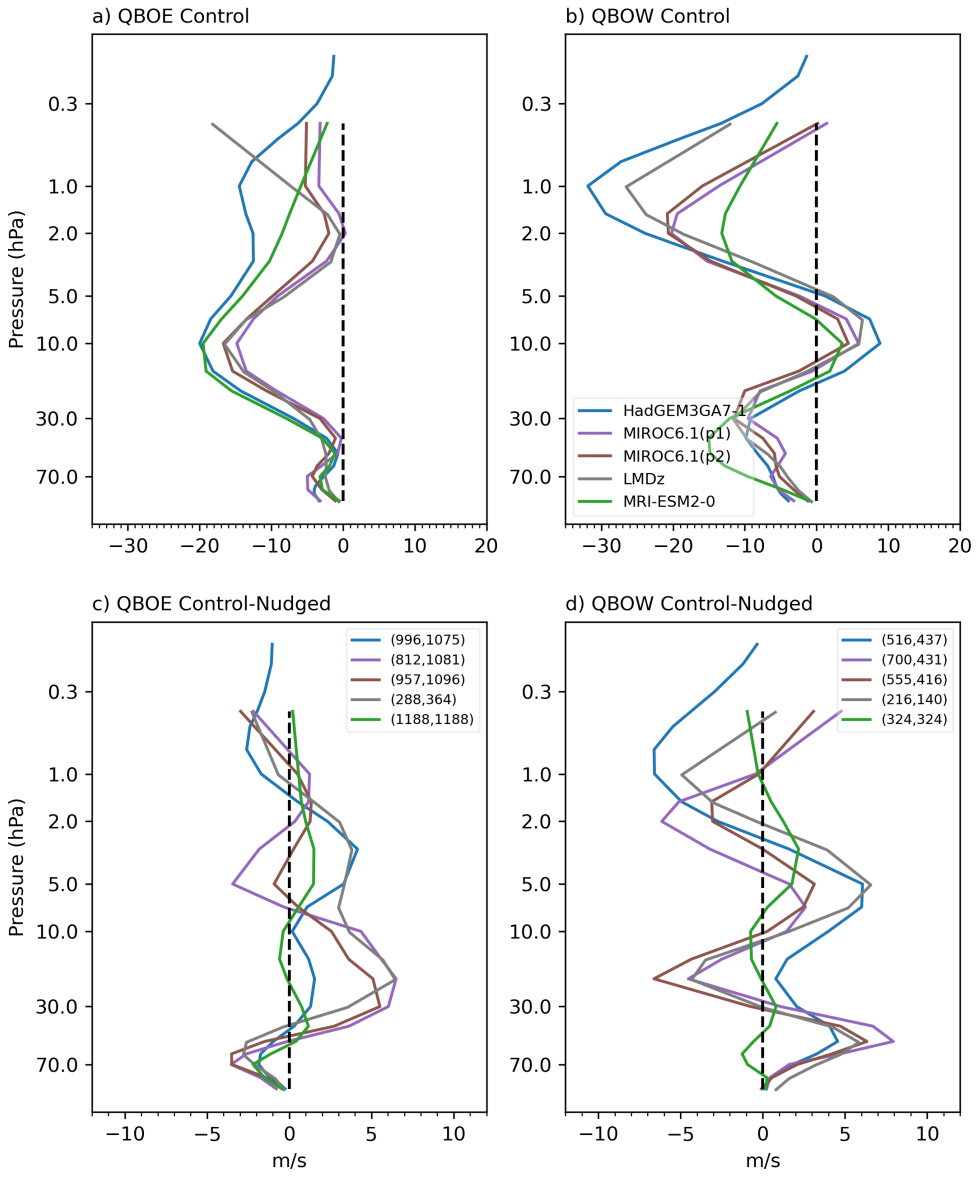

Figure 6.10: Composite of time-mean zonal-mean zonal wind averaged over 15°S-15°N for (a) Control experiment in QBOE months, (b) Control experiment in QBOW months, (c) Control minus Nudged differences during QBOE months, (d) Control minus Nudged differences during QBOW months for 5 models. The numbers in legend in (c,d) implies number of months in the composite for Control and Nudged experiment respectively. Units of zonal-mean zonal wind is ms^{-1}.

models are excluded from the analysis of QBOE and QBOW phases due to their inadequate representation of QBO phase distinctions.

In this chapter, a 10 hPa reference level is used for QBO phase analysis, different from the 50 hPa level used in Chapter 5. This change is due to some models not having QBO propagation below 50 hPa in their Control runs. Calculations show that in the Nudged runs (which are identical to the ERA5 reanalyses), the ratio of QBOE to QBOW months at 50 hPa is around 1.5. In contrast, all models except HadGEM3 and MRI have ratios higher than 3.5 in their Control runs, reaching up to 6.5 in LMDz. Therefore, 50 hPa does not effectively distinguish between QBOE and QBOW phases in most models. The 10 hPa level provides a clearer separation between the QBO phases. At this level, the ratio between QBOE and QBOW months in the Nudged runs is about 2.5, and in the Control runs it ranges from 1 to 3.5, aligning more closely with the Nudged results. Thus, the 10 hPa reference level is used for the analysis in this chapter.

Figure 6.10 a, b shows the QBOE and QBOW composite of zonal-mean zonal wind in the Control runs of all the models. The SAO winds in the QBOW composite are notably more easterly compared to the QBOE composite. This is expected, as more eastward waves are filtered during the QBOW months and more westward waves propagate to higher altitudes unaffected, resulting in an overall easterly shift in SAO winds.

Fig 6.10 c, d shows the difference between Control and Nudged run QBO composites during QBOE and QBOW months. As indicated by the difference plot, above 5 hPa the winds generally become more westerly in the Nudged runs during QBOW phase (since the Control minus Nudged difference is negative in figure 6.10d). When the QBO winds at 10hPa are westerly, the 50 hPa winds roughly have the opposite sign, and are thus in the QBOE phase. Since 50 hPa was used as reference level in chapter 5, HadGEM3 was noted to improve most during QBOE phase. When 10 hPa winds are taken as the reference, HadGEM3, like other Similar group models show maximum improvement in SAO during the QBOW phase (figure 6.10d). The models exhibit only minor changes in SAO during

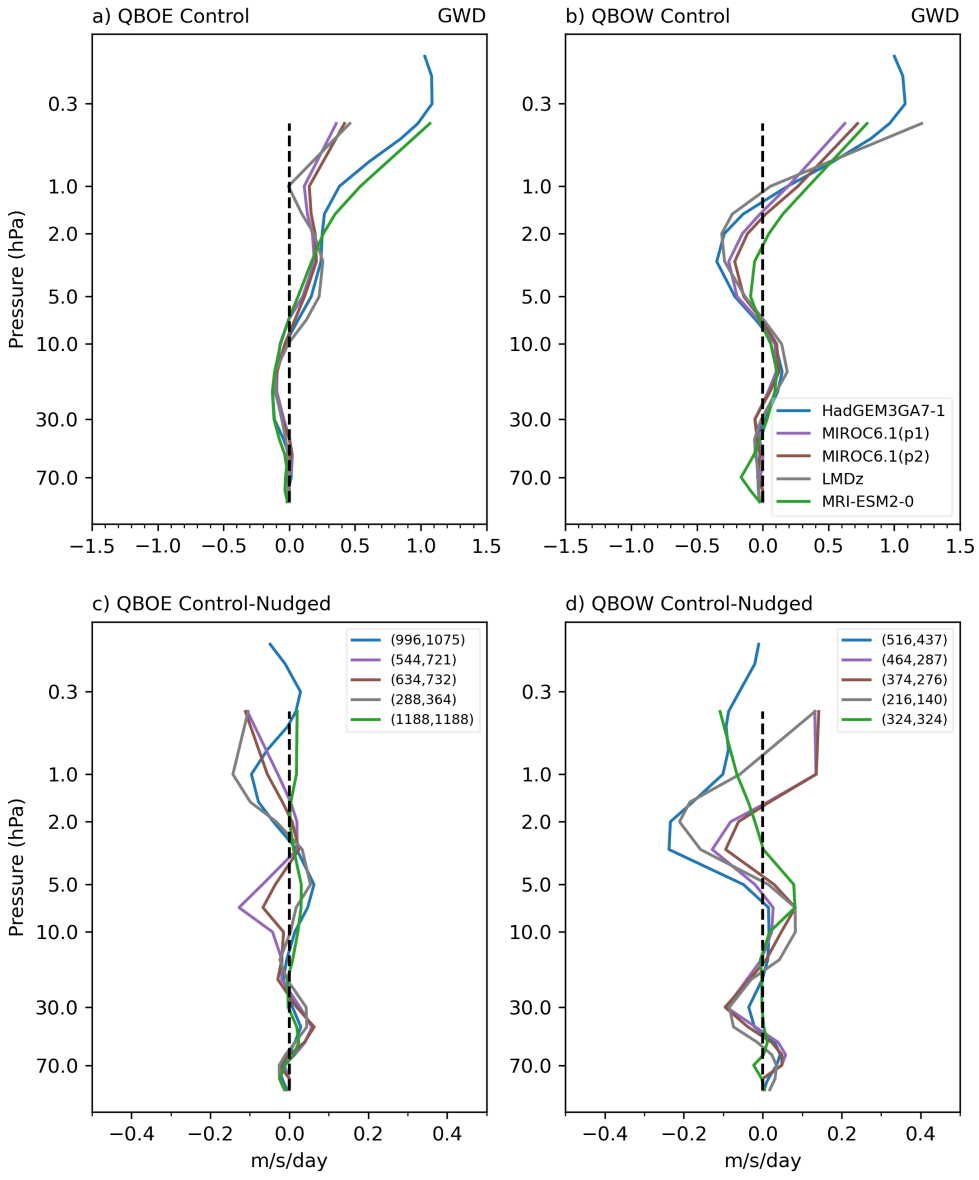

Figure 6.11: Composite of time-mean gravity wave drag averaged over 15°S-15°N for (a) Control experiment in QBOE months, (b) Control experiment in QBOW months, (c) Control minus Nudged differences during QBOE months, (d) Control minus Nudged differences during QBOW months for 5 models. The numbers in legend in (c,d) implies number of months in the composite for Control and Nudged experiment respectively. Units of gravity wave drag is $ms^{-1}day^{-1}$.

QBOE months, despite the QBO changes being of similar magnitude in both phases. MRI shows virtually no changes in either QBO phase.

All the TEM forcing terms discussed earlier were also examined using the QBO phase composite. The GWD composite is shown in figure 6.11. The Control GWD composite during each QBO phase shows pattern that can be expected from the wind profile seen in figure 6.10. During the QBOE phase the Control run has more eastward GWD forcing between 5 hPa to 1 hPa, while this region is occupied by westward GWD during the QBOW phase. This is consistent with more eastward (westward) gravity waves being filtered at critical levels when the QBO winds are westerly (easterly). Above 1 hPa, GWD is eastward during both QBO phases.

In figure 6.11c, d, the profile of Control minus Nudged difference for the GWD term closely resembles the zonal-mean zonal wind profile shown Figures 6.10c, d. During the QBOW phase, GWD above 5 hPa predominantly shifts to more eastward forcing in the Nudged runs, which aligns with the observed westerly shift in winds. MRI also shows increased eastward GWD above 1 hPa, but the zonal-mean zonal wind changes are minimal.

Similar to the GWD term, the vertical advection changes show a modulation by the QBO phases, but generally oppose the GWD forcing (figure A6). When vertical advection changes are near zero and GWD changes are still high, that is when winds change the most in the Nudged runs. EPD and meridional advection changes in most models do not show any modulation by QBO phase. The corresponding figures showing the QBO phase composite of meridional advection, vertical advection and EPD are provided in the appendix (figure A6).

6.3.4 SAO response to removal of the QBO

We have seen that models typically exhibit a westerly bias in the QBO, and when this is corrected by nudging, more eastward waves or fewer westward waves propagate to SAO altitudes, helping to alleviate the easterly bias of SAO. This raises the question of whether QBO variability itself is crucial, or if correcting the climatology in the low to mid-stratosphere could adequately address the lack of eastward waves

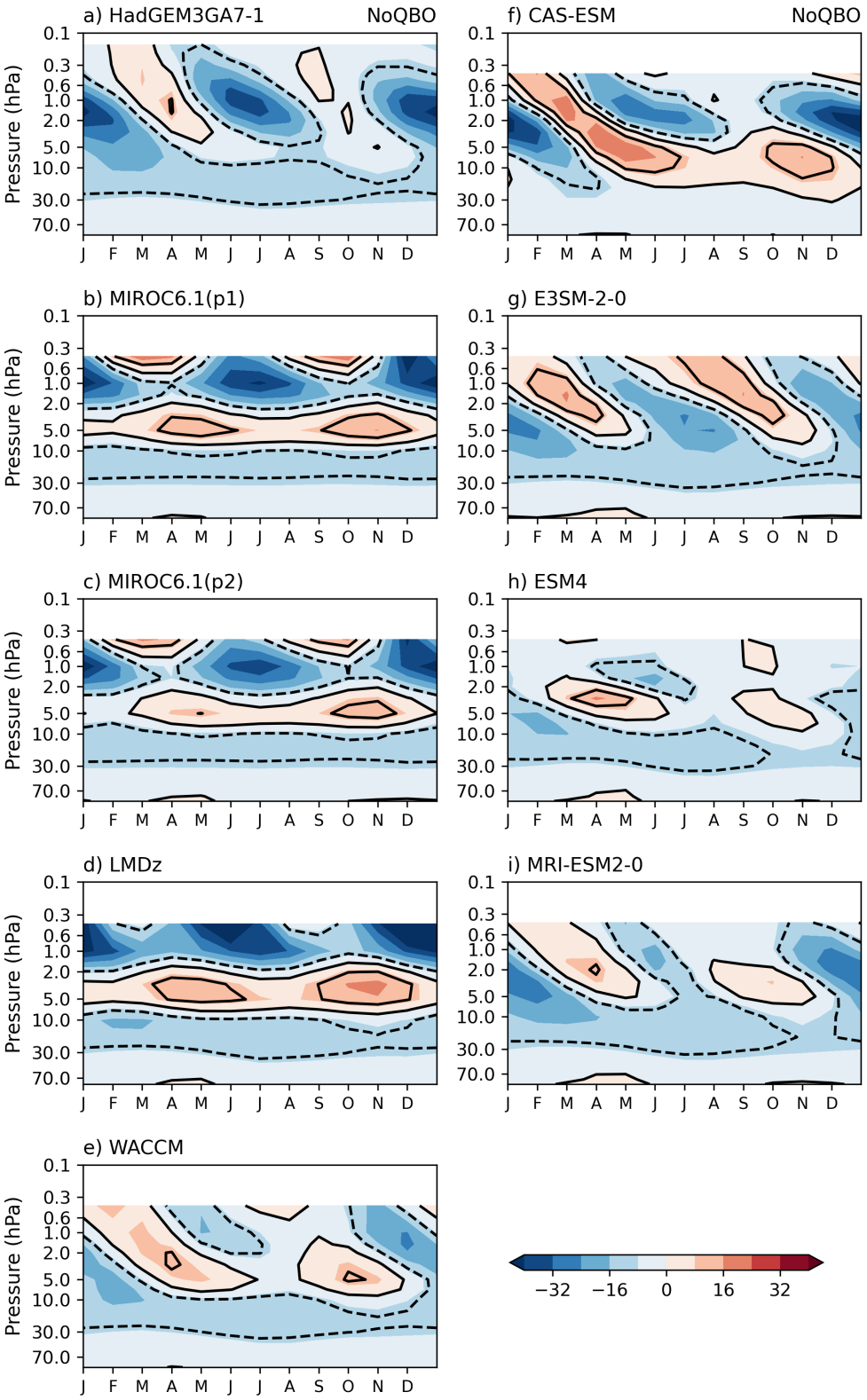

Figure 6.12: Daily mean climatology of zonal-mean zonal wind (ms^{-1}) averaged over 15°N to 15°S for NoQBO ensemble-mean for 9 models, as labelled. Contours of -10, 0, 10 ms^{-1} are overlaid, with dashed contours denoting negative values.

at SAO altitudes. To explore this, results from the NoQBO experiment described in Chapter 3 has been analysed. In this experiment, the winds at QBO altitudes were nudged toward the reanalysis zonal-mean zonal wind climatology, thereby eliminating the QBO in the low to mid-stratosphere. As QBO easterlies are generally stronger than westerlies in reanalyses and observations, the ERA5 zonal-mean zonal wind climatology, towards which the models are nudged, has weak easterlies at QBO altitudes. This should facilitate the propagation of more eastward waves to SAO altitudes. (Note that in the CAS-ESM NoQBO results this is not the case, suggesting that the nudging is not effective in the model).

Examination of the NoQBO zonal-mean zonal wind climatology (figure 6.12) indicates that SAO variability is still present, even without the presence of the QBO, but the SAO representation has not been improved. However, the models exhibit non-uniform response to the removal of the QBO. While some models show a slight increase in westerly (also in easterly in some models) wind magnitude in the NoQBO runs compared to the Control (see figure 6.1 and 6.2), half of the models lose the characteristic SAO pattern of descending westerly and easterly winds with the six-month periodicity.

Removing the QBO has removed the amplitude and depth modulation of the SAO by the QBO. A common feature in NoQBO runs of all models is that the westerlies are present farther down in altitude (see figure 6.12), and in some models, to the extent that westerly winds form a continuous jet throughout the year from 10 hPa to 2 hPa while easterly winds are confined to higher altitudes. It is possible that the effects of nudging might be causing some models (MIROC and LMDz) to have westerlies occupying altitudes from 10 hPa to 2hPa throughout the year. The eastward GWD starts acting right above 10hPa (where the strong nudging ends) in these models, probably due to sharper change in wind speed (see figure A7). This also causes stronger upwelling, preventing easterlies from propagating down. In other models, as the GWD can propagate further down till 10 hPa without encountering QBO easterlies, the increased eastward GWD is helping

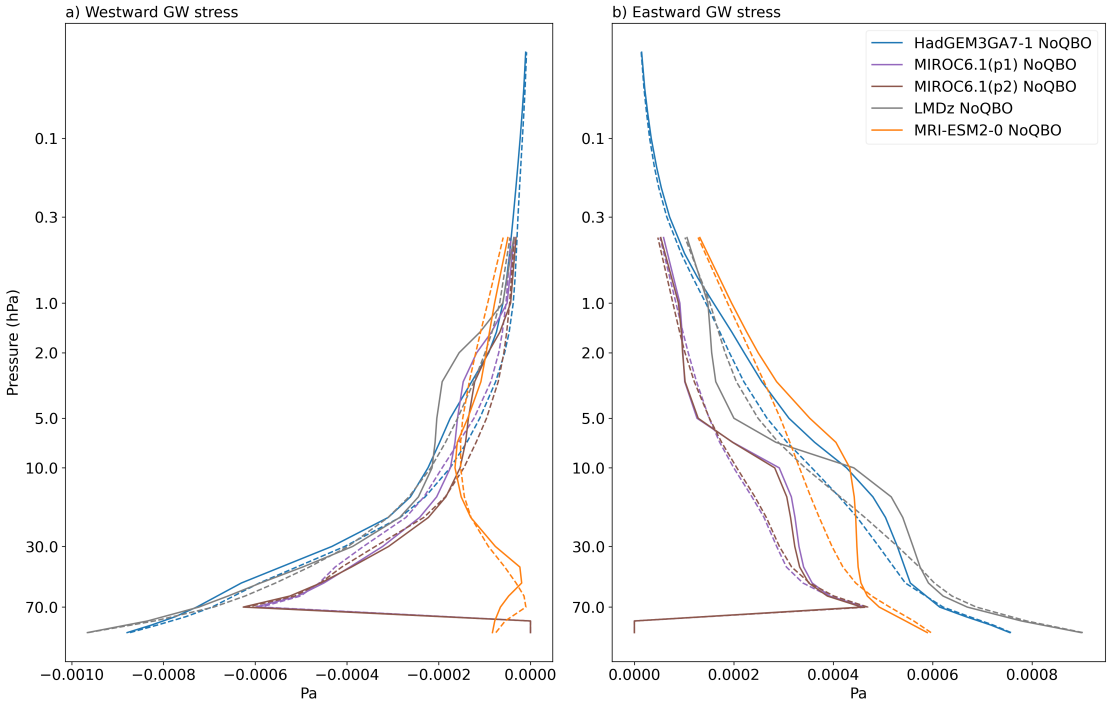

Figure 6.13: Height profiles of the multi-year climatology of equatorial (a) westward and (b) eastward gravity wave stress of the NoQBO simulations (solid line) and Control simulation (dashed line). Units are Pa.

winds to propagate farther down but without achieving the desired increase in westerly magnitude around 1 hPa.

The gravity wave stress profile of the NoQBO run (figure 6.13) confirms that eastward gravity waves propagate almost unaffected through the climatological winds in the QBO region and starts dumping momentum immediately after the nudging ceases. Compared to the Control run, the NoQBO run provides excess eastward GW flux at 10 hPa (figure 6.13). The westward gravity wave flux differences are much more subtle. In MIROC and LMDz, the westward GW flux in the NoQBO run is slightly more damped in the QBO region (around 30hPa to 10hPa) compared to the Control run, which is not the case in HadGEM3. This weaker westward GW flux and strong eastward GW flux availability at 10 hPa might be another reason for the continuous westerlies at those altitudes in MIROC and LMDz NoQBO runs seen in figure 6.12.

The easterly SAO phase, which is mainly driven by meridional advection due to the BDC, is largely unaffected by the changes at QBO altitudes (although some

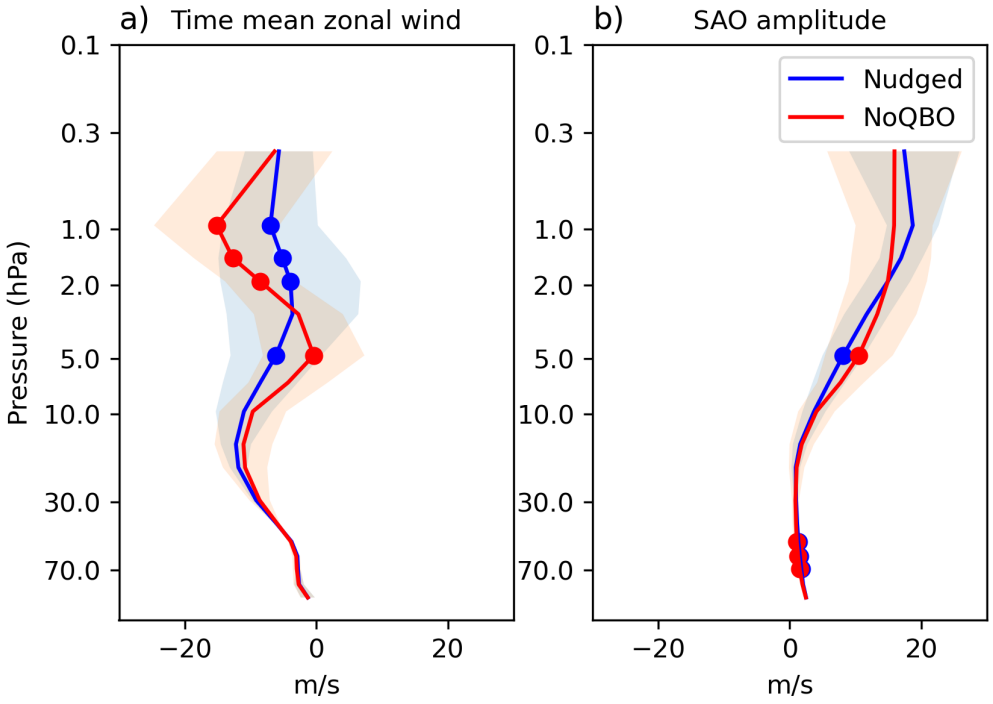

Figure 6.14: Height profiles of multi-model mean of (a) the multi-year climatology of equatorial zonal-mean zonal wind and (b) amplitude of the semi-annual component and of the NoQBO simulations (red line) and Nudged simulation (blue line). Units are ms^{-1}. The standard deviation is shown as red and blue shading. Significantly different points at 95% confidence interval is marked with red and blue dots.

small modifications by the GWD is present) so it continues to peak close to 1 hPa (i.e. at the altitude of maximum meridional advection in the Control run).

Figure 6.14 shows the change in multi-year mean of zonal-mean zonal wind and SAO amplitude in the NoQBO runs in comparison to Nudged runs. It confirms the downward shift of SAO. In the NoQBO runs the time mean wind is more westerly than the Nudged runs around at 5 hPa and has higher SAO amplitude at these altitudes. It is evident that the maximum SAO amplitude (around 2hPa and higher) in the NoQBO runs is smaller than the maximum SAO amplitude of the Nudged runs (around 1 hPa). At altitudes above 2hPa, in the NoQBO runs, the amplitude diminishes compared to the Nudged runs, and the winds become more easterly. In summary, with the removal of QBO variability in the low-mid stratosphere, none of the models achieve an improved SAO variability with stronger westerly winds around 1 hPa.

6.4 Summary

This chapter investigated whether biases in the SAO within various current climate models can be reduced when biases in the QBO are corrected. Ten models participating in the QBOi Phase 2 were analyzed. Each model had three ensembles for three experiments: the Control, Nudged, and NoQBO runs. The Control runs, in which the model was allowed to run freely, was used to assess the baseline SAO behavior. The Nudged runs, where the zonal-mean zonal winds at QBO altitude were nudged towards the ERA5 zonal-mean winds, was used to examine how the SAO is affected when the QBO is nudged. Lastly, a brief analysis of the the NoQBO runs, where the zonal-mean zonal winds at QBO altitude were nudged towards their climatological state, so that inter-annual variability including the QBO has been removed, was conducted to understand the role of climatological biases in the misrepresentation of the SAO.

As seen in QBOi phase 1 (Smith et al., 2019), all the models were found to have an easterly bias at 1 hPa when compared to reanalysis. Correcting the QBO biases generally reduced this overall SAO bias by shifting the SAO more eastward, by more than 4 ms^{-1} in more than half of the models. However, the models displayed a wide range of responses. These ranged from very minimal change in the SAO winds (MRI with 6% change) to significant alterations that led to westerly winds completely occupying the SAO altitudes (ESM4 with 406% change). Consequently, the models were grouped together to gain a clearer understanding of these varied responses.

The study identified a group of models (the Similar group) that produced similar results comparable to those of HadGEM3, as discussed in Chapter 5. These models demonstrated reasonable SAO amplitudes above 5 hPa, with alternating westerly and easterly winds peaking at altitudes higher than 1 hPa, along with a realistic annual cycle variability. In response to the QBO nudging, along with increased eastward GWD and decreased westward GWD, the SAO winds in these models became more westerly. The mean wind became more westerly by 23% to 57% compared to the Control runs in these models. The models also showed

a preference for improvement during periods when the QBO was in its westerly phase (based on 10 hPa QBO winds).

A Distinct group of models was also defined, which exhibited features deviating from those of HadGEM3 and showed extreme responses to the QBO nudging. CAS-ESM, E3SM and ESM4, part of this group, showed the most drastic changes in their Nudged runs. All three models were identified to have a highly biased QBO profile, with no QBO at all in E3SM. The SAO in these models were also suboptimal, either lacking the westerly winds in the SAO second cycle or having an incorrect annual cycle within SAO. While nudging generally shifted the SAO winds toward more westerlies, this did not consistently result in improved SAO variability. For example, in E3SM even though the westerlies increased in magnitude/duration and the easterlies reduced, the model still had an incorrect annual cycle due to incorrect representation of the BDC. The extra-tropical variability in this model needs to be studied and probably altered to achieve a better BDC. In other models, large corrections of QBO westerly bias led to excessive deposition of GWD and changes in other forcing terms at SAO altitudes, leading to unrealistic changes in the SAO winds. GWD played a crucial role in these models as well. The remaining model in the Distinct group, MRI, showed little to no response at SAO altitudes to the QBO nudging.

Analysis of the NoQBO runs indicated that removing the QBO variability does not result in an improved SAO in any of the models. While waves still propagate to SAO altitudes, the westerly winds tend to extend further downward till 10 hPa, without significantly increasing in amplitude around 1 hPa. The presence of QBO winds at altitudes above 10hPa is important to restrict the SAO westerly winds closer to the altitude where the SAO easterlies also peak. Our results suggest that correcting the QBO variability helps to shift SAO winds more westerly in most models, but in none of the models are the changes sufficient to remove the easterly bias of SAO to simulate westerly and easterly phases similar to reanalysis or observations.

Among the forcing terms, GWD is identified as a dominant contributor to improving the SAO representation in the current climate models. In current models, resolved waves have a limited impact on modifying the SAO, with parameterized waves playing the dominant role in the wave forcing term. In conclusion, along with correcting the QBO profile, the non-orographic GW spectrum in the models need to be carefully modified to achieve an SAO similar to observations. Some models might also need improvements to the extra-tropical wave forcing, since the easterly phases are also not well simulated. This chapter suggests that identifying methods to alter the non-orographic GW profile in models to improve the SAO without substantially altering the QBO profile is the next step.

Appendix

Figure A1: Zonal-mean zonal wind (ms^{-1}) averaged over 15°N to 15°S for the years 1980 to 2020 for 10 models, as labelled.

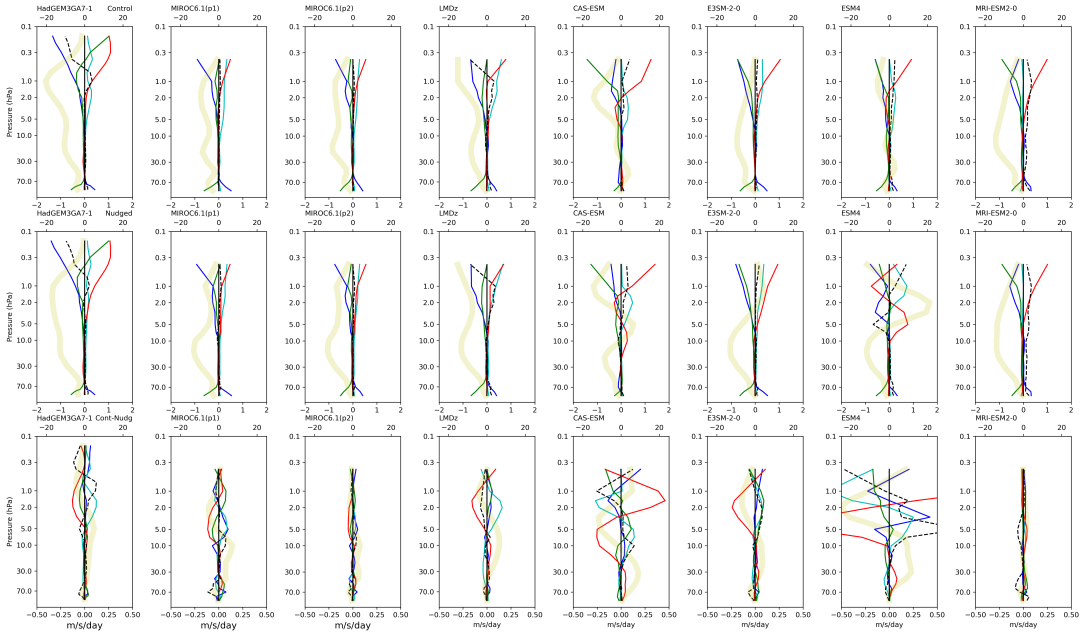

Figure A2: Multi-year time-average of TEM forcing terms (see legend) and zonal-mean zonal winds ('U' thicker light-yellow line) averaged over 15°S-15°N for Control (top row), Nudged (middle row) and Control minus Nudged differences (bottom row) for 8 models, indicated by labels. The legend is same as in figure 6.6 with dashed line showing the residual (remaining forcing term). Units of TEM forcing terms are $ms^{-1}day{-}1$ (lower axis) and zonal-mean zonal wind is ms^{-1} (upper axis).

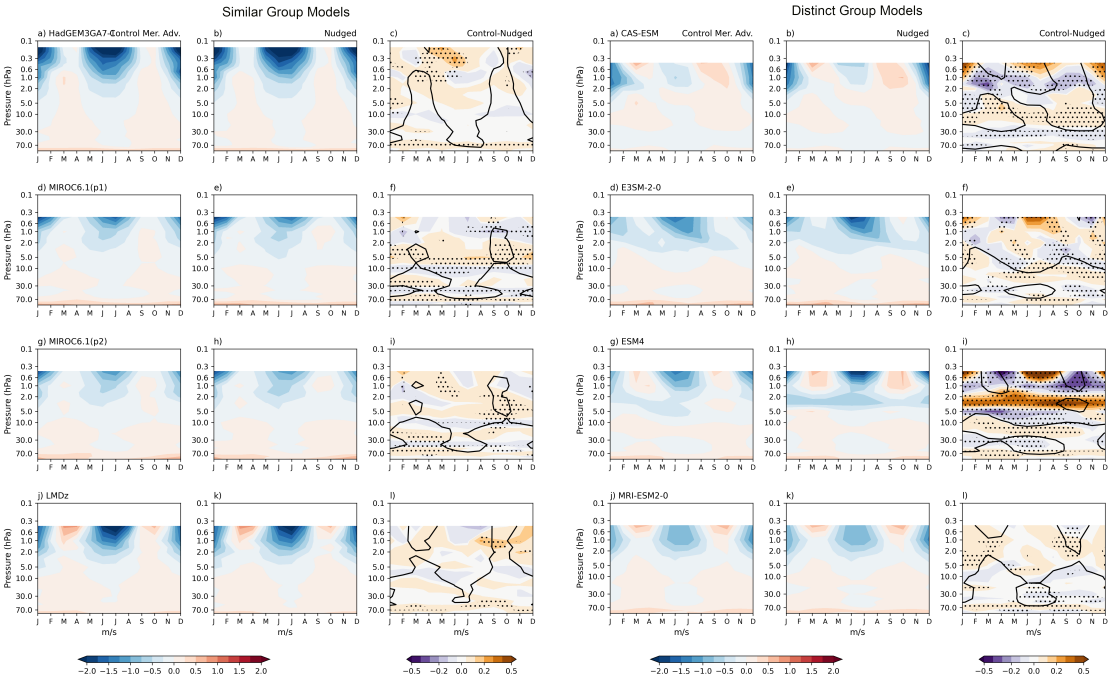

Figure A3: Daily mean climatology of zonal-mean meridional advection ($ms^{-1}day{-}1$) averaged over 15°N to 15°S for Control ensemble-mean, Nudged ensemble-mean and Control minus Nudged differences respectively in 8 models, as labelled. Overlaid in c,f,i and l are the contour from the Control ensemble-mean at $0ms^{-1}$. Stippling denotes 95% confidence interval.

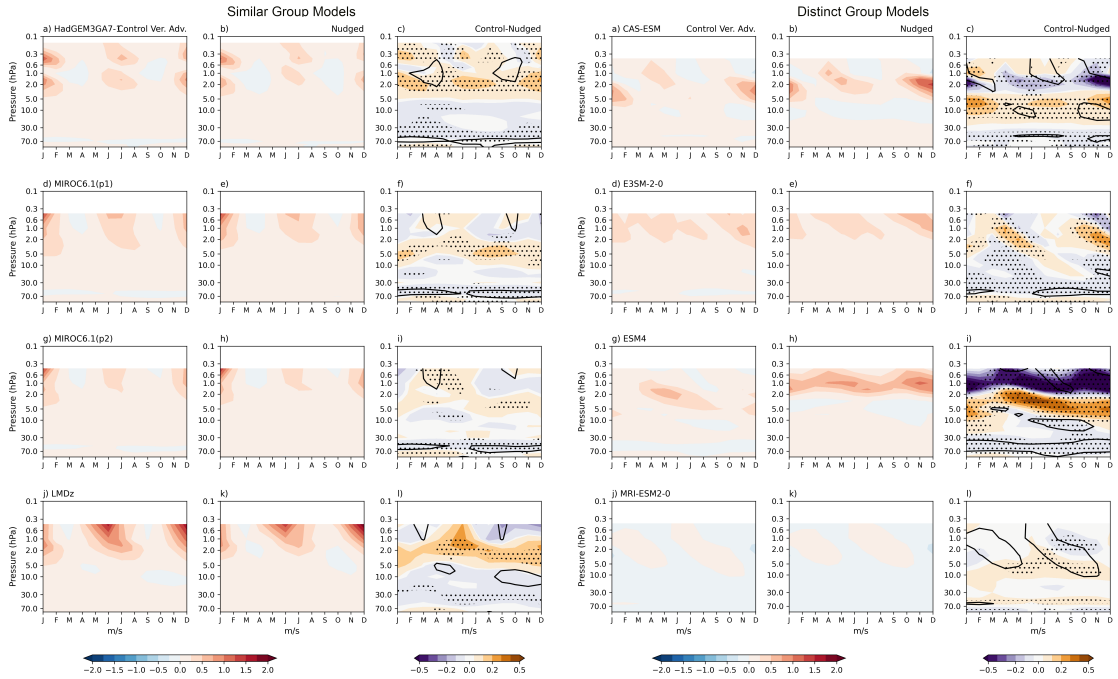

Figure A4: Daily mean climatology of zonal-mean vertical advection ($ms^{-1}day{-}1$) averaged over 15°N to 15°S for Control ensemble-mean, Nudged ensemble-mean and Control minus Nudged differences respectively in 8 models, as labelled. Overlaid in c,f,i and l are the contour from the Control ensemble-mean at $0ms^{-1}$. Stippling denotes 95% confidence interval.

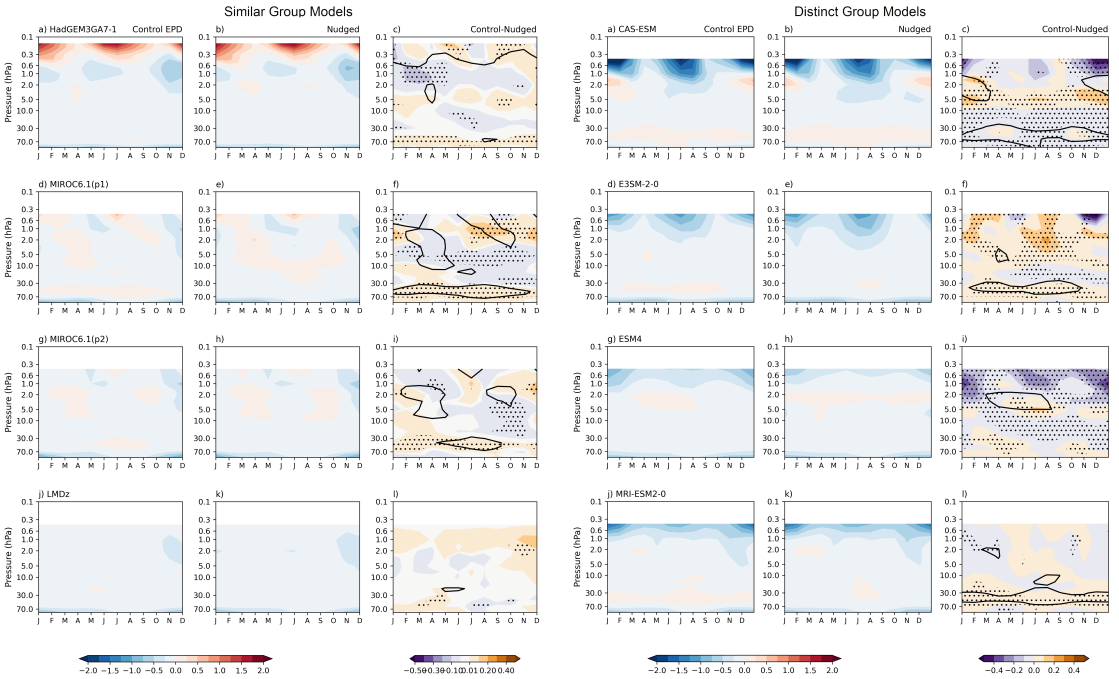

Figure A5: Daily mean climatology of zonal-mean EPD ($ms^{-1}day-1$) averaged over 15°N to 15°S for Control ensemble-mean, Nudged ensemble-mean and Control minus Nudged differences respectively in 8 models, as labelled. Overlaid in c,f,i and l are the contour from the Control ensemble-mean at $0ms^{-1}$. Stippling denotes 95% confidence interval.

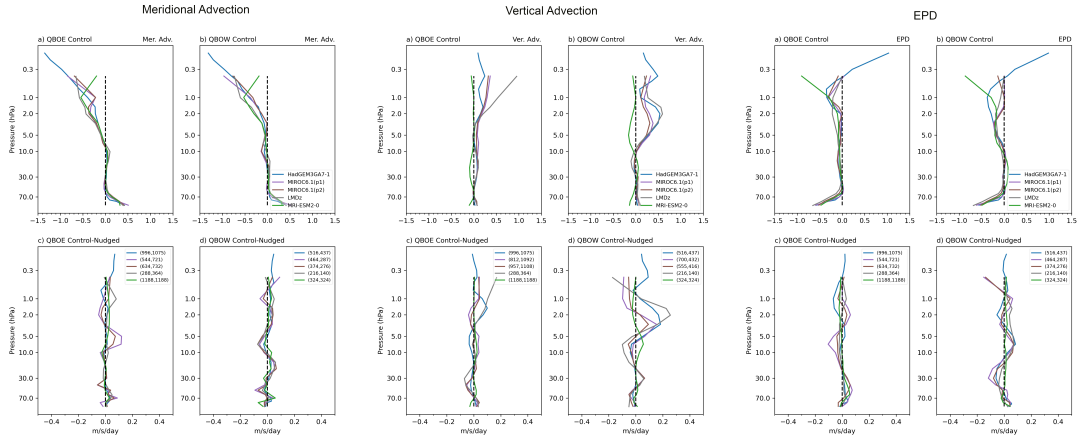

Figure A6: Composite of time-mean meridional advection, vertical advection and EPD averaged over 15S-15N for (a) Control experiment in QBOE months, (b) Control experiment in QBOW months, (c) Control minus Nudged differences during QBOE months, (d) Control minus Nudged differences during QBOW months for 5 models, as labelled. Units are $ms^{-1}day^{-1}$

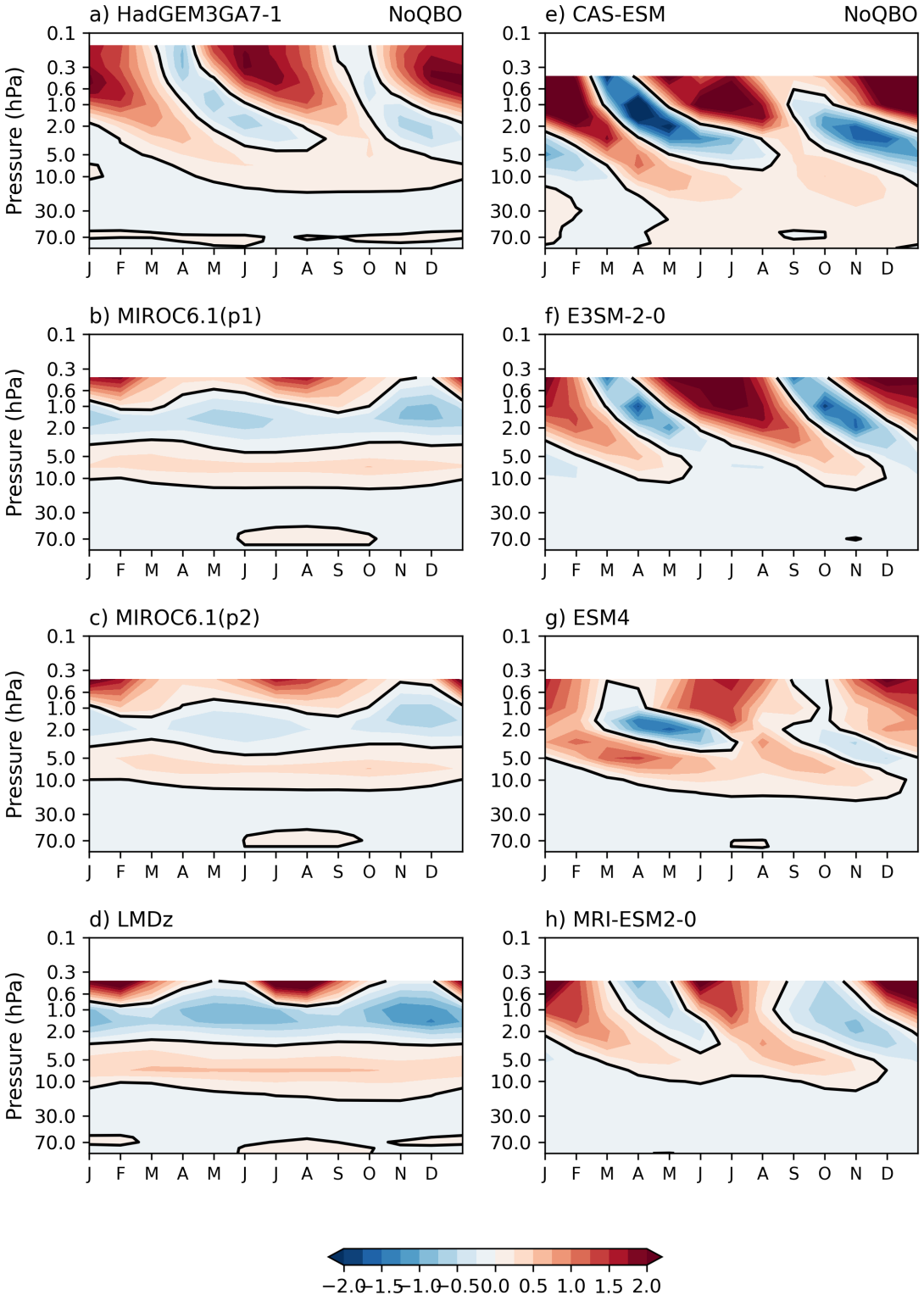

Figure A7: Daily mean climatology of GWD ($ms^{-1}day^{-1}$) averaged over 15°N to 15°S for NoQBO ensemble-mean for 8 models, as labelled. Contours of 0 $ms^{-1}day^{-1}$ are overlaid.

7 Conclusion

7.1 Summary

As we come to the end of this thesis, we revisit the key question that motivated this thesis: why do climate models show biases in the representation of the SAO? To tackle this, we outlined a series of aims in the introduction, primarily focused on understanding the factors that drive SAO variability in both climate models and reanalyses, identifying the processes misrepresented in models, and exploring potential model adjustments that could reduce these biases. To meet these aims, we used multiple present-day climate models and reanalyses, and several methods such as momentum budget analysis and model experiments throughout the thesis. The next few paragraphs summarize the main findings of this thesis, highlighting the dynamics of the SAO and its representation in climate models.

The drivers of the SAO in reanalysis: While previous studies have suggested potential mechanisms for the easterly bias in the SAO, none have examined all of the individual driving mechanisms in order to draw a definitive conclusion on the cause for the easterly bias. To address this gap, we established a reference by analyzing the contributions of individual forcing terms to the SAO in the MERRA-2 reanalysis for comparison with model data. Using TEM momentum budget analysis, we explored the four primary forcing terms: meridional advection, vertical advection, resolved

waves and parametrised gravity wave drag. Our results showed that in MERRA-2, meridional advection is the key driver of the SAO's easterly phase, while GWD plays a dominant role during the westerly phase. Vertical advection and resolved waves play a secondary role. As resolved waves help with weakening of the existing flow, the vertical advection helps to strengthen and prolong the westerly phase.

The reasons behind the easterly bias of SAO in model: With this understanding of the reanalysis data, we then explored the potential causes behind the biases observed in climate models. Using a sample climate model (CESM2-WACCM), the characteristics of biases in the SAO were identified. Weaker westerly phases, slightly stronger easterly phases (especially in the second half of the year) and a weaker annual cycle were seen in the model SAO. The biases in the westerly phase were the most pronounced with differences exceeding 30 ms^{-1} compared to reanalysis during equinox months. Comparing with the MERRA-2 forcing terms, we found that both eastward resolved equatorial waves and the parametrized effects of waves at the equator are under-represented, resulting in a weaker westerly SAO phase in WACCM. The chapter suggests that to improve the modelled SAO we need to identify methods to increase the eastward waves at SAO altitudes, such as by reducing the biases at lower altitudes (QBO region), adjusting convective parametrization to improve resolved waves, and modifying GWD parametrization.

QBO bias correction changes SAO winds up to 25% in a GCM: The documented westerly biases in the modelled QBO could impact the SAO, as the QBO winds act as a filter for waves traveling to SAO altitudes. Using nudging experiments in the HadGEM3 model that relax the modelled QBO zonal-mean zonal wind towards the reanalysis zonal-mean zonal wind, we found that correcting the QBO profile could improve the SAO winds by up to 25%. The wind changes in SAO closely coincided with, and were of similar magnitude to, the wind changes in the QBO. Further analysis revealed that most of the SAO biases occurred when the QBO winds were in the easterly phase at 50 hPa or in the westerly phase at 10 hPa (both roughly coincide). The study pointed out that the stronger QBO westerlies around 10 hPa in models and weaker easterlies at lower altitudes are

strongly influencing the SAO biases, primarily due to the changes in wave filtering as the waves propagate through the QBO region.

GWD shows the greatest variation among the forcing terms in response to QBO bias correction: With the nudging set up in HadGEM3, we explored how each of the SAO forcing terms responded to the correction of the westerly QBO bias. We found that wave forcing played a dominant role in improving the SAO profile, with meridional advection showing minimal changes in response to QBO bias corrections. The eastward GW forcing and resolved waves reaching the SAO altitudes significantly increased, while the westward GW forcing decreased. The changes in the SAO forcing terms, similar to SAO wind changes, are QBO phase dependent, with maximum changes occurring when the QBO at 50 hPa is in the easterly phase. The increased QBO easterlies at 50 hPa due to the nudging increases the westward wave filtering, while reduced QBO westerlies at 10 hPa allow more eastward waves to pass through. Thus, when the QBO is in its easterly phase at 50 hPa, the bias correction leads to more eastward and less westward GW forcing at SAO altitudes which thus reduces the SAO easterly bias. Although the experiment increased the eastward GW forcing at SAO altitudes, it did not fully eliminate the SAO biases. Since results from a single model can be limited by its dynamics and parametrizations, we conducted a multi-model analysis to ensure the robustness of our findings.

Robustness of SAO response to QBO corrections across climate models: The SAO representation in all the current climate models analyzed in this thesis suffers from an easterly bias. Although many models successfully capture the basic characteristics of the SAO, some still face difficulties. One model fails to simulate the westerly phase of the SAO entirely, while some do not accurately represent the annual cycle at SAO altitudes. In all the models a consistent response to the QBO correction was found. All the models showed a reduction in the SAO easterly bias, though the extent of improvement varied, with time-mean SAO wind changes ranging from 0.2 ms^{-1} to 16.9 ms^{-1}, depending on the corresponding QBO corrections in each model. In every case, GW forcing was found to exhibit

the largest change among the forcing terms and the peak changes occurred when the QBO winds at 10 hPa were westerly.

SAO in climate models when the QBO is removed: Finally, we explored the importance of QBO variability in the representation of the SAO in models by analyzing runs with the zonal-mean zonal winds at QBO altitudes nudged towards the long-term climatology of the reanalysis zonal-mean zonal wind, thus removing the QBO variability. Without a QBO, many models still retained an SAO but none of them show any reduction in the easterly bias of SAO. With the zonal-mean zonal wind at QBO altitudes constantly in the easterly direction (because the climatology is easterly), the eastward GW flux at SAO altitudes significantly increased. However, this increase in GW forcing only helped the SAO to propagate to lower altitudes, but not to increase in amplitude. This indicates that simply increasing the eastward gravity wave flux is not sufficient to improve the SAO. Since the SAO is primarily driven by fast waves, enhancing the representation of high-phase-speed waves in the parametrization would be a valuable future direction for improvement.

In summary, this thesis examined the SAO representation in various present-day climate models and concluded that reducing the easterly bias in the SAO requires a significant improvement in the eastward wave forcing. The experiments conducted indicated that part of this insufficient forcing strength arises from the wave filtering biases in the low-mid stratosphere. However, the analyses confirmed that this is not the only factor. The parametrization schemes themselves might need to be modified to enhance the wave forcing in the upper stratosphere.

7.2 Limitations and future work

The findings presented in this thesis have also raised a number of questions. This motivates ideas to explore in the future, a few of which are discussed here.

Lack of enough observations: Lack of enough observational data poses a major challenge in studying the SAO. Direct measurements of winds are sparse at SAO altitudes. Recently, Smith et al. (2017) calculated the geostrophic zonal-mean zonal wind from geopotential height, which is obtained using the hydrostatic relation

by integrating temperature data from satellite observations. Ern et al. (2021) also used satellite temperature data to derive a proxy for GWD. However, the existing temperature data is insufficient for calculating the TEM diagnostics, which are essential for understanding the drivers of the SAO. Thus, we had to rely on reanalysis to get a satisfactory estimate of the momentum budget of the upper stratosphere. In the future years, if direct stratospheric observations of wind become available through more satellite missions, more accurate information about the SAO forcing terms could be obtained to update the current comparisons. It is concerning that satellite direct wind measurements in the upper stratosphere and lower mesosphere are almost non-existent. Instruments such as the Microwave Limb Sounder (MLS) which looks at Doppler shift in microwave radiation by observing specific oxygen lines, and the High Resolution Doppler Imager (HRDI) which focuses on Doppler shift of emitted lights or atmospheric absorption features are used successfully to measure lower stratosphere and mesosphere and lower thermosphere winds. A focus should also be given to identify and build high sensitivity instruments that could measure upper stratospheric winds in our future missions. This could greatly help to advance the field and test some of the ideas mentioned in this thesis. Two proposed missions which would be particularly relevant, bringing new observations are CAIRAT (charting the middle atmosphere in the climate system) and STRIVE (stratosphere troposphere response using infrared vertically-resolved light explorer). These are limb sounders, so they would provide improved vertical resolution to sample waves, and the proposed measurements of temperature and trace gases could provide an improved understanding of the middle atmospheric dynamics.

Limitations of nudging methodology: The nudging in climate models is a highly useful technique and contributes to a significant part of this thesis. However, as nudging is essentially an artificial forcing, in our case applied to a specific region of the atmosphere, there could be induced effects (such as secondary circulation) that we are unaware of. Most models in our study have used nudging of the zonal-mean wind field towards the zonal-mean reanalysis winds. This has been studied in more detail in the past and is suggested to have fewer unrealistic effects in the tropics and

waves are allowed to evolve freely (Hitchcock and Haynes, 2014). The models that use full-field nudging are more likely to restrict the free evolution of waves. Also, as no studies have quantified the possible effects of full-field nudging, there could be induced processes that we are unaware of in the full-field nudged models. On the other hand, a limitation of the zonal-mean zonal wind nudging is that we are only controlling the zonally symmetric state and this prevents us from understanding the role of QBO zonal asymmetries in affecting the SAO biases. Similarly, the nudging scheme is applied uniformly through time although we know that wave forcing is sporadic, so the nudged atmosphere is less likely to evolve far away from thermal wind balance. The nudging approach may therefore under-estimate the strength and influence of QBO-induced meridional circulations. While the multi-model analyses have helped us to investigate the nudging in a range of models and get consistent results, there are still occasional outliers we struggle to understand. A future step could be to explore the effects of QBO zonal-mean zonal wind nudging and full-field nudging using the same model to compare these two techniques.

Closing of TEM momentum budget: The TEM momentum budget is expected to be self-contained in a climate model. However, we have found that this is not true for some models at SAO altitudes, where an additional residual term becomes significant. To obtain accurate results, studies have previously highlighted the relevance of calculating TEM diagnostics using high frequency data and at pressure levels as close to model levels as possible (Gerber and Manzini, 2016). As many models compute TEM online within a model at high frequencies, these should not be a problem. Some models, like EC-Earth3 have explicitly stated the Rayleigh friction and sponge layer at SAO altitudes, which might not be accounted for in the TEM diagnostics, leading to large residual terms. However, in HadGEM3 we found that the TEM budget did not close, although the reason for this was unclear. The model does not use explicit horizontal diffusion or divergence damping. The only explicit diffusion mechanisms in the model are semi-implicit off-centering and damping of the vertical velocity near the model top. Sensitivity experiments that we conducted, changing the damping altitude of vertical velocity, suggested that the

latter is not the major contributor. We found that the residual term had the profile of the second derivative (and higher orders) of zonal-mean zonal wind scaled with density. However, the origin of this is unclear and more investigation of this is needed.

Investigating physical parameters to improve the SAO: The thesis has shown that the biases in the modelled SAO are primarily due to insufficient eastward resolved wave forcing and/or eastward parametrized gravity wave forcing. Several possible routes for improvements might alleviate this lack of strong enough wave forcing in climate models, including improving model resolution, improving convection or gravity wave parametrization, and alleviating low-mid stratosphere QBO wind biases. In this thesis we explored the latter in detail, i.e. the role of QBO wind biases, and concluded that they play an important role in improving the SAO. However there remains a significant easterly bias in the SAO and further increased SAO westerlies are still required to better match the observational data. Here we briefly explore a few of the other ideas – resolution and GW parametrization - to improve the SAO representation which could be pursued further in future.

To identify GW and resolution modifications that are most likely to improve the SAO, we have conducted a few preliminary experiments using the Met Office UM and also analysed the results from some experiments that had previously been performed by Dr. Andrew Bushell (Met Office) to optimize the QBO representation.

1. Resolution

Increased resolution is a potential way forward as the increased horizontal and vertical resolution will better resolve the vertical propagation and dissipation of waves. The improved representation of vertical gradients could also help to increase the GWD forcing. The changes in horizontal and vertical resolution are explored in Dr. Bushell's runs. The runs are 20 years long. The version of UM used in the runs are different from those used elsewhere in this thesis. The version also varies among the horizontal and vertical resolution experiments as well, and has a fixed GW source (i.e. independent of precipitation). Nevertheless, it was

considered useful to analyse the results to explore possible impacts of resolution, since the simulations already existed.

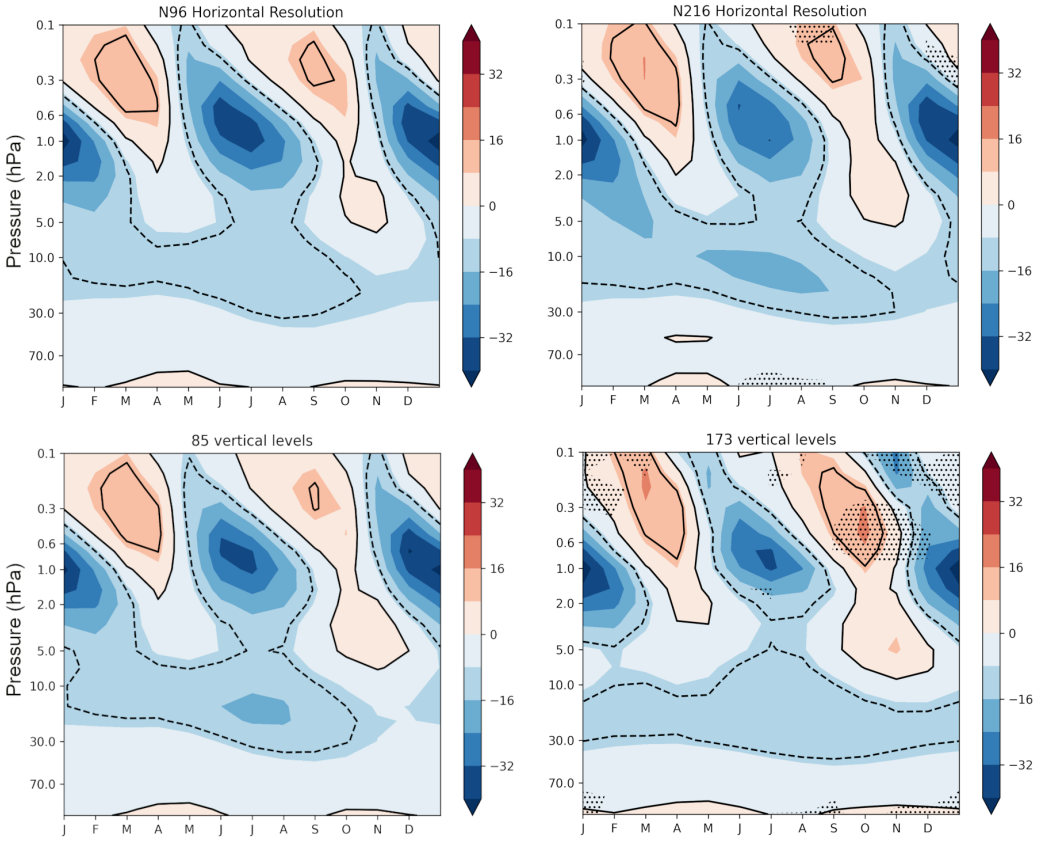

Figure 7.1: Daily mean climatology of zonal-mean zonal wind (ms^{-1}) averaged over 15°N to 15°S for UM run with horizontal resolution N96 (top left), N216 (top right), vertical resolution L85 (bottom left) and L173 (bottom right). Contours of -10, 0, 10 ms^{-1} are overlaid, with dashed contours denoting negative values. The stippling in N216 and L173 denotes significantly different regions in comparison with N96 and L85 respectively at 95% confidence interval.

An increase in horizontal resolution from N96 (1.88° x 1.25°) to N216 (0.83° x 0.56°) showed an improvement in the westerly SAO phase and a reduction in the easterly SAO phase magnitude but the regions with significant changes are minimal. Note that this experiment is just to explore the sensitivity to the horizontal resolution, as the resolution of UM used elsewhere in this thesis is already N216. The vertical resolution tests shown here were also performed at N96 horizontal resolution. An increase in vertical resolution from 85 (50 levels in the troposphere, 35 levels in the stratosphere) to 173 (102 levels in the troposphere, 71 levels in the stratosphere)

levels between the ground and 85km shows more improvement in the SAO westerly phase, especially in the second half of the year (figure 7.1) and no further increase in the easterly phase magnitude is seen, which suggests that this may be a potential direction to explore further. However, the associated costs of increasing the vertical resolution to this extent for the small changes seen does not appear to be justifiable.

2. GW parameterization experiments

Adjusting GW parametrization offers a range of possibilities to explore. GW parametrization in HadGEM3 uses a source proportional to square root of precipitation (Bushell et al., 2015). Details of the GW parametrization in the UM are provided in section 3.4.5. We analyzed experiments performed by Dr. Bushell (Met Office) varying the scaling of the amplitude of gravity waves generated by total precipitation sources. However, this did not result in satisfactory changes at SAO altitudes. Improvements to the coupling between convection and GW source flux might be needed. Increasing the amount of gravity wave flux is another option. The parameter m* denotes the vertical wavelength at which the GW flux is maximum at launch level, below which the GW flux drops drastically (see section 3.4.5). The optimized (for QBO) wavelength value of m* is currently 4.3 km. A decrease in m* would allow more waves to propagate to the upper stratosphere, resulting in an increase of both westerly and easterly phase of SAO (confirmed using an experiment by Dr. Bushell). Since the easterly phase SAO winds are already equal to or higher than the observed winds, it is not desirable to increase it further. We conducted an experiment to check if correcting the QBO bias (Nudged experiment) in a run with reduced wavelength as m* would help to improve the SAO. Both Control and Nudged experiments from chapter 5 were re-run for 10 years with m* set as 3.5 km. The SAO from this experiment is shown in figure 7.2. The stippling indicates regions of statistically significant differences when compared with the control run in chapter 5. In the control run (m*=3.5km), both westerlies and easterlies increase as expected (only easterly changes are significant in this 10-year run). The Nudged

run shows significant improvements in the westerly phase, however this is due to the QBO correction rather than changes in m*.

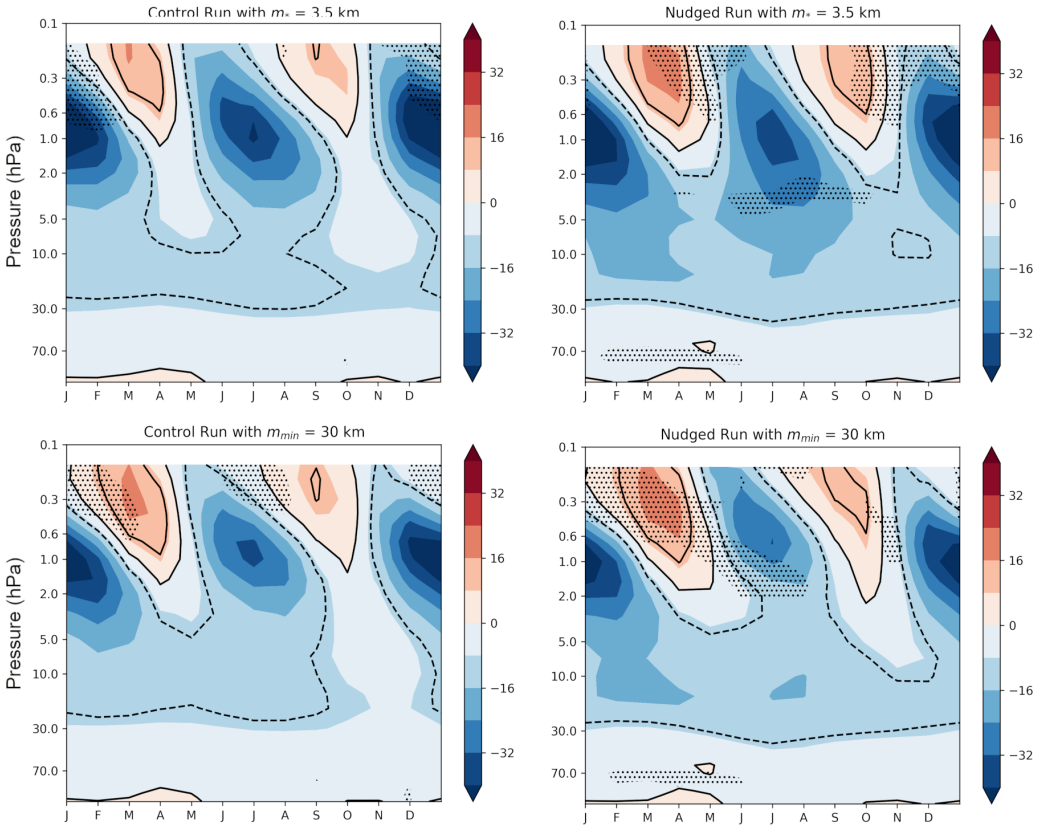

Figure 7.2: Daily mean climatology of zonal-mean zonal wind (ms^{-1}) averaged over 15°N to 15°S for UM Control run with m* 3.5 km (top left), Nudged run with m* 3.5 km (top right), Control run with m_{min} 30 km (bottom left) and Nudged run with m_{min} 30 km (bottom right). Contours of -10, 0, 10 ms^{-1} are overlaid, with dashed contours denoting negative values. The stippling denotes significantly different regions in comparison with Control run in Figure 5.1 at 95% confidence interval.

Refining the GW parameterization scheme to allow more high phase speed waves is another possible solution. This is crucial, as high phase speed waves are known to survive the filtering at lower altitudes and reach the SAO altitudes. The variable m_{min} which decides the cutoff wavelength of the GW flux spectra can be increased, hence allowing larger wavelengths and higher phase speed waves. The generally used value in HadGEM3 is 20 km. We have increased this to 30 km in the HadGEM3 version used in QBOi runs without changing any other parameters. Both control and nudged experiment from chapter 5 were re-run for 10 years with m_{min} set as 30 km.

The resulted SAO is shown in figure 7.2. The control run with the new m_{min} shows clear improvements with stronger westerlies and weaker easterlies. The Nudged run with new m_{min} shows a further improvement in the westerly phase magnitude in the second half of the year and reduced easterlies, thus improving the annual cycle. These are promising preliminary results suggesting that adjusting m_{min} has the potential to improve the SAO. However, it is important to ensure that this approach does not significantly alter the representation of other variabilities, such as the amplitude and period of the QBO. The right balance between changes in the QBO and SAO need to be found so that the representation of both can be optimized.

Another important aspect we have not explored in this thesis is how extra-tropical variability responds to the changes in SAO. Various previous studies (Gray, 2003; Gray et al., 2004, 2022) have shown that the SAO could influence polar vortex variability in winter, including SSWs (especially the time of their occurrence). Analyzing the changes in SSW patterns with respect to a corrected SAO profile in models would be a compelling topic to explore.

Bibliography

Alexander, M. J. and T. J. Dunkerton, 1999: A spectral parameterization of mean-flow forcing due to breaking gravity waves. *Journal of the Atmospheric Sciences*, **56**, 4167 – 4182, doi:10.1175/1520-0469(1999)056<4167:ASPOMF>2.0.CO;2.
URL `https://journals.ametsoc.org/view/journals/atsc/56/24/1520-0469_1999_056_4167_aspomf_2.0.co_2.xml`

Allen, S. J. and R. A. Vincent, 1995: Gravity wave activity in the lower atmosphere: Seasonal and latitudinal variations. *Journal of Geophysical Research: Atmospheres*, **100**, 1327–1350, doi:https://doi.org/10.1029/94JD02688.
URL `https://agupubs.onlinelibrary.wiley.com/doi/abs/10.1029/94JD02688`

Amodei, M., S. Pawson, A. A. Scaife, U. Langematz, W. Lahoz, D. M. Li, and P. Simon, 2001: The sao and kelvin waves in the eurogrips gcms and the uk met. office analyses. *Annales Geophysicae*, **19**, 99–114, doi:10.5194/angeo-19-99-2001.
URL `https://angeo.copernicus.org/articles/19/99/2001/`

Andrews, D. G., J. R. Holton, and C. B. Leovy, 1987: Chapter 3 - basic dynamics. *Middle Atmosphere Dynamics*, D. G. Andrews, J. R. Holton, and C. B. Leovy, eds., Academic Press, volume 40 of *International Geophysics*, 113–149.

Angell, J. K. and J. Korshover, 1964: Quasi-biennial variations in temperature, total ozone, and tropopause height. *Journal of Atmospheric Sciences*, **21**, 479 – 492, doi:10.1175/1520-0469(1964)021<0479:QBVITT>2.0.CO;2.
URL `https://journals.ametsoc.org/view/journals/atsc/21/5/1520-0469_1964_021_0479_qbvitt_2_0_co_2.xml`

Anstey, J. A. and T. G. Shepherd, 2014: High-latitude influence of the quasi-biennial oscillation. *Quarterly Journal of the Royal Meteorological Society*, **140**, 1–21, doi:https://doi.org/10.1002/qj.2132.

Anstey, J. A., I. R. Simpson, J. H. Richter, H. Naoe, M. Taguchi, F. Serva, L. J. Gray, N. Butchart, K. Hamilton, S. Osprey, O. Bellprat, P. Braesicke, A. C. Bushell, C. Cagnazzo, C.-C. Chen, H.-Y. Chun, R. R. Garcia, L. Holt, Y. Kawatani, T. Kerzenmacher, Y.-H. Kim, F. Lott, C. McLandress, J. Scinocca, T. N. Stockdale, S. Versick, S. Watanabe, K. Yoshida, and S. Yukimoto, 2022: Teleconnections of the quasi-biennial oscillation in a multi-model ensemble of qbo-resolving models. *Quarterly Journal of the Royal Meteorological Society*, **148**, 1568–1592, doi:https://doi.org/10.1002/qj.4048.
URL `https://rmets.onlinelibrary.wiley.com/doi/abs/10.1002/qj.4048`

Bacmeister, J. T. and G. L. Stephens, 2011: Spatial statistics of likely convective clouds in cloudsat data. *Journal of Geophysical Research: Atmospheres*, **116**,

doi:https://doi.org/10.1029/2010JD014444.
URL
https://agupubs.onlinelibrary.wiley.com/doi/abs/10.1029/2010JD014444

Bacmeister, J. T., M. J. Suarez, and F. R. Robertson, 2006: Rain reevaporation, boundary layer–convection interactions, and pacific rainfall patterns in an agcm. *Journal of the Atmospheric Sciences*, **63**, 3383 – 3403, doi:10.1175/JAS3791.1.
URL
https://journals.ametsoc.org/view/journals/atsc/63/12/jas3791.1.xml

Baldwin, M. P., B. Ayarzagüena, T. Birner, N. Butchart, A. H. Butler, A. J. Charlton-Perez, D. I. V. Domeisen, C. I. Garfinkel, H. Garny, E. P. Gerber, M. I. Hegglin, U. Langematz, and N. M. Pedatella, 2021: Sudden stratospheric warmings. *Reviews of Geophysics*, **59**, e2020RG000708, doi:https://doi.org/10.1029/2020RG000708, e2020RG000708 10.1029/2020RG000708.
URL
https://agupubs.onlinelibrary.wiley.com/doi/abs/10.1029/2020RG000708

Baldwin, M. P., T. Birner, G. Brasseur, J. Burrows, N. Butchart, R. Garcia, M. Geller, L. Gray, K. Hamilton, N. Harnik, M. I. Hegglin, U. Langematz, A. Robock, K. Sato, and A. A. Scaife, 2019: 100 years of progress in understanding the stratosphere and mesosphere. *Meteorological Monographs*, **59**, 27.1 – 27.62, doi:10.1175/AMSMONOGRAPHS-D-19-0003.1.
URL https://journals.ametsoc.org/view/journals/amsm/59/1/amsmonographs-d-19-0003.1.xml

Baldwin, M. P. and T. J. Dunkerton, 2001: Stratospheric harbingers of anomalous weather regimes. *Science*, **294**, 581–584, doi:10.1126/science.1063315.

Baldwin, M. P., L. J. Gray, T. J. Dunkerton, K. Hamilton, P. H. Haynes, W. J. Randel, J. R. Holton, M. J. Alexander, I. Hirota, T. Horinouchi, D. B. A. Jones, J. S. Kinnersley, C. Marquardt, K. Sato, and M. Takahashi, 2001: The quasi-biennial oscillation. *Reviews of Geophysics*, **39**, 179–229, doi:https://doi.org/10.1029/1999RG000073.

Beres, J. H., M. J. Alexander, and J. R. Holton, 2004: A method of specifying the gravity wave spectrum above convection based on latent heating properties and background wind. *Journal of the Atmospheric Sciences*, **61**, 324 – 337, doi:10.1175/1520-0469(2004)061<0324:AMOSTG>2.0.CO;2.
URL https://journals.ametsoc.org/view/journals/atsc/61/3/1520-0469_2004_061_0324_amostg_2.0.co_2.xml

Beres, J. H., R. R. Garcia, B. A. Boville, and F. Sassi, 2005: Implementation of a gravity wave source spectrum parameterization dependent on the properties of convection in the whole atmosphere community climate model (waccm). *Journal of Geophysical Research: Atmospheres*, **110**, doi:https://doi.org/10.1029/2004JD005504.
URL
https://agupubs.onlinelibrary.wiley.com/doi/abs/10.1029/2004JD005504

Bosilovich, M. G., R. Lucchesi, and M. Suarez, 2015: Merra-2: File specification. Technical report.

Burrage, M. D., R. A. Vincent, H. G. Mayr, W. R. Skinner, N. F. Arnold, and P. B. Hays, 1996: Long-term variability in the equatorial middle atmosphere zonal wind. *Journal of Geophysical Research: Atmospheres*, **101**, 12847–12854, doi:https://doi.org/10.1029/96JD00575.
URL https://agupubs.onlinelibrary.wiley.com/doi/abs/10.1029/96JD00575

Bushell, A. C., J. A. Anstey, N. Butchart, Y. Kawatani, S. M. Osprey, J. H. Richter, F. Serva, P. Braesicke, C. Cagnazzo, C.-C. Chen, H.-Y. Chun, R. R. Garcia, L. J. Gray, K. Hamilton, T. Kerzenmacher, Y.-H. Kim, F. Lott, C. McLandress, H. Naoe, J. Scinocca, A. K. Smith, T. N. Stockdale, S. Versick, S. Watanabe, K. Yoshida, and S. Yukimoto, 2022: Evaluation of the quasi-biennial oscillation in global climate models for the sparc qbo-initiative. *Quarterly Journal of the Royal Meteorological Society*, **148**, 1459–1489, doi:https://doi.org/10.1002/qj.3765.
URL https://rmets.onlinelibrary.wiley.com/doi/abs/10.1002/qj.3765

Bushell, A. C., N. Butchart, S. H. Derbyshire, D. R. Jackson, G. J. Shutts, S. B. Vosper, and S. Webster, 2015: Parameterized gravity wave momentum fluxes from sources related to convection and large-scale precipitation processes in a global atmosphere model. *Journal of the Atmospheric Sciences*, **72**, 4349 – 4371, doi:10.1175/JAS-D-15-0022.1.
URL https://journals.ametsoc.org/view/journals/atsc/72/11/jas-d-15-0022.1.xml

Butchart, N., 2022: The stratosphere: a review of the dynamics and variability. *Weather and Climate Dynamics*, **3**, 1237–1272, doi:10.5194/wcd-3-1237-2022.
URL https://wcd.copernicus.org/articles/3/1237/2022/

Butchart, N., M. B. Andrews, and C. D. Jones, 2023: Qbo phase synchronization in cmip6 historical simulations attributed to ozone forcing. *Geophysical Research Letters*, **50**, e2023GL104401, doi:https://doi.org/10.1029/2023GL104401, e2023GL104401 2023GL104401.
URL https://agupubs.onlinelibrary.wiley.com/doi/abs/10.1029/2023GL104401

Butchart, N., J. A. Anstey, K. Hamilton, S. Osprey, C. McLandress, A. C. Bushell, Y. Kawatani, Y.-H. Kim, F. Lott, J. Scinocca, T. N. Stockdale, M. Andrews, O. Bellprat, P. Braesicke, C. Cagnazzo, C.-C. Chen, H.-Y. Chun, M. Dobrynin, R. R. Garcia, J. Garcia-Serrano, L. J. Gray, L. Holt, T. Kerzenmacher, H. Naoe, H. Pohlmann, J. H. Richter, A. A. Scaife, V. Schenzinger, F. Serva, S. Versick, S. Watanabe, K. Yoshida, and S. Yukimoto, 2018: Overview of experiment design and comparison of models participating in phase 1 of the sparc quasi-biennial oscillation initiative (qboi). *Geoscientific Model Development*, **11**, 1009–1032, doi:10.5194/gmd-11-1009-2018.
URL https://gmd.copernicus.org/articles/11/1009/2018/

Butler, A. H., A. Arribas, M. Athanassiadou, J. Baehr, N. Calvo, A. Charlton-Perez, M. Déqué, D. I. Domeisen, K. Fröhlich, H. Hendon, et al., 2016: The climate-system historical forecast project: do stratosphere-resolving models make better seasonal climate predictions in boreal winter? *Quarterly Journal of the Royal Meteorological Society*, **142**, 1413–1427.

Calvo, N., M. A. Giorgetta, and C. Peña-Ortiz, 2007: Sensitivity of the boreal winter circulation in the middle atmosphere to the quasi-biennial oscillation in maecham5 simulations. *Journal of Geophysical Research: Atmospheres*, **112**, doi:https://doi.org/10.1029/2006JD007844.
URL
https://agupubs.onlinelibrary.wiley.com/doi/abs/10.1029/2006JD007844

Charney, J. G. and P. G. Drazin, 1961: Propagation of planetary-scale disturbances from the lower into the upper atmosphere. *Journal of Geophysical Research (1896-1977)*, **66**, 83–109, doi:https://doi.org/10.1029/JZ066i001p00083.
URL
https://agupubs.onlinelibrary.wiley.com/doi/abs/10.1029/JZ066i001p00083

Charney, J. G. and M. E. Stern, 1962: On the stability of internal baroclinic jets in a rotating atmosphere. *Journal of Atmospheric Sciences*, **19**, 159 – 172, doi:10.1175/1520-0469(1962)019<0159:OTSOIB>2.0.CO;2.
URL https://journals.ametsoc.org/view/journals/atsc/19/2/1520-0469_1962_019_0159_otsoib_2_0_co_2.xml

Charron, M. and E. Manzini, 2002: Gravity waves from fronts: Parameterization and middle atmosphere response in a general circulation model. *Journal of the Atmospheric Sciences*, **59**, 923 – 941, doi:10.1175/1520-0469(2002)059<0923:GWFFPA>2.0.CO;2.
URL https://journals.ametsoc.org/view/journals/atsc/59/5/1520-0469_2002_059_0923_gwffpa_2.0.co_2.xml

Chipperfield, M. P. and L. J. Gray, 1992: Two-dimensional model studies of the interannual variability of trace gases in the middle atmosphere. *Journal of Geophysical Research: Atmospheres*, **97**, 5963–5980, doi:https://doi.org/10.1029/92JD00029.
URL https://agupubs.onlinelibrary.wiley.com/doi/abs/10.1029/92JD00029

Chou, M.-D. and M. J. Suarez, 1994: An efficient thermal infrared radiation parameterization for use in general circulation models.

— 1999: A solar radiation parameterization for atmospheric studies. Technical report.

Cullather, R. I., S. M. J. Nowicki, B. Zhao, and M. J. Suarez, 2014: Evaluation of the surface representation of the greenland ice sheet in a general circulation model. *Journal of Climate*, **27**, 4835 – 4856, doi:10.1175/JCLI-D-13-00635.1.
URL https://journals.ametsoc.org/view/journals/clim/27/13/jcli-d-13-00635.1.xml

Danabasoglu, G., J.-F. Lamarque, J. Bacmeister, D. A. Bailey, A. K. DuVivier, J. Edwards, L. K. Emmons, J. Fasullo, R. Garcia, A. Gettelman, C. Hannay, M. M. Holland, W. G. Large, P. H. Lauritzen, D. M. Lawrence, J. T. M. Lenaerts, K. Lindsay, W. H. Lipscomb, M. J. Mills, R. Neale, K. W. Oleson, B. Otto-Bliesner, A. S. Phillips, W. Sacks, S. Tilmes, L. van Kampenhout, M. Vertenstein, A. Bertini, J. Dennis, C. Deser, C. Fischer, B. Fox-Kemper, J. E. Kay, D. Kinnison, P. J. Kushner, V. E. Larson, M. C. Long, S. Mickelson, J. K. Moore, E. Nienhouse, L. Polvani, P. J. Rasch, and W. G. Strand, 2020: The community earth system model version 2 (cesm2). *Journal of Advances in Modeling Earth Systems*, **12**, e2019MS001916, doi:https://doi.org/10.1029/2019MS001916, e2019MS001916 2019MS001916.

de la Cámara, A. and F. Lott, 2015: A parameterization of gravity waves emitted by fronts and jets. *Geophysical Research Letters*, **42**, 2071–2078, doi:https://doi.org/10.1002/2015GL063298.
URL
https://agupubs.onlinelibrary.wiley.com/doi/abs/10.1002/2015GL063298

Dee, D. P., S. M. Uppala, A. J. Simmons, P. Berrisford, P. Poli, S. Kobayashi, U. Andrae, M. A. Balmaseda, G. Balsamo, P. Bauer, P. Bechtold, A. C. M. Beljaars, L. van de Berg, J. Bidlot, N. Bormann, C. Delsol, R. Dragani, M. Fuentes, A. J. Geer, L. Haimberger, S. B. Healy, H. Hersbach, E. V. Hólm, L. Isaksen, P. Kållberg, M. Köhler, M. Matricardi, A. P. McNally, B. M. Monge-Sanz, J.-J. Morcrette, B.-K. Park, C. Peubey, P. de Rosnay, C. Tavolato, J.-N. Thépaut, and F. Vitart, 2011: The era-interim reanalysis: configuration and performance of the data assimilation system. *Quarterly Journal of the Royal Meteorological Society*, **137**, 553–597, doi:https://doi.org/10.1002/qj.828.

Delisi, D. P. and T. J. Dunkerton, 1988: Seasonal variation of the semiannual oscillation. *Journal of Atmospheric Sciences*, **45**, 2772 – 2787, doi:10.1175/1520-0469(1988)045<2772:SVOTSO>2.0.CO;2.

Dewan, E. M. and R. E. Good, 1986: Saturation and the "universal" spectrum for vertical profiles of horizontal scalar winds in the atmosphere. *Journal of Geophysical Research: Atmospheres*, **91**, 2742–2748, doi:https://doi.org/10.1029/JD091iD02p02742.
URL
https://agupubs.onlinelibrary.wiley.com/doi/abs/10.1029/JD091iD02p02742

Dickinson, R. E., 1969: Theory of planetary wave-zonal flow interaction. *Journal of Atmospheric Sciences*, **26**, 73 – 81, doi:10.1175/1520-0469(1969)026<0073:TOPWZF>2.0.CO;2.

Dimdore-Miles, 2021: *Variability in the polar vortex and its interaction with the climate system*. Ph.D. thesis, University of Oxford.

Döscher, R., M. Acosta, A. Alessandri, P. Anthoni, T. Arsouze, T. Bergman, R. Bernardello, S. Boussetta, L.-P. Caron, G. Carver, M. Castrillo, F. Catalano, I. Cvijanovic, P. Davini, E. Dekker, F. J. Doblas-Reyes, D. Docquier, P. Echevarria, U. Fladrich, R. Fuentes-Franco, M. Gröger, J. v. Hardenberg, J. Hieronymus, M. P. Karami, J.-P. Keskinen, T. Koenigk, R. Makkonen, F. Massonnet, M. Ménégoz, P. A. Miller, E. Moreno-Chamarro, L. Nieradzik, T. van Noije, P. Nolan, D. O'Donnell, P. Ollinaho, G. van den Oord, P. Ortega, O. T. Prims, A. Ramos, T. Reerink, C. Rousset, Y. Ruprich-Robert, P. Le Sager, T. Schmith, R. Schrödner, F. Serva, V. Sicardi, M. Sloth Madsen, B. Smith, T. Tian, E. Tourigny, P. Uotila, M. Vancoppenolle, S. Wang, D. Wårlind, U. Willén, K. Wyser, S. Yang, X. Yepes-Arbós, and Q. Zhang, 2022: The ec-earth3 earth system model for the coupled model intercomparison project 6. *Geoscientific Model Development*, **15**, 2973–3020, doi:10.5194/gmd-15-2973-2022.
URL https://gmd.copernicus.org/articles/15/2973/2022/

Dunkerton, T., 1979: On the role of the kelvin wave in the westerly phase of the semiannual zonal wind oscillation. *Journal of Atmospheric Sciences*, **36**, 32 – 41, doi:10.1175/1520-0469(1979)036<0032:OTROTK>2.0.CO;2.

Dunkerton, T. J., 1981: On the inertial stability f the equatorial middle atmosphere. *Journal of Atmospheric Sciences*, **38**, 2354 – 2364, doi:10.1175/1520-0469(1981)038<2354:OTISFT>2.0.CO;2.

Dunkerton, T. J. and D. P. Delisi, 1997: Interaction of the quasi-biennial oscillation and stratopause semiannual oscillation. *Journal of Geophysical Research: Atmospheres*, **102**, 26107–26116, doi:https://doi.org/10.1029/96JD03678.

Ebdon, R. and R. Veryard, 1961: Fluctuations in equatorial stratospheric winds. *Nature*, **189**, 791–793.

Eliassen, A. and E. Palm, 1961: On the transfer of energy in stationary mountain waves. *Geofys. Publ.*, **22**, 1–23.

Elsbury, D., Y. Peings, and G. Magnusdottir, 2021: Cmip6 models underestimate the holton-tan effect. *Geophysical Research Letters*, **48**, e2021GL094083, doi:https://doi.org/10.1029/2021GL094083, e2021GL094083 2021GL094083. URL `https://agupubs.onlinelibrary.wiley.com/doi/abs/10.1029/2021GL094083`

Ern, M., M. Diallo, P. Preusse, M. G. Mlynczak, M. J. Schwartz, Q. Wu, and M. Riese, 2021: The semiannual oscillation (sao) in the tropical middle atmosphere and its gravity wave driving in reanalyses and satellite observations. *Atmospheric Chemistry and Physics*, **21**, 13763–13795, doi:10.5194/acp-21-13763-2021.

Ern, M., M. A. Diallo, D. Khordakova, I. Krisch, P. Preusse, O. Reitebuch, J. Ungermann, and M. Riese, 2023: The quasi-biennial oscillation (qbo) and global-scale tropical waves in aeolus wind observations, radiosonde data, and reanalyses. *Atmospheric Chemistry and Physics*, **23**, 9549–9583, doi:10.5194/acp-23-9549-2023. URL `https://acp.copernicus.org/articles/23/9549/2023/`

Ern, M. and P. Preusse, 2009: Wave fluxes of equatorial kelvin waves and qbo zonal wind forcing derived from saber and ecmwf temperature space-time spectra. *Atmospheric Chemistry and Physics*, **9**, 3957–3986, doi:10.5194/acp-9-3957-2009. URL `https://acp.copernicus.org/articles/9/3957/2009/`

Ern, M., P. Preusse, S. Kalisch, M. Kaufmann, and M. Riese, 2013: Role of gravity waves in the forcing of quasi two-day waves in the mesosphere: An observational study. *Journal of Geophysical Research: Atmospheres*, **118**, 3467–3485, doi:https://doi.org/10.1029/2012JD018208. URL `https://agupubs.onlinelibrary.wiley.com/doi/abs/10.1029/2012JD018208`

Ern, M., P. Preusse, M. Krebsbach, M. G. Mlynczak, and J. M. Russell III, 2008: Equatorial wave analysis from saber and ecmwf temperatures. *Atmospheric Chemistry and Physics*, **8**, 845–869, doi:10.5194/acp-8-845-2008. URL `https://acp.copernicus.org/articles/8/845/2008/`

Ern, M., P. Preusse, and M. Riese, 2015: Driving of the sao by gravity waves as observed from satellite. *Annales Geophysicae*, **33**, 483–504, doi:10.5194/angeo-33-483-2015. URL `https://angeo.copernicus.org/articles/33/483/2015/`

Eyring, V., S. Bony, G. A. Meehl, C. A. Senior, B. Stevens, R. J. Stouffer, and K. E. Taylor, 2016: Overview of the coupled model intercomparison project phase 6 (cmip6) experimental design and organization. *Geoscientific Model Development*, **9**, 1937–1958, doi:10.5194/gmd-9-1937-2016.

Fels, S. B., 1985: Radiative–dynamical interactions in the middle atmosphere. *Issues in Atmospheric and Oceanic Modeling*, B. Saltzman, ed., Elsevier, volume 28 of *Advances in Geophysics*, 277–300.

Fouquart, Y. and B. Bonnel, 1980: Computations of solar heating of the earth's atmosphere—a new parameterization. *Beitrage zur Physik der Atmosphare*, **53**, 35–62.

Fritts, D. C., R. C. Blanchard, and L. Coy, 1989: Gravity wave structure between 60 and 90 km inferred from space shuttle reentry data. *Journal of Atmospheric Sciences*, **46**, 423 – 434, doi:10.1175/1520-0469(1989)046<0423:GWSBAK>2.0.CO;2.
URL `https://journals.ametsoc.org/view/journals/atsc/46/3/1520-0469_1989_046_0423_gwsbak_2_0_co_2.xml`

Fritts, D. C. and W. Lu, 1993: Spectral estimates of gravity wave energy and momentum fluxes. part ii: Parameterization of wave forcing and variability. *Journal of Atmospheric Sciences*, **50**, 3695 – 3713, doi:10.1175/1520-0469(1993)050<3695:SEOGWE>2.0.CO;2.
URL `https://journals.ametsoc.org/view/journals/atsc/50/22/1520-0469_1993_050_3695_seogwe_2_0_co_2.xml`

Fritts, D. C. and T. E. Vanzandt, 1993: Spectral estimates of gravity wave energy and momentum fluxes. part i: Energy dissipation, acceleration, and constraints. *Journal of Atmospheric Sciences*, **50**, 3685 – 3694,
doi:10.1175/1520-0469(1993)050<3685:SEOGWE>2.0.CO;2.
URL `https://journals.ametsoc.org/view/journals/atsc/50/22/1520-0469_1993_050_3685_seogwe_2_0_co_2.xml`

Garcia, R., T. Dunkerton, R. Lieberman, and R. Vincent, 1997: Climatology of the semiannual oscillation of the tropical middle atmosphere. *Journal of Geophysical Research*, **102**, 26019–26032, doi:10.1029/97JD00207.

Garcia, R. R., 2000: *The Role of Equatorial Waves in the Semiannual Oscillation of The Middle Atmosphere*, American Geophysical Union (AGU). 161–176.
URL `https://agupubs.onlinelibrary.wiley.com/doi/abs/10.1029/GM123p0161`

Garcia, R. R. and B. A. Boville, 1994: "downward control" of the mean meridional circulation and temperature distribution of the polar winter stratosphere. *Journal of Atmospheric Sciences*, **51**, 2238 – 2245,
doi:https://doi.org/10.1175/1520-0469(1994)051<2238:COTMMC>2.0.CO;2.
URL `https://journals.ametsoc.org/view/journals/atsc/51/15/1520-0469_1994_051_2238_cotmmc_2_0_co_2.xml`

Garcia, R. R. and J. H. Richter, 2019: On the momentum budget of the quasi-biennial oscillation in the whole atmosphere community climate model. *Journal of the Atmospheric Sciences*, **76**, 69 – 87, doi:10.1175/JAS-D-18-0088.1.

Garcia, R. R. and F. Sassi, 1999: Modulation of the mesospheric semiannual oscillation by the quasibiennial oscillation. *Earth, planets and space*, **51**, 563–569.

Garfinkel, C. I., E. P. Gerber, O. Shamir, J. Rao, M. Jucker, I. White, and N. Paldor, 2022: A qbo cookbook: Sensitivity of the quasi-biennial oscillation to resolution, resolved waves, and parameterized gravity waves. *Journal of Advances in Modeling Earth Systems*, **14**, e2021MS002568.

Gelaro, R., W. McCarty, M. J. Suárez, R. Todling, A. Molod, L. Takacs, C. A. Randles, A. Darmenov, M. G. Bosilovich, R. Reichle, K. Wargan, L. Coy, R. Cullather, C. Draper, S. Akella, V. Buchard, A. Conaty, A. M. da Silva, W. Gu, G.-K. Kim, R. Koster, R. Lucchesi, D. Merkova, J. E. Nielsen, G. Partyka, S. Pawson, W. Putman, M. Rienecker, S. D. Schubert, M. Sienkiewicz, and B. Zhao, 2017: The modern-era retrospective analysis for research and applications, version 2 (merra-2). *Journal of Climate*, **30**, 5419 – 5454, doi:10.1175/JCLI-D-16-0758.1.

Gerber, E. P. and E. Manzini, 2016: The dynamics and variability model intercomparison project (dynvarmip) for cmip6: assessing the stratosphere–troposphere system. *Geoscientific Model Development*, **9**, 3413–3425, doi:10.5194/gmd-9-3413-2016.
URL `https://gmd.copernicus.org/articles/9/3413/2016/`

Gettelman, A., M. J. Mills, D. E. Kinnison, R. R. Garcia, A. K. Smith, D. R. Marsh, S. Tilmes, F. Vitt, C. G. Bardeen, J. McInerny, H.-L. Liu, S. C. Solomon, L. M. Polvani, L. K. Emmons, J.-F. Lamarque, J. H. Richter, A. S. Glanville, J. T. Bacmeister, A. S. Phillips, R. B. Neale, I. R. Simpson, A. K. DuVivier, A. Hodzic, and W. J. Randel, 2019: The whole atmosphere community climate model version 6 (waccm6). *Journal of Geophysical Research: Atmospheres*, **124**, 12380–12403, doi:https://doi.org/10.1029/2019JD030943.

Gill, A. E., 1980: Some simple solutions for heat-induced tropical circulation. *Quarterly Journal of the Royal Meteorological Society*, **106**, 447–462, doi:https://doi.org/10.1002/qj.49710644905.
URL `https://rmets.onlinelibrary.wiley.com/doi/abs/10.1002/qj.49710644905`

— 1982: *Atmosphere—ocean dynamics*. Academic Press, New York.

Gray, L. J., 2003: The influence of the equatorial upper stratosphere on stratospheric sudden warmings. *Geophysical Research Letters*, **30**, doi:https://doi.org/10.1029/2002GL016430.
URL `https://agupubs.onlinelibrary.wiley.com/doi/abs/10.1029/2002GL016430`

Gray, L. J., S. Crooks, C. Pascoe, S. Sparrow, and M. Palmer, 2004: Solar and qbo influences on the timing of stratospheric sudden warmings. *Journal of the Atmospheric Sciences*, **61**, 2777 – 2796, doi:https://doi.org/10.1175/JAS-3297.1.
URL `https://journals.ametsoc.org/view/journals/atsc/61/23/jas-3297.1.xml`

Gray, L. J., H. Lu, M. J. Brown, J. R. Knight, and M. B. Andrews, 2022: Mechanisms of influence of the semi-annual oscillation on stratospheric sudden warmings. *Quarterly Journal of the Royal Meteorological Society*, **148**, 1223–1241, doi:https://doi.org/10.1002/qj.4256.

Gray, L. J. and J. A. Pyle, 1986: The semi-annual oscillation and equatorial tracer distributions. *Quarterly Journal of the Royal Meteorological Society*, **112**, 387–407, doi:https://doi.org/10.1002/qj.49711247207.

Hamilton, K. and J. D. Mahlman, 1988: General circulation model simulation of the semiannual oscillation of the tropical middle atmosphere. *Journal of Atmospheric Sciences*, **45**, 3212 – 3235, doi:10.1175/1520-0469(1988)045<3212:GCMSOT>2.0.CO;2.

Hardiman, S. C., D. G. Andrews, A. A. White, N. Butchart, and I. Edmond, 2010: Using different formulations of the transformed eulerian mean equations and eliassen–palm diagnostics in general circulation models. *Journal of the Atmospheric Sciences*, **67**, 1983 – 1995, doi:10.1175/2010JAS3355.1.
URL
`https://journals.ametsoc.org/view/journals/atsc/67/6/2010jas3355.1.xml`

Hersbach, H., B. Bell, P. Berrisford, S. Hirahara, A. Horányi, J. Muñoz-Sabater, J. Nicolas, C. Peubey, R. Radu, D. Schepers, A. Simmons, C. Soci, S. Abdalla, X. Abellan, G. Balsamo, P. Bechtold, G. Biavati, J. Bidlot, M. Bonavita, G. De Chiara, P. Dahlgren, D. Dee, M. Diamantakis, R. Dragani, J. Flemming, R. Forbes, M. Fuentes, A. Geer, L. Haimberger, S. Healy, R. J. Hogan, E. Hólm, M. Janisková, S. Keeley, P. Laloyaux, P. Lopez, C. Lupu, G. Radnoti, P. de Rosnay, I. Rozum, F. Vamborg, S. Villaume, and J.-N. Thépaut, 2020: The era5 global reanalysis. *Quarterly Journal of the Royal Meteorological Society*, **146**, 1999–2049, doi:https://doi.org/10.1002/qj.3803.
URL `https://rmets.onlinelibrary.wiley.com/doi/abs/10.1002/qj.3803`

Hines, C. O., 1991: The saturation of gravity waves in the middle atmosphere. part ii: Development of doppler-spread theory. *Journal of Atmospheric Sciences*, **48**, 1361 – 1379, doi:10.1175/1520-0469(1991)048<1361:TSOGWI>2.0.CO;2.
URL `https://journals.ametsoc.org/view/journals/atsc/48/11/1520-0469_1991_048_1361_tsogwi_2_0_co_2.xml`

— 1997: Doppler-spread parameterization of gravity-wave momentum deposition in the middle atmosphere. part 2: Broad and quasi monochromatic spectra, and implementation. *Journal of Atmospheric and Solar-Terrestrial Physics*, **59**, 387–400, doi:https://doi.org/10.1016/S1364-6826(96)00080-6.
URL
`https://www.sciencedirect.com/science/article/pii/S1364682696000806`

Hirota, I., 1978: Equatorial waves in the upper stratosphere and mesosphere in relation to the semiannual oscillation of the zonal wind. *Journal of Atmospheric Sciences*, **35**, 714 – 722, doi:10.1175/1520-0469(1978)035<0714:EWITUS>2.0.CO;2.

— 1980: Observational evidence of the semiannual oscillation in the tropical middle atmosphere—a review. *pure and applied geophysics*, **118**, 217–238.

Hitchcock, P., A. Butler, A. Charlton-Perez, C. I. Garfinkel, T. Stockdale, J. Anstey, D. Mitchell, D. I. V. Domeisen, T. Wu, Y. Lu, D. Mastrangelo, P. Malguzzi, H. Lin, R. Muncaster, B. Merryfield, M. Sigmond, B. Xiang, L. Jia, Y.-K. Hyun, J. Oh, D. Specq, I. R. Simpson, J. H. Richter, C. Barton, J. Knight, E.-P. Lim, and H. Hendon, 2022: Stratospheric nudging and predictable surface impacts (snapsi): a

protocol for investigating the role of stratospheric polar vortex disturbances in subseasonal to seasonal forecasts. *Geoscientific Model Development*, **15**, 5073–5092, doi:10.5194/gmd-15-5073-2022.
URL https://gmd.copernicus.org/articles/15/5073/2022/

Hitchcock, P. and P. H. Haynes, 2014: Zonally symmetric adjustment in the presence of artificial relaxation. *Journal of the Atmospheric Sciences*, **71**, 4349 – 4368, doi:10.1175/JAS-D-14-0013.1.
URL https://journals.ametsoc.org/view/journals/atsc/71/11/jas-d-14-0013.1.xml

Hitchcock, P. and I. R. Simpson, 2014: The downward influence of stratospheric sudden warmings. *Journal of the Atmospheric Sciences*, **71**, 3856 – 3876, doi:10.1175/JAS-D-14-0012.1.
URL https://journals.ametsoc.org/view/journals/atsc/71/10/jas-d-14-0012.1.xml

Hitchman, M. H. and C. B. Leovy, 1986: Evolution of the zonal mean state in the equatorial middle atmosphere during october 1978-may 1979. *Journal of Atmospheric Sciences*, **43**, 3159 – 3176, doi:10.1175/1520-0469(1986)043<3159:EOTZMS>2.0.CO;2.

— 1988: Estimation of the kelvin wave contribution to the semiannual oscillation. *Journal of Atmospheric Sciences*, **45**, 1462 – 1475, doi:10.1175/1520-0469(1988)045<1462:EOTKWC>2.0.CO;2.

Holt, L. A., F. Lott, R. R. Garcia, G. N. Kiladis, Y.-M. Cheng, J. A. Anstey, P. Braesicke, A. C. Bushell, N. Butchart, C. Cagnazzo, C.-C. Chen, H.-Y. Chun, Y. Kawatani, T. Kerzenmacher, Y.-H. Kim, C. McLandress, H. Naoe, S. Osprey, J. H. Richter, A. A. Scaife, J. Scinocca, F. Serva, S. Versick, S. Watanabe, K. Yoshida, and S. Yukimoto, 2022: An evaluation of tropical waves and wave forcing of the qbo in the qboi models. *Quarterly Journal of the Royal Meteorological Society*, **148**, 1541–1567, doi:https://doi.org/10.1002/qj.3827.
URL https://rmets.onlinelibrary.wiley.com/doi/abs/10.1002/qj.3827

Holton, J. R., P. H. Haynes, M. E. McIntyre, A. R. Douglass, R. B. Rood, and L. Pfister, 1995: Stratosphere-troposphere exchange. *Rev. Geophys.*, **33**, 403–439.

Holton, J. R. and R. S. Lindzen, 1972: An updated theory for the quasi-biennial cycle of the tropical stratosphere. *Journal of Atmospheric Sciences*, **29**, 1076 – 1080, doi:10.1175/1520-0469(1972)029<1076:AUTFTQ>2.0.CO;2.
URL https://journals.ametsoc.org/view/journals/atsc/29/6/1520-0469_1972_029_1076_autftq_2_0_co_2.xml

Holton, J. R. and H.-C. Tan, 1980: The influence of the equatorial quasi-biennial oscillation on the global circulation at 50 mb. *Journal of Atmospheric Sciences*, **37**, 2200 – 2208, doi:10.1175/1520-0469(1980)037<2200:TIOTEQ>2.0.CO;2.

Holton, J. R. and W. M. Wehrbein, 1980: A numerical model of the zonal mean circulation of the middle atmosphere. *pure and applied geophysics*, **118**, 284–306.

Hopkins, R. H., 1975: Evidence of polar-tropical coupling in upper stratospheric zonal wind anomalies. *Journal of Atmospheric Sciences*, **32**, 712 – 719, doi:10.1175/1520-0469(1975)032<0712:EOPTCI>2.0.CO;2.

Jackson, D. R. and L. J. Gray, 1994: Simulation of the semi-annual oscillation of the equatorial middle atmosphere using the extended ugamp general circulation model. *Quarterly Journal of the Royal Meteorological Society*, **120**, 1559–1588, doi:https://doi.org/10.1002/qj.49712052007.
URL
https://rmets.onlinelibrary.wiley.com/doi/abs/10.1002/qj.49712052007

Jaison, A. M., L. J. Gray, S. Osprey, A. K. Smith, and R. R. Garcia, 2024: A momentum budget study of the semi-annual oscillation in the whole atmosphere community climate model. *Quarterly Journal of the Royal Meteorological Society*, **n/a**, doi:https://doi.org/10.1002/qj.4782.
URL https://rmets.onlinelibrary.wiley.com/doi/abs/10.1002/qj.4782

Kawatani, Y., T. Hirooka, K. Hamilton, A. K. Smith, and M. Fujiwara, 2020: Representation of the equatorial stratopause semiannual oscillation in global atmospheric reanalyses. *Atmospheric Chemistry and Physics*, **20**, 9115–9133, doi:10.5194/acp-20-9115-2020.

Kiladis, G. N., M. C. Wheeler, P. T. Haertel, K. H. Straub, and P. E. Roundy, 2009: Convectively coupled equatorial waves. *Reviews of Geophysics*, **47**, doi:https://doi.org/10.1029/2008RG000266.
URL
https://agupubs.onlinelibrary.wiley.com/doi/abs/10.1029/2008RG000266

Kleist, D. T., D. F. Parrish, J. C. Derber, R. Treadon, W.-S. Wu, and S. Lord, 2009: Introduction of the gsi into the ncep global data assimilation system. *Weather and Forecasting*, **24**, 1691 – 1705, doi:10.1175/2009WAF2222201.1.
URL https:
//journals.ametsoc.org/view/journals/wefo/24/6/2009waf2222201_1.xml

Knippertz, P., M. Gehne, G. N. Kiladis, K. Kikuchi, A. Rasheeda Satheesh, P. E. Roundy, G.-Y. Yang, N. Žagar, J. Dias, A. H. Fink, J. Methven, A. Schlueter, F. Sielmann, and M. C. Wheeler, 2022: The intricacies of identifying equatorial waves. *Quarterly Journal of the Royal Meteorological Society*, **148**, 2814–2852, doi:https://doi.org/10.1002/qj.4338.
URL https://rmets.onlinelibrary.wiley.com/doi/abs/10.1002/qj.4338

Koster, R. D., M. J. Suarez, A. Ducharne, M. Stieglitz, and P. Kumar, 2000: A catchment-based approach to modeling land surface processes in a general circulation model: 1. model structure. *Journal of Geophysical Research: Atmospheres*, **105**, 24809–24822, doi:https://doi.org/10.1029/2000JD900327.
URL
https://agupubs.onlinelibrary.wiley.com/doi/abs/10.1029/2000JD900327

Krismer, T. R., M. A. Giorgetta, and M. Esch, 2013: Seasonal aspects of the quasi-biennial oscillation in the max planck institute earth system model and era-40.

Journal of Advances in Modeling Earth Systems, **5**, 406–421, doi:https://doi.org/10.1002/jame.20024.

Lee, H.-K., M.-J. Kang, H.-Y. Chun, D. Kim, and D.-B. Shin, 2022: Characteristics of latent heating rate from gpm and convective gravity wave momentum flux calculated using the gpm data. *Journal of Geophysical Research: Atmospheres*, **127**, e2022JD037003, doi:https://doi.org/10.1029/2022JD037003, e2022JD037003 2022JD037003.
URL
https://agupubs.onlinelibrary.wiley.com/doi/abs/10.1029/2022JD037003

Lieberman, R. S., J. France, D. A. Ortland, and S. D. Eckermann, 2021: The role of inertial instability in cross-hemispheric coupling. *Journal of the Atmospheric Sciences*, **78**, 1113 – 1127, doi:10.1175/JAS-D-20-0119.1.

Lin, S.-J. and R. B. Rood, 1997: An explicit flux-form semi-lagrangian shallow-water model on the sphere. *Quarterly Journal of the Royal Meteorological Society*, **123**, 2477–2498, doi:https://doi.org/10.1002/qj.49712354416.
URL
https://rmets.onlinelibrary.wiley.com/doi/abs/10.1002/qj.49712354416

Lindzen, R. S., 1981: Turbulence and stress owing to gravity wave and tidal breakdown. *Journal of Geophysical Research: Oceans*, **86**, 9707–9714, doi:https://doi.org/10.1029/JC086iC10p09707.
URL
https://agupubs.onlinelibrary.wiley.com/doi/abs/10.1029/JC086iC10p09707

Lindzen, R. S. and J. R. Holton, 1968: A theory of the quasi-biennial oscillation. *Journal of Atmospheric Sciences*, **25**, 1095 – 1107, doi:10.1175/1520-0469(1968)025<1095:ATOTQB>2.0.CO;2.
URL https://journals.ametsoc.org/view/journals/atsc/25/6/1520-0469_1968_025_1095_atotqb_2_0_co_2.xml

Liu, C., J. Alexander, J. Richter, and J. Bacmeister, 2022: Using trmm latent heat as a source to estimate convection induced gravity wave momentum flux in the lower stratosphere. *Journal of Geophysical Research: Atmospheres*, **127**, e2021JD035785, doi:https://doi.org/10.1029/2021JD035785, e2021JD035785 2021JD035785.
URL
https://agupubs.onlinelibrary.wiley.com/doi/abs/10.1029/2021JD035785

Lock, A. P., A. R. Brown, M. R. Bush, G. M. Martin, and R. N. B. Smith, 2000: A new boundary layer mixing scheme. part i: Scheme description and single-column model tests. *Monthly Weather Review*, **128**, 3187 – 3199, doi:10.1175/1520-0493(2000)128<3187:ANBLMS>2.0.CO;2.
URL https://journals.ametsoc.org/view/journals/mwre/128/9/1520-0493_2000_128_3187_anblms_2.0.co_2.xml

Lott, F. and L. Guez, 2013: A stochastic parameterization of the gravity waves due to convection and its impact on the equatorial stratosphere. *Journal of Geophysical Research: Atmospheres*, **118**, 8897–8909, doi:https://doi.org/10.1002/jgrd.50705.
URL https://agupubs.onlinelibrary.wiley.com/doi/abs/10.1002/jgrd.50705

Lott, F., L. Guez, and P. Maury, 2012: A stochastic parameterization of non-orographic gravity waves: Formalism and impact on the equatorial stratosphere. *Geophysical Research Letters*, **39**, doi:https://doi.org/10.1029/2012GL051001.
URL
https://agupubs.onlinelibrary.wiley.com/doi/abs/10.1029/2012GL051001

Lott, F. and M. J. Miller, 1997: A new subgrid-scale orographic drag parametrization: Its formulation and testing. *Quarterly Journal of the Royal Meteorological Society*, **123**, 101–127, doi:https://doi.org/10.1002/qj.49712353704.
URL
https://rmets.onlinelibrary.wiley.com/doi/abs/10.1002/qj.49712353704

Lott, F., R. Rani, C. McLandress, A. Podglajen, A. Bushell, M. Bramberger, H.-K. Lee, J. Alexander, J. Anstey, H.-Y. Chun, A. Hertzog, N. Butchart, Y.-H. Kim, Y. Kawatani, B. Legras, E. Manzini, H. Naoe, S. Osprey, R. Plougonven, H. Pohlmann, J. H. Richter, J. Scinocca, J. García-Serrano, F. Serva, T. Stockdale, S. Versick, S. Watanabe, and K. Yoshida, 2024: Comparison between non-orographic gravity-wave parameterizations used in qboi models and strateole 2 constant-level balloons. *Quarterly Journal of the Royal Meteorological Society*, **150**, 3721–3736, doi:https://doi.org/10.1002/qj.4793.
URL https://rmets.onlinelibrary.wiley.com/doi/abs/10.1002/qj.4793

Louis, J.-F., M. Tiedtke, and J.-F. Geleyn, 1982: *A short history of the PBL parameterization at ECMWF*. Ph.D. thesis, Shinfield Park, Reading, 59-79 pp.

Lu, H., T. J. Bracegirdle, T. Phillips, A. Bushell, and L. Gray, 2014: Mechanisms for the holton-tan relationship and its decadal variation. *Journal of Geophysical Research: Atmospheres*, **119**, 2811–2830, doi:https://doi.org/10.1002/2013JD021352.
URL
https://agupubs.onlinelibrary.wiley.com/doi/abs/10.1002/2013JD021352

Lu, H., L. J. Gray, P. Martineau, J. C. King, and T. J. Bracegirdle, 2021: Regime behavior in the upper stratosphere as a precursor of stratosphere–troposphere coupling in the northern winter. *Journal of Climate*, **34**, 7677 – 7696, doi:https://doi.org/10.1175/JCLI-D-20-0831.1.
URL https:
//journals.ametsoc.org/view/journals/clim/34/18/JCLI-D-20-0831.1.xml

Lu, H., M. H. Hitchman, L. J. Gray, J. A. Anstey, and S. M. Osprey, 2020: On the role of rossby wave breaking in the quasi-biennial modulation of the stratospheric polar vortex during boreal winter. *Quarterly Journal of the Royal Meteorological Society*, **146**, 1939–1959.

Martin, Z., C. Orbe, S. Wang, and A. Sobel, 2021: The mjo–qbo relationship in a gcm with stratospheric nudging. *Journal of Climate*, **34**, 4603 – 4624, doi:10.1175/JCLI-D-20-0636.1.
URL https:
//journals.ametsoc.org/view/journals/clim/34/11/JCLI-D-20-0636.1.xml

Maruyama, T., 1969: Long-term behaviour of kelvin waves and mixed rassby. gravity waves. *Journal of the Meteorological Society of Japan. Ser. II*, **47**, 245–254.

Matsuno, T., 1966: Quasi-geostrophic motions in the equatorial area. *Journal of the Meteorological Society of Japan. Ser. II*, **44**, 25–43, doi:10.2151/jmsj1965.44.1$_2$5.

McFarlane, N. A., 1987: The effect of orographically excited gravity wave drag on the general circulation of the lower stratosphere and troposphere. *Journal of Atmospheric Sciences*, **44**, 1775 – 1800, doi:https://doi.org/10.1175/1520-0469(1987)044<1775:TEOOEG>2.0.CO;2. URL https://journals.ametsoc.org/view/journals/atsc/44/14/1520-0469_1987_044_1775_teooeg_2_0_co_2.xml

Menary, M. B., T. Kuhlbrodt, J. Ridley, M. B. Andrews, O. B. Dimdore-Miles, J. Deshayes, R. Eade, L. Gray, S. Ineson, J. Mignot, C. D. Roberts, J. Robson, R. A. Wood, and P. Xavier, 2018: Preindustrial control simulations with hadgem3-gc3.1 for cmip6. *Journal of Advances in Modeling Earth Systems*, **10**, 3049–3075, doi:https://doi.org/10.1029/2018MS001495. URL https://agupubs.onlinelibrary.wiley.com/doi/abs/10.1029/2018MS001495

Meyer, W. D., 1970: A diagnostic numerical study of the semiannual variation of the zonal wind in the tropical stratosphere and mesosphere. *Journal of Atmospheric Sciences*, **27**, 820 – 830, doi:10.1175/1520-0469(1970)027<0820:ADNSOT>2.0.CO;2.

Mlawer, E. J., S. J. Taubman, P. D. Brown, M. J. Iacono, and S. A. Clough, 1997: Radiative transfer for inhomogeneous atmospheres: Rrtm, a validated correlated-k model for the longwave. *Journal of Geophysical Research: Atmospheres*, **102**, 16663–16682, doi:https://doi.org/10.1029/97JD00237. URL https://agupubs.onlinelibrary.wiley.com/doi/abs/10.1029/97JD00237

Molod, A., L. Takacs, M. Suarez, and J. Bacmeister, 2015: Development of the geos-5 atmospheric general circulation model: evolution from merra to merra2. *Geoscientific Model Development*, **8**, 1339–1356, doi:10.5194/gmd-8-1339-2015. URL https://gmd.copernicus.org/articles/8/1339/2015/

Moolakkunnel Jaison, A., L. J. Gray, S. M. Osprey, J. R. Knight, and M. B. Andrews, 2024: Role of the quasi-biennial oscillation on alleviating biases in the semi-annual oscillation. *EGUsphere*, **2024**, 1–26, doi:10.5194/egusphere-2024-1818. URL https://egusphere.copernicus.org/preprints/2024/egusphere-2024-1818/

Moorthi, S. and M. J. Suarez, 1992: Relaxed arakawa-schubert. a parameterization of moist convection for general circulation models. *Monthly Weather Review*, **120**, 978 – 1002, doi:10.1175/1520-0493(1992)120<0978:RASAPO>2.0.CO;2. URL https://journals.ametsoc.org/view/journals/mwre/120/6/1520-0493_1992_120_0978_rasapo_2_0_co_2.xml

Mukougawa, H., T. Hirooka, and Y. Kuroda, 2009: Influence of stratospheric circulation on the predictability of the tropospheric northern annular mode. *Geophysical Research Letters*, **36**.

Müller, K. M., U. Langematz, and S. Pawson, 1997: The Stratopause Semiannual Oscillation in the Berlin Troposphere-Stratosphere-Mesosphere GCM. *Journal of Atmospheric Sciences*, **54**, 2749–2759, doi:10.1175/1520-0469(1997)054<2749:TSSOIT>2.0.CO;2.

Murgatroyd, R. J. and F. Singleton, 1961: Possible meridional circulations in the stratosphere and mesosphere. *Quarterly Journal of the Royal Meteorological Society*, **87**, 125–135, doi:https://doi.org/10.1002/qj.49708737202.
URL `https://rmets.onlinelibrary.wiley.com/doi/abs/10.1002/qj.49708737202`

Norton, W. A. and J. Thuburn, 1996: The two-day wave in a middle atmosphere gcm. *Geophysical Research Letters*, **23**, 2113–2116, doi:https://doi.org/10.1029/96GL01956.
URL `https://agupubs.onlinelibrary.wiley.com/doi/abs/10.1029/96GL01956`

Orr, A., P. Bechtold, J. Scinocca, M. Ern, and M. Janiskova, 2010: Improved middle atmosphere climate and forecasts in the ecmwf model through a nonorographic gravity wave drag parameterization. *Journal of Climate*, **23**, 5905 – 5926, doi:https://doi.org/10.1175/2010JCLI3490.1.
URL
`https://journals.ametsoc.org/view/journals/clim/23/22/2010jcli3490.1.xml`

Pahlavan, H. A., Q. Fu, J. M. Wallace, and G. N. Kiladis, 2021: Revisiting the quasi-biennial oscillation as seen in era5. part i: Description and momentum budget. *Journal of the Atmospheric Sciences*, **78**, 673 – 691, doi:10.1175/JAS-D-20-0248.1.

Pascoe, C. L., L. J. Gray, S. A. Crooks, M. N. Juckes, and M. P. Baldwin, 2005: The quasi-biennial oscillation: Analysis using era-40 data. *Journal of Geophysical Research: Atmospheres*, **110**, doi:https://doi.org/10.1029/2004JD004941.
URL `https://agupubs.onlinelibrary.wiley.com/doi/abs/10.1029/2004JD004941`

Pascoe, C. L., L. J. Gray, and A. A. Scaife, 2006: A gcm study of the influence of equatorial winds on the timing of sudden stratospheric warmings. *Geophysical Research Letters*, **33**, doi:https://doi.org/10.1029/2005GL024715.
URL `https://agupubs.onlinelibrary.wiley.com/doi/abs/10.1029/2005GL024715`

Peña-Ortiz, C., P. Ribera, R. García-Herrera, M. A. Giorgetta, and R. R. García, 2008: Forcing mechanism of the seasonally asymmetric quasi-biennial oscillation secondary circulation in era-40 and maecham5. *Journal of Geophysical Research: Atmospheres*, **113**, doi:https://doi.org/10.1029/2007JD009288.
URL `https://agupubs.onlinelibrary.wiley.com/doi/abs/10.1029/2007JD009288`

Peña-Ortiz, C., H. Schmidt, M. A. Giorgetta, and M. Keller, 2010: Qbo modulation of the semiannual oscillation in maecham5 and hammonia. *Journal of Geophysical Research: Atmospheres*, **115**, doi:https://doi.org/10.1029/2010JD013898.
URL `https://agupubs.onlinelibrary.wiley.com/doi/abs/10.1029/2010JD013898`

Plumb, R. A., 1983: Baroclinic instability of the summer mesosphere: A mechanism for the quasi-two-day wave? *Journal of Atmospheric Sciences*, **40**, 262 – 270, doi:https://doi.org/10.1175/1520-0469(1983)040<0262:BIOTSM>2.0.CO;2.
URL `https://journals.ametsoc.org/view/journals/atsc/40/1/1520-0469_1983_040_0262_biotsm_2_0_co_2.xml`

— 1984: The quasi-biennial oscillation. *Dynamics of the Middle Atmosphere*, 217–251, doi:10.1007/978-94-009-6390-$0_1$3.

Plumb, R. A. and R. C. Bell, 1982: A model of the quasi-biennial oscillation on an equatorial beta-plane. *Quarterly Journal of the Royal Meteorological Society*, **108**, 335–352, doi:https://doi.org/10.1002/qj.49710845604.
URL https://rmets.onlinelibrary.wiley.com/doi/abs/10.1002/qj.49710845604

Polichtchouk, I., R. J. Hogan, T. G. Shepherd, P. Bechtold, T. Stockdale, S. Malardel, S.-J. Lock, and L. Magnusson, 2017: *What influences the middle atmosphere circulation in the IFS?*. European Centre for Medium Range Weather Forecasts.

Quiroz, R. S. and A. J. Miller, 1967: Note on the semi-annual wind variation in the equatorial stratosphere. *Monthly Weather Review*, **95**, 635 – 641, doi:10.1175/1520-0493(1967)095<0635:NOTSAW>2.3.CO;2.

Rajendran, K., I. M. Moroz, P. L. Read, and S. M. Osprey, 2016: Synchronisation of the equatorial qbo by the annual cycle in tropical upwelling in a warming climate. *Quarterly Journal of the Royal Meteorological Society*, **142**, 1111–1120, doi:https://doi.org/10.1002/qj.2714.
URL https://rmets.onlinelibrary.wiley.com/doi/abs/10.1002/qj.2714

Rao, J., C. I. Garfinkel, and I. P. White, 2020: Impact of the quasi-biennial oscillation on the northern winter stratospheric polar vortex in cmip5/6 models. *Journal of Climate*, **33**, 4787 – 4813, doi:https://doi.org/10.1175/JCLI-D-19-0663.1.
URL https://journals.ametsoc.org/view/journals/clim/33/11/jcli-d-19-0663.1.xml

Rapp, M., A. Dörnbrack, and P. Preusse, 2018: Large midlatitude stratospheric temperature variability caused by inertial instability: A potential source of bias for gravity wave climatologies. *Geophysical Research Letters*, **45**, 10,682–10,690, doi:https://doi.org/10.1029/2018GL079142.
URL https://agupubs.onlinelibrary.wiley.com/doi/abs/10.1029/2018GL079142

Ray, E. A., M. J. Alexander, and J. R. Holton, 1998: An analysis of the structure and forcing of the equatorial semiannual oscillation in zonal wind. *Journal of Geophysical Research: Atmospheres*, **103**, 1759–1774, doi:https://doi.org/10.1029/97JD02679.

Ray, E. A., J. R. Holton, E. F. Fishbein, L. Froidevaux, and J. W. Waters, 1994: The tropical semiannual oscillations in temperature and ozone as observed by the mls. *Journal of Atmospheric Sciences*, **51**, 3045 – 3052, doi:10.1175/1520-0469(1994)051<3045:TTSOIT>2.0.CO;2.
URL https://journals.ametsoc.org/view/journals/atsc/51/20/1520-0469_1994_051_3045_ttsoit_2_0_co_2.xml

Reed, R. J., 1966: Zonal wind behavior in the equatorial stratosphere and lower mesosphere. *Journal of Geophysical Research*, **71**, 4223–4233.

Reed, R. J., W. J. Campbell, L. A. Rasmussen, and D. G. Rogers, 1961: Evidence of a downward-propagating, annual wind reversal in the equatorial stratosphere. *Journal of Geophysical Research (1896-1977)*, **66**, 813–818, doi:https://doi.org/10.1029/JZ066i003p00813.
URL https://agupubs.onlinelibrary.wiley.com/doi/abs/10.1029/JZ066i003p00813

Richter, J. H. and R. R. Garcia, 2006: On the forcing of the mesospheric semi-annual oscillation in the whole atmosphere community climate model. *Geophysical Research Letters*, **33**, doi:https://doi.org/10.1029/2005GL024378.
URL https://agupubs.onlinelibrary.wiley.com/doi/abs/10.1029/2005GL024378

Richter, J. H., F. Sassi, and R. R. Garcia, 2010: Toward a physically based gravity wave source parameterization in a general circulation model. *Journal of the Atmospheric Sciences*, **67**, 136 – 156, doi:10.1175/2009JAS3112.1.

Salby, M. L., 1981: The 2-day wave in the middle atmosphere: Observations and theory. *Journal of Geophysical Research: Oceans*, **86**, 9654–9660, doi:https://doi.org/10.1029/JC086iC10p09654.
URL https://agupubs.onlinelibrary.wiley.com/doi/abs/10.1029/JC086iC10p09654

— 1984: Survey of planetary-scale traveling waves: The state of theory and observations. *Reviews of Geophysics*, **22**, 209–236, doi:https://doi.org/10.1029/RG022i002p00209.
URL https://agupubs.onlinelibrary.wiley.com/doi/abs/10.1029/RG022i002p00209

Scaife, A. A., N. Butchart, C. D. Warner, and R. Swinbank, 2002: Impact of a spectral gravity wave parameterization on the stratosphere in the met office unified model. *Journal of the Atmospheric Sciences*, **59**, 1473 – 1489, doi:10.1175/1520-0469(2002)059<1473:IOASGW>2.0.CO;2.
URL https://journals.ametsoc.org/view/journals/atsc/59/9/1520-0469_2002_059_1473_ioasgw_2.0.co_2.xml

Scaife, A. A., J. R. Knight, G. K. Vallis, and C. K. Folland, 2005: A stratospheric influence on the winter nao and north atlantic surface climate. *Geophysical Research Letters*, **32**.

Scinocca, J. F., 2003a: An accurate spectral nonorographic gravity wave drag parameterization for general circulation models. *Journal of the Atmospheric Sciences*, **60**, 667 – 682, doi:10.1175/1520-0469(2003)060<0667:AASNGW>2.0.CO;2.
URL https://journals.ametsoc.org/view/journals/atsc/60/4/1520-0469_2003_060_0667_aasngw_2.0.co_2.xml

— 2003b: An accurate spectral nonorographic gravity wave drag parameterization for general circulation models. *Journal of the Atmospheric Sciences*, **60**, 667 – 682, doi:10.1175/1520-0469(2003)060<0667:AASNGW>2.0.CO;2.
URL https://journals.ametsoc.org/view/journals/atsc/60/4/1520-0469_2003_060_0667_aasngw_2.0.co_2.xml

Serva, F., B. Christiansen, P. Davini, J. von Hardenberg, G. van den Oord, T. J. Reerink, K. Wyser, and S. Yang, 2024: Changes in stratospheric dynamics simulated by the ec-earth model from cmip5 to cmip6. *Journal of Advances in Modeling Earth Systems*, **16**, e2023MS003756, doi:https://doi.org/10.1029/2023MS003756, e2023MS003756 2023MS003756.
URL https://agupubs.onlinelibrary.wiley.com/doi/abs/10.1029/2023MS003756

Shepherd, T., I. Polichtchouk, R. Hogan, and A. Simmons, 2018: Report on stratosphere task force. doi:10.21957/0vkp0t1xx.

Shu, J., W. Tian, D. Hu, J. Zhang, L. Shang, H. Tian, and F. Xie, 2013: Effects of the quasi-biennial oscillation and stratospheric semiannual oscillation on tracer transport in the upper stratosphere. *Journal of the Atmospheric Sciences*, **70**, 1370 – 1389, doi:10.1175/JAS-D-12-053.1.

Sigmond, M., J. Scinocca, V. Kharin, and T. Shepherd, 2013: Enhanced seasonal forecast skill following stratospheric sudden warmings. *Nature Geoscience*, **6**, 98–102.

Smith, A. K., R. R. Garcia, A. C. Moss, and N. J. Mitchell, 2017: The semiannual oscillation of the tropical zonal wind in the middle atmosphere derived from satellite geopotential height retrievals. *Journal of the Atmospheric Sciences*, **74**, 2413 – 2425, doi:10.1175/JAS-D-17-0067.1.

Smith, A. K., L. J. Gray, and R. R. Garcia, 2023: Evidence for the influence of the quasi-biennial oscillation on the semiannual oscillation in the tropical middle atmosphere. *Journal of the Atmospheric Sciences*, **80**, 1755 – 1769, doi:https://doi.org/10.1175/JAS-D-22-0255.1.
URL
https://journals.ametsoc.org/view/journals/atsc/80/7/JAS-D-22-0255.1.xml

Smith, A. K., L. A. Holt, R. R. Garcia, J. A. Anstey, F. Serva, N. Butchart, S. Osprey, A. C. Bushell, Y. Kawatani, Y.-H. Kim, F. Lott, P. Braesicke, C. Cagnazzo, C.-C. Chen, H.-Y. Chun, L. Gray, T. Kerzenmacher, H. Naoe, J. Richter, S. Versick, V. Schenzinger, S. Watanabe, and K. Yoshida, 2019: The equatorial stratospheric semiannual oscillation and time-mean winds in qboi models. *Quarterly Journal of the Royal Meteorological Society*, **148**, 1593–1609, doi:https://doi.org/10.1002/qj.3690.

Smith, S. A., D. C. Fritts, and T. E. Vanzandt, 1987: Evidence for a saturated spectrum of atmospheric gravity waves. *Journal of Atmospheric Sciences*, **44**, 1404 – 1410, doi:10.1175/1520-0469(1987)044<1404:EFASSO>2.0.CO;2.
URL https://journals.ametsoc.org/view/journals/atsc/44/10/1520-0469_1987_044_1404_efasso_2_0_co_2.xml

Solomon, S., J. T. Kiehl, R. R. Garcia, and W. Grose, 1986: Tracer transport by the diabatic circulation deduced from satellite observations. *Journal of Atmospheric Sciences*, **43**, 1603 – 1617, doi:10.1175/1520-0469(1986)043<1603:TTBTDC>2.0.CO;2.
URL https://journals.ametsoc.org/view/journals/atsc/43/15/1520-0469_1986_043_1603_ttbtdc_2_0_co_2.xml

SPARC, 2021: Cambridge University Press. 533–582.

— 2022: Sparc reanalysis intercomparison project (s-rip) final report. Technical report, 10th assessment report of the SPARC project, published by the International Project Office at DLR-IPA. also: WCRP Report 6/2021.
URL https://elib.dlr.de/148623/

Strube, C., M. Ern, P. Preusse, and M. Riese, 2020: Removing spurious inertial instability signals from gravity wave temperature perturbations using spectral filtering methods. *Atmospheric Measurement Techniques*, **13**, 4927–4945, doi:10.5194/amt-13-4927-2020.
URL https://amt.copernicus.org/articles/13/4927/2020/

Tiedtke, M., 1989: A comprehensive mass flux scheme for cumulus parameterization in large-scale models. *Monthly Weather Review*, **117**, 1779 – 1800, doi:10.1175/1520-0493(1989)117<1779:ACMFSF>2.0.CO;2.
URL https://journals.ametsoc.org/view/journals/mwre/117/8/1520-0493_1989_117_1779_acmfsf_2_0_co_2.xml

— 1993: Representation of clouds in large-scale models. *Monthly Weather Review*, **121**, 3040 – 3061, doi:10.1175/1520-0493(1993)121<3040:ROCILS>2.0.CO;2.
URL https://journals.ametsoc.org/view/journals/mwre/121/11/1520-0493_1993_121_3040_rocils_2_0_co_2.xml

Tompkins, A. M., K. Gierens, and G. Rädel, 2007: Ice supersaturation in the ecmwf integrated forecast system. *Quarterly Journal of the Royal Meteorological Society*, **133**, 53–63, doi:https://doi.org/10.1002/qj.14.
URL https://rmets.onlinelibrary.wiley.com/doi/abs/10.1002/qj.14

Vallis, G. K., 2017: *The Stratosphere*, Cambridge University Press. 2 edition, 627–672.

VanZandt, T. E., 1982: A universal spectrum of buoyancy waves in the atmosphere. *Geophysical Research Letters*, **9**, 575–578, doi:https://doi.org/10.1029/GL009i005p00575.
URL
https://agupubs.onlinelibrary.wiley.com/doi/abs/10.1029/GL009i005p00575

Wallace, J. M., 1967: A note on the role of radiation in the biennial oscillation. *Journal of Atmospheric Sciences*, **24**, 598 – 599, doi:https://doi.org/10.1175/1520-0469(1967)024<0598:ANOTRO>2.0.CO;2.
URL https://journals.ametsoc.org/view/journals/atsc/24/5/1520-0469_1967_024_0598_anotro_2_0_co_2.xml

Wallace, J. M. and J. R. Holton, 1968: A diagnostic numerical model of the quasi-biennial oscillation. *Journal of Atmospheric Sciences*, **25**, 280 – 292, doi:https://doi.org/10.1175/1520-0469(1968)025<0280:ADNMOT>2.0.CO;2.
URL https://journals.ametsoc.org/view/journals/atsc/25/2/1520-0469_1968_025_0280_adnmot_2_0_co_2.xml

Warner, C. D. and M. E. McIntyre, 1996: On the propagation and dissipation of gravity wave spectra through a realistic middle atmosphere. *Journal of Atmospheric Sciences*, **53**, 3213 – 3235, doi:10.1175/1520-0469(1996)053<3213:OTPADO>2.0.CO;2.
URL https://journals.ametsoc.org/view/journals/atsc/53/22/1520-0469_1996_053_3213_otpado_2_0_co_2.xml

— 1999: Toward an ultra-simple spectral gravity wave parameterization for general circulation models. *Earth, planets and space*, **51**, 475–484.

— 2001: An ultrasimple spectral parameterization for nonorographic gravity waves. *Journal of the Atmospheric Sciences*, **58**, 1837 – 1857, doi:10.1175/1520-0469(2001)058<1837:AUSPFN>2.0.CO;2.
URL https://journals.ametsoc.org/view/journals/atsc/58/14/1520-0469_2001_058_1837_auspfn_2.0.co_2.xml

Webb, W. L., 1967: Structure of the stratosphere and mesosphere, by w. l. webb. new york and london (academic press). 1966. pp. 380, 183 figures. *Quarterly Journal of the Royal Meteorological Society*, **93**, 407–407, doi:https://doi.org/10.1002/qj.49709339722.

Wheeler, M. and G. N. Kiladis, 1999: Convectively coupled equatorial waves: Analysis of clouds and temperature in the wavenumber–frequency domain. *Journal of the Atmospheric Sciences*, **56**, 374 – 399, doi:https://doi.org/10.1175/1520-0469(1999)056<0374:CCEWAO>2.0.CO;2.
URL `https://journals.ametsoc.org/view/journals/atsc/56/3/1520-0469_1999_056_0374_ccewao_2.0.co_2.xml`

Wu, W.-S., R. J. Purser, and D. F. Parrish, 2002: Three-dimensional variational analysis with spatially inhomogeneous covariances. *Monthly Weather Review*, **130**, 2905 – 2916, doi:10.1175/1520-0493(2002)130<2905:TDVAWS>2.0.CO;2.
URL `https://journals.ametsoc.org/view/journals/mwre/130/12/1520-0493_2002_130_2905_tdvaws_2.0.co_2.xml`